



**HAL**  
open science

# Digital Signal Processing for Next-Generation Passive Optical Networks

Tuan-Anh Truong

► **To cite this version:**

Tuan-Anh Truong. Digital Signal Processing for Next-Generation Passive Optical Networks. Signal and Image processing. Télécom Bretagne; Université de Bretagne Occidentale, 2014. English. NNT : . tel-01191521

**HAL Id: tel-01191521**

**<https://hal.science/tel-01191521>**

Submitted on 2 Sep 2015

**HAL** is a multi-disciplinary open access archive for the deposit and dissemination of scientific research documents, whether they are published or not. The documents may come from teaching and research institutions in France or abroad, or from public or private research centers.

L'archive ouverte pluridisciplinaire **HAL**, est destinée au dépôt et à la diffusion de documents scientifiques de niveau recherche, publiés ou non, émanant des établissements d'enseignement et de recherche français ou étrangers, des laboratoires publics ou privés.



**THÈSE / Télécom Bretagne**  
sous le sceau de l'Université européenne de Bretagne  
pour obtenir le grade de Docteur de Télécom Bretagne  
En accréditation conjointe avec l'École Doctorale Sicma  
mention : Sciences et Technologies de l'Information et de la Communication

présentée par

**Tuan Anh Truong**

préparée dans le département Électronique  
Laboratoire Labsticc

# Digital Signal Processing for Next-Generation Passive Optical Networks

Thèse soutenue le 28 novembre 2014

Devant le jury composé de :

**Jean-François Hélaré**  
Professeur, Insa - Rennes / président

**Michel Joindot**  
Professeur Émérite, Enssat - Lannion / rapporteur

**Didier Erasme**  
Professeur, Télécom ParisTech / rapporteur

**Naveena Genay**  
Ingénieur de recherche, FT/Orange Labs - Lannion / examinatrice

**Bruno Jahan**  
Ingénieur de recherche, FT/Orange Labs - Cesson Sévigné / examinateur

**Hao Lin**  
Ingénieur de recherche, FT/Orange Labs - Cesson Sévigné / examinateur

**Mathieu Arzel**  
Maître de Conférences, Télécom Bretagne / examinateur

**Michel Jézéquel**  
Professeur, Télécom Bretagne / directeur de thèse

**Sous le sceau de l'Université européenne de Bretagne**

# **Télécom Bretagne**

**En accréditation conjointe avec l'Ecole Doctorale Sicma**

---

## **DIGITAL SIGNAL PROCESSING FOR NEXT-GENERATION PASSIVE OPTICAL NETWORKS**

---

### **Thèse de Doctorat**

Mention : STIC

Présentée par **Tuan Anh Truong**

Département : ELEC

Laboratoire : Lab-STICC. Equipe : IAS

Directeur de thèse : Michel Jézéquel

Soutenue le 28 Novembre 2014

#### **Jury :**

M. Jean-François Hélard	Professeur, INSA Rennes	Président
M. Michel Joindot	Professeur, ENSSAT	Rapporteur
M. Didier Erasme	Professeur, Télécom ParisTech	Rapporteur
Mme. Naveena Genay	Ingénieur R&D, Orange Labs Lannion	Examinatrice
M. Michel Jézéquel	Professeur, Télécom Bretagne	Directeur de thèse
M. Matthieu Arzel	Maître de Conférences, Télécom Bretagne	Examineur
M. Hao Lin	Ingénieur R&D, Orange Labs Rennes	Examineur
M. Bruno Jahan	Ingénieur R&D, Orange Labs Rennes	Examineur



*To my parents*



# Acknowledgment

Foremost, I would like to express my sincere gratitude to my supervisors Mr. Bruno JAHAN and Dr. Hao LIN at Orange Labs, in Rennes for the continuous support of my PhD study and research, for their patience, motivation and enthusiasm. Their guidance helped me in all the time of research and writing of this thesis.

I would also like to thank my academic supervisors Dr. Matthieu ARZEL and Prof. Michel JEZEQUEL at Télécom Bretagne, in Brest for their guidance and suggestions during the PhD period. Your advice and guidance have been priceless.

I would like to thank my committee members: Prof. Michel JOINDOT, Prof. Didier ERASME, Prof. Jean-François HELARD and Mrs. Naveena GENAY for agreeing to review my thesis and for their useful remarks.

Many thanks also for the team ASHA at Orange Labs, in Lannion for the help during my stay at Lannion. Particularly, I would like to thank Mrs. Naveena GENAY for her detailed instructions in the laboratory. Without her help, I would not achieve this work. I would also like to thank Prof. Didier ERASME for accepting my visit at Télécom Paris Tech where we had many fruitful discussions. I would like to express my deep thanks to Mr. Yves JAOUEN at Télécom Paris Tech for his help on my work. Your knowledge and patience have been really invaluable to me.

I am also deeply grateful to my host team, the CREM in Rennes. I wish to thank my team leader Mr. Jean-Christophe RAULT for giving me the opportunity to work on this project. I would also like to thank all the CREM members for useful discussions.

A special thanks to my family. My gratitude to my parents cannot be expressed by words. I would like to thank them for all of the sacrifices that they have made on my behalf. I would also like to thank my friends who were always my support at the most difficult moments during this PhD period.

Rennes, June 27, 2014.



# Abstract

This thesis aims at improving the spectral efficiency of fiber-based optical transmissions in the context of access networks where an Intensity Modulated/Direct Detected (IMDD) technique is used. In such a context, an increase of fiber length or data rate might lead to significant inter symbol interference problem. For the reason of cost, instead of investing in expensive technologies, a telecom operator might prefer compensating transmission detriments by means of signal processing techniques. In this thesis, the compensation of transmission detriments using signal processing techniques is addressed. In addition, the potential of advanced modulation techniques such as the Orthogonal Frequency Division Multiplexing (OFDM) is also studied. The studies described in this thesis are extensively based on numerical simulation results. Therefore, the first part of this thesis is dedicated to the modeling of an optical transmission link. Both model parameter extraction and model validation are carried out by means of experimental measures.

Based on the channel model, the first study concerns channel equalization techniques for a conventional on-off-keying non return-to-zero transmission. It is found that linear equalization techniques may extend transmission reach by tens of kilometers. When nonlinear equalizers are used, reach is further extended by tens of kilometers and chromatic dispersion-induced power penalty is improved by up to 2 dB. Moreover, when the Nyquist pulse-shaping technique is used, the power penalty is further improved by 2 dB.

The second study in this thesis is dedicated to the performance evaluation of OFDM modulation. Particularly, conventional Levin-Campello bit/power loading OFDM systems are subjected to the study. Based on the Discrete Fourier Transform (DFT) precoding technique, a precoded OFDM system is also proposed. Having the same data-rate performance when compared to the Levin-Campello system, the proposed system significantly reduces the Peak-to-Average Power Ratio (PAPR) of a transmitted signal, resulting in reduced power consumption of the power amplifier on the transmitter side. Moreover, when compared to the actual on-off-keying modulation, the OFDM modulation is shown to be more robust against chromatic dispersion and laser chirps.

Finally, conventional and proposed techniques to compensate for OFDM disadvantages including the important PAPR and the sensitivity to timing synchronization are investigated. The proposed synchronization techniques are shown to outperform conventional techniques in terms of timing offset variance and complexity. To reduce the PAPR of a transmitted OFDM signal, a contiguous-tone tone reservation technique is proposed. When this technique is used in a precoded OFDM system, the PAPR is shown to be reduced by up to 4 dB.



# Résumé

Cette thèse vise à améliorer l'efficacité spectrale des transmissions sur fibres optiques dans le cadre de réseaux d'accès où une technique de modulation d'intensité et de détection directe (IMDD) est utilisée. Dans un tel contexte, une augmentation de la longueur de fibre ou du débit de données pourrait conduire à une importante interférence entre symboles. Dans cette thèse, l'utilisation des techniques de traitement du signal pour compenser des défauts du canal de transmission est analysée. En outre, le potentiel de techniques de modulation avancées telles que le multiplexage par répartition orthogonale de la fréquence (OFDM) est également étudié. Puisque les études décrites dans cette thèse sont largement basées sur les résultats de simulations numériques, la première partie de ce mémoire est dédiée à la modélisation avancée d'une liaison de transmission sur fibres optiques. À la fois l'extraction des paramètres et la validation du modèle sont réalisées avec des mesures expérimentales.

Exploitant le modèle du canal, la première étude concerne les techniques d'égalisation de canal pour une transmission classique de type non retour à zéro (NRZ). Il se trouve que les techniques d'égalisation linéaires peuvent augmenter la portée de transmission par une douzaine de kilomètres. Lorsque des égaliseurs non linéaires sont utilisés, la portée est davantage augmentée par plusieurs dizaines de kilomètres et la pénalité de puissance à cause de la dispersion chromatique est améliorée jusqu'à 2 dB. En outre, lorsque le filtre de mise en forme de Nyquist est utilisé, la pénalité de puissance est encore améliorée par 2 dB.

La deuxième étude de cette thèse est consacrée à l'évaluation des performances de la modulation OFDM. En particulier, les systèmes conventionnels de modulation adaptés proposés par Levin-Campello sont soumis à l'étude. En précodant des symboles OFDM par une matrice de la transformation de Fourier discrète (DFT), un système OFDM précodé est également proposé. Ayant les mêmes performances en termes de débit par rapport au système Levin-Campello, le système proposé permet de réduire de manière significative le facteur de crête (PAPR) d'un signal transmis, ce qui réduit la consommation de puissance d'un amplificateur de puissance à l'émetteur. De plus, par rapport à la modulation tout ou rien (OOK), la modulation OFDM est montrée comme plus robuste contre la dispersion chromatique et les chirps du laser.

Enfin, les techniques conventionnelles et proposées pour compenser des défauts d'une modulation OFDM, y compris l'important PAPR et la sensibilité à la synchronisation temporelle sont étudiées. Les techniques proposées pour la synchronisation temporelle ont des meilleures performances en termes de précision et complexité par rapport aux techniques classiques. Pour réduire le PAPR d'un signal OFDM, une technique basée sur des pilotes réservées est proposée. Dans un système OFDM précodé, cette technique apporte une réduction de PAPR pouvant atteindre 4 dB dans le contexte du réseau d'accès optique.

## Chapitre 1 – Les systèmes de transmission basés sur la technique IMDD

Le premier chapitre qui suit la courte introduction générale décrit les systèmes de transmission à modulation d'intensité et détection directe. Ce choix est justifié par le fait que l'étude se place dans le cadre du développement industriel mené par l'opérateur de télécommunications Orange qui accueille la thèse. Selon sa stratégie de développement du réseau d'accès optique, le réseau PON (Passive Optical Network) a été choisi. Dans ce premier chapitre, différents composants et différents effets physiques rencontrés dans ce type de liaison ont été décrits :

- les sources de bruit dans une chaîne de transmission IMDD,
- les effets linéaires y compris l'atténuation et la dispersion chromatique du lien de transmission sur fibre optique,
- les effets non-linéaires principaux d'une transmission IMDD y compris l'auto-modulation de phase, la modulation croisée et le mélange à quatre ondes.

Le chapitre se termine par l'identification des composants principaux dans une chaîne de transmission IMDD y compris :

- le laser qui convertit un signal électrique en un signal optique ; les paramètres du laser y compris la bande passante, le chirp adiabatique et transitoire a un impact direct sur la capacité d'une transmission IMDD ;
- la fibre optique dont l'atténuation, la dispersion chromatique et le paramètre de non-linéarité sont des principales sources de perturbation du signal reçu,

le photo-détecteur dont les sources de bruit sont parmi des facteurs qui limitent le débit d'une transmission IMDD.

## Chapitre 2 – Modélisation numérique du canal

Après avoir identifié les composants clés dans une liaison IMDD, le deuxième chapitre est consacré à la conception d'un modèle numérique représentatif du canal de transmission. A partir des modèles existant dans la littérature, ce chapitre justifie le choix d'un modèle plus réaliste. L'extraction des paramètres du modèle a été effectuée sur des composants réels dans le laboratoire Orange Labs à Lannion. Les paramètres extraits sont la base du modèle numérique du canal. Une conclusion importante de ce chapitre est que, le modèle numérique se base sur des composants réels et la simulation numérique a été validée avec des mesures expérimentales. Ce modèle est essentiel pour l'évaluation des performances des techniques de traitement du signal proposées dans le cadre de la thèse. Le modèle réaliste développé dans ce chapitre est un résultat aussi important et critique pour la thèse que pour les études à venir de l'entité Orange Labs. Avec ce modèle, des techniques de traitement du signal innovantes pourraient être analysées sans avoir une contrainte sur la disponibilité des équipements laboratoires.

Pour la modélisation du laser, nous avons repris le modèle de « rate equations » qui est bien connu dans la littérature. Ces équations décrivent la relation de la puissance et la phase du signal optique avec la densité du porteur électrique, qui est modulée par le signal électrique à transmettre. Dans ce modèle, il y a des paramètres non-connus qui peuvent être extraits à partir des mesures expérimentales.

La propagation d'un signal optique dans une fibre optique peut être décrite par l'équation non-linéaire de Schrodinger, ce qui prend en compte les effets linéaires et les effets non-linéaires de Kerr. Cette équation non-linéaire peut être résolue numériquement par la méthode « Split Step Fourier ».

Pour les applications dans le cadre du réseau d'accès, la bande passante de la photodiode est suffisamment large par rapport à la bande passante du signal transmis. Il est donc possible de négliger la réponse fréquentielle de la photodiode. Par conséquence, nous nous intéressons seulement au bruit de la photodiode.

Le modèle a aussi été validé par des mesures expérimentales. Dans cette validation, nous avons comparé le signal reçu à l'issue de la simulation numérique avec celui à l'issue de l'expérimentation. Afin de quantifier la validité du modèle, nous avons défini le paramètre MSER (Model Signal-to-Error Ratio) qui est le rapport entre la puissance du signal transmis et la puissance de l'erreur entre la simulation et l'expérimentation. Selon la validation, un MSER jusqu'à 17 dB a été obtenu, ce qui valide le modèle du canal.

## Chapitre 3 – L'égalisation et la mise en forme Nyquist pour les futurs PONs

Dans une transmission IMDD, la dispersion chromatique rend le canal sélectif en fréquence. Pour cette raison, une proposition d'amélioration est l'utilisation des techniques d'égalisation de canal. Dans ce chapitre, plusieurs types d'égaliseur ont été étudiés

- égalisation par filtre transverse (le signal reçu est filtré par un filtre de réponse impulsionnelle finie afin de minimiser l'erreur quadratique moyenne),
- égalisation par retour de décision (l'interférence résiduelle après le filtre transverse est réduite grâce au retour de décision),
- estimateur par maximum vraisemblance (la séquence de symboles transmis est estimée grâce à l'algorithme de Viterbi).

De plus, la mise en forme par le filtre Nyquist a été aussi proposée pour remplacer la mise en forme conventionnelle de type NRZ.

Les études dans ce chapitre ont montré que, pour une transmission à 10 giga bits par second (Gb/s), l'égalisation par filtre transverse permet d'étendre la portée de dizaine de kilomètres. L'égalisation par retour de décision a une meilleure performance que l'égalisation par filtre transverse et l'estimateur par maximum vraisemblance donne la meilleure performance parmi les trois techniques d'égalisation. De plus, lorsque la mise en forme de type Nyquist est utilisée, la pénalité de la dispersion chromatique et le chirp du laser est réduite de 2 dB par rapport à la mise en forme classique de type NRZ.

Nous avons aussi montré que, même si des techniques d'égalisation permettent d'amélioration de la modulation OOK classique, le gain apporté par ces techniques est encore limité. La pénalité en termes de puissance optique est encore élevée à cause de la dispersion chromatique et les effets de chirp du laser. Cette conclusion pousse les études vers la modulation multi-porteuse de type OFDM (Orthogonal Frequency Division Multiplexing).

## Chapitre 4 – Proposition de système « OFDM précodé » pour les futurs PONs

Le chapitre 4 analyse les forces et faiblesses de la modulation OFDM. Dans la littérature, pour une transmission IMDD, la technique bit/power loading inventé par Levin et Campello a montré une excellente performance en termes de débit. Nous pouvons résumer cette technique comme suit :

- le taux d'erreur de symbole du système est choisi ;
- selon le gain de canal à chaque sous-porteuse OFDM, l'ordre de constellation et la puissance de chaque sous-porteuse ont calculés ;
- le débit de la transmission est donc optimisé en respectant le taux d'erreur de symbole ciblé.

Pourtant, comme tous les systèmes basés sur la modulation OFDM, le signal transmis dans le système de Levin/Campello a un important PAPR (Peak to Average Power Ratio). Ce PAPR important réduit fortement l'efficacité énergétique d'un amplificateur électrique à l'émission.

Le premier résultat important dans ce chapitre est que nous avons proposé un système alternatif basé sur la technique de précodage du symbole OFDM. La technique proposée peut être résumée comme suit :

- avec l'algorithme proposé, nous pouvons choisir des sous-porteuses actives et des sous-porteuses inactives (qui sont mises à zéros) ;
- le taux d'erreur de symbole est fixe ;
- les symboles correspondant aux sous-porteuses actives sont précodés par une matrice DFT.

Nous avons proposé un algorithme simple qui permet d'optimiser le débit de la transmission en garantissant un taux d'erreur de symbole ciblé. Par rapport au système conventionnel de Levin/Campello, le système proposé réduit le PAPR du signal transmis par 2 dB. En termes de capacité de transmission, les deux systèmes ont une même performance. Ce travail a fait l'objet d'une publication dans la revue « Journal of Lightwave Technology ».

Le second résultat important dans ce chapitre est la comparaison entre les systèmes OFDM et les systèmes conventionnels de type OOK, avec une mise en forme NRZ ou Nyquist. Nous avons montré que la modulation OFDM a une plus forte robustesse vis-à-vis du canal IMDD, dont la sélectivité fréquentielle est importante, que la modulation mono-porteuse OOK. Avec un modulateur qui présente un chirp important (le facteur d'élargissement de spectre est de l'ordre de 3), la modulation OFDM permet d'étendre la portée de la transmission au-delà de 80 km tandis que la modulation OOK se limite à 20 km avec un égaliseur de type filtre transverse. Ces résultats sont intéressants pour un opérateur de télécommunication comme Orange puisque dans les futurs réseaux d'accès optique, si la modulation OFDM était utilisée, l'infrastructure y compris la fibre optique et le laser pourraient être réutilisée, ce qui permettrait d'augmenter la rentabilité du réseau.

## **Chapitre 5 – Les techniques OFDM proposées pour les futurs PONs**

Le chapitre 5 est dédié à l'étude des inconvénients d'un système basé sur l'OFDM et les techniques de compensation associées. Après avoir identifié deux inconvénients importants qui sont le PAPR et la synchronisation temporelle, les techniques de compensation conventionnelles ainsi que des techniques originales sont détaillées.

### **Les techniques de réduction du PAPR**

Dans cette section, nous avons étudié différentes techniques de réduction du PAPR, qui sont bien connues dans la littérature. Les gains apportés par des techniques sont ainsi donnés par la simulation numérique. En prenant en compte la caractéristique du canal IMDD, nous avons proposé une technique basée sur la réservation de pilote et le précodage du symbole OFDM. Nous avons montré que la technique proposée pourrait apporter un gain jusqu'à 4 dB en termes de réduction du PAPR. Par rapport à des techniques existant dans la littérature, la technique proposée est un bon compromis entre complexité et performance. Ce travail a fait l'objet d'une publication dans la conférence « IEEE Photonics ».

### **La synchronisation temporelle pour le système OFDM**

Dans un système OFDM, la synchronisation temporelle permet de détecter le début d'un symbole OFDM avant de pouvoir le démoduler avec une IFFT. Dans cette section, nous avons étudié différentes techniques de synchronisation existant dans la littérature. Avec la simulation numérique, nous avons analysé les performances en termes de précision, robustesse vis-à-vis au canal et complexité de ces techniques. Dans le cadre de la thèse, nous avons proposé deux nouvelles techniques qui donnent une meilleure performance en termes de précision et complexité par rapport aux techniques conventionnelles.

La première technique proposée est une version modifiée de la technique proposée par Park. La technique proposée permet d'avoir une synchronisation précise lorsque le SNR est important. Pourtant, la complexité de cette technique est encore élevée par rapport à d'autres techniques. Ce travail a fait l'objet d'une publication dans la conférence OFC/NFOEC.

Pour résoudre le problème de complexité, nous avons proposé une deuxième technique se basant sur une nouvelle structure de préambule. La technique se compose de deux phases : une phase de synchronisation grossière et une phase de synchronisation fine. Selon la simulation numérique, la technique proposée donne un bon compromis entre la complexité matérielle de calcul et les performances en termes de précision et robustesse vis-à-vis au canal. Cette technique a fait l'objet d'une publication dans la revue « Optics Express » et d'un brevet.

## Perspectives

Nous avons proposé trois pistes de recherche pour les travaux à venir.

La première piste est d'étudier les performances de l'OFDM et la technique de mise en forme Nyquist dans le contexte d'un système de multiplexage en longueur d'onde (WDM). Puisque la modulation OFDM et la mise en forme de Nyquist réduisent fortement les radiations hors bande par rapport à la modulation de type NRZ, elles pourraient aussi réduire l'interférence entre canaux dans un système WDM.

La deuxième perspective est l'étude des performances de l'OFDM pour le voie montant dans un contexte où un accès multiple de type OFDMA (Orthogonal Frequency Division Multiple Access) est utilisé. Puisque les longueurs d'onde des signaux venant des différents utilisateurs sont différentes, un accès multiple de type OFDMA peut provoquer des interférences entre utilisateurs. Des techniques qui permettent d'éliminer ces interférences pourraient être un sujet de recherche pour les travaux à venir.

Une étude plus approfondie sur notre système proposée « OFDM précodé » pourrait être aussi un sujet de recherche intéressant. Dans les travaux à venir, le système « OFDM précodé » dans lequel les données des différents utilisateurs sont précodées par différentes matrices DFT peut être analysé.





2.5.2.	Experimental results and model validation .....	53
2.6.	Influence of parameter extraction precision on the model .....	56
2.7.	Conclusion.....	58
<b>Chapter 3</b>	<b>Nyquist pulse shaping technique for future PONs</b>	<b>59</b>
3.1.	Introduction .....	59
3.2.	State-of-the-art equalizer structures .....	62
3.2.1.	Equivalent discrete channel .....	62
3.2.2.	Linear equalizers.....	62
3.2.3.	Non-linear equalizers .....	67
3.2.4.	Automatic synthesis .....	71
3.3.	Optical IMDD receiver design .....	73
3.3.1.	Finite-length fractionally spaced transversal filter.....	73
3.3.2.	Non-linear receivers .....	73
3.4.	Performance comparison in optical IMDD transmissions .....	76
3.4.1.	Simulation parameters and set-up .....	76
3.4.2.	Optimum number of FSTF and feedback filter taps .....	76
3.4.3.	Required optical received power versus transmission distance.....	77
3.4.4.	Required optical received power versus alpha factor .....	78
3.5.	Conclusion.....	79
<b>Chapter 4</b>	<b>DFT-precoded OFDM – a proposed candidate for future PONs</b>	<b>81</b>
4.1.	Introduction .....	81
4.2.	OFDM modulation .....	83
4.2.1.	OFDM modulation/demodulation principle .....	83
4.2.2.	Cyclic prefix – how does it work in an optical IMDD system .....	86
4.3.	The water-filling optimization.....	88
4.4.	Levin-Campello discrete bit/power loading .....	90
4.4.1.	Definitions and notations .....	91
4.4.2.	Levin-Campello efficientizing algorithm .....	92
4.4.3.	Levin-Campello rate adaptive algorithm .....	92
4.4.4.	Levin-Campello margin adaptive algorithm .....	94
4.4.5.	Levin-Campello bit/power loading for optical IMDD systems .....	95
4.5.	The proposed rate adaptive precoded OFDM system .....	96
4.5.1.	Transmission schemes .....	97
4.5.2.	Theoretical basis .....	99

4.5.3.	Algorithm description .....	104
4.5.4.	Model mismatch.....	106
4.6.	Performance analysis .....	106
4.6.1.	Simulation setup.....	106
4.6.2.	Optimum operating parameters of the laser .....	107
4.6.3.	Power consumption analysis .....	108
4.6.4.	Reach-versus-data rate performance comparison .....	111
4.6.5.	Conclusion .....	113
4.7.	Proposed system versus conventional NRZ system.....	114
4.7.1.	Tolerance to chromatic dispersion.....	114
4.7.2.	Tolerance to laser linewidth enhancement factor.....	116
4.8.	Conclusion .....	117
<b>Chapter 5</b>	<b>Proposed OFDM techniques for future PONs</b>	<b>119</b>
5.1.	Introduction .....	119
5.2.	Peak-to-average power ratio.....	120
5.2.1.	PAPR of real-valued OFDM signals .....	120
5.2.2.	Consequences of high PAPR .....	121
5.2.3.	PAPR reduction techniques.....	122
5.2.4.	Conclusion .....	133
5.3.	OFDM timing synchronization .....	135
5.3.1.	Simulation setup.....	136
5.3.2.	State-of-the-art preamble-based OFDM synchronization techniques .....	137
5.3.3.	Proposed timing synchronization methods .....	142
5.3.4.	Performance analysis .....	146
5.3.5.	Conclusion .....	158
5.4.	Conclusion .....	159
<b>Conclusion</b>		<b>161</b>
<b>Contributions</b>		<b>165</b>
<b>Appendix A</b>	<b>Recursive computation of the proposed synchronization technique</b>	<b>167</b>
<b>Appendix B</b>	<b>Channel estimation techniques</b>	<b>169</b>
<b>References</b>		<b>173</b>



# List of figures

1.1	Optical IMDD transmission diagram. ....	4
1.2	Transmission function of: (a) EAMs and (b) MZMs. ....	5
1.3	p-n photodiode structure.....	7
1.4	p-i-n photodiode structure. ....	8
1.5	Avalanche photodiode structure.....	8
1.6	A simplified transimpedance amplifier structure. ....	9
1.7	RIN PSD at several bias current values. ....	10
1.8	Attenuation in SSMF fibers as a function of wavelength. ....	14
1.9	Pulse enlargement due to chromatic dispersion .....	15
1.10	Chromatic dispersion parameter in standard single mode fibers. ....	16
1.11	Small-signal IMDD channel frequency response from Eq. (1.19). Laser linewidth enhancement factor is 2.68. Adiabatic frequency is 1.4 GHz.....	18
1.12	Illustration of the PMD in a short fiber. ....	19
1.13	Long fiber birefringence model.....	20
1.14	Illustration of pulse enlargement due to PMD in a long fiber.....	20
1.15	Illustration of PMD by the first order approximation. ....	21
1.16	The dependence of receiver penalty in the actual DGD.....	22
1.17	Major nonlinear effects in fibers. ....	23
1.18	State transition of silica molecules and the resulted Stokes wave $\omega_S$ . ....	25
1.19	Normalized Raman gain coefficient as a function of frequency shift. Solid curve: Stokes wave and pump wave are copolarized; dot curve: orthogonally polarized. ....	26
1.20	Brillouin gain spectra. (a) silica-core fiber. (b) depressed-cladding fiber. (c) dispersion-shifted fiber.....	27
2.1	DML-based optical IMDD transmission diagram.....	30
2.2	DML two-port model. ....	30
2.3	Laser parasitics approximation by an RC circuit. Left: equivalent RC circuit of laser parasitics along with input and output signal. Right: magnitude and phase response of the RC circuit. ....	31

2.4	Experiment setup for the P-I measurement.....	38
2.5	Experiment setup of AM response and fiber response measurement. ....	39
2.6	Measured and fitted model light-current curves. Left: linear scale. Right: log scale. ....	39
2.7	Measured laser small-signal AM response as a function of bias current. ....	40
2.8	Subtracted laser small-signal AM response. Bias current is 65 mA.....	41
2.9	Squared resonance frequency as a function of bias current.....	41
2.10	Laser damping rate as a function of bias current. ....	42
2.11	Fiber small-signal frequency response. Fiber length is 25 km. ....	43
2.12	Fiber small signal frequency response. Bias current is 70 mA. Fiber length is 25 km. ....	44
2.13	Adiabatic frequency as a function of bias current. ....	44
2.14	Laser parasitic frequency response. Bias current is 65 mA.....	45
2.15	Averaged parasitic frequency response. ....	45
2.16	Validated laser light-current relationship. ....	46
2.17	Validated laser small-signal AM response. ....	47
2.18	Validated fiber small-signal frequency response.....	47
2.19	Transmission diagram for model validation in large-signal regimes. ....	51
2.20	Simulated and experimental OFDM waveforms in back-to-back transmissions. ....	54
2.21	Simulated and experimental OFDM waveforms in 25-km transmissions.....	54
2.22	Simulated and experimental OFDM waveforms in 50-km transmissions.....	55
2.23	Signal-to-error ratio as a function of linewidth enhancement factor. ....	57
2.24	Signal-to-error ratio as a function of $\tau c$ .....	57
2.25	Signal-to-error ratio as a function of photon lifetime $\tau p$ .....	58
3.1	Simulated 10-Gb/s OOK NRZ signal eye diagrams. (a) Transmitter side. (b) Receiver side. Transmission distance is 10 km. ....	60
3.2	Simple linearized discrete equivalent channel model.....	62
3.3	Conventional linear receiver.....	63
3.4	Linear receiver based on a fractionally spaced transversal equalizer. ....	65
3.5	Predictive decision feedback equalizer structure.....	68
3.6	Conventional decision feedback equalizer structure. ....	69
3.7	Sufficient statistic illustration for an OOK transmission.....	70
3.8	MLSE receiver developed via DFE. ....	71
3.9	Automatic synthesis scheme.....	72
3.10	Finite-length fractionally spaced transversal equalizer structure. ....	73

3.11 Finite-length fractionally spaced transversal filter with decision feedback equalizer. ....	74
3.12 Finite-length FSTF with Viterbi-based MLSE.....	75
3.13 Required optical power as a function of FSTF taps. Laser linewidth enhancement factor is 1.....	76
3.14 Required optical power as a function of feedback filter taps. Fiber length is 50 km. Laser linewidth enhancement factor is 1.....	77
3.15 Required power versus reach comparison. Laser linewidth enhancement factor is 2.68. ....	78
3.16 Required power versus laser linewidth enhancement factor. Fiber length is 30 km.....	79
4.1 Small-signal IMDD channel response as a function of transmission distance. Laser linewidth enhancement factor is 2.68. Laser adiabatic chirp frequency is 2.1 GHz. Injected optical power is 0 dBm. ....	81
4.2 Illustration of parallel sub-channel transmission. For each sub-channel, ISI is negligible because the channel response is quasi-flat. ....	83
4.3 Discrete OFDM signal generation scheme.....	84
4.4 OFDM signal spectrum illustration.....	85
4.5 Principal functions of an OFDM receiver. ....	85
4.6 Cyclic prefix insertion principle.....	86
4.7 Chromatic dispersion in simplified linearized IMDD transmission without cyclic prefix.....	87
4.8 Chromatic dispersion in simplified linearized IMDD transmission with cyclic prefix. ....	88
4.9 Illustration of the water-filling technique.....	90
4.10 Transmission diagram of the LC AMOOFDM and POOFDM modems.....	98
4.11 Equivalent channel model for a POOFDM transmission.....	99
4.12 Approximation error power as a function of transmitted optical power and fiber length. 16-QAM constellation, 8-bit quantization. Modulation index $m = 0.9$ . Received signals are equalized and the power is normalized to unity. ....	103
4.13 Coefficient of variation as a function of transmitted optical power and fiber length. The approximation error is found to be negligible. Quantization noise has no significant impacts on the approximation. ....	104
4.14 Transmission data rate as a function of laser bias current and fiber length at optimal modulation indices. Insertion loss is 4 dB. ....	107
4.15 Modulation index as a function of fiber length. The modulation index increases with the fiber length to compensate for the fiber loss. Laser bias current is 60 mA. Insertion loss is 4 dB. ....	108
4.16 OFDM and POOFDM signals CCDF comparison. ....	109
4.17 PAPR performance as a function of transmission distance.....	110

4.18	Average power of driving signals and the corresponding DC power supply for the PA as a function of transmission distance. Insertion loss is 4 dB. ....	111
4.19	Capacity-versus-reach performance as a function of insertion loss. ....	112
4.20	Capacity-versus-reach performance with and without fiber loss. Insertion loss is 4 dB. ....	112
4.21	Capacity-versus-reach performance of different modulators: perfect modulator; DML modulator with and without laser phase noise. Insertion loss is 4 dB. ....	114
4.22	Required power versus reach performance comparison. Bit rate is 10 Gb/s. Laser linewidth enhancement factor is 2.68. ....	115
4.23	Required power versus linewidth enhancement factor performance comparison. Bit rate is 10 Gb/s. (a) Fiber length is 30 km. (b) Fiber length is 60 km. ....	116
4.24	Channel frequency response as a function of laser linewidth enhancement factor. Fiber length is 60 km. Laser adiabatic frequency $f_c = 2.1$ GHz. ....	116
5.1	CCDF of a real-valued OFDM signal. FFT size is 256. The QPSK constellation is used. ....	121
5.2	Power transfer function of a typical power amplifier. High IBO leads to low PA efficiency. ....	122
5.3	The block diagram of the SLM technique. ....	124
5.4	CCDF performance of the SLM technique. FFT size is 256. 16-QAM constellation is used. Phase factors are taken from the set $0, \pi/2, -\pi/2, \pi$ . ....	124
5.5	PTS technique. (a) An example of adjacent partitioning. (b) A block diagram of the PTS technique for optical IMDD transmissions. ....	126
5.6	CCDF performance of the PTS technique. FFT size is 256. 16-QAM constellation is used. Phase factors are taken from the set $0, \pi/2, -\pi/2, \pi$ . ....	126
5.7	Clipping-based TR technique principle. ....	128
5.8	Gradient-based TR technique principle. ....	130
5.9	PAPR reduction tones pattern in a 40-km AMOOFDM transmission. ....	130
5.10	PAPR reduction performance of the proposed contiguous-tone TR technique in a 40-km AMOOFDM transmission. TR threshold $TTR = 9$ dB. ....	131
5.11	PAPR reduction performance of the proposed contiguous-tone TR technique in a 40-km POFDM transmission. TR threshold $TTR = 8$ dB. ....	132
5.12	Timing metric of Schmidl-Cox's technique in a 10-km IMDD channel. ....	138
5.13	Timing metric of Minn's technique in a 10-km IMDD channel. ....	139
5.14	Timing metric of Shi-Serpedin's technique in a 10-km IMDD channel. ....	140
5.15	Timing metric of Park's technique. (a) Fiber length is 0 km. (b) Fiber length is 40 km. ....	141
5.16	Timing metric of the Proposed I technique. Only 15% low-frequency subcarriers is used to build the preamble. (a) Fiber length is 0 km. (b) Fiber length is 40 km. ....	143

5.17	The Proposed II preamble structure. ....	144
5.18	(a) Two-stage synchronization illustration. (b) An example of the proposed coarse and fine metrics. Fiber length is 20 km. Received optical power is -20 dBm. ....	145
5.19	Timing offset variance of the proposed technique versus preamble bandwidth. Received optical power is -14 dBm. Bias current is 60 mA. Modulation index is 0.6. ....	146
5.20	Timing offset variance as a function of laser bias current. Fiber length is 40 km. Received optical power is -14 dBm. ....	147
5.21	Variance of timing offset as a function of modulation index. Fiber length is 10 km. (a) Received optical power is -14 dBm. (b) Received optical power is -20 dBm. ....	148
5.22	Variance of timing offset as a function of modulation index. Fiber length is 80 km. (a) Received optical power is -14 dBm. (b) Received optical power is -20 dBm. ....	149
5.23	Tolerance to fiber length performance comparison. (a) Mean of peaks of the timing metric versus transmission distance. Received optical power is -8 dBm. In order to isolate the impact of a random sampling phase, for each value of the fiber length the sampling instant is chosen to give the best performance. (b) Variance of timing offset as a function of transmission distance. Received optical power is -14 dBm. ....	150
5.24	Fine timing metrics. (a) Cross-correlation method used in [122]. (b) The proposed II method. Fiber length is 20 km. Received optical power is -10 dBm. ....	151
5.25	Variance of metric's peak as a function of transmission distance. Received optical power is -8 dBm. ....	152
5.26	Variance of timing offset as a function of received optical power. Fiber length is 40 km. ....	153
5.27	Packet miss probability performance comparison. (a) Packet miss probability as a function of timing threshold. Fiber length 40 km. Received optical power -14 dBm. (b) Required threshold for $10^{-3}$ packet miss rate as a function of received optical power. ....	154
5.28	Capacity of transmissions employing different synchronization techniques. (a) 8-sample cyclic prefix. (b) 4-sample cyclic prefix. ....	155
5.29	Probability that the searching window covers the correct timing point as a function of the window size. The larger the research window, the more probably the correct timing point falls into this window. The timing thresholds are chosen so that the packet miss probability is maintained at $10^{-3}$ . Fiber length is 40 km. Received optical power is -14 dBm. ....	156



# List of tables

2.1	DML large-signal model parameters.....	32
2.2	Extracted laser parameters. ....	42
2.3	Model parameters used for simulations. ....	53
2.4	Model signal-to-error ratio (dB) as a function of distance and bandwidth. ....	56
5.1	PAPR reduction technique comparison.....	134
5.2	Number of operations per received sample for coarse metric computation.....	156



# Acronyms

<b>ACE</b>	Active Constellation Extension
<b>ACK</b>	Acknowledgment
<b>ADC</b>	Analog-to-Digital Converter
<b>AM</b>	Amplitude Modulation
<b>AMO</b>	Adaptive Modulation Optical
<b>APD</b>	Avalanche Photodiode
<b>ASE</b>	Amplified Spontaneous Emission
<b>AWG</b>	Arbitrary Waveform Generator
<b>BER</b>	Bit Error Rate
<b>CCDF</b>	Complementary Cumulative Distribution Function
<b>CD</b>	Chromatic Dispersion
<b>CFO</b>	Carrier Frequency Offset
<b>CL</b>	Correlation Length
<b>CO</b>	Coherent Optical
<b>CP</b>	Cyclic Prefix
<b>CPR</b>	Common Phase Rotation
<b>DAC</b>	Digital-to-Analog Converter
<b>DC</b>	Direct Current
<b>DCF</b>	Dispersion Compensation Fiber
<b>DFT</b>	Discrete Fourier Transform

<b>DIR</b>	Desired Impulse Response
<b>DFB</b>	Distributed Feedback
<b>DFE</b>	Decision Feedback Equalizer
<b>DGD</b>	Differential Group Delay
<b>DML</b>	Directly Modulated Laser
<b>DSL</b>	Digital Subscriber Lines
<b>DSO</b>	Digital Storage Oscilloscope
<b>DSP</b>	Digital Signal Processing
<b>DVB</b>	Digital Video Broadcasting
<b>DVB-T</b>	Digital Video Broadcasting – Terrestrial
<b>DWDM</b>	Dense Wavelength Division Multiplexing
<b>EAM</b>	ElectroAbsorption Modulator
<b>FEC</b>	Forward Error Correction
<b>FFT</b>	Fast Fourier Transform
<b>FM</b>	Frequency Modulation
<b>FSTF</b>	Fractionally Spaced Transversal Filter
<b>FWM</b>	Four Wave Mixing
<b>Gb/s</b>	Giga-Bit Per Second
<b>GPON</b>	Gigabit Passive Optical Network
<b>GS/s</b>	Giga-Sample Per Second
<b>IBO</b>	Input Back-Off
<b>ICI</b>	Inter-Carrier Interference
<b>IDFT</b>	Inverse Discrete Fourier Transform
<b>IFFT</b>	Inverse Fast Fourier Transform
<b>IMDD</b>	Intensity Modulated Direct Detected
<b>ISI</b>	Inter-Symbol Interference

<b>LC</b>	Levin-Campello
<b>LMMSE</b>	Linear Minimum Mean Square Error
<b>LMS</b>	Least Mean Square
<b>LPF</b>	Low Pass Filter
<b>MA</b>	Margin Adaptive
<b>ML</b>	Maximum Likelihood
<b>MLSE</b>	Maximum Likelihood Sequence Estimator
<b>MSE</b>	Mean Square Error
<b>MMSE</b>	Minimum Mean Square Error
<b>MZM</b>	Mach-Zehnder Modulator
<b>MSER</b>	Model Signal-to-Error Ratio
<b>NLS</b>	Nonlinear Schrödinger
<b>NRZ</b>	Non Return-to-Zero
<b>OFDM</b>	Orthogonal Frequency Division Multiplexing
<b>OFDMA</b>	Orthogonal Frequency Division Multiple Access
<b>ONU</b>	Optical Network Unit
<b>OOK</b>	On Off Keying
<b>OLT</b>	Optical Line Terminal
<b>OTDM</b>	Optical Time Division Multiplexing
<b>PAM</b>	Pulse Amplitude Modulation
<b>PAPR</b>	Peak-to-Average Power Ratio
<b>PDL</b>	Polarization Dependent Loss
<b>PM</b>	Phase Modulation
<b>PMD</b>	Polarization Mode Dispersion
<b>POFDM</b>	Precoded Orthogonal Frequency Division Multiplexing
<b>PON</b>	Passive Optical Network

<b>PPM</b>	Part Per Million
<b>PRT</b>	PAPR Reduction Tone
<b>PSD</b>	Power Spectral Density
<b>PSK</b>	Phase Shift Keying
<b>PTS</b>	Partial Transmitted Sequence
<b>QAM</b>	Quadrature Amplitude Modulation
<b>QPSK</b>	Quadrature Phase Shift Keying
<b>RA</b>	Rate Adaptive
<b>RF</b>	Radio Frequency
<b>RIN</b>	Relative Intensity Noise
<b>RMSD</b>	Root Mean Square Deviation
<b>RSP</b>	Random Sampling Phase
<b>SBS</b>	Stimulated Brillouin Scattering
<b>SFO</b>	Sampling Frequency Offset
<b>SLM</b>	Selected Mapping
<b>SMF</b>	Single Mode Fiber
<b>SSMF</b>	Standard Single Mode Fiber
<b>SNR</b>	Signal-to-Noise Ratio
<b>SPM</b>	Self Phase Modulation
<b>SRS</b>	Stimulated Raman Scattering
<b>SSF</b>	Split-Step Fourier
<b>SSMF</b>	Standard Single Mode Fiber
<b>TI</b>	Tone Injection
<b>TIA</b>	TransImpedance Amplifier
<b>TR</b>	Tone Reservation
<b>VEA</b>	Variable Electrical Attenuator

<b>VOA</b>	Variable Optical Attenuator
<b>WDM</b>	Wavelength Division Multiplexing
<b>XGPON</b>	Ten Gigabit Passive Optical Network
<b>XPM</b>	Cross Phase Modulation
<b>ZF</b>	Zero Forcing



# Notation

## Constant

$h$	Planck constant
$q$	Electron charge
$c$	Light speed in vacuum
$k_B$	Boltzmann constant

## Laser

$\alpha$	Linewidth enhancement factor
$N(t)$	Carrier density
$N_{th}$	Carrier density at threshold
$S(t)$	Photon density
$\phi(t)$	Laser output optical field phase
$\Gamma$	Optical confinement factor
$g_0$	Intrinsic laser gain slope
$N_t$	Carrier density at transparency
$\epsilon$	Laser gain saturation parameter
$\beta$	Laser spontaneous emission factor
$V_a$	Volume of the laser active region
$\eta$	Total quantum efficiency
$\tau_p$	Photon lifetime
$\tau_n$	Carrier lifetime

---

$I_{th}$	Laser emission threshold current
$\kappa$	Adiabatic chirp constant
$\gamma$	Laser damping rate
$f_0$	Laser relaxation oscillation frequency
$\omega_0$	Laser relaxation oscillation angular frequency
$K$	Laser K-factor
$I_0$	Laser DC bias current
$I_S$	Laser characteristic current
$f_c$	Laser adiabatic frequency
$\Delta\nu$	3-dB Lorentzian laser linewidth
$H_{FM}(f)$	Small-signal laser frequency modulation response

### Fiber and propagation

$L$	Fiber length
$L_w$	Four wave mixing walk-off length
$M_{SSF}$	Number of fiber sections in Split Step Fourier method
$d_{12}$	Differential group velocity
$\lambda$	Optical wavelength
$D$	Dispersion parameter
$A$	Optical pulse envelope
$\beta$	Propagation constant
$\gamma_F$	Fiber nonlinearity coefficient
$A_{eff}$	Principle mode effective area
$\nu$	Optical frequency
$E$	Electrical field of an optical signal
$n_2$	Nonlinear index coefficient
$n$	Refractive index

$\alpha_{att}$	Fiber attenuation coefficient
$\alpha_R$	Attenuation factor due to Rayleigh scattering
$P$	Optical power
$\bar{P}$	Average optical power
$v_g$	Group velocity
$f_D$	Dispersion frequency
$\chi$	Fiber susceptibility
$P_{NL}$	Nonlinear polarization term
$g_R$	Raman gain
$I_s$	Stokes wave intensity
$I_p$	Pump wave intensity
$H_F(f)$	Fiber frequency response in IMDD channel

**Photodetector**

$R$	Photodiode responsivity
$\theta$	Absolute temperature
$\Delta f$	Receiver effective bandwidth
$M$	Avalanche gain
$F_A$	Avalanche photodiode excess noise factor
$F_{no}$	Amplifier noise figure
$\sigma_S^2$	Shot noise variance
$\sigma_T^2$	Thermal noise variance
$n(t)$	Photodetector noise
$N_0$	Power spectral density of photodetector noise

**Mathematic and statistic**

$E\{x\}$	Expectation value of $x$
----------	--------------------------

$\tilde{A}$	Fourier transform of $A$
$\mathcal{F}$	Fourier transform operation
$\delta(t)$	Dirac delta function
$\delta_{i,j}$	Kronecker delta
$\gamma(d, a)$	Incomplete gamma function
$\Gamma(x)$	Gamma function
$erfc(\cdot)$	Complementary error function
$(\cdot)^T$	Transpose operator
$(\cdot)^H$	Hermitian transpose operator

### Signal and signal processing

$x(t)$	Electrical transmitted signal
$\{x_k\}$	Discrete electrical transmitted signal
$y(t)$	Received signal after photodetector
$\{y_k\}$	Discrete received signal after photodetector
$\mathbf{y}_k$	Received samples vector after photodetector at time $kT_S$
$r(t)$	Received signal after receive filter
$\{r_k\}$	Discrete signal after receive filter
$\mathbf{r}_k$	Received samples vector after receive filter at time $kT_S$
$Q$	Q-factor
$f_{os}$	Oversampling factor

#### NRZ system

$T_B$	Bit duration
$T_S$	Sampling time
$\tau$	Sampling time in oversampled system
$\{a_k\}$	Transmitted symbol sequence
$\{\hat{a}_k\}$	Detected symbol sequence

$g(t)$	Impulse response of pulse shaping filter
$G(f)$	Frequency response of pulse shaping filter
$p(t)$	Channel impulse response
$P(f)$	Channel frequency response
$h(t)$	Equivalent channel (pulse shaping filter and channel) impulse response
$H(f)$	Equivalent channel frequency response
$g_{rcv}(t)$	Receive filter impulse response
$G_{rcv}(f)$	Receive filter frequency response
$q(t)$	End-to-end equivalent channel impulse response
$q_n$	Discrete equivalent channel filter taps
$Q(f)$	End-to-end equivalent channel frequency response
$S_q(f)$ $0 \leq f \leq 1/T_S$	Folded frequency response of the end-to-end equivalent channel
$c(f)$	Equalizer frequency response
$C_{ZF}(f)$	Zero forcing equalizer frequency response
$C_{MMSE}(f)$	MMSE equalizer frequency response
$e(t)$	Time-domain distortion (noise and residual ISI) signal
$E(f)$	Frequency-domain distortion signal
$w_k$	Discrete photodetector noise filtered by the receive filter
$\sigma_{MSE}^2$	Mean square error
$c_k$	Forward filter tap
$\mathbf{c}_k$	A vector of forward filter taps at time $kT_S$
$c_k^{FSTF}$	Fractionally spaced transversal filter tap
$\mathbf{c}_k^{FSTF}$	A vector of fractionally spaced transversal filter taps at time $kT_S$
$N_c$	Number of forward filter taps
$u_k$	Feedback filter tap

$N_u$	Number of feedback filter taps
$\{d_k\}$	Equalized discrete signal
$\mathbf{R}_{rr}$	Covariance matrix of the column vector $\mathbf{r}$
$r_{ar}$	Cross-correlation between the transmitted sample $a_k$ and the received samples vector $\mathbf{r}_k$
$\mu$	Step size of the least mean square method
$\alpha_{rof}$	Roll-off factor

**OFDM system**

$\mathbf{X}$	Transmitted data symbol vector
$X_n$	Transmitted data symbol on the $n^{th}$ subcarrier
$X_n^k$	Transmitted data symbol on the $k^{th}$ OFDM symbol, $n^{th}$ subcarrier
$\mathbf{Z}$	Received data symbol after FFT
$Z_n$	Received data symbol after FFT on the $n^{th}$ subcarrier
$Z_n^k$	Received data symbol after FFT on the $k^{th}$ OFDM symbol, $n^{th}$ subcarrier
$x_k(m)$	$k^{th}$ OFDM symbol discrete signal
$N$	FFT length, number of subcarriers
$N_g$	Cyclic prefix length (sample)
$\zeta$	Constellation granularity
$\mathcal{E}$	SNR gap
$\varrho$	Power amplifier efficiency
$R_{BR}$	Transmission bit rate
$\mathbf{b}$	Bit distribution vector
$b_n$	Number of bits carried by the $n^{th}$ subcarrier
$E_n(b_n)$	Energy of a constellation point carrying $b_n$ bits
$e_n(b_n)$	Incremental energy when the number of bits increases from $b_n - \zeta$ to $b_n$
$\mathcal{E}_n$	$n^{th}$ subcarrier energy

$\bar{\mathcal{E}}$	Average subcarrier energy
$Q_n$	Channel gain at $n^{th}$ subcarrier
$\Phi_{n,k}(t)$	An orthonormal basis function of the signal space
$f_n$	$n^{th}$ subcarrier frequency
$l_N$	Number of training OFDM symbols for noise power estimation
$ICI_n$	Nonlinear noise on the $n^{th}$ subcarrier
$ICI'_n$	Nonlinear noise on the $n^{th}$ subcarrier after channel compensation
$\sigma_{ICI',n}^2$	Power of $ICI'_n$
$\hat{\sigma}_{ICI',n}^2$	Estimated power of $ICI'_n$
$N_n$	Photodetector noise on the $n^{th}$ subcarrier
$N'_n$	Photodetector noise on the $n^{th}$ subcarrier after channel equalization
$\sigma_{N',n}^2$	Power of $N'_n$
$\hat{\sigma}_{N',n}^2$	Estimated power of $N'_n$
$n_n$	Noise on the $n^{th}$ subcarrier before channel equalization
$\mathbf{n}$	Vector containing noise samples on subcarriers before channel equalization
$\sigma_n^2$	Noise power on the $n^{th}$ subcarrier before channel equalization
$\sigma_n'^2 = \sigma_{ICI',n}^2 + \sigma_{N',n}^2$	Noise power on the $n^{th}$ subcarrier after channel equalization
$\hat{\sigma}_n'^2$	Estimate of $\sigma_n'^2$
$\boldsymbol{\sigma}'^2$	Noise power vector after channel equalization
$\hat{\boldsymbol{\sigma}}'^2$	Estimate of $\boldsymbol{\sigma}'^2$

### Proposed DFT-precoded OFDM system

$Y$	Transmitted data symbol after the DFT precoding
$\hat{Y}$	Received data symbol before the IDFT decoding (after channel equalization)

$\hat{X}$	Detected data symbol (after IDFT decoding)
$N_{act}$	Number of active subcarriers
$N_{null}$	Number of null subcarrier
$N_{equiv, m}$	Equivalent noise on the $m^{th}$ subchannel after the IDFT decoding
$\sigma_{equiv, m}^2$	Equivalent noise power on the $m^{th}$ subchannel after the IDFT decoding
$\hat{\sigma}_{equiv, m}^2$	Estimated equivalent noise power on the $m^{th}$ subchannel after the IDFT decoding
$\sigma_{equiv, approx, m}^2$	Approximation of equivalent noise power on the $m^{th}$ subchannel after the IDFT decoding
$\hat{\sigma}_{equiv, approx, m}^2$	Estimate of $\sigma_{equiv, approx, m}^2$
$\sigma'_{act}{}^2$	Noise power vector on active subcarriers after channel equalization
$\hat{\sigma}'_{act}{}^2$	Estimate of $\sigma'_{act}{}^2$
$SNR_{equiv}$	Equivalent SNR in the proposed precoded OFDM system
$ptn_{act}$	Optimal active-subcarrier pattern
$m_{opt}$	Optimal number of bits carried by a QAM symbol in the proposed precoded OFDM system
$\bar{P}_{out}$	Average power at the power amplifier output
$P_{DC}$	DC power or bias power of a power amplifier
$P_{saving}$	Power saving of the proposed POFDM system when compared to a conventional LC AMO OFDM system

**PAPR reduction techniques**

$n_d$	Number of data bits in coding technique
$n_c$	Number of code word bits in coding technique
$l$	Number of phase branches in SLM technique
$\phi^i$	Phase factor vector corresponding to the $i^{th}$ branch in SLM technique
$\phi_n^i$	Phase factor corresponding to the $i^{th}$ branch, $n^{th}$ subcarrier
$n_p$	Number of partitions in PTS technique

$\phi_{PTS}$	Phase factor vector in PTS technique
$\phi_{PTS}^i$	Phase factor corresponding to the $i^{th}$ partition in PTS technique
<i>TR technique</i>	
$c_{PRT}(t)$	Peak-correcting signal
$c_{PRT}^k(t)$	Peak-correcting signal after $k$ iterations
$x_{TR}(t)$	Peak-corrected signal
$x_{TR}^k(t)$	Peak-corrected signal after $k$ iterations
$N_{PRT}$	Number of PAPR reduction tones
$1_{PRT}$	Frequency domain kernel signal
$K_0$	Time-domain kernel signal
$i_k$	Index of maximum peak of $x_{TR}^k(t)$
$K_{i_k}$	Circular-shifted kernel signal
$\alpha_{i_k}^k$	Scaling factor on the $k^{th}$ iteration
$\zeta$	Desired amplitude level
$T_{TR}$	Tone reservation threshold

**Time synchronization techniques**

$d$	Received sample index
$\bar{d}$	Timing position detected by coarse synchronization step
$d_{timing\ point}$	Timing position detected by fine synchronization step
$M(d)$	Timing metric
$T_{th}$	Timing threshold
$W$	Fine synchronization searching window
$\Delta$	Fine synchronization searching window length
$l_1$	The length of the first sequence in the proposed preamble
$l_2$	The length of the second sequence in the proposed preamble
$fliplr(\cdot)$	Left-right-flipped operator

### Channel equalization techniques

$\text{diag}(\mathbf{X})$	Transform the vector $\mathbf{X}$ into a diagonal matrix
$l_c$	Number of training OFDM symbols for channel estimation
$l_a$	Number of adjacent subcarriers used in frequency-domain averaging method
$\Delta_{l,k}$	Differential channel gain between the $l^{\text{th}}$ and the $k^{\text{th}}$ subcarriers
$\Lambda_l$	Likelihood function
$\hat{Q}_k^{ML}$	Maximum likelihood estimate of the $k^{\text{th}}$ subchannel gain
$\bar{Q}_k^{ML}$	Average maximum likelihood channel gain estimate
$\mathbf{W}_{MMSE}$	MMSE channel estimation matrix
$\hat{\mathbf{Q}}_{MMSE}$	Vector containing MMSE channel estimates
$\mathbf{R}_{qz}$	Channel-received signal cross-correlation matrix
$\mathbf{R}_{zz}$	Covariance matrix of received signal
$\mathbf{R}_{nn}$	Noise covariance matrix
$\mathbf{R}_{qq}$	Channel covariance matrix
$\mathbf{W}_{LMMSE}$	LMMSE channel estimation matrix
$\hat{\mathbf{Q}}_{LMMSE}$	Vector containing LMMSE channel estimates

# Introduction and context

In response to the continuously increasing demand of transmission capacity, extensive research has been carried out to look for high-bit-rate and extended-reach transmission systems. When an access network designer implements a fiber-based optical transmission system, system cost is always priority. For this reason, Intensity Modulated Direct Detected (IMDD) systems have been widely installed in existing optical access network infrastructures. In the future, the IMDD technique seems to continue to attract more attention when compared to coherent systems thanks to its simplicity and low cost, at least in the context of access network. In terms of modulation types, Pulse Amplitude Modulation (PAM) is preferable thanks to its simplicity. The On-Off-Keying (OOK) Non Return-to-Zero (NRZ) modulation technique is one of the principal modulation techniques in actual Passive Optical Network (PON) standards. For instance, the optical bandwidth is still large enough to accept such a naive modulation technique. However, for Next Generation (NG) PONs, the increase of data rate and transmission reach give rise to two critical issues as follows.

- Firstly, Inter Symbol Interference (ISI) should be much more severe than that in actual generation PONs. This might lead to the degradation of the transmission Bit Error Rate (BER).
- Secondly, electronic and optical devices are supposed to work at much faster rhythm.

One of the interesting approaches to increase the transmission capacity and reach is to compensate for all optical-link detriments by means of signal processing techniques in the electrical domain. Given that the rapidity of electronic devices continues to increase and still follows the Moore's law, one could hope that multi-GHz electronic devices will be available for NGPONs. In such contexts, this research project has been created by two Orange Labs teams: the CREM team, who is an expert in the radio signal processing domain, and the ASHA team, who benefits from strong skills in the fiber-based optical communication domain. The project aims, by means of radio signal processing techniques, to improve the transmission data rate and reach of optical transmissions in future PONs. In addition, advanced modulation schemes such as the Orthogonal Frequency Division Multiplexing (OFDM) is also proposed and studied in order to clarify their potential in the context of future PONs. This thesis is organized as follows.

- Chapter 1 gives an overview about an IMDD transmission link. Key components in an IMDD transmission and impairments generated by the optical channel are discussed.

- In Chapter 2, techniques for channel modeling are described. Model parameter extraction and validation by experimentations are detailed. For the sake of a realistic modeling, the model is validated in both small-signal and large-signal regimes.
- In Chapter 3 the author proposes to use the Nyquist pulse shaping technique to replace the conventional Non Return-to-Zero (NRZ) technique for future PONs. Conventional channel equalization schemes, which have been proposed for radio communications, are also adapted for the optical IMDD channel. Simulation results show that the Nyquist pulse shaping technique improves the chromatic dispersion-induced power penalty up to 2 dB at  $10^{-3}$  BER and the reach is extended by tens of kilometers, which corresponds to a reach increase of about 20%.
- Chapter 4 reports the performance in terms of power consumption and transmission throughput of a conventional OFDM modulation and that of the proposed DFT-precoded OFDM modulation in the context of optical IMDD transmissions. The conventional Levin Campello bit/power loading and the proposed rate adaptive DFT-precoded OFDM techniques are discussed in details. In this chapter, the author also reveals some advantages of the proposed technique over the conventional OOK NRZ technique in future PONs.
- Chapter 5 concentrates on techniques which compensate for OFDM modulation disadvantages including the important Peak-to-Average Power Ratio (PAPR) and the sensitivity to time and frequency synchronization. Both conventional and proposed techniques are described. Their performance is analyzed by means of numerical simulations.

The contributions of the author can be summarized as follows.

- A realistic numerical model for an optical IMDD transmission is studied and implemented. The model is also validated by means of experimentations. This model should ease future collaboration between the two teams and help any researcher which needs an accurate model for PON transmission and short simulation times.
- A transmission system based on Discrete Fourier Transform (DFT) precoding OFDM technique is proposed for future PONs. The proposed transmission system is found to significantly reduce the power consumption of the power amplifier on the transmitter side when compared to a conventional OFDM transmission system. The proposed system is published in [1].
- The author also proposes two time synchronization techniques [2], [3] for optical IMDD OFDM transmissions. The proposed techniques are shown to have better performance than conventional techniques in terms of timing offset variance. In addition, complexity is also reduced. A patent concerning the second proposition was also submitted [4].
- A PAPR reduction scheme based on the tone reservation technique for an IMDD OFDM transmission is also proposed and published in [5].

# Optical IMDD transmission system and optical channel detriments

## 1.1. Introduction

This thesis concerns data communication over single-mode fibers. More specifically, the works throughout this thesis focus on techniques to transmit and receive data over an IMDD channel. Like any transmission systems, before discussing signal processing techniques, it is important to study the channel in which the signal is transmitted. This helps well designing signal processing techniques in order to maximize transmission capacity. For this reason, we begin this report with the fundamentals of an optical IMDD transmission including modulation and detection techniques. The characteristics of an optical channel will be also studied. This is important because of two reasons. Firstly, by understanding the impacts of the channel on a transmitted signal, appropriate signal processing techniques can be used in order to optimize transmission performance in terms of capacity, complexity, and cost, *etc.* Secondly, a profound study of modulation/detection techniques and the channel also help identify the key components in a transmission link and the principal phenomena of the optical channel. This helps well designing a numerical model, which is one of the main objectives of this thesis.

## 1.2. Optical IMDD transmission fundamentals

In general, fiber-based optical communication systems include:

- A modulator which imprints data on an optical carrier;
- A fiber link over which the optical signal propagates; in some transmission architectures, on-line optical amplifiers can be used to compensate for fiber loss;
- A photodetector which detects the data from the received optical signal.

In optical IMDD transmission in particular, the data are coded on the optical intensity. On the receiver side, the received optical signal intensity is detected by means of a photodiode. The transmission diagram of an optical IMDD system is illustrated in Figure 1.1. Within the scope of this thesis, only Standard Single Mode Fiber (SSMF) is considered.

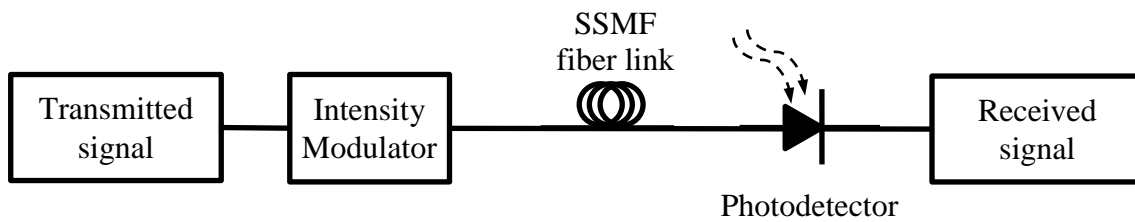


Figure 1.1 – Optical IMDD transmission diagram.

IMDD system is one of the most cost-effective optical transmission systems because the receiver structure is simpler when compared to that of coherent receivers and the transmitter can make use of low-cost modulators such as Electroabsorption Modulators (EAMs) or Directly Modulated Lasers (DMLs). However, as the phase information of the optical field is not detected on the receiver side, the chromatic dispersion results in frequency-dependent attenuation in the frequency channel response. In addition, when fiber length increases, the polarization mode dispersion becomes one of the main capacity-limiting factors. For this reason, an IMDD system is only suitable for short-reach transmission in the context of access networks, where the system cost is one of the most important criteria for a network designer.

In the next sections we discuss intensity modulation technologies, the propagation of an optical signal in the fiber link and the direct detection by photodetector.

### 1.2.1. Intensity modulation technologies

The throughput of an optical communication system explicitly depends on the speed of optoelectronic components including modulator and detector. Hence, it is important for a system designer to consider practical aspects of each of these components. Optical modulation technology in general and intensity modulation technology in particular make use of three basic components: DML, EAM and Mach-Zehnder Modulator (MZM).

#### 1.2.1.1. Directly Modulated Lasers

The simplest way to imprint information into optical intensity is using a DML. In this technique, the laser input current is driven by an electrical signal. In linear regime, the output optical intensity is proportional to the driving signal. Hence, if transmitted data is modulated onto the laser driving current, the information is transformed into the intensity of an optical carrier, which propagates through a fiber link to the receiver. One of the most naive modulation techniques simply involves switching on and off the laser according to a binary data bit pattern. The resulting modulation waveform is Non Return-to-Zero (NRZ) which is widely used in optical access and metropolitan networks [6]. Due to their compactness and low cost, compact DML-based transponders are available with modulation speed up to 10 Giga-Bit Per Second (Gb/s). The principal limitations of DMLs are small extinction ratio, which is in the order of 10 dB, and inherent chirp, because of which a residual phase modulation accompanies the desired intensity modulation. The small extinction ratio limits the maximum achievable Signal-to-Noise Ratio (SNR) on the receiver side. The inherent laser chirp broadens the transmitted signal bandwidth, resulting in inter-channel interference in Dense Wavelength Division Multiplexing (DWDM) systems.

### 1.2.1.2. Electroabsorption Modulators

Unlike DMLs where a modulation of laser carrier density results in a modulated output photon density, EAMs work on the absorption principle. An EAM is composed of an active region sandwiched between a p-doped and an n-doped layer. When a bias voltage is applied across the p-n junction, the bandgap of the active region is changed. This phenomenon is known as Franz-Keldysh effect. When the bias voltage is small, the bandgap is wide enough so that the device is transparent to the laser light. However, when the bias voltage increases, the bandgap is reduced such that the active region begins to absorb the laser light. The transmission function of an EAM is shown in Figure 1.2. In linear regime, the output light intensity has a linear relationship with the input bias voltage, resulting in an intensity modulation of light.

In practice an EAM can be integrated with a Distributed Feedback (DFB) laser, which serves as the CW light source, on the same substrate to form an EML. This compact design reduces the important insertion loss of an EAM device. Similar to DMLs, EMLs are compact and low-cost. They are available with modulation speed up to 80 Gb/s. The device also produces some residual chirp and the extinction ratio is in the order of 10 dB.

### 1.2.1.3. Mach-Zehnder Modulators

Unlike EAMs, which work on absorption principle, MZMs work on the principle of interference. The input optical signal is split into two paths at an input coupler. At the device output, the optical signals are recombined. According to the phase difference between the two optical fields, the recombination can be destructive or constructive, resulting in an intensity modulation. In order to control the phase change of the output optical light, each path (or arm) is equipped with a phase modulator such that the phase shift is linearly proportional to the applied electrical voltage. The transmission function of an MZM is illustrated in Figure 1.2.

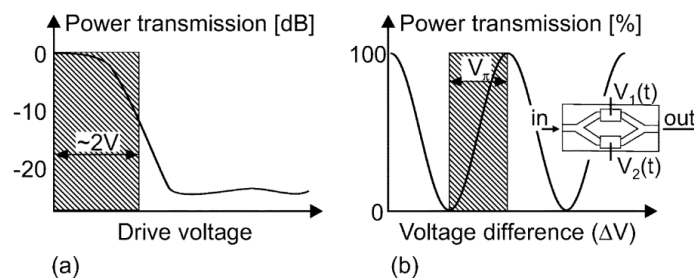


Figure 1.2 – Transmission function of: (a) EAMs and (b) MZMs.

(Source: [7]).

When compared to DMLs and EMLs, MZMs can be used to create an intensity modulation without generating chirp. MZMs have an excellent extinction ratio which is in the order of 20 dB. For these reasons MZMs are extensively used in optical transmission systems where the data rate exceeds 10 Gb/s. Due to the possibility of independently modulating the optical intensity and phase, MZMs can be used to create many advanced optical modulation formats [7].

### 1.2.2. Fiber-based optical propagation

The propagation of an optical signal over fibers is an electromagnetic propagation. Hence, like all electromagnetic phenomena, it is governed by Maxwell's equations. In general, the propagation equations have several solutions corresponding to different modes in a fiber. The number of solutions (or modes) depends on the characteristics of the fiber. For further details of this aspect the reader is invited to read the second chapter in [8]. Nowadays, fiber-based optical communication infrastructures are extensively implemented with Single-Mode Fibers (SMFs). In this type of fiber the propagation equations have only one solution, which is referred to as the central  $HE_{11}$  mode. Because the fiber supports only one mode, the transmission is hence immune to intermodal dispersion. In this thesis the SMF is considered as being the one used in access networks. The propagation of an optical signal in an SMF can be described by the well-known nonlinear Schrödinger (NLS) equation [8], [9]

$$\frac{\partial A}{\partial z} = -\frac{\alpha_{att}}{2}A - \beta_1 \frac{\partial A}{\partial t} - \frac{j}{2}\beta_2 \frac{\partial^2 A}{\partial t^2} + j\gamma_F(\omega_0)|A|^2A, \quad (1.1)$$

where  $A(z, t)$  denotes the slowly varying pulse envelop,  $\alpha_{att}$  ( $\text{dB} * \text{m}^{-1}$ ) is the fiber attenuation coefficient,  $\beta_1$  ( $\text{s} * \text{m}^{-1}$ ) corresponds to the group velocity,  $\beta_2$  ( $\text{s}^2 * \text{m}^{-1}$ ) is the dispersion parameter and  $\gamma_F$  ( $\text{W}^{-1}\text{m}^{-1}$ ) is the fiber nonlinearity coefficient. Different physical phenomena are presented in Eq. (1.1) as follows. The first term on the right hand side corresponds to linear attenuation in the fiber. The second term corresponds to the group velocity (or the time propagation in the fiber). The third term is responsible for pulse enlargement due to chromatic dispersion and the last term corresponds to Kerr effects. Physical origin of these phenomena and the impacts on optical transmissions in general and on optical IMDD transmissions in particular are detailed in the next sections of this chapter.

It must be noted that Eq. (1.1) is only valid in single-polarization transmissions where the pulse polarization is maintained along the fiber. In this equation the power transfer between polarizations due to birefringence is not taken into account. However, in the context of access networks where the transmission distance is relatively short, Eq. (1.1) is valid to evaluate the transmission performance. It is also noted that high-order chromatic dispersion is negligible because it only becomes non-negligible in ultra-short pulse transmissions [8]. Another important point that is worth noting is that in Eq. (1.1) only non-resonant third-order process is concerned. This means that the nonlinear polarization response only acts on the optical field intensity [10]. Because of this approximation, the third-harmonic generation and degenerate four wave mixing are not included in this NLS equation [8]. However, appropriate phase-matching conditions are required for these phenomena to occur. In the context of optical transmissions in access networks, Eq. (1.1) covers most of the physically fundamental phenomena such as second-order chromatic dispersion, self-phase modulation, cross phase modulation, non-degenerate four-wave mixing, modulation instability or even the existence of optical solitons. In addition, this equation has also been used by most of the authors in the literature to evaluate the performance of a fiber-based optical transmission [9], [11]–[13]. For the sake of simplicity, in the scope of this report Eq. (1.1) is used to describe the optical signal propagation in single-mode fiber.

### 1.2.3. Direct Detection

As data information can be imprinted to both optical carrier phase and amplitude, on the receiver side depending on the detector structure both optical phase and amplitude can be detected. In an IMDD transmission in particular, only information on the optical carrier amplitude is detected. In this case the photodetector converts the optical signal back to the electrical domain by only detecting the optical power. This is one of the simplest photodetector structures and is in general composed of a photodiode followed by a transimpedance amplifier.

#### 1.2.3.1. Photodiode

##### 1.2.3.1.1. p-n photodiode

A p-n photodiode structure is simply a p-n junction reversed biased by an external voltage in order to oppose electrons flow from the n-doped layer to the p-doped one (and holes from p to n). The junction has of a region known as depletion region that is free from free charge carrier. When the p-n junction is exposed to incoming light, electrons and holes are created in both p-doped and n-doped layers due to absorption. Because of the reversed bias voltage, flows of electrons and holes are formed in the depletion region. The resulting current flow intensity is proportional to the intensity of the incident light.

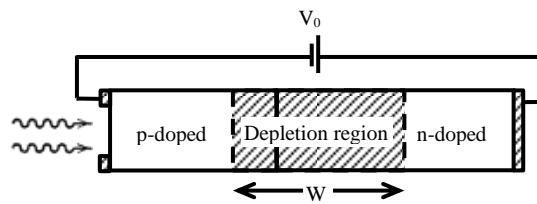


Figure 1.3 – p-n photodiode structure.

A p-n photodiode has a high responsivity, which is in the order of  $1 \text{ A/W}$  due to a high quantum efficiency. However, the bandwidth of the device is limited by the electron/hole transit time which depends on the depletion region width, the bias voltage and the transit velocity [14]. The transit velocity is often limited by the fact that electrons created in the p-doped layer must diffuse to the depletion region before drifting to the n-doped layer (and the same for holes generated in the n-layer). Hence, it is obvious that a simple way to improve the device bandwidth is to increase the depletion region width and reduce that of the n-doped and p-doped layers. This principle is used in p-i-n photodiode structure that is discussed next.

##### 1.2.3.1.2. p-i-n photodiode

As indicated by its name, a p-i-n photodiode is composed of an intrinsic layer sandwiched in between a p-n junction. Because the i-layer is devoid of free charge carrier, it is covered by the depletion region. Hence, in p-i-n structure the depletion region width can be easily adjusted by changing the i-layer's width. Common p-i-n photodiodes have a responsivity in the range from 0.6 to 0.9  $\text{A/W}$  and a bandwidth varying from 1 to 10 GHz.

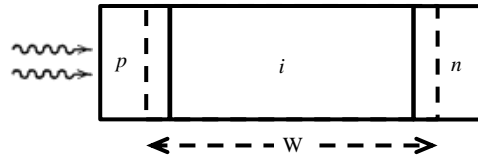


Figure 1.4 – p-i-n photodiode structure.

### 1.2.3.1.3. Avalanche photodiode

In both p-n and p-i-n photodiodes the responsivity is limited by  $R_{max} = q/h\nu$  when the quantum efficiency is 100% [14], where  $q$  is the electron charge,  $h$  is the Planck constant and  $\nu$  is the optical frequency. Hence, the sensitivity of such photodetectors is limited, e.g. -20 dBm for a p-i-n-based photodetector.

In practice, an Avalanche Photodiode (APD) is used to improve the receiver sensitivity. Such a photodiode works on the principle of impact ionization [15] according to which an accelerating electron can generate a new electron-hole pair (this is also valid for an accelerating hole). In order that this electron-hole multiplication takes place, avalanche photodiode structure has an additional layer which is a p-doped layer sandwiched in between the i-type and the n-doped layers of a p-i-n structure. This layer is referred to as the multiplication layer where the impact ionization takes place. The common value of the responsivity of an APD is from 5 to 20 A/W and the bandwidth is from 1 to 10 GHz.

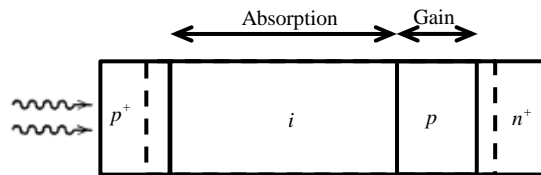


Figure 1.5 – Avalanche photodiode structure.

### 1.2.3.2. Transimpedance Amplifier

In a photodetector, the photodiode is in general followed by a Transimpedance Amplifier (TIA) in order to convert photodiode output current into output voltage. A TIA is designed with two criteria. First, it presents low impedance to the photodiode. And second, it isolates the photodiode from the output voltage. The first criterion is to limit the power of thermal noise generated during the current-voltage conversion. This is discussed more in detail in section 1.3.1.3. The simplified structure of a TIA is shown in Figure 1.6. An operational amplifier is used to amplify the photodiode output current for further processing.

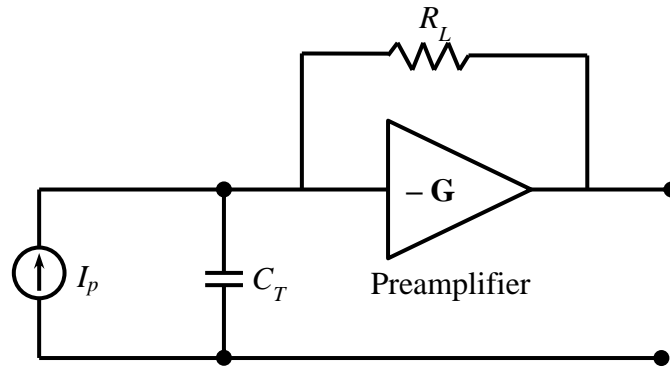


Figure 1.6 – A simplified transimpedance amplifier structure.

### 1.3. Optical channel impairments

This section describes different noise sources as well as linear and nonlinear channel impairments in an optical communication system. According to the transmission architecture, one impairment becomes dominant when compared to another. For example, in the context of access network where in-line optical amplifiers are not usually implemented, the Amplified Spontaneous Emission (ASE) noise does not exist. And the thermal noise of a photodiode is often the principal noise source in this context. Another example is that in a short-reach transmission the impact of polarization mode dispersion is often considered negligible. Although this thesis focuses on optical IMDD transmission, a panorama of impairments coming from the modulator, the fiber link and the photodetector is given. This gives a better understanding of fiber-based optical communication and the feasibility of signal processing techniques discussed in this thesis. For some proposed techniques, the application scope is not limited by only IMDD transmissions.

#### 1.3.1. Noise sources

##### 1.3.1.1. Relative Intensity Noise

Laser Relative Intensity Noise (RIN) is important when the laser intensity is directly modulated by a driving current (*e.g.* DMLs). RIN corresponds to a variation of laser power around the average power. It is defined as the ratio between the noise power  $E\{(\Delta P)^2\}$  and the square of average laser power

$$RIN = \frac{E\{(\Delta P)^2\}}{\bar{P}^2}, \quad (1.2)$$

in dB

$$RIN_{dB} = 10 \log \left( \frac{E\{(\Delta P)^2\}}{\bar{P}^2} \right). \quad (1.3)$$

For a DFB laser used in access networks, the typical value of RIN is about  $-140 \text{ dB} \cdot \text{Hz}^{-1}$ .

According to [16], both the statistical distribution and the Power Spectral Density (PSD) of RIN depend on the intrinsic laser and bias current. When the bias current is much

more important than the laser emission threshold current, RIN can be considered as a Gaussian noise. However, at low bias current, the distribution is not Gaussian any more and is not symmetric. An example of RIN PSD as a function of bias current is illustrated in Figure 1.7. The higher the bias current value, the lower the RIN power is. The noise power achieves its maximum at the laser resonance frequency which depends also on bias current. Obviously, RIN is not a white noise.

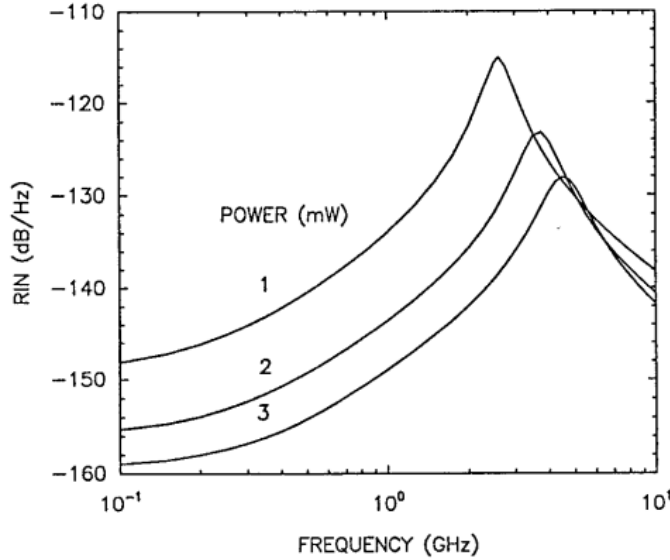


Figure 1.7 – RIN PSD at several bias current values.

(Source: [14]).

### 1.3.1.2. Laser phase noise

Even when driven by a constant bias current, the phase of the optical field at the laser output is not constant but randomly changes over time. More concretely, according to [17], the laser phase noise can be modeled by a Wiener-Levy process, which is a zero-mean Gaussian process. The variance of the laser phase fluctuation between the time instants  $t$  and  $t + \tau$  can be expressed as

$$E \{ (\Delta\phi(\tau))^2 \} = 2\pi\Delta\nu|\tau|, \quad (1.4)$$

where  $\Delta\nu$  is the 3-dB Lorentzian laser linewidth. The typical value of  $\Delta\nu$  is 100 kHz for an External-Cavity diode Laser (ECL) and 5 MHz for a DFB laser. The laser phase noise is responsible for the enlargement of the transmitted signal spectrum. With the presence of laser phase noise, the optical carrier is not completely monochromatic. It is rather a carrier with specific bandwidth.

In coherent transmission systems, laser phase noise is one of the main detriment factors since it causes random rotation of the received signal constellation. This phase rotation can be treated by carrier phase estimation techniques [18], [19]. In an Orthogonal Frequency Division Multiplexing (OFDM) transmission, the laser phase noise results in Common Phase Rotation (CPR) of the entire OFDM subcarriers and Inter Carrier Interference (ICI). The CPR can be easily estimated and compensated with subcarrier

pilots [20], [21]. And the ICI can be eliminated by compensating directly the phase noise in the time domain with a Radio Frequency (RF) pilot tone [22]–[24].

In the context of IMDD transmissions where the signal intensity is detected by photodiode (direct detection), only the amplitude of the received signal is acquired. Hence, the transmission system is found to be highly tolerant to the laser phase noise. However, because of chromatic dispersion, the phase noise of the optical field can be converted into intensity noise after the photodiode due to Phase Modulation (PM)-to-Amplitude Modulation (AM) noise conversion process [25]–[27]. According to analysis in [25], the power penalty is only remarkable when the laser linewidth is in the order of several hundreds of MHz, the transmission bit rate exceeds several Gb/s and the accumulated chromatic dispersion is in the order of several thousands of ps/nm. In the context of access networks, where the transmission distance is limited at several tens of kilometers and the typical value of the linewidth of a DFB laser is several MHz, the impact of the laser phase noise on the transmission performance may not be significant.

### 1.3.1.3. Photodetector noises

#### 1.3.1.3.1. Quantum shot noise

The quantum shot noise results from the photon-current conversion process of the photodiode. On the receiver side, due to absorption of the photodiode, the incident light generates electron-hole pairs, which contribute to the output current of the photodetector. Hence, the output current intensity is proportional to the intensity of the received optical signal. However, a part of the incident photons does not generate electron-hole pairs. The number of electron-hole pairs generated during a time interval  $\Delta\tau$  can be characterized by a Poisson random variable. This random generation of electron-hole pairs causes a fluctuation of the photodiode output current even with a constant incident light intensity. This fluctuation is generalized by shot noise or "quantum shot noise". According to [17], the Poisson random process of shot noise can be approximated by a Gaussian process. The power of the white, Gaussian quantum shot noise can be expressed as

$$E\{(i_{shot\ noise})^2\} = 2q\bar{I}\Delta f, \quad (1.5)$$

where

- $\bar{I}$  : Average output current.
- $\Delta f$  : Effective received signal bandwidth.
- $q$  : Electron charge.

#### 1.3.1.3.2. Dark current noise

Even without the presence of incident light, a photodiode itself randomly creates electron-hole pairs due to thermal effects or stray light. These electron-hole pairs contribute to the dark current  $I_{dark}$  of the photodiode, resulting in dark-current-induced shot noise. Therefore, the total power of the photodiode noise can be expressed as

$$E\{(i_{noise})^2\} = 2q(\bar{I} + I_{dark})\Delta f. \quad (1.6)$$

The dark current of common photodetectors is about 10 nA which should be negligible when compared to quantum shot noise or receiver thermal noise.

### 1.3.1.3.3. Thermal noise

In general, after the optical-to-electrical conversion performed by the photodiode, a TIA is used for converting current variation into voltage variation. In typical photodetector designs, this current-voltage conversion is mostly carried out by a transimpedance front end which is composed of a load resistor and an operational amplifier as shown in Figure 1.6. Thermal effects cause random motion of electrons in the load resistance. This causes thermal noise on the output voltage. Amplification is then applied to compensate for the loss due to the optical-electrical conversion. By amplifying the output signal power, the noise power is also amplified. The thermal noise is shown to be a quasi-white (the PSD is constant up to 1 THz), Gaussian noise. The power of thermal noise causes by load resistance  $R_L$  is expressed as

$$E\{(i_{thermal})^2\} = \frac{4k_B\theta}{R_L} \Delta f, \quad (1.7)$$

where

- $\theta$  : Absolute temperature.
- $k_B$  : Boltzmann constant.

### 1.3.1.4. Amplified spontaneous emission noise

The ASE noise comes from the optical signal amplification. This type of noise has no relationship with the signal. It is often modeled by a Gaussian noise whose PSD (W/Hz) can be expressed as

$$S_{ASE}(v) = GF_{no}hv/2, \quad (1.8)$$

where

- $G$  : Amplifier gain (linear)
- $hv$  : The energy of a photon
- $F_{no}$  : Amplifier noise figure (linear), which is the ratio between the SNR at the amplifier input and that at the amplifier output. The typical value is between 3 and 7 dB.

In a system where there are several optical amplifiers, according to Friis formula, the equivalent noise figure is expressed as [28]

$$F_{no} = F_{no,1} + \frac{F_{no,2} - 1}{G_1} + \frac{F_{no,3} - 1}{G_1 G_2} + \dots + \frac{F_{no,K} - 1}{G_1 G_2 \dots G_{K-1}}. \quad (1.9)$$

ASE noise might be the dominant noise in a long-haul and metropolitan optical fiber-based transmission because several optical amplifiers are needed to compensate for the accumulated fiber attenuation. In contrast, for access network applications where the transmission distance is relatively short and especially due to the problem of cost, usually

no in-line optical amplifier is implemented. Hence, the ASE noise may be negligible in this application.

### 1.3.1.5. Laser reflection noise

Because of the discontinuity of the refractive index occurring at the couplings such as laser-fiber, fiber-fiber, *etc.*, a small part of the transmitted signal can be reflected. It can disrupt the laser operation and increase the laser intensity noise. However, nowadays, couplers that make this noise negligible are available.

## 1.3.2. Linear impairments of the optical channel

### 1.3.2.1. Attenuation

Due to fiber attenuation, the relationship between received signal power and the transmitted signal after an  $L$ -km transmission can be expressed as

$$P_{out} = P_{in} \exp(-\alpha_{att}L), \quad (1.10)$$

where  $\alpha_{att}$  denotes the attenuation constant. This quantity is often expressed in dB/km as

$$\alpha_{att,dB} \approx 4.343\alpha_{att} \text{ dB/km}. \quad (1.11)$$

In an optical fiber, the signal attenuation originates from several phenomena. The most significant phenomena that are considered here are the material absorption, the intrinsic attenuation (Rayleigh scattering) and the fiber imperfection. The fiber attenuation as a function of wavelength is shown in Figure 1.8.

#### 1.3.2.1.1. Material absorption

Material absorption depends on the nature of the fiber and on the wavelength. The material absorption can be divided into two categories: intrinsic absorption which depends on the nature of the fiber and extrinsic absorption depending on extrinsic impurities of the fiber. In Figure 1.8 extrinsic impurities result in the attenuation peak at 1.38  $\mu\text{m}$  which corresponds to the presence in minute quantities of  $\text{OH}^-$  ion from water dissolved in glass.

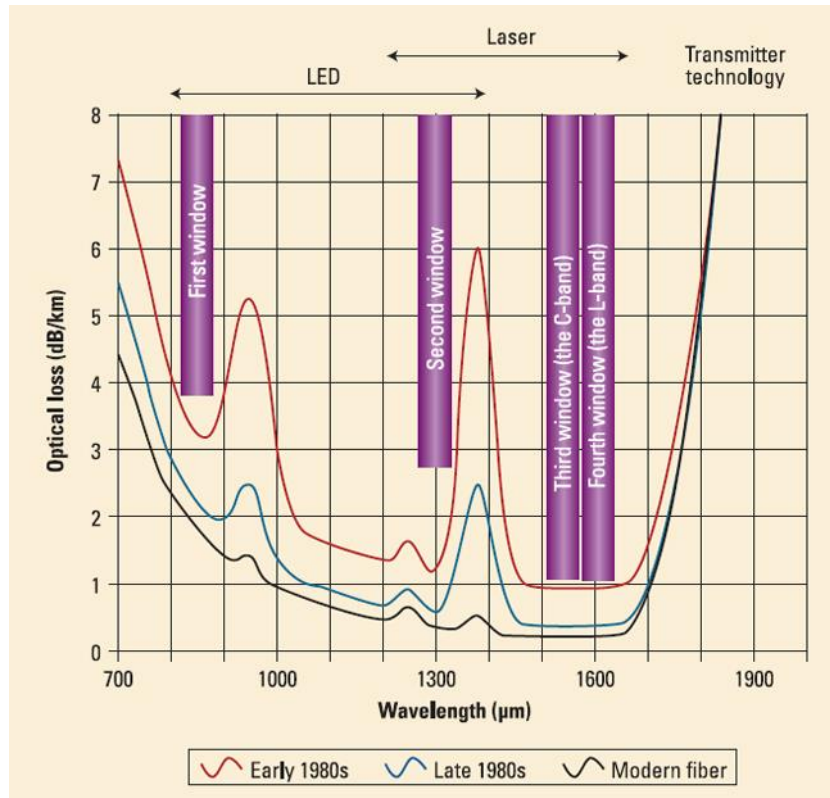


Figure 1.8 – Attenuation in SSMF fibers as a function of wavelength.

(Source: [29]).

### 1.3.2.1.2. Rayleigh scattering

Because of the manufacturing technology of optical fiber, the density of silicone molecules is not uniform in the fiber. The microscopic fluctuation in the density of molecules causes the fluctuation of the refractive index of the fiber. This is the origin of the inherent loss or Rayleigh scattering. According to [8], the intrinsic attenuation can be written as

$$\alpha_R = \frac{C}{\lambda^4} \text{ dB/km}, \quad (1.12)$$

where

C : A constant between 0.7 and 0.9  $\left(\frac{\text{dB}}{\text{km}}\right) \mu\text{m}^4$ .

$\lambda$  : Wavelength ( $\mu\text{m}$ ).

Rayleigh scattering is the main factor causing the attenuation in the optical fiber. Many modern optical communication standards make use of the wavelength zone around 1.5  $\mu\text{m}$  corresponding to the minimum value of fiber attenuation.

### 1.3.2.1.3. Imperfection of the fiber

Because of manufacturing technology, a fiber is not perfectly cylindrical. This imperfection causes an additional loss of energy at the edges of the fiber.

### 1.3.2.2. Second order chromatic dispersion

Chromatic dispersion results from the fact that the refractive index of the material depends on the wavelength of light. As a result, in the optical fiber, different wavelengths (or frequencies) propagate with different speeds. If one sends an impulse having a bandwidth of  $B$  Hz, different spectral components of the signal propagate at different speeds. On the receiver side, a larger pulse should be observed. The figure below illustrates this fact

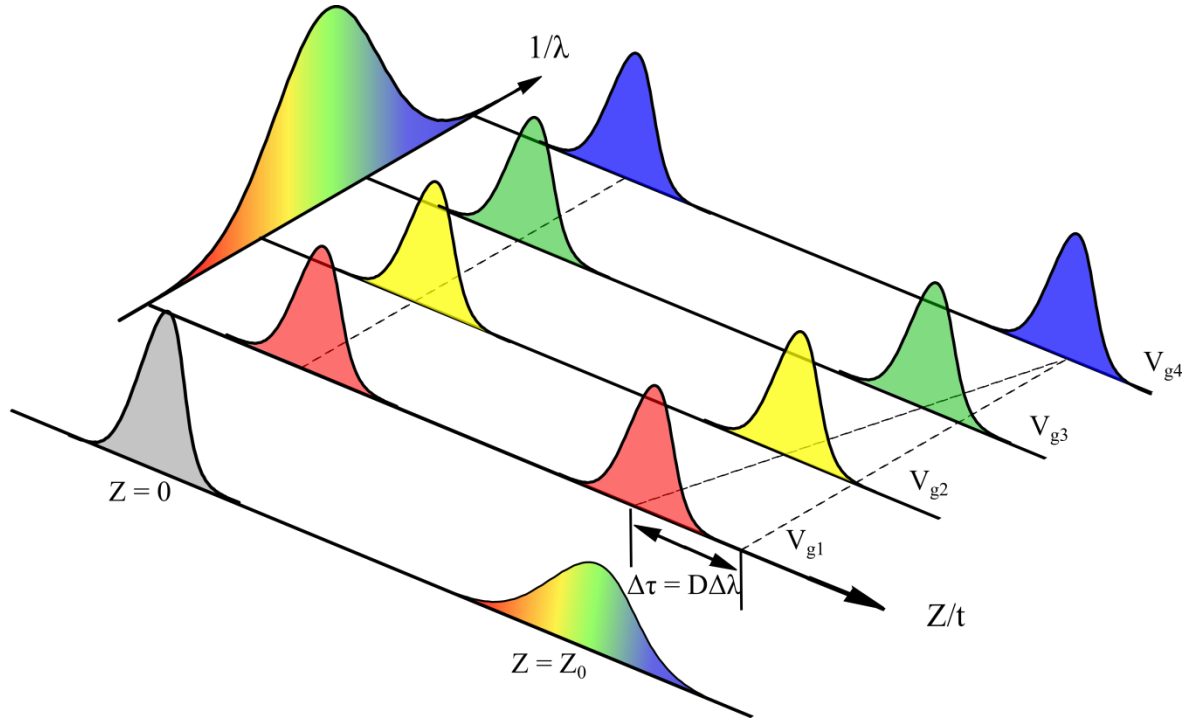


Figure 1.9 – Pulse enlargement due to chromatic dispersion.

To better understand the origin of the chromatic dispersion it is common in the literature to develop the Taylor series of the propagation constant  $\beta(\omega)$

$$\begin{aligned} \beta(\omega) &= \beta(\omega_0) + \frac{1}{1} \left( \frac{\partial \beta}{\partial \omega} \right)_{\omega_0} (\omega - \omega_0) + \frac{1}{2} \left( \frac{\partial^2 \beta}{\partial \omega^2} \right)_{\omega_0} (\omega - \omega_0)^2 + \dots \\ &= \beta_0 + \beta_1 (\omega - \omega_0) + \frac{1}{2} \beta_2 (\omega - \omega_0)^2 + \dots \end{aligned} \quad (1.13)$$

According to [8]

$$\begin{aligned} \beta_1 &= \frac{1}{v_g} = \frac{n_g}{c} = \frac{1}{c} \left( n + \omega \frac{dn}{d\omega} \right), \\ \beta_2 &= \frac{\partial \beta_1}{\partial \omega} = \frac{1}{c} \left( \frac{dn}{d\omega} + \omega \frac{d^2 n}{d\omega^2} \right). \end{aligned} \quad (1.14)$$

The term  $\beta_1$  corresponds to the group velocity of the signal and the term  $\beta_2$  corresponds to the dispersion of the group velocity. In other words, in the fiber, a frequency component  $\omega$  propagates with a group velocity  $v_g(\omega)$ . When  $\beta_2$ , which

corresponds to the frequency-dependent group velocity, is not null, different wavelengths have different group velocities. Hence,  $\beta_2$  is responsible for the pulse enlargement.

To characterize the chromatic dispersion, it is common in the literature to use the chromatic dispersion parameter

$$D = \frac{d\beta_1}{d\lambda} = -\frac{2\pi c}{\lambda^2} \beta_2 = -\frac{\lambda}{c} \frac{d^2 n}{d\lambda^2} \text{ ps}/(\text{nm} \cdot \text{km}). \quad (1.15)$$

Physically, in the area where  $\beta_2 > 0$  (normal zone), high-frequency spectral components propagate more slowly than low-frequency components and vice versa, in the area where  $\beta_2 < 0$  (abnormal zone), high-frequency components propagate faster than low-frequency components. The dispersion described so far is referred to as the material dispersion as shown in the figure below. In actual fibers, the effective mode index is slightly lower than the material index due to the effect of waveguide dispersion. In this case, the wave's phase velocity depends on its frequency due to the structure geometry. Waveguide dispersion slightly shifts the zero-dispersion wavelength  $\lambda_{ZD}$  toward longer wavelength. Because waveguide dispersion depends on fiber parameters such as core radius and core-cladding index difference,  $\lambda_{ZD}$  can be shifted toward 1.55  $\mu\text{m}$  where the loss is minimum, resulting in dispersion-shifted fibers used in many applications of optical communication systems.

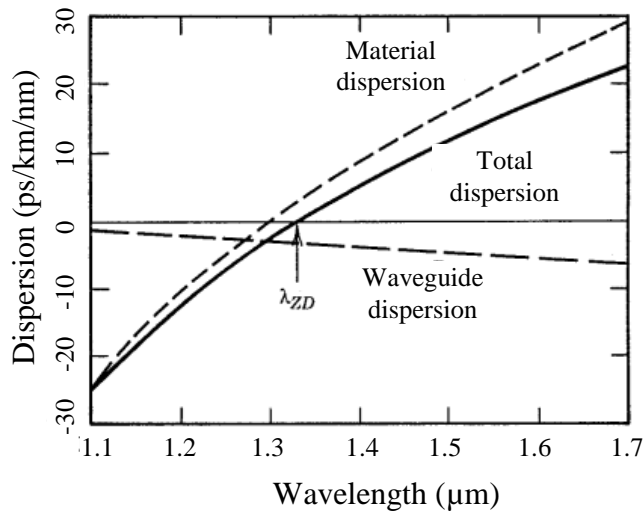


Figure 1.10 – Chromatic dispersion parameter in standard single mode fibers.

(Source: [14]).

The effects of the second order chromatic dispersion can also be addressed by the nonlinear Schrödinger equation [8]. The second order chromatic dispersion can be described from Eq. (1.1)

$$\frac{\partial A}{\partial z} = -\frac{j}{2} \beta_2 \frac{\partial^2 A}{\partial t^2}. \quad (1.16)$$

It is not difficult to find the solution of the equation above in the Fourier-transformed domain

$$\tilde{A}(z, \omega) = \tilde{A}(0, \omega) \exp\left(\frac{j}{2} \beta_2 \omega^2 z\right), \quad (1.17)$$

where  $\tilde{A}(z, \omega)$  is the Fourier transform of  $A(z, t)$  and is defined as

$$\tilde{A}(z, \omega) = \int_{-\infty}^{+\infty} A(z, t) \exp(j\omega t) dt. \quad (1.18)$$

From Eq. (1.17) it is obvious that the second order chromatic dispersion does not change the pulse amplitude during the propagation. However, it changes the phase of the optical pulse and the phase change depends on the dispersion parameter, the frequency and the transmission distance.

In coherent single carrier optical transmission [30], the chromatic dispersion enlarges the transmitted pulses. On the receiver side, the received sample is composed of not only the sample of interest but also precursor and postcursor interferences. In order to eliminate the Inter Symbol Interference (ISI), both time-domain filtering [31] or frequency domain equalization techniques [31], [32] give good performance. Alternatively, the ISI problem can be treated by the use of multicarrier modulation such as the OFDM. In coherent optical OFDM transmission [17], [21], with a sufficient cyclic prefix the chromatic dispersion results only in a phase rotation on each subcarrier. A simple phase compensator is sufficient to eliminate this effect.

On the contrary, the effect of chromatic dispersion is much more annoying in an optical IMDD transmission. In conventional IMDD systems, the transmitted signal is in general a double side band signal because of the constraint of a real-valued laser-modulating current. Over a dispersive channel, the phase change of a positive frequency component is different from that of the corresponding negative frequency component. Due to the direct detection of the photodiode, the amplitude of the received signal frequency component is attenuated according to the phase difference of the two frequency components [33], [34]. The destructive beat of the frequency components with the optical carrier depends on the signal frequency, the chromatic dispersion parameter and the fiber length. More concretely, when the laser is modulated with a small-amplitude monochromatic signal, the IMDD channel response can be written as [35], [36]

$$H_F(f) = \cos\left(\pi \frac{f^2}{f_D^2}\right) - \alpha \left(1 - j \frac{f_c}{f}\right) \sin\left(\pi \frac{f^2}{f_D^2}\right), \quad (1.19)$$

where the dispersion frequency  $f_D$  given by

$$f_D^2 = \frac{c}{\lambda^2 DL}, \quad (1.20)$$

$\alpha$  denotes the laser linewidth enhancement and  $f_c$  (Hz) is the adiabatic frequency. The “small-signal” channel frequency response is also illustrated in Figure 1.11

---

<sup>1</sup> In “Nonlinear Fiber Optics”, the Fourier transform convention is different from the mathematical conventional convention. The sign of the optical carrier angular velocity is also inverted. This aspect must be taken into account.

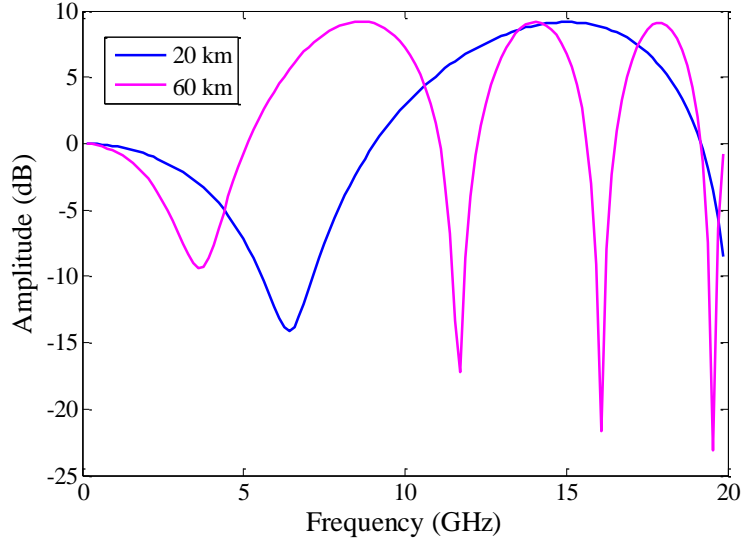


Figure 1.11 – Small-signal IMDD channel frequency response from Eq. (1.19). Laser linewidth enhancement factor is 2.68. Adiabatic frequency is 1.4 GHz.

The attenuation dips in Figure 1.11 correspond also to information loss which cannot be recovered. In conventional NRZ transmissions, channel equalization techniques can be implemented to improve the transmission performance even though the improvement is still limited [37]–[39]. When OFDM modulation is used, the information loss can be avoided by using single side band transmissions [40], [41]. Otherwise, adaptive modulation which adapts the subcarrier constellation and power according to the channel gain is also shown to bring excellent performance [11], [42]–[46]. In addition, the presence of chromatic dispersion also causes Frequency Modulation (FM) to AM conversion effects, which degrade the SNR on the receiver side [26]. Chromatic dispersion is also shown to aggravate the problem of laser phase noise to intensity noise conversion although the impacts are only significant when lasers having large linewidth (in the order of hundreds of MHz) are used [25].

Last but not least, the chromatic dispersion does not only raise problems for an optical transmission system. Indeed, it is rather a good factor for fiber nonlinearity mitigation such as Four Wave Mixing (FWM) mitigation. It is well known that the FWM process depends strongly on the phase matching between different frequency components [8]. When chromatic dispersion becomes significant, the phase change on a frequency component is less likely to be coherent with that of another frequency component. In the literature the phase coherence between two pulses with corresponding wavelengths  $\lambda_1$  and  $\lambda_2$  can be evaluated by the walk-off length defined as

$$L_w = \frac{\tau_0}{d_{12}}, \quad (1.21)$$

where  $\tau_0$  is the pulse time duration and  $d_{12}$  denotes the difference of the group velocities which can be expressed as

$$d_{12} = \beta_1(\lambda_1) - \beta_1(\lambda_2). \quad (1.22)$$

From Eq. (1.21) and (1.22) it is obvious that when chromatic dispersion is significant, the walk-off length becomes small which means that phase coherence between different wavelengths becomes weak. The power of eventual FWM products is hence reduced.

### 1.3.2.3. Polarization mode dispersion

Single mode fiber has actually two modes of propagation with two orthogonal polarizations. The two orthogonal polarizations propagate through the fiber with different speeds. The origin of the polarization dispersion is related to the birefringence of a fiber. Ideally, if a fiber is perfectly cylindrical and there is no outside influence, the two modes propagate with the same speed. In fact, because of fiber imperfection, thermal variation, mechanical vibrations, bending of the fiber or electromagnetic fields, a fiber has a birefringence and the refractive indices of two polarizations are not the same. As a result, the two modes propagate with different speeds.

#### 1.3.2.3.1. Polarization mode dispersion in short fibers

An optical fiber is considered short if its length is smaller than the Correlation Length (CL), which is defined as the length over which two polarization components remain correlated. Typical values of CL are in the order of 10 m. In this case, fiber birefringence is characterized by two axes of birefringence called fast axis and slow axis. It can be expressed as the difference between the propagation constants of modes

$$\Delta\beta = \frac{\omega\Delta n}{c}, \quad (1.23)$$

where  $\Delta n$  is the difference between the refractive indices of the fast and slow axes. If on the transmitter side a pulse is polarized along one of the two axes of birefringence, it will propagate without deformation and on the receiver side an identical pulse is observed (note that this is only true when the impact of chromatic dispersion is excluded). Otherwise, if the polarization axis of the pulse does not correspond to one of the two axes of birefringence, on the receiver side Polarization Mode Dispersion (PMD) is reflected by the fact that one receives two pulses separated by an amount of time corresponding to the Differential Group Delay (DGD) as illustrated in the figure below.



Figure 1.12 – Illustration of the PMD in a short fiber.

#### 1.3.2.3.2. Polarization mode dispersion in long fibers

If the fiber length is much longer than the CL ( $L > 0.1$  km), it is then considered as a long fiber. In this case, the amplitude as well as the direction of birefringence changes randomly

along a fiber. In this case a fiber can be modeled by a set of short sections possessing different birefringence as shown in the figure below

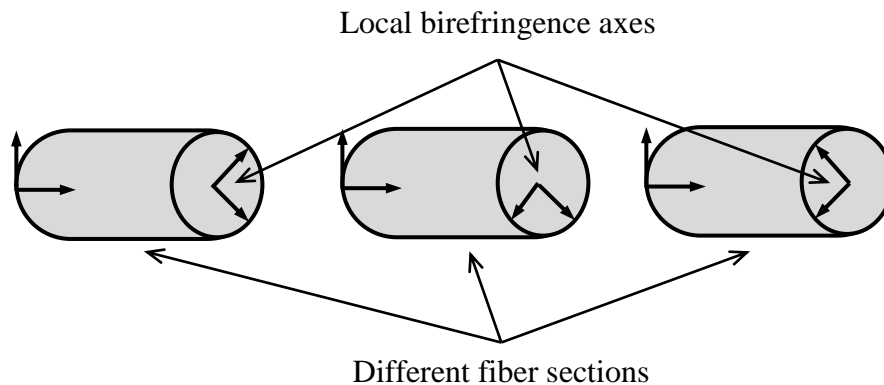


Figure 1.13 – Long fiber birefringence model.

### 1.3.2.3.3. Coupling mode

Random change of birefringence in a long fiber causes energy exchange between two polarization modes. After each section of short fiber, a transmitted pulse results in two pulses having different delays. On the receiver side, one observes a large number of pulses having random delays such that the resulting problem of polarization dispersion may become fairly complicated as shown in the figure below

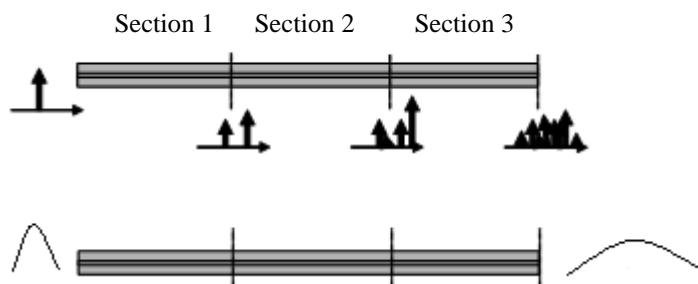


Figure 1.14 – Illustration of pulse enlargement due to PMD in a long fiber.

### 1.3.2.3.4. Model of the principle polarization states

The model of principle polarization states has been invented thanks to the works of Poole and Wagner [47]. Supposing that the transmitted signal band is narrow<sup>2</sup>, there is always a pair of the Principle State of Polarizations (PSP) that characterized a long fiber. If the signal is aligned along one of the two PSPs, on the receiver side there is a polarization state in which the polarization of the output signal does not depend on the frequency to the first order. Specifically, first derivative with respect to frequency of the polarization vector is equal to zero. In addition, the two main states are orthogonal in the absence of the Polarization Dependent Loss (PDL). Physically, with an approximation to first order, when

<sup>2</sup> The supposition of narrow band signal is true if the signal bandwidth is much smaller than the optical carrier frequency.

a pulse is aligned to one of the two main states, it propagates through the fiber and experiences randomly changed polarization states. However, on the receiver side there is always a polarization state in which the received pulse is not deformed. The two principle states that characterize a long fiber can be considered as the two modes that characterize the fiber birefringence of a short fiber except that in the principle state model, the polarization of the signal randomly changes along the fiber.



Figure 1.15 – Illustration of PMD by the first order approximation.

A signal having any polarization can be considered as a superposition of two principle states. The principle states and the corresponding DGD change over time. According to [8], the DGD is a Maxwellian random variable:

$$PMD = \sqrt{E(\Delta T^2)} = D_p \sqrt{L} \quad (1.24)$$

$D_p$  : Polarization dispersion parameter (ps/ $\sqrt{\text{km}}$ )

$\Delta T$  : The delay between two principle states.

$L$  : Fiber length (km).

In fiber-based optical communications, PMD provokes a power transfer between the two principle states. In coherent systems it is impractical to implement a SISO (Single Input Single Output) system because of such power transfer. On the transmitter side, the signal polarized on an arbitrary polarization can be decomposed into two signals having two orthogonal polarization states. On the receiver side, a received signal is a superimposition of an attenuated transmitted signal, which is due to the power transfer, and echoes, which are due to the DGD. However, thanks to the model of the principle polarization states, a transmitted signal can be easily reconstituted by means of polarization multiplexing [17]. The receiver can be designed to receive two arbitrary orthogonal polarization states. In this case the frequency channel transfer function can be modeled by a 2x2 matrix, which can be equalized for example by a simple matrix inversion<sup>3</sup> (zero forcing method).

In multi-Gb/s optical IMDD transmissions, PMD is one of the principle capacity-limiting factors when the fiber length increases. It is shown in Figure 1.16 that the power penalty due to PMD is below one dB when DGD is below the 30%-bit-time. Hence, in designing the transmission system, one of the thumb rules is that the maximum DGD must not exceed the 30%-bit duration. Because DGD is a random variable, in practice if a designer wants to guarantee that the probability of DGD exceeding DGD max is less than  $4.2 \times 10^{-5}$ , then he must design the link with a PMD that is 1/3 of the DGD max. PMD design rule can be deduced as

<sup>3</sup> The matrix inversion is effectuated in the frequency domain. In the time domain, FIR filters can be used.

$$\begin{aligned}
 DGD_{max} &< 0.3T_B \\
 \Leftrightarrow 3 \cdot PMD &< 0.3T_B \\
 \Leftrightarrow PMD &< T_B/10,
 \end{aligned}
 \tag{1.25}$$

where  $T_B$  is the bit duration. As indicated in IUT standard G.652 [48], the typical value of PMD parameter of standard single mode fiber is about  $0.5 \text{ ps}/\sqrt{\text{km}}$ . Hence, it is straight forward that as long as the data rate and the fiber length are respectively below 20 Gb/s and 100 km, the PMD is well below the tolerance value. In the context of access networks, the impact of PMD can hence be considered as negligible.

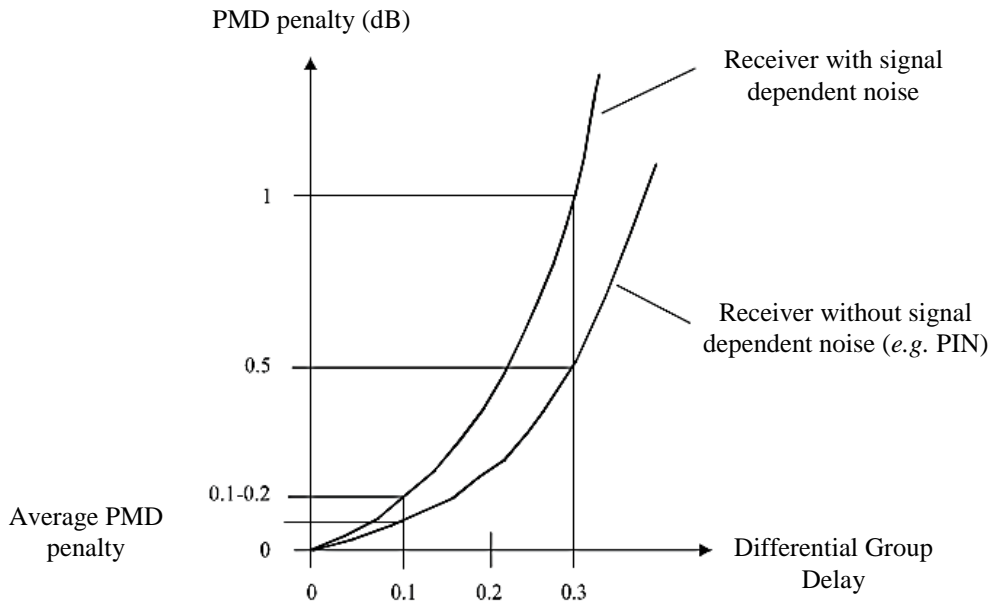


Figure 1.16 – The dependence of receiver penalty in the actual DGD.

(Source: [49]).

#### 1.3.2.4. Polarization dependent loss

In an optical communication link, an optical component always introduces insertion loss. In general, the losses caused by two polarizations are not identical. Similarly, when implementing an optical amplifier (EDFA for Erbium-Doped Fiber Amplifier), the amplifier gain is also polarization-dependent.

The PDL may be the cause of the asymmetry of optical components. In the absence of PDL, the transfer matrix of PMD is unitary and the model of principal states is valid. On the contrary, in the presence of PDL, this matrix is not unitary and the model of Poole and Wagner loses its generality. Through experiments, several abnormal effects produced by the PDL are observed [8]

- Abnormal DGD
- Abnormal group velocity
- Impulsion widening even in the case of absent DGD

### 1.3.3. Nonlinear effects of the optical channel

In fiber-based optical transmissions, the system performance is limited not only by linear effects described above but also by nonlinear effects originated from the susceptibility  $\chi^{(3)}$  [8] whose the real part leads to Self-Phase Modulation (SPM), Cross-Phase Modulation (XPM), FWM and the imaginary part leads to Stimulated Raman Scattering (SRS) and Stimulated Brillouin Scattering (SBS). Different fiber nonlinear effects are summed up in Figure 1.17.

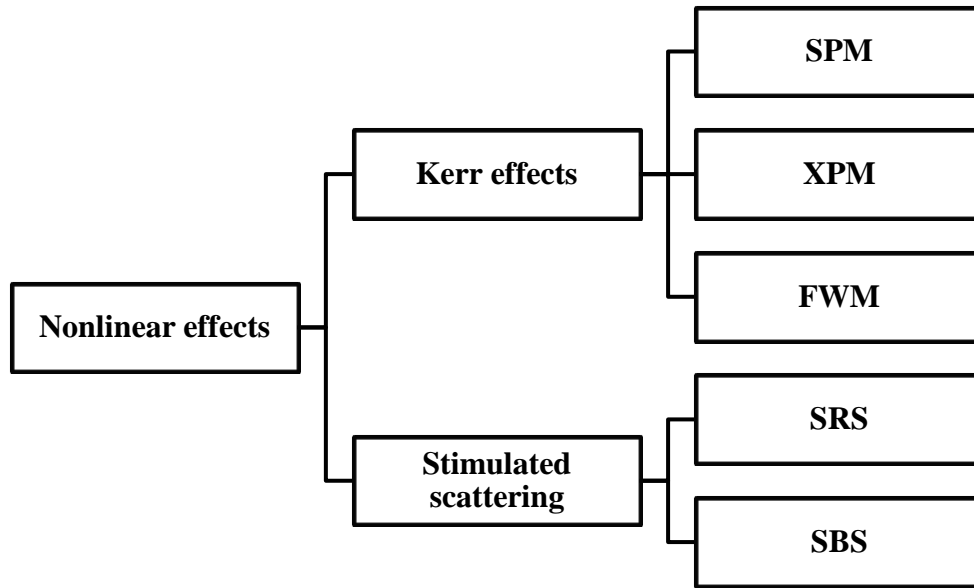


Figure 1.17 – Major nonlinear effects in fibers.

#### 1.3.3.1. Kerr effects

Nonlinear Kerr effects are generated due to the dependence of the refractive index of a fiber in the optical intensity. This dependence leads to nonlinear phenomena including self-phase modulation, cross-phase modulation and four-wave mixing.

##### 1.3.3.1.1. Self-phase modulation

Due to the dependence of the fiber refractive index in the optical intensity, an intensity modulation generates itself a phase modulation. This phenomenon is well described by the NLS propagation equation. We recall the NLS equation by only taking into account the nonlinear term

$$\frac{\partial A}{\partial z} = j\gamma_F(\omega_0)|A|^2A. \quad (1.26)$$

Nonlinear coefficient  $\gamma_F$  ( $W^{-1}/km$ ) is defined as

$$\gamma_F = \frac{2\pi n_2}{\lambda A_{eff}}, \quad (1.27)$$

where  $n_2$  ( $\text{m}^2/\text{W}$ ) is the nonlinear-index coefficient and  $A_{eff}$  ( $\text{m}^2$ ) is the effective area of the principal mode in a mono-mode fiber [8]. The solution of Eq. (1.26) can be obtained as

$$A(L, t) = A(0, t) \exp(j\Phi_{NL}(t)), \quad (1.28)$$

where

$$\Phi_{NL}(t) = \gamma_F L |A(0, t)|^2. \quad (1.29)$$

As shown in Eq. (1.29), the nonlinear phase shift depends on the nonlinear coefficient  $\gamma_F$ , the fiber length  $L$  and the pulse power. On the negative side, SPM causes spectral broadening of a transmitted signal which degrades the system performance. In addition, modulation instability caused by SPM often enhances system noise. On the positive side, SPM can be used for fast optical switching. It can also be used to generate solitons such that the nonlinear phase shift due to SPM can be compensated by the phase shift due to chromatic dispersion. In this case the pulse shape either does not change along the fiber length or follows a periodic evolution pattern [8]. In addition, modulation instability can be used to generate ultra-short pulses. In general, SPM is considered as a detrimental phenomenon for a fiber-based optical transmission. In optical IMDD transmission in particular, phase modulation caused by SPM enhances noise on the receiver side through the phase modulation-to-intensity modulation noise conversion process [26], [27].

### 1.3.3.1.2. Cross-phase modulation

When two optical pulses having different wavelengths propagate through a fiber, the fiber refractive index with respect to one pulse depends not only on the pulse power but also on the power of the other pulse. In this case the NLS equation can be written as the following set of two coupled equations

$$\frac{\partial A_1}{\partial z} = -\frac{\alpha_{att}}{2} A_1 - \beta_1(\omega_1) \frac{\partial A_1}{\partial t} - \frac{j}{2} \beta_2(\omega_1) \frac{\partial^2 A_1}{\partial t^2} + j\gamma_F(\omega_1)(|A_1|^2 + 2|A_2|^2)A_1, \quad (1.30)$$

$$\frac{\partial A_2}{\partial z} = -\frac{\alpha_{att}}{2} A_2 - \beta_1(\omega_2) \frac{\partial A_2}{\partial t} - \frac{j}{2} \beta_2(\omega_2) \frac{\partial^2 A_2}{\partial t^2} + j\gamma_F(\omega_2)(|A_2|^2 + 2|A_1|^2)A_2. \quad (1.31)$$

Like SPM, XPM causes nonlinear phase shift, resulting in spectral broadening of a transmitted pulse. XPM also causes inter-channel crosstalk in Wavelength Division Multiplexing (WDM) transmissions. In optical OFDM transmissions in particular, XPM causes inter-carrier interference that cannot be suppressed by a cyclic prefix. On the positive side, XPM can be used for ultrafast optical switching, demultiplexing of Optical Time Division Multiplexing (OTDM) channels [50], [51] or wavelength conversion of WDM channels [52].

### 1.3.3.1.3. Four-wave mixing

Also resulted from the third-order susceptibility  $\chi^{(3)}$ , when one or more optical frequencies are injected in a fiber, new frequency components are created. This effects can be

illustrated by developing the nonlinear polarization term  $\mathbf{P}_{NL}$  in the case where two optical frequencies are launched into a fiber [8]

$$\mathbf{P}_{NL} = \frac{3\varepsilon_0}{4} \chi^{(3)} |E_1 + E_2|^2 (E_1 + E_2) \quad (1.32)$$

$$= \frac{3\varepsilon_0}{4} \chi^{(3)} [(|E_1|^2 + 2|E_2|^2)E_1 + (|E_2|^2 + 2|E_1|^2)E_2 + E_1^2 E_2^* + E_2^2 E_1^*]. \quad (1.33)$$

As shown in Eq. (1.33), when two frequencies  $\omega_1$  and  $\omega_2$  are launched into the fiber, the nonlinear polarization response creates two new frequencies  $2\omega_1 - \omega_2$  and  $2\omega_2 - \omega_1$ .

In WDM transmissions, FWM causes inter-channel interference. In an OFDM optical transmission, each subcarrier can be seen as a monochromatic pulse. Because of this phenomenon, the received signal on a subcarrier also includes FWM products generated from other subcarriers. Hence, FWM causes inter-carrier interference that cannot be suppressed by a cyclic prefix.

### 1.3.3.2. Stimulated Raman scattering

Stimulated Raman scattering is described as a scattering of light from vibrating silica molecules. The principle of SRS is shown in Figure 1.18 where silica molecules are excited to the virtual state by pump photons of energy  $h\nu_p$ ; Stokes photons of reduced energy  $h\nu_s$  are created before the molecules return to the vibrational state.

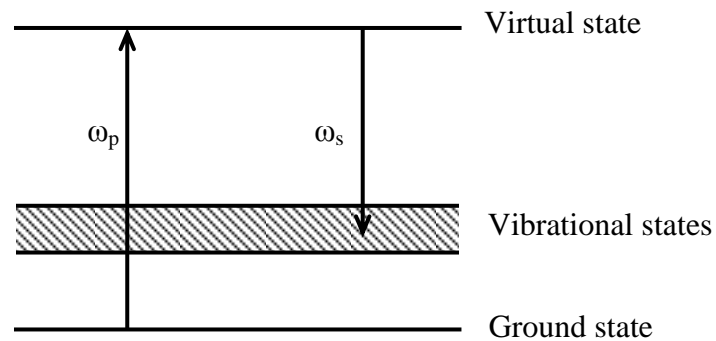


Figure 1.18 – State transition of silica molecules and the resulted Stokes wave  $\omega_s$ .

#### 1.3.3.2.1. Raman gain spectrum

The growth of Stokes waves along the fiber length is described as [8]

$$\frac{dI_s}{dz} = g_R I_p I_s, \quad (1.34)$$

where  $I_s, I_p, g_R$  is Stokes intensity, pump intensity and Raman gain, respectively. The Raman gain coefficient  $g_R$  as a function of frequency shift  $\Omega = \nu_p - \nu_s$  is illustrated in Figure 1.19.

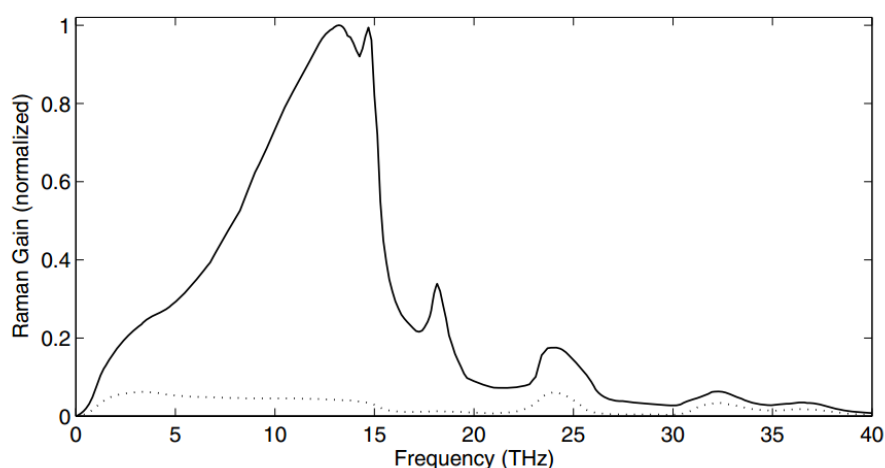


Figure 1.19 – Normalized Raman gain coefficient as a function of frequency shift. Solid curve: Stokes wave and pump wave are copolarized; dot curve: orthogonally polarized.

(Source: [8]).

In principle, when a pump pulse is injected into a fiber, it generates, through SRS, Stokes waves having a spectrum extending up to 40 THz. As shown in Figure 1.19, the Raman gain achieves its maximal value when the frequency shift is around 13 THz. In WDM transmissions SRS causes inter-channel crosstalk that limit the number of channels and the power of each channel.

### 1.3.3.2.2. Raman threshold

From Eq. (1.34) the Stokes power increases with that of the pump power. Raman threshold is defined as input pump power at which total Stokes power is equal to pump power at the fiber output. In conventional fiber-based optical transmission systems, the typical value of Raman threshold is 1 W (30 dBm). In actual IMDD systems, optical launched power is usually limited by 4 dBm. Obviously, in single channel optical transmission the Raman threshold is too high to be of concern.

### 1.3.3.3. Stimulated Brillouin scattering

Unlike SRS which is a scattering of light from vibrating silica molecules, SBS is a scattering of light from acoustic waves. When a pump field is injected into a fiber, it generates acoustic waves through the process of electrostriction. These acoustic waves in turns modulate the refractive index of glass. This generates frequency-downshifted scattered waves whose direction is backward in single-mode fibers. In addition, the frequency shift of generated Stokes waves depends on the acoustic velocity.

#### 1.3.3.3.1. Brillouin gain spectrum

In contrast to SRS where the gain spectrum extends up to 40 THz, the gain spectrum of SBS is more localized and its spectrum width is only in the order of 10 MHz as shown in Figure 1.20.

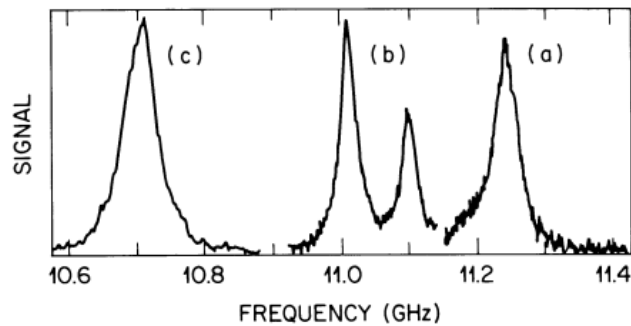


Figure 1.20 – Brillouin gain spectra. (a) silica-core fiber. (b) depressed-cladding fiber. (c) dispersion-shifted fiber.

(Source: [8]).

### 1.3.3.3.2. Brillouin threshold

In order to quantify the power of backward Stokes waves generated through SBS, similar to the Raman threshold, the Brillouin threshold is also defined as input pump power at which scattered light power is equal to that of pump power at the fiber output. In fiber-based optical transmission systems the Brillouin threshold is in the order of 1 mW, which is much lower than that of SRS.

## 1.4. Conclusion

In this chapter the fundamental of IMDD optical transmission systems is described. Principal components from the transmitter side to the receiver side of an IMDD optical transmission link are discussed. Linear and nonlinear impairments of an optical channel and their impacts on an optical transmission in general and an IMDD transmission in particular are also given.

For the choice of an optical modulator, in the context of access network, an operator usually opts for a DML due to its compactness and low cost. It is later shown that in this case, the capacity of an optical transmission significantly depends on the laser characteristics such as laser parasitic cut-off frequency, the frequency response of the intrinsic laser, laser chirps and noise *etc.* In the following chapter in this thesis, only IMDD transmissions using a DML as the modulator are concerned.

Because single-mode fibers are widely implemented all around the world as the transmission support in the context of access networks, in this report they are also considered as the transmission support for different transmission systems. Also for the reason of cost, in access networks no in-line optical amplifier is used. A transmission is hence free from ASE noise. However, fiber nonlinearity-induced noise should be taken into account when the transmission performance is evaluated.

On the receiver side, an access network designer usually uses the direct detection technique by means of a photodiode followed by a TIA. In this type of receiver, the thermal noise is found to be one of the principal capacity-limiting factors.

After identifying the key components in an optical IMDD transmission link described above, we now proceed in the numerical simulation model for transmission systems used in optical access networks.



# CHAPTER 2 Key components in IMDD optical transmissions and numerical modeling

## 2.1. Introduction

In practice, in order to evaluate the performance of a transmission system, it is necessary to carry out extensive measurements and tests. In this context numerical simulation is a good solution to reduce the system evaluation time since experimental implementations are in general bulky, time-consuming and expensive. In addition, the CREM team of Orange Labs in Rennes does not have a fiber-based optical communication laboratory. In order to stimulate and enhance exchanges between the CREM team, which has signal processing competence, and the ASHA team in Lannion, which has optical communication competence, a reliable and realistic numerical model of a fiber-based optical transmission is important. Thanks to the model, CREM team can evaluate beforehand signal processing algorithms without having to come to the laboratory. Then, the techniques already tested by numerical simulations can be implemented in a real transmission link for a final evaluation.

In the scope of this thesis, only optical transmission systems for access networks are concerned. In this context the transmission reach is relatively short and in general limited by tens of kilometers. Unlike core or submarine networks where transmission bit rate is in the order of hundreds of gigabits per second, in the context of access networks it is only in the order of tens of gigabits per second. Hence, for a telecom operator, it is always preferable for an access network to be simple and low-cost. In selecting an optical modulator, direct modulation of laser intensity is shown to be a great benefice since a DML is far cheaper than an external modulator. Moreover, single-mode fibers are widely installed all around the world and conventional detection techniques are mostly based on direct detection because of its simplicity. For these reasons, this thesis also focuses on such a transmission system where the optical modulator is simply a DML, the fiber links are standard single-mode fibers and the receiver is based on a photodiode. On the transmitter side, a transmitted analog signal is biased with a Direct Current (DC) component before directly modulating the intensity of a laser. Ideally, the optical intensity at the laser output is proportional to the driving current. The resulting optical signal propagates to the receiver side through a single-mode fiber link. On the receiver side, the

optical received signal power is detected by means of a photodiode. The transmission diagram is shown in Figure 2.1.

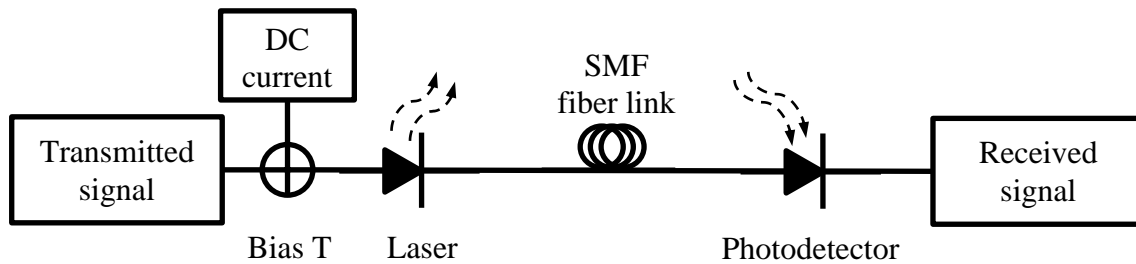


Figure 2.1 – DML-based optical IMDD transmission diagram.

In this chapter the modeling of the modulator, the transmission link and the receiver is described. To be realistic, component parameters are extracted either from manufacturer datasheets or from experimental extraction. In the latter case, extracted parameters are validated by means of experimentation. The channel modeling is validated in both “small signal” regime, where the amplitude of a driving current is small when compared to the DC component, and “large signal” regime, where the modulation index is large.

## 2.2. DML modeling

A DML is responsible for transforming a transmitted electrical signal into the corresponding optical signal, which then propagates over a fiber link to the receiver. Since the laser intensity is directly modulated by an electrical signal, a DML can be modeled by three cascaded subsections [53] including linear parasitics, non-linear parasitics and an intrinsic laser as shown in Figure 2.2.

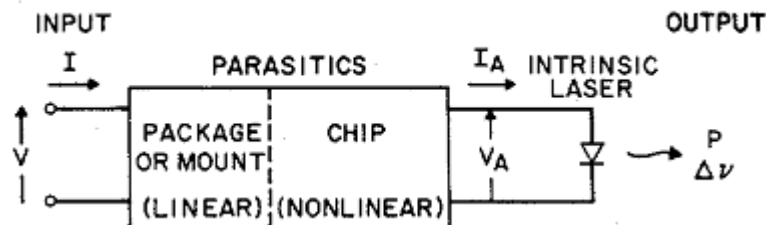


Figure 2.2 – DML two-port model.

(Source: [53]).

### 2.2.1. Laser parasitics

In general, laser parasitics act as a low-pass filter which limits the signal bandwidth. In the time domain laser parasitics suppress the fast transients of a driving current, resulting in a slower turn-on time than that of the case without parasitics. In some cases, laser parasitics can also cause nonlinear behaviors of a laser. In general non-linear parasitic can be neglected. Laser parasitics strongly depend on chip and mount structures. In the literature, laser parasitics are assumed to consist of a series resistance and a parallel capacitance as shown in Figure 2.3. Hence, they can be considered as an RC low-pass filter [54] whose magnitude and phase responses are shown in the subsets of Figure 2.3.

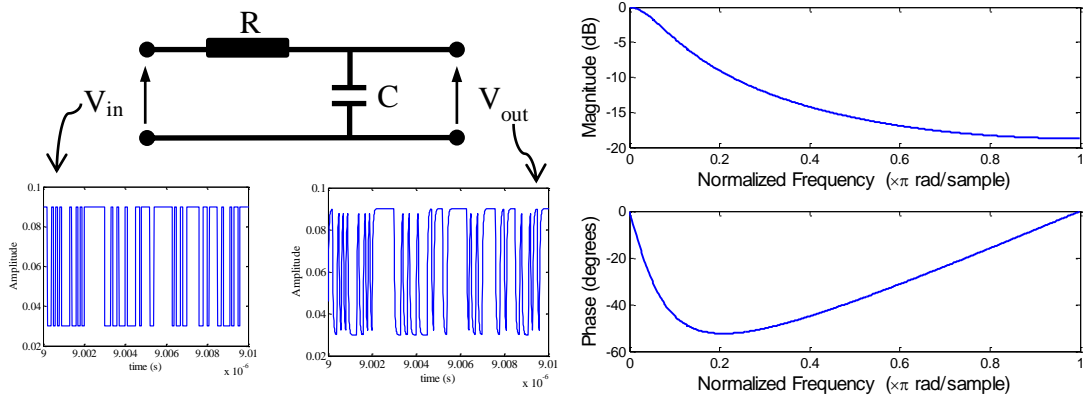


Figure 2.3 – Laser parasitics approximation by an RC circuit. Left: equivalent RC circuit of laser parasitics along with input and output signal. Right: magnitude and phase response of the RC circuit.

### 2.2.2. Laser phase noise

According to [17], laser phase noise can be modeled by a Wiener process where the phase change between two consecutive samples can be modeled as a central Gaussian random variable. Supposing that  $T_S$  is the sampling time and  $\Delta\nu$  is the laser linewidth, laser phase noise power can be written as  $E\{(\Delta\phi(T_S))^2\} = 2\pi\Delta\nu T_S$ . For a DFB laser, the typical value of  $\Delta\nu$  is 5 MHz at 1 mW output optical power.

### 2.2.3. Intrinsic laser

In small-signal regime, the intrinsic laser can be characterized by its AM response and Frequency Modulation (FM) response. Laser AM response, similar to laser parasitic, is a second-order low-pass filter which introduces a resonance peak depending on the DC bias current. Laser FM response represents the relationship between optical frequency shift and optical power. Laser chirps, including transient chirp and adiabatic chirp, enlarge the optical signal bandwidth. Hence, when chromatic dispersion is present, the optical channel response and the nonlinear noise (or sometimes called intermodulation noise) depend on the interplay between laser chirps and chromatic dispersion. In order that all these characteristics of a DML are taken into account and that a laser model is realistic, the laser modeling used in this thesis is based on a rate-equation model, which is used by many authors in the literature [12], [36], [53], [55]. In this section different techniques to extract the model parameters are also discussed. For some reasons that will be detailed in the next paragraphs, the parameter extraction method described in [36] is adopted. The results of the parameter extraction procedure performed on a commercial laser are also given. The extracted parameters are validated by comparing measured data to that obtained by numerical simulations.

The large-signal rate-equation model describes the relationship between the laser-driving current  $I(t)$ , the time-varying carrier density  $N(t)$ , the photon density  $S(t)$ , the phase of the laser output electrical field  $\phi(t)$  and the optical output power  $P(t)$ . The rate equations can be written as

$$\frac{dS(t)}{dt} = \Gamma g_0 \frac{N(t) - N_t}{1 + \epsilon S(t)} S(t) - \frac{S(t)}{\tau_p} + \frac{\Gamma \rho N(t)}{\tau_n}. \quad (2.1)$$

$$\frac{dN(t)}{dt} = \frac{I(t)}{eV_a} - g_0 \cdot \frac{N(t) - N_t}{1 + \epsilon S(t)} S(t) - \frac{N(t)}{\tau_n}. \quad (2.2)$$

$$\frac{d\phi(t)}{dt} = \frac{1}{2} \alpha \Gamma g_0 (N(t) - N_{th}). \quad (2.3)$$

$$P(t) = \frac{V_a \eta h \nu}{2\Gamma \tau_p} S(t). \quad (2.4)$$

The dimension and the physical meaning of different parameters are given in the table below

Parameter	Dimension	Physical meaning
$\Gamma$	---	Optical confinement factor
$g_0$	$\text{m}^3/\text{s}$	Gain slope
$N_t$	$\text{m}^{-3}$	Carrier density at transparency
$\epsilon$	$\text{m}^3$	Gain saturation parameter
$\tau_p$	s	Photon lifetime
$\rho$	---	Spontaneous emission factor
$\tau_n$	s	Carrier lifetime
$e$	C	Electron charge, $1.6 \times 10^{-19}$
$V_a$	$\text{m}^3$	Volume of the active region
$\alpha$	---	Linewidth enhancement factor
$N_{th}$	$\text{m}^{-3}$	Carrier density at threshold
$\eta$	---	Total quantum efficiency
$h$	Js	Planck constant, $6.63 \times 10^{-34}$
$\nu$	Hz	Optical frequency

Table 2.1 – DML large-signal model parameters.

It is noted that Eqs. (2.1) – (2.4) are a simplified model of a real DFB laser. In practice, the gain slope  $g_0$  and the linewidth enhancement factor  $\alpha$  also depend on the carrier density  $N(t)$ . However, even with this simplified model, according to [36], the numerical

simulation results correspond well to the experimental results in terms of intensity and chirp waveform. It is also noted that when the laser RIN is taken into account, a noise term, known as the Langevin force, can be added into each of the Eqs. (2.1) – (2.3) [14]. These differential equations can be numerically solved thanks to the Runge–Kutta method. In Matlab this can be carried out by using ODE functions. In order to make the model realistic, different laser parameters presented in Eqs. (2.1) – (2.4) must be extracted from a real laser. One can identify ten unknown parameters  $\Gamma$ ,  $g_0$ ,  $N_t$ ,  $\epsilon$ ,  $\tau_p$ ,  $\rho$ ,  $\tau_n$ ,  $V_a$ ,  $\alpha$ ,  $\eta$  in addition to the laser central wavelength  $\lambda$ . In the next sections different extraction methods are discussed.

### 2.2.3.1. Transformed-rate-equation method

Leif Bjerkan *et al.* proposed in [36] a transformed-rate-equation method in order to simulate a semiconductor intrinsic laser. In this method the rate equations are rewritten under a transformed form where several new quantities, which can be expressed as a function of the unknown parameters, are introduced. The idea of the method is that all the introduced parameters can be extracted by measurements of steady state and small-signal modulation.

#### 2.2.3.1.1. Steady state power versus current (P-I) measurement

On condition that the temperature is stable, in steady state regime, the time derivatives in Eqs. (2.1) – (2.3) are set to zero. After some algebraic computations, one can easily obtain the analytic P-I relation as

$$\left(1 + \frac{\tau_c \rho}{\tau_n}\right) I - (1 - \rho) I_{th} + \frac{I_s I}{FP} = \left(1 + \frac{\tau_c}{\tau_n}\right) FP + I_s, \quad (2.5)$$

in which the following new parameters are introduced

$$B = \frac{\Gamma g_0}{e V_a}; \quad \tau_c = \frac{\epsilon}{g_0}; \quad F = \frac{2e\lambda}{hc\eta}; \quad I_s = \frac{\rho}{B\tau_n\tau_p};$$

and the emission threshold current can be expressed as

$$I_{th} = \frac{e V_a N_{th}}{\tau_n} = \frac{e V_a}{\tau_n} \left( N_t + \frac{1}{\Gamma g_0 \tau_p} \right). \quad (2.6)$$

In practice the values of both  $\rho$  and  $\tau_c/\tau_n$  are small, resulting in the following approximation

$$(FP)^2 - (I - I_{th} - I_s)FP - I_s I \approx 0. \quad (2.7)$$

From the steady state P-I measurement, a nonlinear least squares fitting method can be used to fit the measured curve and the corresponding theoretical curve from Eq. (2.7). The quantities  $F$ ,  $I_{th}$  and  $I_s$  can be extracted. The P-I measurement procedure can be described as follows.

### Measurement procedure

- The laser is driven by a DC bias current. It is noted that the temperature of the laser is maintained stable by means of a temperature control.
- At several bias current values  $I_0$ , the corresponding output light power values are recorded.
- Once the P-I curve is obtained, a nonlinear least squares fitting method such as the Levenberg-Marquardt algorithm [56] can be used to fit the measured data to the theoretical P-I curve given by Eq. (2.7). The quantities  $F, I_{th}$  and  $I_S$  can be extracted.

#### 2.2.3.1.2. Small-signal AM response measurement

The laser small-signal AM response can be measured by superimposing a harmonic on a DC bias current above the emission threshold. A network analyzer can be used to measure the AM transfer function of the laser. The normalized AM response of a laser under a small-signal regime can be written as

$$H_{AM}(\omega) = \frac{\omega_0^2}{\omega_0^2 - \omega^2 + 2j\gamma\omega}, \quad (2.8)$$

where  $f_0 = \omega_0/2\pi$  denotes the relaxation oscillation frequency and  $\gamma$  denotes the laser damping rate. These quantities can be expressed as

$$\omega_0^2 = B(I_0 - I_{th}), \quad (2.9)$$

$$\gamma = \frac{1}{2} \left( \frac{1}{\tau_n} + Kf_0^2 \right), \quad (2.10)$$

$$K = 4\pi^2(\tau_p + \tau_c), \quad (2.11)$$

where  $I_0$  is the DC bias current and  $K$  denotes the K-factor [36]. According to the AM response measurements, parameters  $B, K$  and  $\tau_n$  can be extracted. The measurement and extraction procedures can be described as follows.

#### Measurement procedure:

- With a specific value of  $I_0$  above the laser emission threshold, the AM response is measured.
- In order to eliminate all bias-current-independent components such as laser parasitics and the internal frequency response of the network analyzer, the frequency response subtraction method described in [57] can be used.
- A nonlinear least squares curve fitting method such as the Levenberg-Marquardt algorithm [56] can be used to fit a measured AM response with the theoretical response given by Eq. (2.8). The parameters  $\omega_0(I_0)$  and  $\gamma(I_0)$  as a function of  $I_0$  can be extracted.
- The AM response measurement and fitting procedure are repeated for a set of different values of the bias current  $I_0$ . Once the curves  $\omega_0^2(I_0)$  and  $\gamma(f_0^2)$  are

obtained, a second fitting procedure can be applied to Eqs. (2.9) and (2.10) in order to extract the parameters  $B, K$  and  $\tau_n$ .

### 2.2.3.1.3. Small-signal FM response measurement

Once the parameters  $B, K$  and  $\tau_n$  are obtained by the AM measurement, an FM measurement procedure can be carried out in order to extract the other unknown parameters. It is well known that a direct modulation of laser intensity causes a frequency modulation. The relationship between the optical frequency shift and the optical power can be expressed as [53]

$$\Delta\nu = \frac{1}{2\pi} \frac{d\phi}{dt} = \frac{\alpha}{4\pi} \left( \frac{1}{P} \frac{dP}{dt} + \kappa P \right), \quad (2.12)$$

where the adiabatic chirp constant  $\kappa$  can be written as

$$\kappa = \frac{2\Gamma\epsilon}{\eta h\nu V_a} = FB\tau_c. \quad (2.13)$$

The small-signal FM response describing the relationship between the phase and the power of an electrical field can be expressed as

$$\frac{\Phi(f)}{P(f)} = H_{FM}(f) = \alpha \left( 1 - \frac{jf_c}{f} \right), \quad (2.14)$$

$$f_c = \frac{\tau_c B (I_0 - I_{th})}{2\pi}. \quad (2.15)$$

Bjerkkan *et al.* proposed three different methods in order to extract the linewidth enhancement factor  $\alpha$  and the parameter  $\tau_c$ . In this thesis only the method basing on small-signal fiber transfer function is concerned because of its simplicity. This method also allows the estimation of the fiber dispersion parameter  $D$ .

The small-signal fiber transfer function can be written as

$$H_F(f) = \cos\left(\pi \frac{f^2}{f_D^2}\right) - H_{FM}(f) \sin\left(\pi \frac{f^2}{f_D^2}\right), \quad (2.16)$$

$$f_D^2 = \frac{c}{\lambda^2 DL}, \quad (2.17)$$

where  $D \left( \frac{ps}{nm.km} \right)$  is the dispersion parameter and  $L (m)$  denotes the fiber length. The measurement and extraction procedures can be described as follows.

#### Measurement procedure:

- For each bias current value  $I_0$  the fiber frequency response is measured by means of a network analyzer.
- In order to extract only the fiber response, the channel response measured by the network analyzer must be compensated by the laser AM response including the

laser parasitics and the intrinsic laser. The response subtraction method can be used.

- A nonlinear least squares curve fitting method can be used to fit the measured response with the theoretical one described in Eq. (2.16). Hence, one can extract the parameters  $\alpha$ ,  $f_c$  and  $D$  if necessary.
- The procedure is repeated for different values of the bias current  $I_0$ . Once the curve  $f_c(I_0)$  as a function of  $I_0$  is obtained, a second fitting procedure can be applied to Eq. (2.15). The parameter  $\tau_c$  can be extracted.
- Once  $\tau_c$  is available,  $\tau_p$  can be deduced from Eq. (2.11).

#### 2.2.3.1.4. Transformed rate equations

The rate equations are rewritten under a transformed form whose parameters can be measured by the procedures described above.

$$\frac{dP(t)}{dt} = \frac{B\tau_n I_{th}(X(t) - 1) + \frac{1}{\tau_p} P(t) - \frac{P(t)}{\tau_p} + \frac{I_s I_{th} B \tau_n}{F} X(t)}{1 + FB\tau_p \tau_c P(t)} \quad (2.18)$$

$$\frac{dX(t)}{dt} = \frac{I(t)}{I_{th} \tau_n} - \frac{FB\tau_p(X(t) - 1) + \frac{F}{I_{th} \tau_n} P(t) - \frac{X(t)}{\tau_n}}{1 + FB\tau_p \tau_c P(t)} \quad (2.19)$$

$$\frac{d\Phi(t)}{dt} = \frac{\alpha}{2} B\tau_n I_{th}(X(t) - 1), \quad (2.20)$$

Eqs. (2.18) – (2.20) can be numerically solved and the laser output optical power and phase can be obtained. The advantage of this method is that all the unknown parameters  $F, B, I_s, I_{th}, \tau_p, \tau_n, \tau_c$  and  $\alpha$  can be extracted by means of experimental measures. Hence, the laser response in terms of waveform and chirp obtained by simulation approaches that of a real laser.

#### 2.2.3.2. Parameter approximation method

John C. Cartledge proposed in [55] an extraction technique based on approximation and minimization. In [55] a more exact small signal AM response of the laser is used

$$H(f, Y, Z) = \frac{Z}{(j2\pi f)^2 + j2\pi f Y + Z} \quad (2.21)$$

where  $Y$  and  $Z$  are function of laser parameters and the bias current

$$Y = g_0 \frac{\bar{S}}{1 + \epsilon \bar{S}} + \frac{1}{\tau_n} - \Gamma g_0 (\bar{N} - N_t) \frac{1}{(1 + \epsilon \bar{S})^2} + \frac{1}{\tau_p} \quad (2.22)$$

$$Z = g_0 \frac{\bar{S}}{1 + \epsilon \bar{S}} \frac{1}{\tau_p} + (\rho - 1) \frac{\Gamma g_0}{\tau_n} (\bar{N} - N_t) \frac{1}{(1 + \epsilon \bar{S})^2} + \frac{1}{\tau_n \tau_p} \quad (2.23)$$

The damping factor and the relaxation oscillation frequency are given by

$$2\gamma = Y, \quad (2.24)$$

$$\omega_0^2 = Z - 0.5Y^2. \quad (2.25)$$

In the transformed rate equation method described in the previous section, the approximation below is used

$$\omega_0^2 = Z, \quad (2.26)$$

resulting in the laser AM response given by Eq. (2.8). In this technique the AM response is measured for different bias current values. The curve fitting procedure can be applied to Eq. (2.21) in order to estimate the parameters  $Y$  and  $Z$ , from which the damping factor and the resonance frequency can be deduced.

In order to predict the optical extinction ratio, the author considered the threshold current and the optical power, which can be written as

$$I_{th} = \frac{eV_a N_{th}}{\tau_n}, \quad (2.27)$$

$$\bar{P} = \frac{\bar{S}V_a \eta h\nu}{2\Gamma\tau_p}. \quad (2.28)$$

From the measured values of  $Y, Z, I_{th}$  and  $\bar{P}$ , the minimization over these four variables is carried out in order to extract the unknown parameters in Eqs. (2.22), (2.23), (2.27) and (2.28). The technique requires a physically reasonable initial guess. The extraction process may result in different sets of parameters depending on the initial guess. However, it is shown that as long as the set of parameters results in the same values of  $Y, Z, I_{th}$  and  $\bar{P}$  as the measured values, the receiver sensitivity can be well evaluated.

Compared to the transformed rate equations method, the approximation method requires fewer measurements. However, the first method is preferable since all the model parameters are extracted according to measurement results and no approximation is used. In the model using approximation method, only the laser AM response approaches that of the real laser. In terms of chirp response, this model does not guarantee a good response. Hence, the model may be only suitable for the performance evaluation of low bit-rate NRZ transmissions where the bit-transition ringing caused by laser chirps is not important. For the sake of the performance evaluation of signal processing techniques in high-bit-rate transmissions ( $> 10$  Gb/s), the model using approximation method might be less suitable than the transformed-rate-equation model.

#### 2.2.4. Laser parameter extraction results and model validation

For the reasons explained in the previous paragraphs, the laser model proposed by Bjerkan *et al.* is shown to be more suitable because it considers all principal characteristics and parameters of a laser. In addition, the model is not based on any initial guess of any physical parameter. As instead, all the coefficients in the model can be extracted by means of experimental measurements. Hence, simulated waveforms should fit well the experimental waveforms at the laser output. In this section the results of a parameter

extraction performed in the DFB laser model 14B7M commercialized by the EM4 company is reported. The extracted parameters are validated by comparing the simulation results and the measured data. The laser rate equation model described by Eqs. (2.1) – (2.4) is also validated in both small-signal and large-signal modulation regimes.

### 2.2.4.1. Experimental setup

In order to extract all the unknown parameters for the large-signal laser model, three measurements are effectuated:

- The P-I measurement which measures the relationship between light power and laser bias current.
- The small-signal AM response measurement which measures the small-signal intrinsic laser response.
- The small-signal fiber response measurement which captures the optical fiber channel response.

#### 2.2.4.1.1. P-I measurement setup

Figure 2.4 shows the experiment setup for the P-I measurement. The DC bias current can be regulated by a voltage power supply. An ampere meter is used in order to measure the exact bias current. At the laser output an optical power meter is used to measure the optical power. It is noted that the power supply must not exceed the maximum acceptable bias voltage of the laser. In the measurement setup, the bias current is limited to 130 mA, which respects the maximum acceptable bias current described in the datasheet. In addition, when the bias current exceeds 100 mA, the laser begins to be saturated.

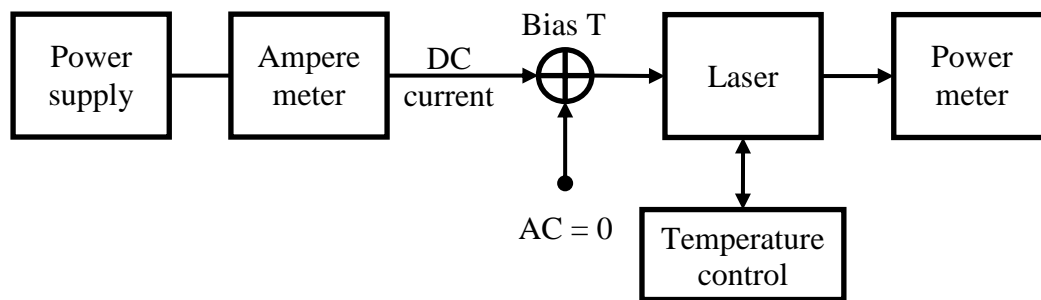


Figure 2.4 – Experiment setup for the P-I measurement.

#### 2.2.4.1.2. Laser AM response and fiber response measurement setup

The experiment setup of the AM and FM response measurement is illustrated in Figure 2.5. The fiber link is removed in the AM response measurement. In this measurement a network analyzer is used to capture the system frequency response. The RF sweep signal is superimposed with a DC bias current to modulate the laser. The RF power is limited by 0 dBm to satisfy the small-signal modulation condition. In order to stabilize measured responses, the sweep time of the RF signal must be long. In the measurement a sweep time of 8 seconds is used. Longer sweep times do not further improve the stability of the measurement results. The photodiode is not used in order to isolate the laser response from the photodiode response. The network analyzer must function in Electrical/Optical (E/O)

mode because it receives an optical signal. The intrinsic frequency response of the network analyzer is ignored because in the working frequency band (from 0 to 12 GHz) it is almost flat.

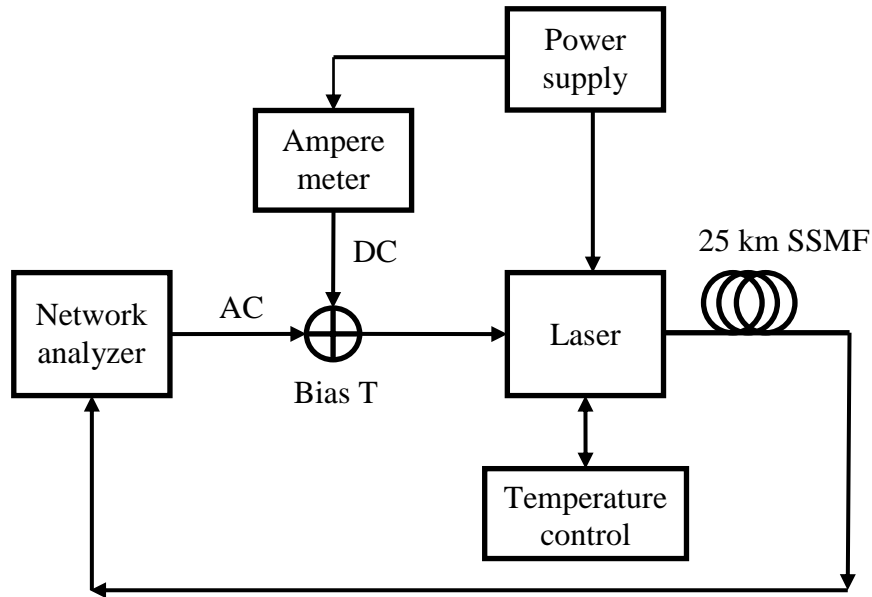


Figure 2.5 – Experiment setup of AM response and fiber response measurement.

### 2.2.4.2. Parameter extraction results

#### 2.2.4.2.1. P-I extraction

The P-I relationship of the concerned laser is presented in Figure 2.6. The laser power begins to be saturated when the bias current exceeds 100 mA. The Levenberg-Marquardt non-linear least squares fitting algorithm is applied to Eq. (2.7) to extract the conversion parameter  $F$ , the emission threshold current  $I_{th}$  and the characteristic current  $I_S$ . The values of these parameters are given in Table 2.2.

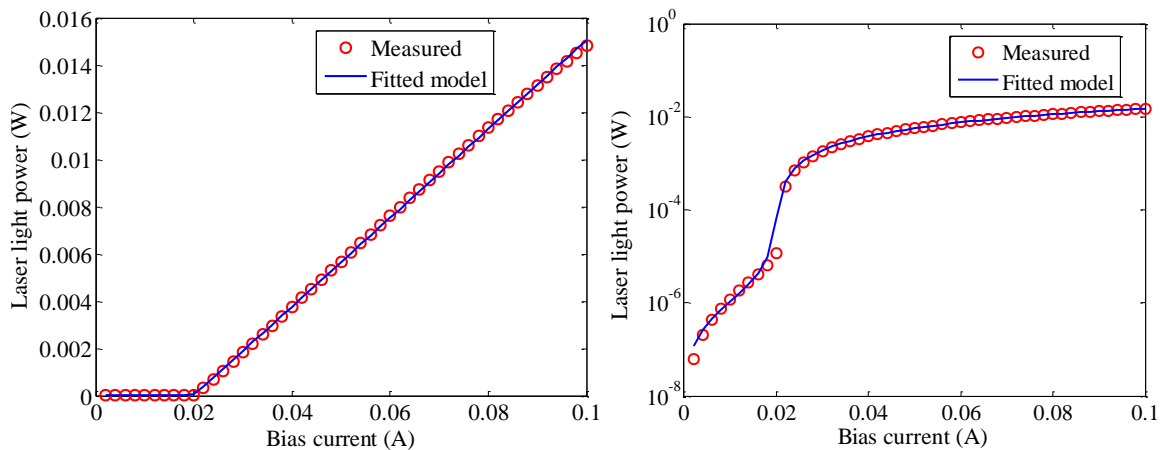


Figure 2.6 – Measured and fitted model light-current curves. Left: linear scale. Right: log scale.

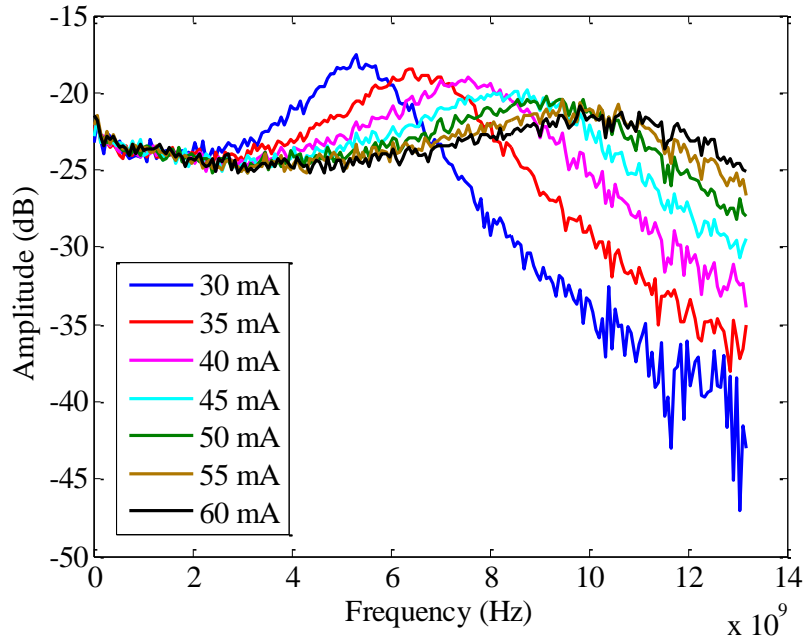


Figure 2.7 – Measured laser small-signal AM response as a function of bias current.

#### 2.2.4.2.2. Small-signal AM response extraction

Small-signal AM response as a function of bias current is shown in Figure 2.7. From these measures resonance frequency and laser damping rate can be extracted. When bias current increases, resonance frequency also increases. It is noted that the extracted values are less reliable if the to-be-measured values fall out of the measured frequency band, which is 12 GHz in this experimentation. In order to eliminate the impact on the extraction precision of the laser parasitic frequency response and that of the measuring equipment, the frequency response subtraction method described in [57] is used. The AM response corresponding to the bias current value of 30 mA (the blue curve in Figure 2.7) is referred to as the reference. For each bias current value, the Levenberg-Marquardt non-linear least squares fitting algorithm is used to extract the value of the resonance frequency  $f_0$  and the laser damping rate  $\gamma$  according to Eq. (2.8). It is noted that in this data fitting algorithm, the value of the Jacobian matrix is very small in general. The algorithm risks of finding local minimum values rather than the global minimum. To resolve this problem a constant of  $10^6$  is multiplied with the measured frequency response. The same constant is also presented in the theoretical response. As shown in Figure 2.8, when the fitting algorithm converges, the model corresponds very well to the measured subtracted response.

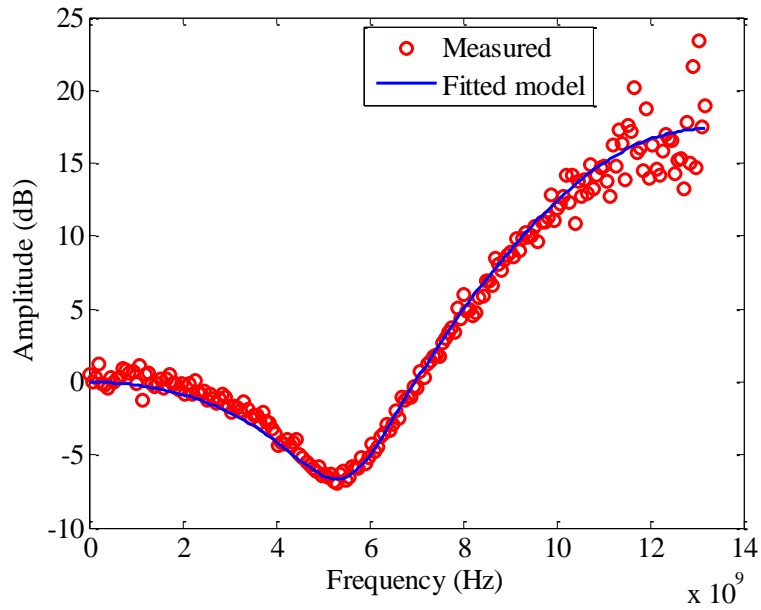


Figure 2.8 – Subtracted laser small-signal AM response. Bias current is 65 mA.

The extracted resonance frequency as a function of bias current is presented in Figure 2.9. From Eq. (2.9) the squared resonance frequency is also shown to be linearly proportional to the bias current. Hence, A simple linear data fitting can be used to extract the parameter  $B$ .

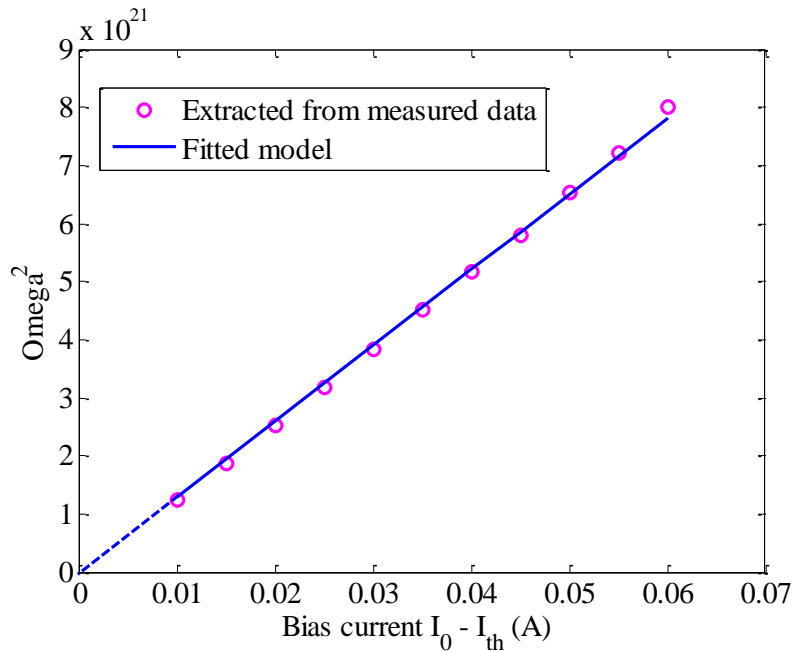


Figure 2.9 – Squared resonance frequency as a function of bias current.

Similarly, the extracted laser damping rate  $\gamma$  as a function of bias current is presented in Figure 2.10. From Eqs. (2.9) and (2.10) the laser damping rate is shown to be a linear function of the bias current as shown in Eq. (2.29)

$$\gamma = \frac{1}{2} \left( \frac{1}{\tau_n} + K \frac{B(I_0 - I_{th})}{4\pi^2} \right). \quad (2.29)$$

Therefore, once the parameter  $B$  is available, the linear Least Mean Square (LMS) fitting algorithm can be used to extract the K-factor and the carrier lifetime  $\tau_n$ . The value of  $B, K$  and  $\tau_n$  is given in Table 2.2.

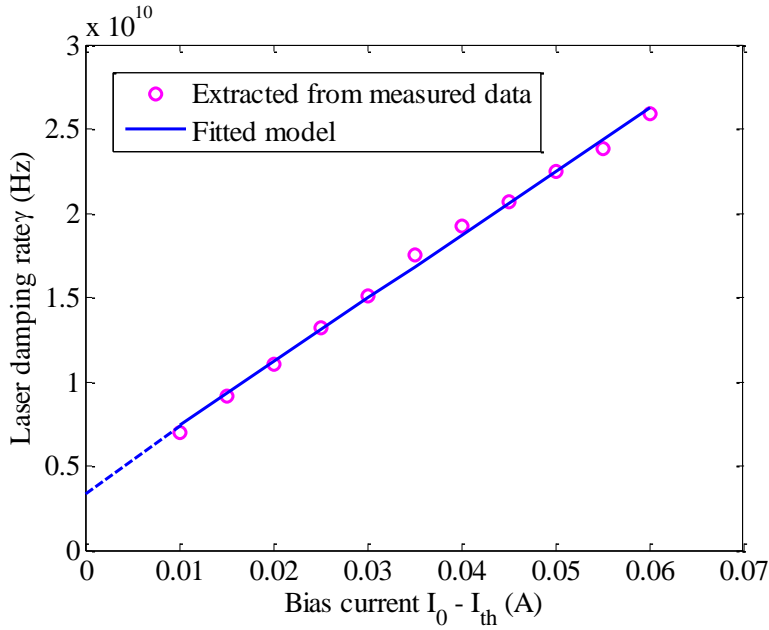


Figure 2.10 – Laser damping rate as a function of bias current.

Parameter	Dimension	Value
$F$	A/W	5.32
$I_{th}$	mA	20
$I_s$	$\mu$ A	5.65
$B$	$\frac{\text{Hz}^2}{\text{A}}$	1.3e23
$\tau_p$	ps	4.12
$\tau_n$	ns	0.14
$\alpha$	---	2.68
$\tau_c$	ns	1.65

Table 2.2 – Extracted laser parameters.

### 2.2.4.2.3. Small-signal FM response extraction

Figure 2.11 presents the small-signal frequency response of a 25-km SSMF link as a function of bias current. In order to obtain the fiber response, the small-signal AM response obtained at the same bias current is subtracted from the overall measured frequency response. The constant attenuation in Figure 2.11 is due to the fiber loss.

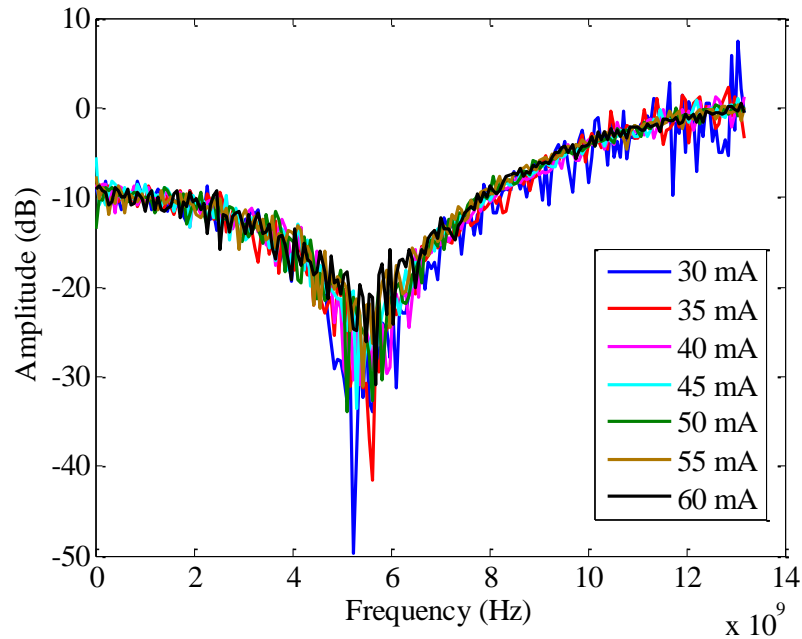


Figure 2.11 – Fiber small-signal frequency response. Fiber length is 25 km.

The unknown parameters  $D$ ,  $\alpha$  and  $f_c$  in Eq. (2.16) can be extracted by using the Levenberg-Marquardt fitting algorithm. Similar to the fitting procedure used for the small-signal AM response, a constant of  $10^6$  is introduced to the measured and theoretical responses in order to avoid local minimums. Figure 2.12 illustrates the normalized measured fiber response and the fitted model fiber response of a 25-km-length fiber link when the bias current is equal to 70 mA. The fiber response is measured for different values of the bias current. For each bias current value, the parameters  $D$ ,  $\alpha$  and  $f_c$  are extracted. The extracted values of the adiabatic frequency  $f_c$  as a function of bias current are presented in Figure 2.13, a simple linear data fitting algorithm can be applied to Eq. (2.15) to extract the parameter  $\tau_c$ . Once  $\tau_c$  is available, the photon lifetime  $\tau_p$  can be deduced from Eq. (2.11). Because the enhancement factor  $\alpha$  and the dispersion parameter  $D$  are independent in the bias current, their values are calculated as the average of the extracted values corresponding to different bias currents. This averaging reduces the impact of noise on the extraction precision of the parameters.

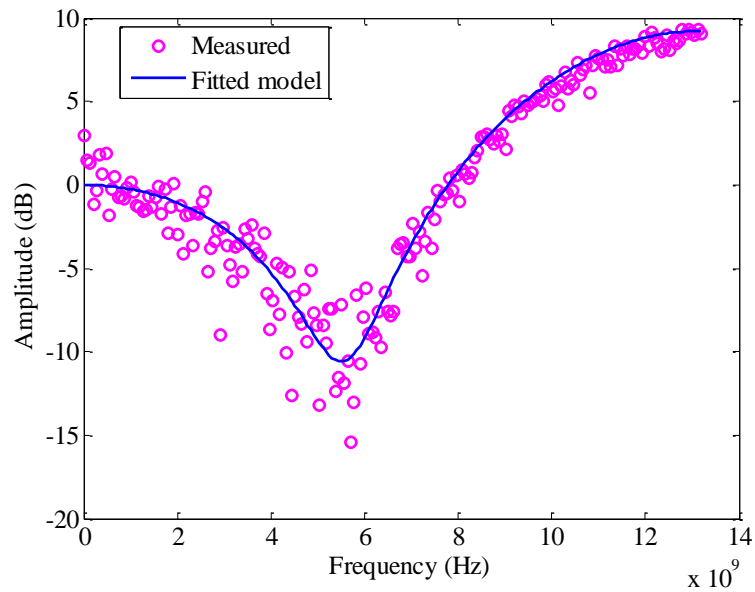


Figure 2.12 – Fiber small signal frequency response. Bias current is 70 mA. Fiber length is 25 km.

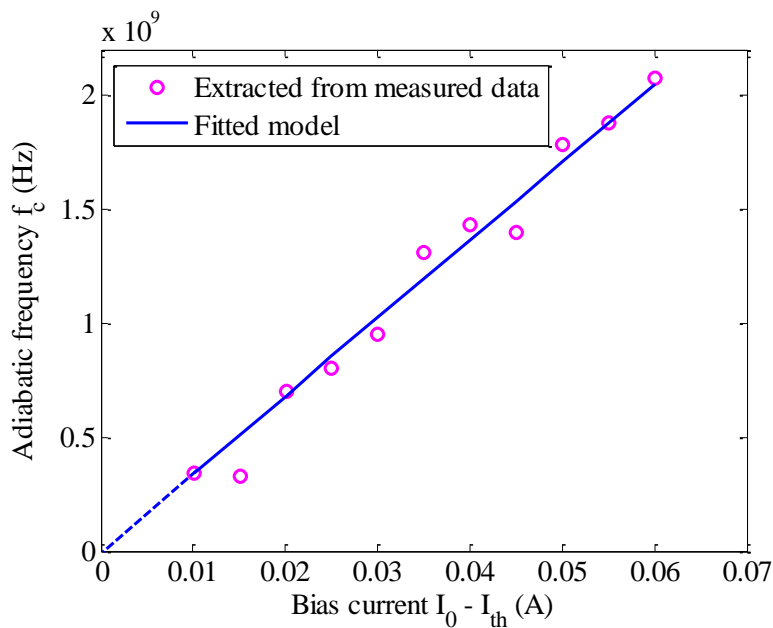


Figure 2.13 – Adiabatic frequency as a function of bias current.

#### 2.2.4.2.4. Laser parasitic extraction

As long as the frequency response of the measuring equipment is negligible, the measured small-signal AM response includes the intrinsic laser and the laser parasitic. Once the laser resonance frequency  $f_0$  and the laser damping rate  $\gamma$  are extracted, the intrinsic laser response can be calculated according to Eq. (2.8). Then the laser parasitic can be deduced by the response subtraction method. Figure 2.14 illustrates the measured small-signal AM response, the fitted model from extracted values according to Eq. (2.8) and the deduced laser parasitic. The laser bias current is equal to 65 mA. In this figure, the plain curve is the model laser AM response. The curve with “o” marker is the measured channel response

including the laser AM response and the laser parasitic response. Hence, the subtraction of the two curves results in the laser parasitic response.

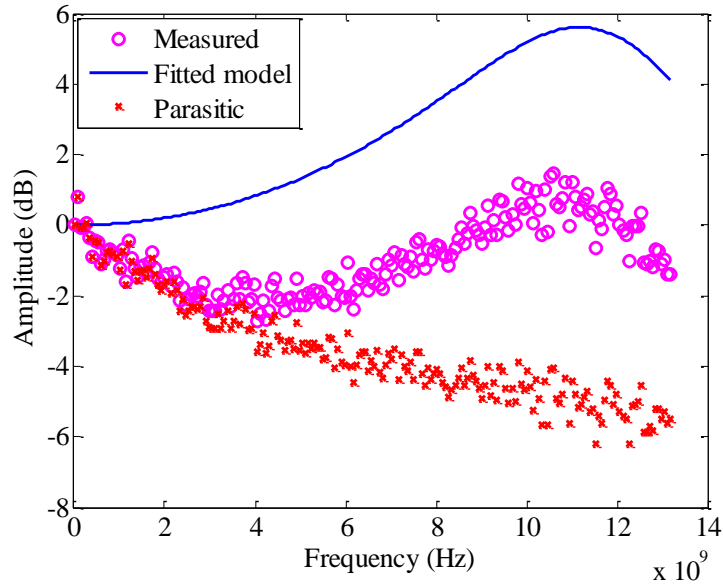


Figure 2.14 – Laser parasitic frequency response. Bias current is 65 mA.

In order to reduce the impact of noise on the extraction precision of the parasitic response, averaging over different responses corresponding to different bias current values can be used. Figure 2.15 presents the averaged parasitic frequency response. The laser parasitic frequency response extraction is important because the parasitic is one of the principle capacity-limiting factors of a DML-based IMDD transmission. The laser parasitic directly limits the driving signal bandwidth. Its response strongly depends on the electrical driving circuit and the laser package, which may vary from one laser to another.

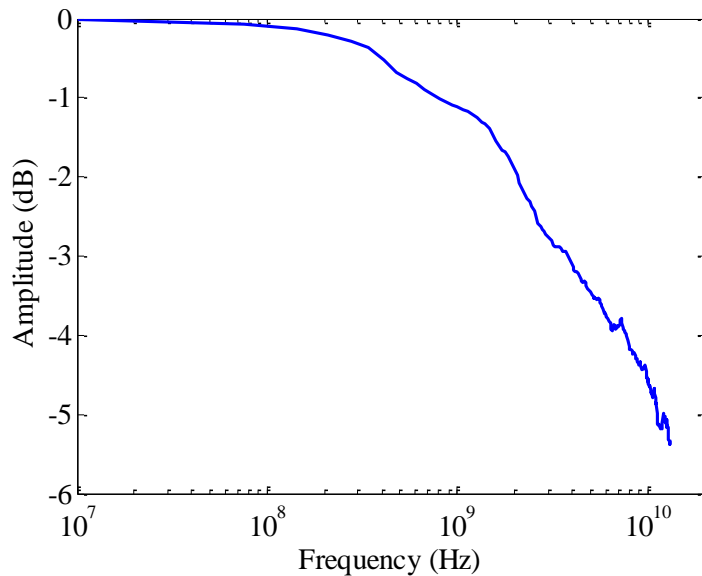


Figure 2.15 – Averaged parasitic frequency response.

### 2.2.4.3. Extraction validation

So far the results of a parameter extraction performed on a commercialized DFB laser have been reported. All the laser parameters required for the rate-equation model are extracted and given in Table 2.2. In this section the extracted parameters are validated. Because the parameters are extracted in small-signal modulation regimes, the extraction procedure is also validated by comparing the measured data to the data obtained by the numerical model in small-signal modulation regimes. Such data to be compared include the P-I response, the small-signal AM frequency response and the small-signal FM frequency response. The model validation in large-signal regime is preserved for the last section of this chapter, after that the modeling of the fiber link and that of the photodetector are presented.

In order to simulate the evolution of the laser's intensity and phase, the rate equations (2.18) – (2.20) must be numerically solved. In Matlab this can be carried out by using the built-in function `ode45`. It is noted that in order to guarantee the convergence of the numerical solution, the time step must be small. This constraint can be satisfied by oversampling the transmitted signal. In this validation an oversampling factor of 12 is used. The oversampling is also necessary to take into account high-order harmonics of the optical field generated by nonlinearity effects such as FWM and the nonlinear laser P-I curve. On the electrical side, the oversampling guarantees a good model of the Digital-to-Analog Converter (DAC). In general, large oversampling factor increases the simulation reliability at the expense of an increased simulation run-time. The oversampling factor of 12 is used for a complexity-precision compromise.

Figure 2.16 illustrates the P-I curve of the concerned laser. The simulated curve perfectly corresponds to the theoretical model expressed in Eq. (2.7) and the measured data.

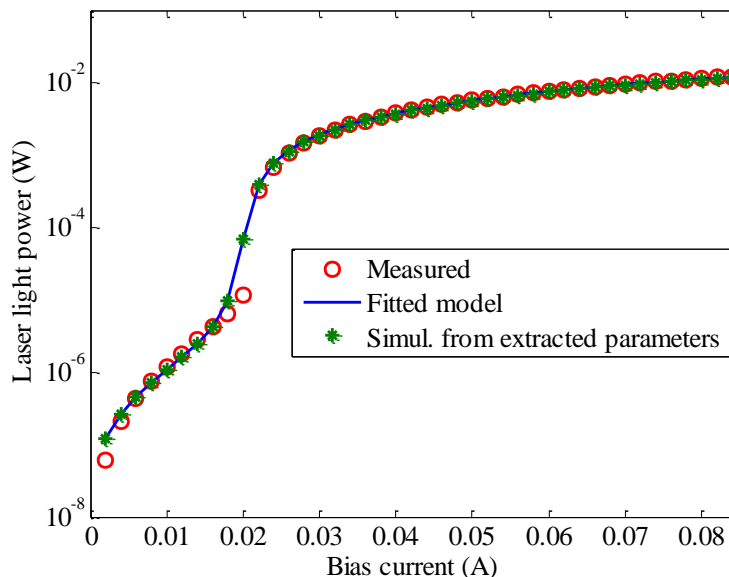


Figure 2.16 – Validated laser light-current relationship.

Similarly, in terms of small-signal AM response (Figure 2.17) and FM response (Figure 2.18), data obtained by simulation fit very well the theoretical and measured data. In the high-frequency zone the measured curves in Figure 2.18 are noisy due to fiber attenuation. The extraction procedure is hence validated. The model is also shown to perfectly simulate a DFB laser in a small-signal regime. It is noted that in order to obtain

the simulated fiber response shown in Figure 2.18, the split-step Fourier method is used for the fiber modeling, which is discussed in more detail in the next section.

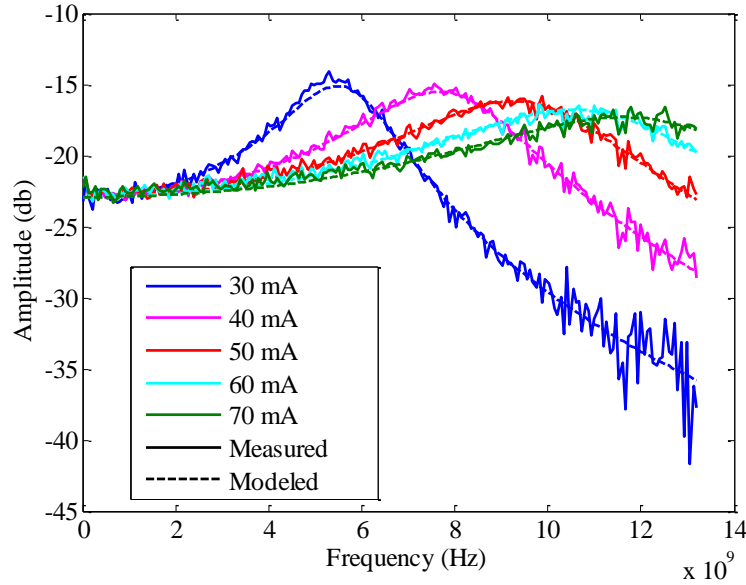


Figure 2.17 – Validated laser small-signal AM response.

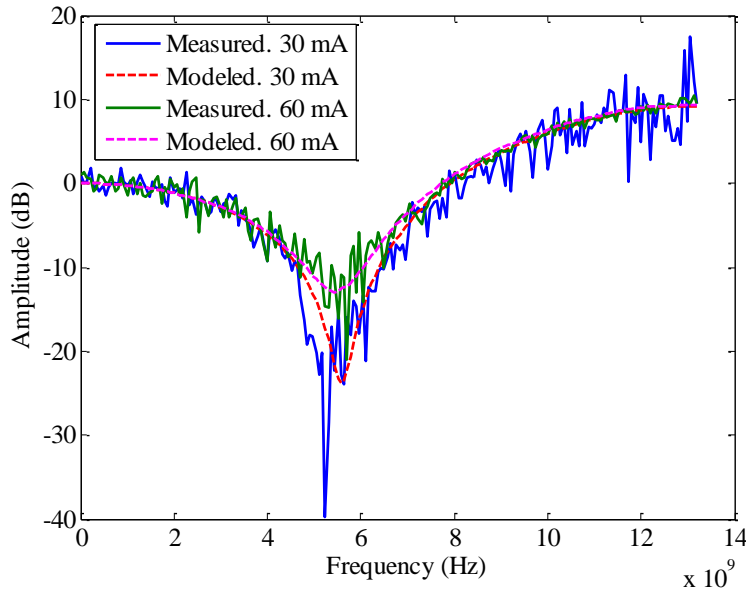


Figure 2.18 – Validated fiber small-signal frequency response.

### 2.3. Fiber link modeling – split-step Fourier method

As discussed in chapter 2, section 1.2.2, the propagation of an optical signal over a single-mode fiber is governed by the simplified NLS equation. To recall, this equation is written as

$$\frac{\partial A(z, t)}{\partial z} = -\frac{\alpha_{att}}{2} A(z, t) - \beta_1 \frac{\partial A(z, t)}{\partial t} - \frac{j}{2} \beta_2 \frac{\partial^2 A(z, t)}{\partial t^2} + j\gamma_F |A(z, t)|^2 A(z, t). \quad (2.30)$$

In this equation the impact of SRS and SBS is not taken into account. However, as discussed in section 1.3.3.2, the Raman threshold is too high to be of concern in a fiber-based optical transmission. The Brillouin threshold, on the other hand, is low enough to be considered. However, when a large-band signal ( $> 10$  GHz bandwidth) is injected into the fiber, the Brillouin threshold is found to be improved by 2 dB. In addition, according to recent works on 10-Gb/s NRZ transmissions, the SBS-induced power penalty is found to be well below 1 dB as long as the transmitted optical power is below 10 dBm [58]. Nowadays, in Passive Optical Network (PON) standards the typical value of injected optical power is about 4 dBm [6]. Hence, in conventional transmissions where the injected optical power is equal to 0 dBm, it is reasonable to neglect the impact of SBS. However, a network designer must keep in mind that when the injected power is increased, SBS might limit the SNR on the receiver side due to low Brillouin threshold. Hence, in this case SBS may become one of the principal capacity-limiting factors. The impact of SBS can be integrated into the model by means of an additional loss.

Eq. (2.30) can be further simplified by neglecting the term  $\beta_1$ , which is simply proportional to the propagation time of an optical pulse from an end to the other

$$\begin{aligned} \frac{\partial A(z, t)}{\partial z} &= -\frac{\alpha_{att}}{2} A(z, t) - \frac{j}{2} \beta_2 \frac{\partial^2 A(z, t)}{\partial t^2} + j\gamma_F |A(z, t)|^2 A(z, t), \\ \frac{\partial A(z, t)}{\partial z} &= (\hat{L} + \hat{N}) A(z, t), \end{aligned} \quad (2.31)$$

where  $\hat{L}$  and  $\hat{N}$  correspond to linear and nonlinear effects, respectively.

$$\hat{L} = -\frac{\alpha_{att}}{2} - \frac{j}{2} \beta_2 \frac{\partial^2}{\partial t^2}, \quad (2.32)$$

$$\hat{N} = j\gamma_F |A(z, t)|^2. \quad (2.33)$$

One of the numerical methods that have been used to solve the problem of propagation in nonlinear dispersive media is the Split-Step Fourier (SSF) method [8], [59], [60]. In the literature this method has been extensively used thanks to its accuracy and relative speed when compared to other finite-difference methods. This method provides an approximate solution of the NLS equation by supposing that over a small propagation distance  $\Delta z$  the linear and nonlinear effects act independently. The propagation from  $z$  to  $z + \Delta z$  can be divided into two steps. In the first step, nonlinear effects act alone, which means that  $\hat{L} = 0$ . And in the second step, linear effects act alone, which means that  $\hat{N} = 0$ . In the optical field domain, the evolution of a pulse complex envelope from  $z$  to  $z + \Delta z$  can be described as

$$A(z + \Delta z, t) \approx \exp(\Delta z \hat{L}) \exp(\Delta z \hat{N}) A(z, t). \quad (2.34)$$

In the equation above the term  $\exp(\Delta z \hat{N})$  corresponds to the nonlinear phase shift caused by nonlinear effects during the first step (*c.f.* Eq. (1.29)). The impact of linear effects in the second step is mathematically illustrated by the term  $\exp(\Delta z \hat{L})$ , which can be evaluated in the Fourier domain as follows

$$\exp(\Delta z \hat{L}) B(z, t) = \mathcal{F}^{-1}\{\exp[\Delta z \hat{L}(-j\omega)] \mathcal{F}[B(z, t)]\}, \quad (2.35)$$

where  $\mathcal{F}$  denotes the Fourier transform operation,  $\hat{L}(-j\omega)$  is obtained from Eq. (2.32) by replacing  $\partial/\partial t$  by  $-j\omega$ . In this method, because the noncommutating nature of the operators  $\hat{L}$  and  $\hat{N}$  is ignored, the approximation error is in the order of  $\Delta z^2$  [8].

### Symmetrized split-step Fourier method

The accuracy of the SSF method can be further improved by replacing Eq. (2.34) by

$$A(z + \Delta z, t) \approx \exp\left(\frac{\Delta z}{2} \hat{L}\right) \exp\left(\int_z^{z+\Delta z} \hat{N}(z') dz'\right) \exp\left(\frac{\Delta z}{2} \hat{L}\right) A(z, t). \quad (2.36)$$

Here, the main difference from Eq. (2.34) is that the nonlinear effects are included in the middle of the segment rather than at the segment boundaries. When the step size  $\Delta z$  is small, the integral can be approximated by  $\Delta z \hat{N}$  and Eq. (2.36) becomes

$$A(z + \Delta z, t) \approx \exp\left(\frac{\Delta z}{2} \hat{L}\right) \exp(\Delta z \hat{N}) \exp\left(\frac{\Delta z}{2} \hat{L}\right) A(z, t). \quad (2.37)$$

It is noted in Eq. (2.37) that from  $z$  to  $z + \Delta z$ , the SSF method uses four Fourier transform operations to evaluate the linear operator  $\hat{L}$ . In practice, the number of required Fourier transform operators can be reduced by two thanks to rewriting the SSF method under the following form

$$A(L, t) \approx \exp\left(-\frac{\Delta z}{2} \hat{L}\right) \left(\prod_{m=1}^{M_{SSF}} \exp(\Delta z \hat{L}) \exp(\Delta z \hat{N})\right) \exp\left(\frac{\Delta z}{2} \hat{L}\right) A(0, t), \quad (2.38)$$

where  $L = M_{SSF} \Delta z$  denotes the fiber length and  $M_{SSF}$  is the number of short fiber sections. Except the first and the last section of length  $\Delta z/2$ , from  $z$  to  $z + \Delta z$  the method requires only two Fourier transform operations to evaluate the linear effect.

## 2.4. Photodetector modeling

For a p-i-n-based photodetector, the receiver bandwidth can go up to 35 GHz [61]. In the scope of this thesis, the sampling rate of the DAC in the simulations and experimentations is limited to 12 Giga-Sample Per Second (GS/s). Hence, the frequency response of a photodetector can be considered flat in the transmission systems considered in this thesis. For this reason, on the receiver side only the receiver noise is considered. The power of shot noise and thermal noise can be calculated according to the receiver sensitivity, which is defined as the average received optical power to obtain a certain value of Bit Error Rate (BER) in an on-off-keying NRZ transmission [14]. Supposing that the receiver noise is Gaussian, the BER of an NRZ transmission can be written as

$$BER = \frac{1}{2} \operatorname{erfc}\left(\frac{Q}{\sqrt{2}}\right), \quad (2.39)$$

with

$$Q = \frac{I_1 - I_0}{\sigma_1 + \sigma_0}, \quad (2.40)$$

where  $I$  denotes the photodetector output current and  $\sigma$  denotes the noise standard deviation. Subscripts  $0, 1$  denote the received bit 0 and 1, respectively.  $erfc(\cdot)$  is the complementary error function which is defined as

$$erfc(x) = \frac{2}{\sqrt{\pi}} \int_x^{\infty} e^{-t^2} dt. \quad (2.41)$$

In general the value of the dark current is small and it can be neglected. In this case the quality factor  $Q$  can be written as

$$Q = \frac{I_1}{\sigma_1 + \sigma_0} = \frac{2MR\bar{P}}{\sqrt{\sigma_S^2 + \sigma_T^2} + \sigma_T}, \quad (2.42)$$

where  $M$  is the avalanche gain and  $M$  is equal to 1 in the case of a p-i-n photodiode.  $R$  (A/W) is the photodiode responsivity.  $\bar{P}$  is the average received optical power. The power of shot noise and thermal noise is expressed as (c.f. Eq. (1.6) and (1.7))

$$\sigma_S^2 = 2qM^2F_A R(2\bar{P})\Delta f, \quad (2.43)$$

$$\sigma_T^2 = \left(\frac{4k_B\theta}{R_L}\right) F_{no}\Delta f, \quad (2.44)$$

where  $F_A$  is the excess noise factor of an avalanche photodiode.  $F_{no}$  is referred to as the amplifier noise figure corresponding to the noise enhancement due to the amplification of a TIA. By solving Eq. (2.42), one can write the expression of the average optical power as a function of the quality factor

$$\bar{P} = \frac{Q}{R} \left( qF_A Q \Delta f + \frac{\sigma_T}{M} \right). \quad (2.45)$$

In principle, according to the value of BER, one can calculate the Q-factor by using Eq. (2.39). By definition, the value of  $\bar{P}$  in Eq. (2.45) also corresponds to the value of the receiver sensitivity. Hence, once the receiver sensitivity is available, the power of the thermal noise can be deduced by using Eq. (2.45). And the power of shot noise can be calculated according to (2.43).

When a p-i-n photodiode is used, the shot noise power is found to be negligible when compared to that of the thermal noise [8]. In this case, for the sake of simplicity the receiver noise can be modeled as a centered white Gaussian noise whose power can be written as

$$\sigma_T^2 \approx \left(\frac{R\bar{P}}{Q}\right)^2. \quad (2.46)$$

For example, supposing that the sensitivity of a p-i-n-based photodetector is -26 dBm, the photodiode responsivity is equal to 0.6 and the Q-factor is equal to 6 at  $10^{-9}$  BER, the noise standard deviation can be deduced as

$$\sigma_T \approx \frac{R\bar{P}}{Q} = \frac{0.6(10^{-2.6}10^{-3})}{6} = 0.25 \text{ } (\mu\text{A}). \quad (2.47)$$

## 2.5. Large-signal regime model validation

In this section the channel model is validated in a “large-signal” regime. The validation is carried out by comparing the signal waveforms obtained by numerical simulation to the ones obtained by experimentation. In the scope of this thesis, for the sake of performance evaluation of the OFDM modulation in the context of optical IMDD transmission, the channel model should be validated with an OFDM modulation. In addition, when compared to the conventional NRZ waveform or other mono-carrier signal waveforms, OFDM signals have a larger Peak-to-Average Power Ratio (PAPR). The large power peaks of an OFDM signal might cause nonlinear effects in a transmission, in particular nonlinear effects of the fiber link. Therefore, it is important for a channel model to correctly simulate an OFDM transmission. The modulation index, which is defined as the ratio between the largest driving current amplitude and laser threshold current, is chosen to be equal to 0.6, which is a typical value in an optical IMDD OFDM transmission.

### 2.5.1. Experiment set-up

The transmission diagram used for the validation is shown in Figure 2.19.

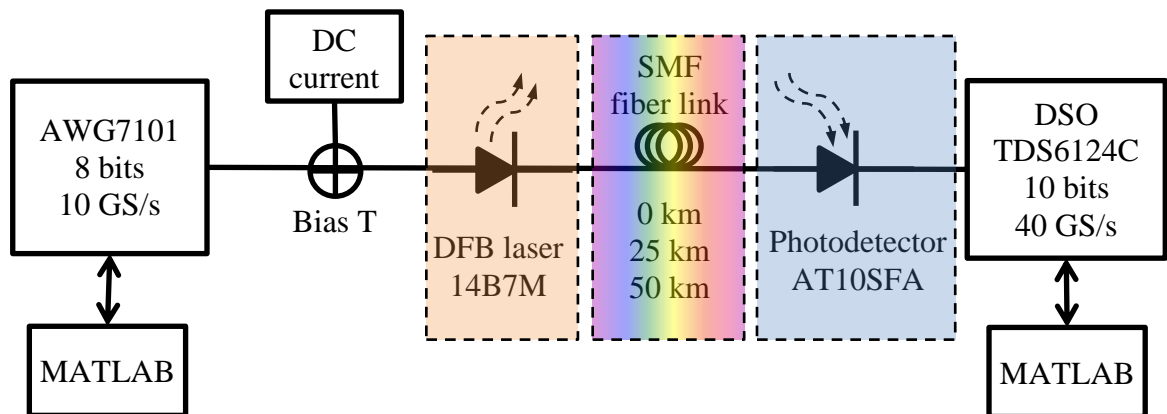


Figure 2.19 – Transmission diagram for model validation in large-signal regimes.

#### 2.5.1.1. Transmitter

OFDM signals are offline prepared by using Matlab. The signals are transmitted to an Arbitrary Waveform Generator (AWG) having 8 quantization bits and operating at 10 GS/s. AWG output signals are amplified by an electrical amplifier before being biased by a 60-mA DC current, which is chosen so that the laser functions in a linear regime (*c.f.* Figure 2.6). The signal modulation index can be adjusted by means of a Variable Electrical Attenuator (VEA) located at the output of the amplifier. The driving signals then modulate the DFB laser (model 14B7M). At the laser output a Variable Optical Attenuator (VOA) is

used so that the optical power injected into the fiber is maintained at 0 dBm, which is a typical value used in PONs.

### **2.5.1.2. Fiber link**

The model is validated with three fiber length values: 0 km, 25 km and 50 km. Due to the absence of optical amplifier in the fiber link, larger values of fiber length cannot be validated because of poor SNRs on the receiver side.

### **2.5.1.3. Photodetector**

In terms of photodetector, an 8-GHz avalanche photodiode AT10SFA is used. In order to limit the impact of the receiver noise on the experimental waveforms and not to exceed the maximum values accepted by the photodiode, the received optical power is always maintained at -10 dBm by means of a second VOA located before the photodiode. The output signals of the photodetector are captured by a Digital Storage Oscilloscope (DSO) TDS6124C having 10 quantization bits and sampling at 40 GS/s. The digitized DSO output signals are offline processed by means of Matlab. In order to eliminate the impact on the experimental waveforms of Sampling Frequency Offset (SFO) between the AWG and the DSO, the SFO value is estimated by using pilot subcarriers [62]. The estimated SFO is found to be in the order of 1 part per million (ppm). The SFO is then compensated by means of interpolation in the time domain. Model parameters of the laser, the fiber link and the photodetector used for simulation are given in Table 2.3. Laser and fiber dispersion parameters are extracted from the laser and the fiber link used in this experimentation.

### **2.5.1.4. OFDM modulation**

In the validation setup, the Fast Fourier Transform (FFT) size is 256. Since the sampling frequency of the AWG is limited by 10 GS/s, the OFDM signal bandwidth is limited by 5 GHz. In order to validate the model for various values of the signal bandwidth, the OFDM signal bandwidth can be one of the following values

- (a) 4.22 GHz,
- (b) 3.44 GHz,
- (c) 2.66 GHz,
- (d) 1.88 GHz.

The above values of signal bandwidths are chosen so that both full-band signal (case (a)) and narrow-band signals (case (d)) are considered. In addition, the model precision as a function of signal bandwidth can also be studied.

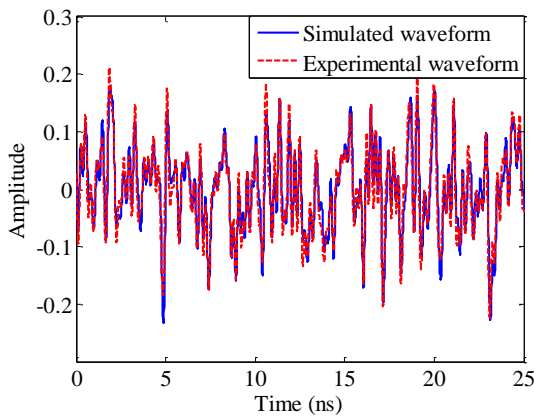
Symbol	Physical meaning	Unit	Value
$F$	newly defined laser parameter. Inverse P-I conversion factor.	A/W	5.32
$I_{th}$	laser threshold current	mA	20
$I_S$	laser characteristic current	$\mu$ A	5.65
$B$	newly defined laser parameter	Hz <sup>2</sup> /A	1.3e23
$\tau_p$	photon lifetime	ps	4.12
$\tau_n$	carrier lifetime	ns	0.14
$\tau_c$	newly defined laser parameter. Gain saturation to gain slope ratio.	ps	1.65
$\alpha$	laser linewidth enhancement factor	---	2.68
$D$	dispersion parameter	ns/(nm.km)	17
$\alpha_{att}$	fiber attenuation coefficient	dB/km	0.2
$\lambda$	optical wavelength	$\mu$ m	1.55
$A_{eff}$	fiber effective area	m <sup>2</sup>	80e-12
$n_2$	fiber nonlinear index	m <sup>2</sup> W <sup>-1</sup>	2.5e-20
$Se$	photodetector sensitivity	dBm	-20

Table 2.3 – Model parameters used for simulations.

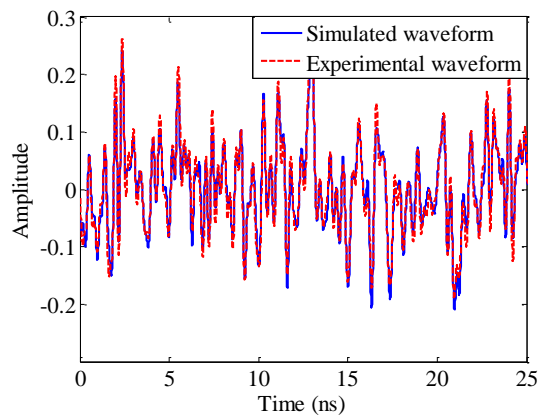
## 2.5.2. Experimental results and model validation

The OFDM waveforms obtained by experimentation and the corresponding waveforms obtained by numerical simulation are illustrated in the figures below. Subscripts (a), (b), (c), (d) correspond to four bandwidth values described in the previous paragraphs.

### 2.5.2.1. Back-to-back transmission



(a)



(b)

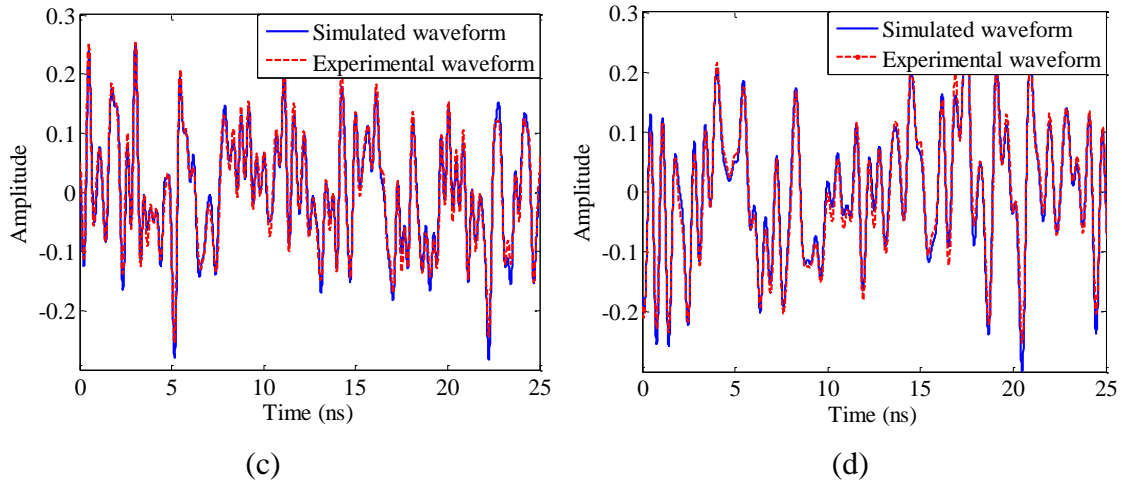


Figure 2.20 – Simulated and experimental OFDM waveforms in back-to-back transmissions.

**2.5.2.2. 25-km transmission**

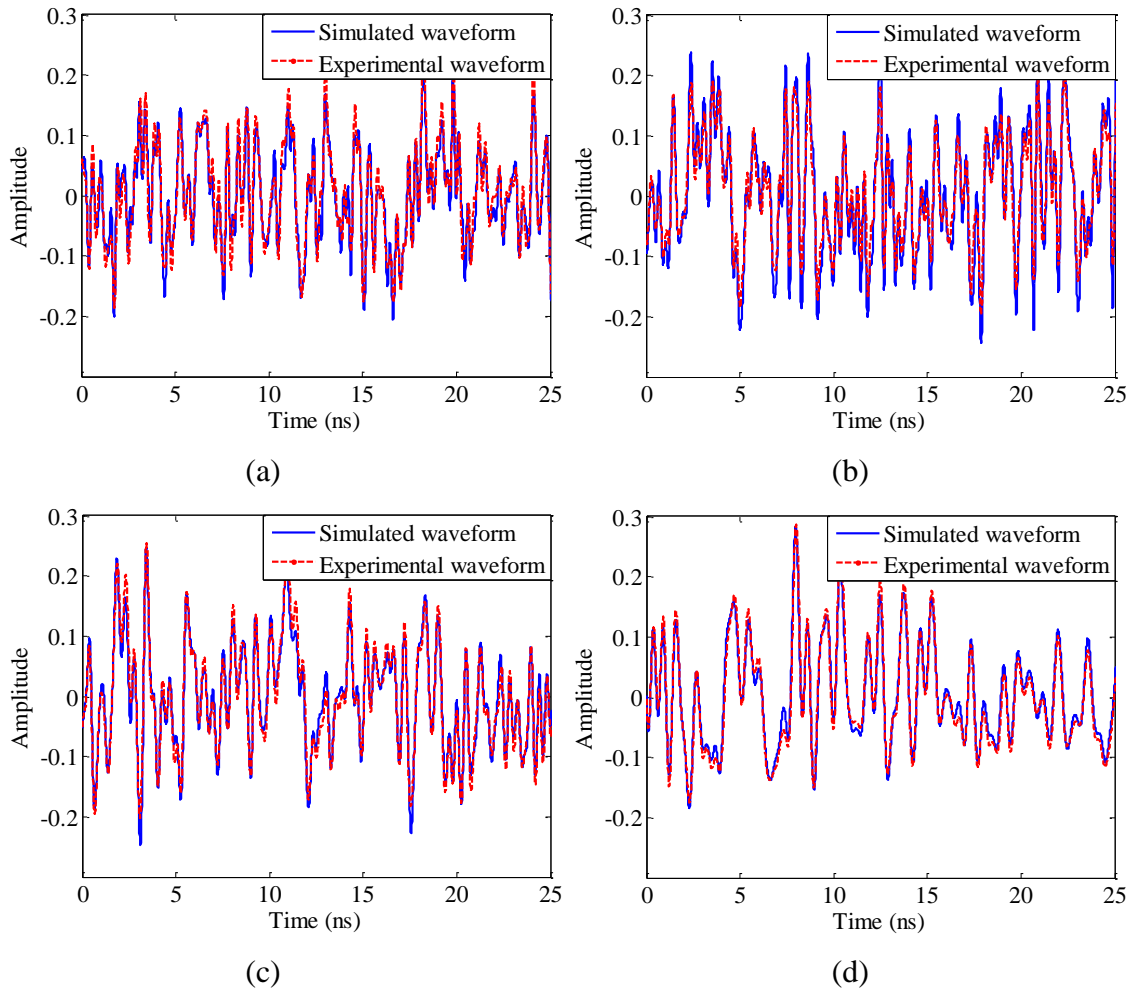


Figure 2.21 – Simulated and experimental OFDM waveforms in 25-km transmissions.

### 2.5.2.3. 50 km transmission

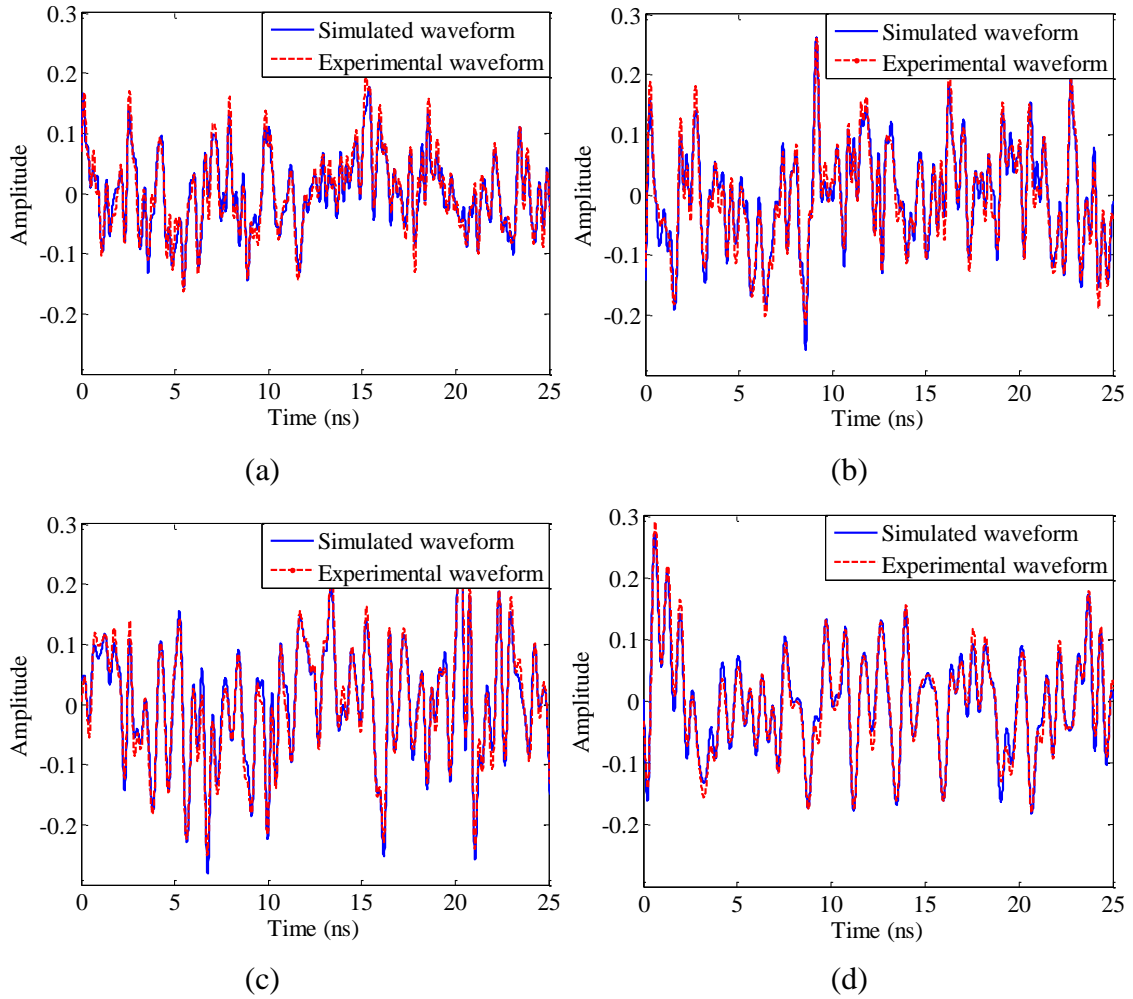


Figure 2.22 – Simulated and experimental OFDM waveforms in 50-km transmissions.

### 2.5.2.4. Model error analysis

As shown in the figures above, in general the simulation results are compliant with the experimental results. In all the configurations the simulated waveforms correspond well to the experimental waveforms. In terms of PAPR peaks of the OFDM signals, the simulation results fit perfectly to the experimentations. In order to quantify the compliance between the numerical simulation and the experimentation, the Model Signal-to-Error Ratio (MSER) is defined as

$$MSER = \frac{\text{var}(x_s(t))}{\text{var}(x_s(t) - x_m(t))}, \quad (2.48)$$

where  $x_s(t)$ ,  $x_m(t)$  denote the simulated waveform and the corresponding experimental waveform, respectively. The value of the MSER in different transmission configurations is given in Table 2.4. The model error is found to be independent in the fiber length. When the signal bandwidth decreases, the power of the channel noise and the nonlinearity-induced noise also decreases. Hence, the MSER increases. It is noted that the experimental

waveforms also depend on the frequency response of the measuring equipment. This also decreases the MSER value.

	(a) 4.22 GHz	(b) 3.44 GHz	(c) 2.66 GHz	(d) 1.88 GHz
<b>0 km</b>	11	14	15.9	17.2
<b>25 km</b>	11	12.8	14.7	16.4
<b>50 km</b>	10.9	12.2	15	15.4

Table 2.4 – Model signal-to-error ratio (dB) as a function of distance and bandwidth.

## 2.6. Influence of parameter extraction precision on the model

In the previous section, the optical IMDD channel model is validated in large-signal modulation regimes. When the signal bandwidth is well below (20%) the Nyquist frequency, up to 17-dB MSER is obtained. Obviously, the MSER strongly depends on the precision of each extracted parameter. Supposing that there is an optimal set of parameter values which maximizes the MSER, a deviation from the optimal values of the extracted parameters may cause a degradation of MSER. In this section we study the MSER penalty as a function of parameter value deviation. This study helps identifying parameters of which a small deviation from the optimal values should lead to a significant MSER decrease. In this case, the extraction precision of such parameters should be carefully paid attention to.

In general, fiber and receiver parameters are given by the manufacturer. However, the parameters of the intrinsic laser must be extracted with experimental extraction as described in section 2.2. In the extraction procedures, the P-I relationship and the laser AM response measurements are not significantly noisy because fiber is not present. However, extracted parameters from the laser FM measurement could be very noisy because of fiber attenuation (c.f. Figure 2.12 and Figure 2.13). Given that the linewidth enhancement factor  $\alpha$ , the parameter  $\tau_c$  and the photon lifetime  $\tau_p$  are extracted from a noisy FM measurement, in the following paragraphs these parameters are chosen as the subjects of our study.

In this study, the parameter values given in Table 2.2 are considered as reference values. Therefore, a waveform obtained by numerical simulation using these parameter values is also a reference waveform. When the value of one of the three parameters varies, the resulting waveform differs from the reference one. In this case, the difference is defined as the error signal. In order to evaluate the model dependence on the variation of parameter value, a signal-to-error ratio, which is the ratio between the reference signal power and that of the error signal, is calculated.

Figure 2.23 illustrates the signal-to-error ratio as a function of enhancement factor variation. In this illustration the linewidth enhancement factor reference value is equal to 2.68. Since the optical IMDD frequency channel response depends on the interplay between chromatic dispersion and laser chirps, the signal-to-error ratio degradation also depends on fiber length. When fiber length is equal to 60 km, a deviation of 0.2 from the reference value leads to a degradation of 1 dB of the signal-to-error ratio. This is also equivalent to a degradation of 1 dB of the MSER. Hence, if 1-dB MSER degradation is considered acceptable for the model, the value extraction of laser linewidth enhancement factor should guarantee a precision of  $\pm 0.2$ .

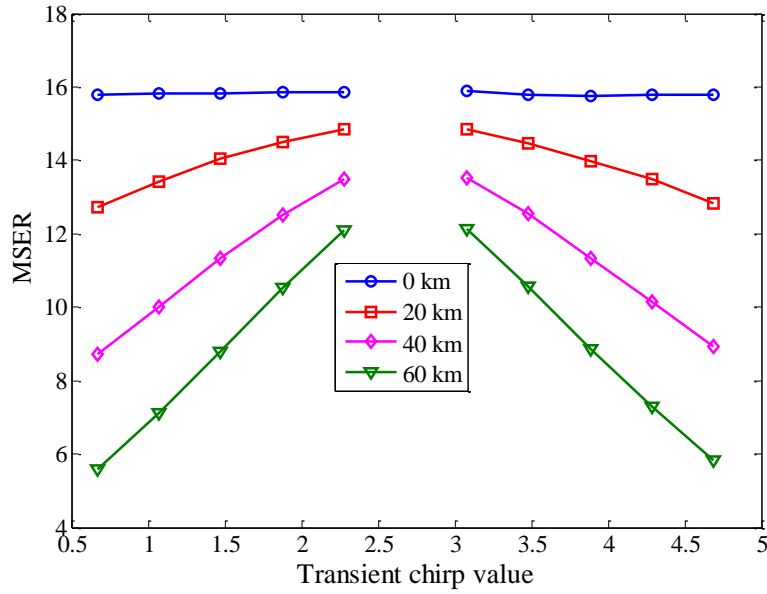


Figure 2.23 – Signal-to-error ratio as a function of linewidth enhancement factor.

Figure 2.24 shows the signal-to-error ratio as a function of  $\tau_c$  variation. According to Eq. (2.15), the laser adiabatic frequency explicitly depends on the value of  $\tau_c$ , which in turn has an impact on the channel response because of the interplay with the chromatic dispersion. Hence, the signal-to-error ratio degradation also depends on fiber length. As shown in Figure 2.24, when fiber length is equal to 60 km, a variation of 0.6 ps results in a signal-to-error ratio degradation of 1 dB. Hence, if 1-dB MSER degradation is considered acceptable for the model, the value extraction of  $\tau_c$  should guarantee a precision of  $\pm 0.6$  ps.

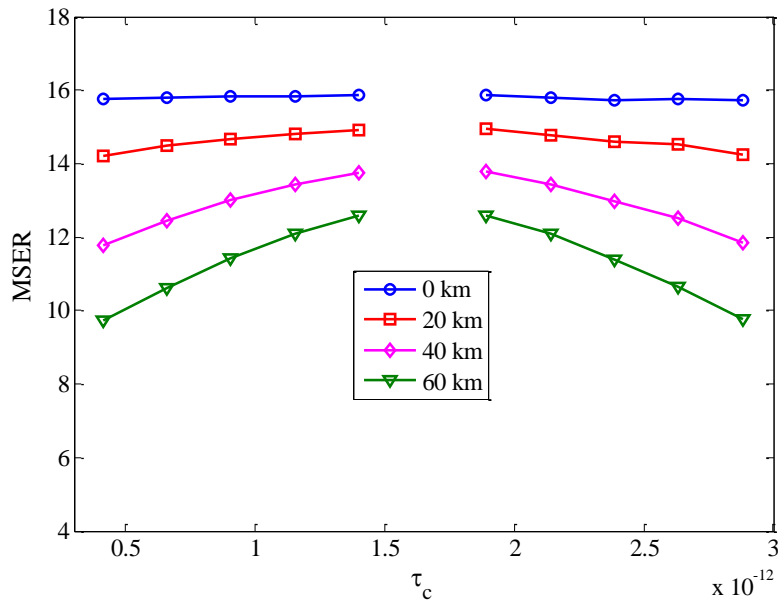


Figure 2.24 – Signal-to-error ratio as a function of  $\tau_c$ .

In Figure 2.25, the same study is carried out for the photon lifetime  $\tau_p$ . Unlike the variation of laser linewidth enhancement factor or that of the parameter  $\tau_c$ , the photon lifetime value variation does not have a significant impact on the signal-to-error ratio degradation. Hence, an extracted value of  $\tau_p$  can be considered acceptable for the model as long as it is in the order of several picoseconds, which is the typical value for a DFB laser in the context of access network.

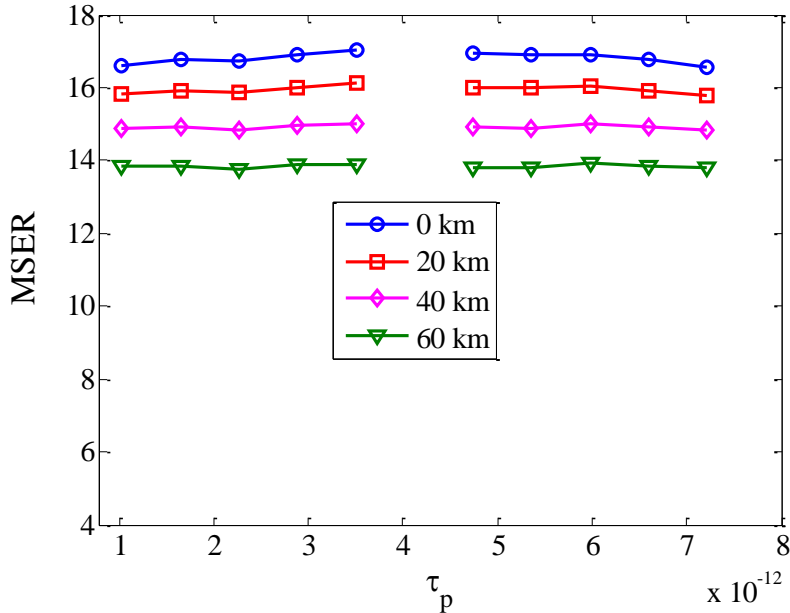


Figure 2.25 – Signal-to-error ratio as a function of photon lifetime  $\tau_p$ .

## 2.7. Conclusion

In this chapter the fundamental components of a fiber-based optical IMDD transmission in the context of access networks are identified. A numerical simulation model is also studied. The model is found to be realistic because its parameters are extracted from real components by means of experimental extraction procedures. The reliability of the model is also validated in both “small-signal” and “large-signal” modulation regimes. The waveforms obtained by simulation are found to be compliant with the ones obtained by experimentation. For the rest of the report, this channel model is used to evaluate different signal processing techniques as long as different transmission systems.

The author would like to thank the ASHA team in Lannion, in particular Mrs. Naveena Genay for the help during the laser extraction and model validation procedures.

# Nyquist pulse shaping technique for future PONs

## 3.1. Introduction

In order to satisfy the ever growing demand on data traffic in the context of optical access networks, extensive research has been carried out to look for cost-effective, high-speed optical transmission systems. In the next generations of optical access network, the transmission must guarantee multiple gigabit-per-second communications over a single fiber which can reach as far as tens of kilometers. As discussed in the previous chapters, for the reason of cost, a telecom operator always prefers low cost systems among which the optical Intensity Modulated Direct Detected (IMDD) system is always one of the most suitable candidates. In terms of signal modulation, Pulse Amplitude Modulation (PAM) remains one of the first choices thanks to its simplicity. In conventional NRZ transmissions, an increase of fiber length and/or an increase of transmission data rate always aggravate the problem of ISI due to the interplay between laser chirps and accumulating chromatic dispersion in the fiber link. When the distance and the data rate become significant, a receiver can no longer be able to distinguish two consecutive transmitted bits, resulting in a significantly increased BER of a transmission. Figure 3.1 illustrates the signal eye diagram of a 10-Gb/s On Off Keying (OOK) NRZ on the transmitter and the receiver sides. The “eye” begins to close only after a 10-km transmission. For this reason, equalization techniques, which compensate for ISI in order to extend reach and/or useful data rate, become critical in an optical transmission.

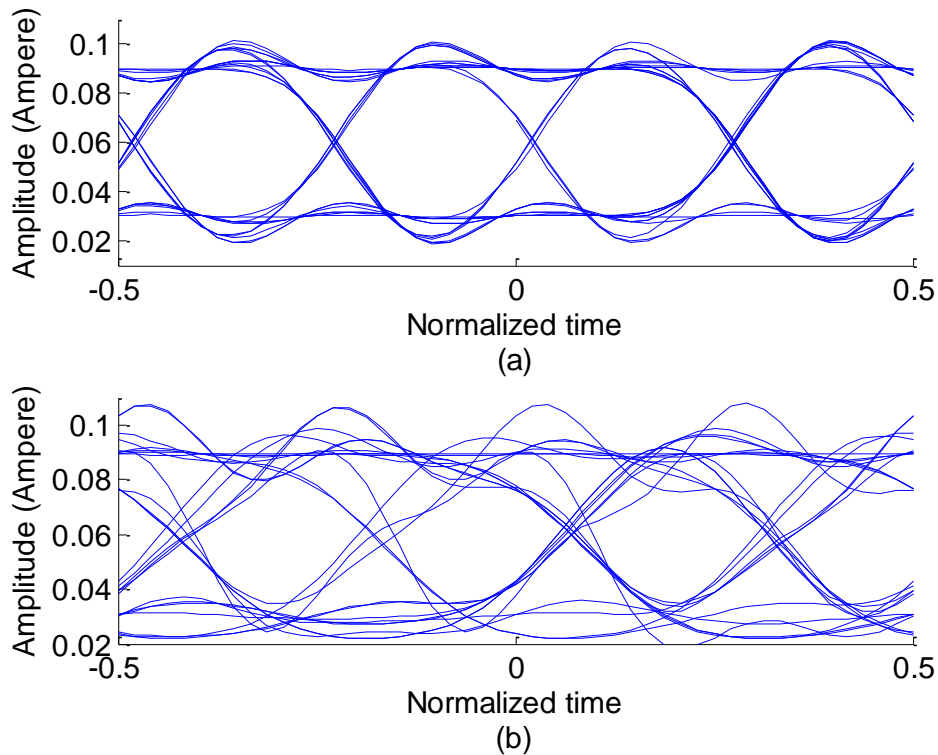


Figure 3.1 – Simulated 10-Gb/s OOK NRZ signal eye diagrams. (a) Transmitter side. (b) Receiver side. Transmission distance is 10 km.

One of the first approaches to extend the reach and to increase the transmission bit rate is to directly compensate for chromatic dispersion in the optical line by means of Dispersion Compensation Fibers (DCFs). Because the sign and the slope of the dispersion parameter in a DCF are different from that of the fiber link, accumulating chromatic dispersion in the fiber link is compensated for. However, the implementation of DCFs is bulky and expensive. Another approach is to transmit a signal within the zero-dispersion zone of the fiber. However, because of increased bandwidth demand, any optical wavelength has to be exploited.

Another interesting approach for eliminating ISI is to compensate for all detriments in the electrical domain. More concretely, ISI will be eliminated by means of channel equalization techniques. Actually, in wired and wireless communications the problem of ISI is well-known and extensive studies of equalization techniques have been reported. Some authors are interested in linear transversal filter equalizers [63]–[65]. Others focus on equalizer performance improvement by using decision feedback structures [66]–[68] or Maximum Likelihood Sequence Estimator (MLSE) structures [69]–[72]. In the context of optical access networks, as indicated in the XG-PON standard [6] the actual data rate per wavelength is only 10 Gb/s and the transmission distance is limited by 20 km. The standard also imposes some constraints on the chirp value of the modulator. In such a transmission context the impact of ISI might still be noncritical. However, when a conventional DML modulator, whose linewidth enhancement factor is large, is used and when either per-wavelength bit rate or transmission distance is about to further increase, the impact of ISI will no longer be negligible. In the context of optical IMDD transmissions several studies have illustrated the interests of a transversal filter and a Decision Feedback Equalizer (DFE) [38], [39], [73]. It is also reported that due to fiber nonlinearities, a DFE has very limited performance when compared to an MLSE equalizer

[74]–[76]. However, most of the reported research paid attention only on the impact of chromatic dispersion, polarization mode dispersion and/or the impact of ASE noise in long-haul and metropolitan transmissions. The impact of laser chirps including transient chirp and adiabatic chirp and fiber nonlinearities (Kerr effects in particular) on the performance of conventional equalizers has not been adequately studied. In this chapter the performance of conventional equalization schemes, which have been proposed for wired and wireless communications, is analyzed in the context of optical IMDD transmissions. Some practical receiver designs are also proposed. The analysis focuses on the resistance of equalization techniques to various channel parameters such as fiber length, laser linewidth enhancement factor and receiver noise.

In terms of signal modulation technique, the first part of this chapter discusses the conventional NRZ pulse-shape which is actually implemented in most access network standards such as the Gigabits Passive Optical Network (GPON) or the XG-PON (Ten-gigabit-per-second PON). The conventional NRZ waveform is found to have high power penalty when distance or laser linewidth enhancement factor value increase. Recently, Nyquist pulse-shaping technique has been proposed to replace the conventional NRZ waveform in the context of optical communications. Nyquist WDM systems were also successfully demonstrated in both coherent systems [77] and IMDD systems [78]. The rectangular shape in frequency domain of a Nyquist waveform is shown to reduce the impact of ICI, relaxing the constraint of frequency guard-band between adjacent WDM channels. However, to the best of author's knowledge, the tolerance of a Nyquist waveform to chromatic dispersion and modulator chirp in an IMDD transmission has not been adequately studied. Moreover, the performance of channel equalization schemes for future PONs has not been reported yet.

In this chapter, we compare the performance of conventional NRZ and Nyquist waveforms in an IMDD channel using various equalization structures. When compared to the classical NRZ waveform, the Nyquist waveform usually used in radio communications has several advantages as follows.

- The spectral efficiency of a transmission is increased by a factor of  $2/(1 + \alpha_{rof})$  where  $\alpha_{rof}$  is the roll-off factor of the pulse-shape filter.
- Because signal spectrum is reduced, ISI caused by chromatic dispersion and laser chirps is less severe.
- Also because of a spectrally reduced signal, receiver noise power is also reduced given that noise power is proportional to the receiver effective bandwidth.

According to simulation results, the Nyquist pulse shape has better BER performance when compared to the conventional NRZ pulse shape at the expense of increased signal generation complexity. We show that the Nyquist pulse shaping, along with proposed channel equalization schemes, extends the transmission reach by tens of kilometers and decreases power penalty by 2 dB when compared to the conventional NRZ pulse shaping. In addition, a Nyquist waveform is also shown to decrease chirp-induced power penalty by up to 2 dB. The chapter is organized as follows. Section 3.2 summarizes state-of-the-art linear and nonlinear equalization schemes. Some practical receiver designs are illustrated in section 3.3. In section 3.4 the performance in terms of BER and power penalty of equalization techniques is given. A comparison in terms of power penalty between classical NRZ and Nyquist transmissions is also presented. Finally, section 3.5 concludes the chapter.

## 3.2. State-of-the-art equalizer structures

In this section, the most common equalization techniques used in radio communications are described. It is noted that such techniques have been used for a linear channel in which the ISI is linear. The notions such as “sufficient statistic” or “optimum linear receiver” are only valid for a linear channel like a multi-path channel in radio transmissions. In the context of optical IMDD transmissions, the interference is nonlinear due to a direct detection and the optical channel is itself nonlinear. Hence, these notions are no longer validated. To the best of author’s knowledge, so far there has been no study about the statistic sufficiency of the sampling theory or the optimum receiver in optical communications. However, according to simulation results, despite the nonlinearities of an optical channel, equalization schemes, in particular nonlinear equalizers, still significantly improve the transmission BER performance. In order to simplify mathematical analyses of various equalizer structures, in the following paragraphs the impact of nonlinearities is not taken into account. In section 3.3 where we discuss different structures, especially nonlinear equalizer structures, of an optical IMDD receiver, the impact of nonlinearities is considered in order to optimize transmission performance.

### 3.2.1. Equivalent discrete channel

Figure 3.2 illustrates the discrete equivalent channel model of a conventional transmission. On the transmitter side, a pulse-shaping filter  $g(t)$  is applied on a data sequence  $\{a_k\}$ . In the context of classical OOK NRZ transmission the data symbol  $\{a_k\}$  is a binary signal and the pulse-shaping waveform is the NRZ. If a Nyquist waveform is used  $g(t)$  is the well-known square-root raised cosine filter. The signal is then transmitted through the channel whose impulse response is denoted by  $p(t)$ . The channel includes a laser, a DAC, a fiber link and a photodetector.  $h(t) = g(t) * p(t)$  denotes the equivalent transmission channel.  $N_0$  is the PSD of the receiver noise  $n(t)$ .

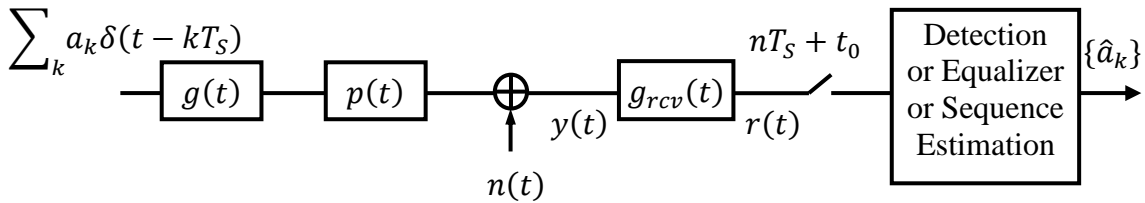


Figure 3.2 – Simple linearized discrete equivalent channel model.

### 3.2.2. Linear equalizers

Conventional linear receiver structure is shown in Figure 3.3. According to Forney’s development [69], on condition that the timing phase is correct, a matched filter followed by a  $T_s$ -spaced sampling gives a set of sufficient statistics for estimation of the transmitted sequence  $\{a_k\}$ . The filtering impact of the pulse-shaping filter, the channel and the matched filter can be modeled by an end-to-end equivalent filter having the impulse response  $q(t)$  and the corresponding frequency response  $Q(f) = |H(f)|^2$ . After the sampler  $S_q(f)$  denotes the folded (or aliased) frequency response of the end-to-end equivalent filter. It is noted that when the receiver filter is a matched filter,  $S_q(f)$  is also the spectrum of the received signal before the matched filter.

$$S_q(f) = \sum_n |H(f - n/T_S)|^2, \quad 0 \leq f \leq 1/T_S \quad (3.1)$$

The received discrete symbol can be written as

$$y_k = \sum_n q_n a_{k-n} + w_k, \quad (3.2)$$

where  $q_n$  denotes the filter taps of the equivalent discrete channel filter and  $w_k$  denotes the receiver noise filtered by the receive filter. It is clearly shown in Eq. (3.2) that a received symbol is made up of a transmitted symbol, an ISI term and a noise term. In order to reduce the impact of ISI, a large number of equalization techniques have been proposed and studied.

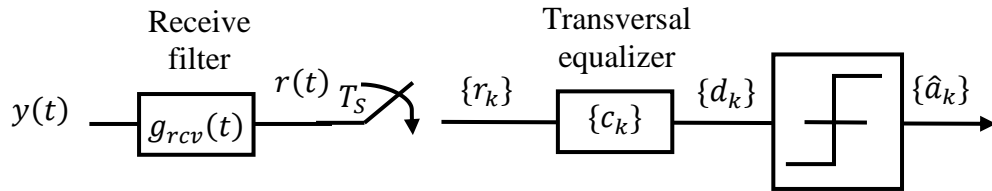


Figure 3.3 – Conventional linear receiver.

### 3.2.2.1. Zero-forcing equalizer

The zero-forcing (ZF) equalization consists in completely eliminating the ISI term in Eq. (3.2). In the time domain the overall channel (including the equivalent channel and the equalizer) impulse response is only non-null at the time instant  $t_0$ , and null at instants  $iT_S + t_0$  for  $i \neq 0$ . In the frequency domain the overall channel response is flat, which respects the Nyquist criterion. In this case the equalizer frequency response is the inverse of the folded equivalent channel response

$$C_{ZF}(f) = \frac{1}{S_q(f)}, \quad (3.3)$$

The mean square error achieved by such an equalizer is expressed as

$$\sigma_{MSE}^2(ZF) = T_S \int_0^{\frac{1}{T_S}} \frac{N_0}{S_q(f)} df. \quad (3.4)$$

Although the ISI should be completely eliminated by a ZF equalizer, this equalizer structure has some important disadvantages

- The inversion of a channel response is not always realizable, for example when the channel frequency response introduces zeros in the Nyquist frequency band.
- Since the equalizer amplifies attenuated frequency components, it also amplifies noise power.
- In general, the impulse response of an equalizer is infinite and in some cases non-causal. The realization of such an equalizer is not practical. One practical

approach is to implement a finite-length transversal filter. The equalizer impulse response is truncated and a time delay is introduced to make the equalizer causal. The truncation degrades the equalizer performance. In severely frequency selective channel, the number of filter taps is generally large, resulting an increased equalizer complexity.

### 3.2.2.2. Minimum mean square error equalizer

Unlike a ZF equalizer, a Minimum Mean Square Error (MMSE) equalizer does not try to completely get rid of ISI. Actually, an MMSE equalizer minimizes the Mean Square Error (MSE) of an equalized symbol  $d_k$  and a transmitted symbol  $a_k$

$$MSE = E\{|d_k - a_k|^2\}. \quad (3.5)$$

Minimizing the MSE leads to the MMSE equalizer frequency response

$$C_{MMSE}(f) = \frac{1}{S_q(f) + N_0}. \quad (3.6)$$

It is interesting to consider two limit cases.

- When the receiver noise becomes negligible  $N_0 \ll S_q(f)$ : the MMSE equalizer approaches the ZF one.
- When the receiver noise becomes dominant  $N_0 \gg S_q(f)$ : the MMSE equalizer response becomes a constant. The receiver filter becomes a matched filter  $\frac{H^*(f)}{N_0}$ .

The MSE obtained with an MMSE equalizer can be written as

$$\sigma_{MSE}^2(MMSE) = T_S \int_0^{\frac{1}{T_S}} \frac{N_0}{N_0 + S_q(f)} df. \quad (3.7)$$

With this technique, the overall channel frequency response is not necessarily flat. The equalizer accepts an amount of residual ISI in order to reduce the impact of noise power amplification. Hence, in general BER performance of this equalizer is better than that of a ZF equalizer. One of the most important disadvantages of this equalizer structure is that its impulse response is infinite, making practice implementation difficult. From Eq. (3.7), the MSE at the output of an MMSE equalizer increases when  $S_q(f)$  decreases. Hence, the performance of such an equalizer is limited in extremely frequency selective channels.

### 3.2.2.3. Fractional spaced transversal filter

In a conventional linear receiver, a received signal is filtered with a matched filter followed by a symbol-rate (or  $T_S$ -spaced) sampler, a  $T_S$ -spaced transversal filter and a memoryless detector. The  $T_S$ -spaced transversal filter (or equalizer) can be designed with different criteria of optimality. Without loss of generality, the order of the symbol-rate sampler and the equalizer can be interchanged. Hence, the equivalent frequency response of the receiver can be written as  $G_{rcv}(f)C(f) = H^*(f)C(f)$ . Supposing that the received signal frequency response  $H(f) = 0$  outside the frequency range  $|f| \leq \frac{1}{2\tau}$ ,  $\tau \leq T_S$ , according to the Nyquist

sampling theory the receiver frequency response can be realized by an infinite-length  $\tau$ -spaced transversal filter. The equalizer frequency response  $C(f)$  can be designed according to any criterion of optimality. An MMSE equalizer can be obtained when  $C(f)$  is designed according to Eq. (3.6) for example. When the output of the  $\tau$ -spaced transversal filter is downsampled to produce a symbol-rate signal, the receiver has a desired aliased frequency response as in the case of a conventional linear receiver. Linear receiver based on a Fractionally Spaced Transversal Filter (FSTF) is shown in the figure below.

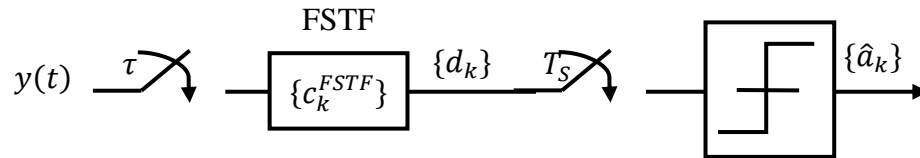


Figure 3.4 – Linear receiver based on a fractionally spaced transversal equalizer.

Denoting  $c_k^{FSTF}$  the fractional spaced transversal filter taps, the output of the equalizer can be written as

$$d_k = \sum_i c_i^{FSTF} y(kT_S - i\tau). \quad (3.8)$$

It is interesting to note that a fractional spaced transversal filter is at once able to play the role of a matched filter and a  $T_S$ -spaced transversal filter on condition that the  $\tau$ -rate sampling respects the sampling theory, which means the received signal PSD is null outside the frequency range  $|f| \leq \frac{1}{2\tau}$ . This property cannot be found in a conventional  $T_S$ -spaced transversal filter because the symbol-rate sampled signal suffers from aliasing problem. Its spectrum is an aliased folded spectrum which spreads from 0 to  $1/T_S$  Hz. However, a  $T_S$ -spaced transversal filter cannot correct frequency components outside the range  $|f| \leq \frac{1}{2T_S}$ . In practice, the sampling time of an FSTF is chosen so that  $\tau = aT_S/b$ , where  $a$  and  $b$  are relatively prime integers and  $a < b$ .

#### 3.2.2.4. Finite-length MMSE equalizer

The entire linear receiver structures mentioned so far are not practical for two reasons. Firstly, optimal transversal filters have an infinite number of taps. Secondly, it is impractical to design beforehand a matched filter which matches various channel responses. In particular, the channel response of an optical IMDD transmission explicitly depends on fiber length and laser characteristics. Moreover, the channel response is in general time-varying. In practice, the matched filter on the receiver side is replaced by a fixed filter. This filter can be designed to match the pulse-shaping filter on the transmitter side. It is also the optimal receiver filter in the case of a frequency non-selective channel. Another possibility is to design the receiver filter to match a particular expected channel response. One example is that the square-root raised cosine filter can be used as both the pulse-shaping filter and the receiver filter. In an OOK NRZ transmission, the receiver filter can simply be a low-pass filter. From Figure 3.3, the end-to-end channel impulse response becomes

$$q(t) = g(t) * p(t) * g_{rcv}(t). \quad (3.9)$$

As for the equalizer, the number of taps is constrained to be finite and the filter coefficients are optimized according to the criterion of optimality MMSE. By referring to Figure 3.3, denoting  $N_c$  equalizer coefficients at time instant  $kT_S$  by the column vector  $\mathbf{c}_k$ , and the discrete samples stored in the equalizer delay line by the vector  $\mathbf{r}_k$ , the optimal taps of an  $N_c$ -tap MMSE equalizer at time instant  $kT_S$  can be written as

$$\mathbf{c}_k = \mathbf{R}_{rr}^{-1} \mathbf{r}_{ar}, \quad (3.10)$$

where  $\mathbf{R}_{rr}$  is an  $N_c \times N_c$  Hermitian covariance matrix  $E\{\mathbf{r}_k^* \mathbf{r}_k^T\}$  and  $\mathbf{r}_{ar}$  is an  $N_c$ -element cross-correlation vector  $E\{\mathbf{r}_k^* a_k\}$ . When the data sequence  $\{a_k\}$  is uncorrelated and has unit power, the elements of the covariance matrix  $\mathbf{R}_{rr}$  and those of the cross-correlation vector  $\mathbf{r}_{ar}$  can be expressed as

$$\mathbf{R}_{rr_{i,j}} = \sum_k q^*(kT_S) q(kT_S + iT_S - jT_S) + N_0 \int g_{rcv}^*(t) g_{rcv}(t + iT_S - jT_S) dt, \quad (3.11)$$

and

$$\mathbf{r}_{ar_i} = q^*(-iT_S). \quad (3.12)$$

The corresponding MSE is expressed as

$$\sigma_{MSE}^2(MMSE) = 1 - \mathbf{r}_{ar}^H \mathbf{R}_{rr}^{-1} \mathbf{r}_{ar}. \quad (3.13)$$

### 3.2.2.5. Finite-length fractional spaced transversal filter

A finite-length FSTF is a sub-optimal and practical form of an infinite-length FSTF described in section 3.2.2.3. When the number of filter taps  $N_c$  tends to infinity, the performance of an FSTF approaches that of the optimal one. Supposing that the received signal is sampled with the rhythm  $aT_S/b$  such that no aliasing occurs, which means  $H(f) = 0 \forall |f| > b/2aT_S$ , by referring to Figure 3.4, the output of a finite-length FSTF can be expressed as

$$\begin{aligned} d_k &= \sum_{i=0}^{N_c-1} c_i^{FSTF} y\left(kT_S - i \frac{aT_S}{b}\right) \\ &= (\mathbf{c}_k^{FSTF})^T \mathbf{y}_k, \end{aligned} \quad (3.14)$$

where  $\mathbf{c}_k^{FSTF}$  and  $\mathbf{y}_k$  denote the filter coefficient vector and the  $aT_S/b$ -second-spaced signal samples vector at time instant  $kT_S$ , respectively. The optimal filter taps according to the MMSE criterion can be written as

$$\mathbf{c}_k^{FSTF} = \mathbf{R}_{yy}^{-1} \mathbf{r}_{ay}, \quad (3.15)$$

where  $\mathbf{R}_{yy}$  is an  $N_c \times N_c$  Hermitian covariance matrix  $E\{\mathbf{y}_k^* \mathbf{y}_k^T\}$ , and  $\mathbf{r}_{ay}$  is an  $N_c$ -element cross-correlation vector  $E\{\mathbf{y}_k^* a_k\}$ . When the data sequence  $\{a_k\}$  is uncorrelated and has unit power, the elements of the covariance matrix  $\mathbf{R}_{yy}$  and those of the cross-correlation vector  $\mathbf{r}_{ay}$  can be expressed as

$$\mathbf{R}_{yy_{i,j}} = \sum_k h^* \left( kT_s - \frac{iaT_s}{b} \right) h(kT_s - jaT_s/b) + N_0 \delta_{i,j}, \quad (3.16)$$

and

$$\mathbf{r}_{ay_i} = h^*(-iaT_s/b). \quad (3.17)$$

The MSE achieved by this sub-optimal receiver is given by

$$\sigma_{MSE}^2(FSTF) = 1 - \mathbf{r}_{ay}^H \mathbf{R}_{yy}^{-1} \mathbf{r}_{ay}. \quad (3.18)$$

Although the mathematical expressions of a finite-length FSTF is quite similar to that of a  $T_s$ -spaced transversal MMSE filter (*c.f.* Eq. (3.13) and Eq. (3.18)), it is interesting to note several important differences which lead to significant performance improvement of an FSTF.

- Firstly, the fixed-filter  $g_{rcv}(t)$  is not necessary for an FSTF-based receiver because the fractional spaced filter also plays the role of a matched filter. The FSTF is capable of matching the transmission channel, resulting in an improvement of the SNR on the receiver side, whereas a  $T_s$ -spaced transversal filter cannot perform in the same way because of aliasing problem.
- Secondly, thanks to the elimination of aliasing, an FSTF can compensate for the sampling phase. Hence, the performance of an FSTF does not depend on the sampling phase on the receiver side. On the contrary, in a  $T_s$ -spaced transversal filter, at the input of the equalizer, the receiver sampling phase already results in an amplitude fluctuation in the signal spectrum. The equalizer cannot recover the phase information to compensate for. Hence, the equalizer performance strongly depends on the sampling phase.

### 3.2.3. Non-linear equalizers

So far several conventional linear equalizer structures have been investigated. The ZF equalizer is proved to be very sensible to noise amplification due to a channel frequency response inversion. By minimizing the MSE of the equalized signal, an MMSE equalizer performs better than a zero forcing one. However, from Eq. (3.6) it is obvious that the performance of such an equalizer is poor in severely selective frequency channels. One solution to further improve the BER performance of an MMSE equalizer is to use nonlinear equalizers. In this section the structure of a DFE and that of a MLSE are investigated. Thanks to a data feedback which compensates for postcursor ISI without amplifying the receiver noise, a DFE performs better than zero forcing or MMSE equalizers. Despite a complex receiver structure, an MLSE preceded by a white-matched filter is proved to be an optimal receiver [69].

#### 3.2.3.1. Decision feedback equalizer

This section starts with the structure of infinite-length equalizers, then practical equalizer structures are discussed.

### 3.2.3.1.1. Predictive decision feedback equalizer

Starting from an MMSE linear equalizer (*c.f.* section 3.2.2.2), the power spectrum of total distortion (noise and residual ISI) can be expressed as

$$|E(f)|^2 = \frac{N_0}{N_0 + S_q(f)}. \quad (3.19)$$

From Eq. (3.19) it is clear that the distortion is white only when  $S_q(f)$  is a constant. In this case the MSE cannot be further improved. In general this is not the case because of a frequency selective channel. Therefore, MSE improvement of an MMSE linear receiver is possible. The idea of a predictive DFE is that, supposing that transmitted past samples are known on the receiver side (these samples can be detected by hard decision), interference caused by them can be estimated by a linear prediction. The estimated ISI is then subtracted from a current sample to eliminate the residual ISI. The structure of a predictive DFE is illustrated in Figure 3.5. Firstly, a received signal is filtered by a matched filter followed by an MMSE  $T_S$ -spaced transversal filter. The residual ISI in an equalized signal is then eliminated by a feedback filter, which is optimized in order to minimize the final MSE.

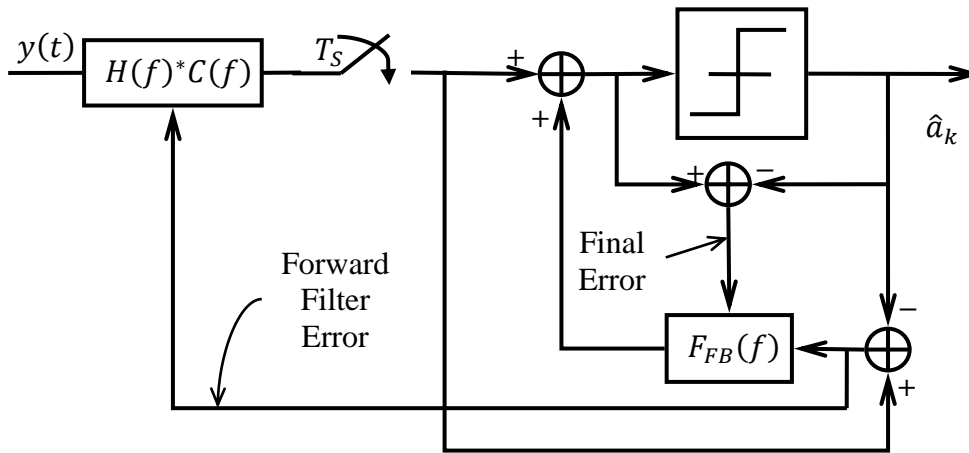


Figure 3.5 – Predictive decision feedback equalizer structure.

The optimal frequency response  $F_{FB}(f)$  of the feedback filter can be expressed as

$$F_{FB}(f) = \frac{\Lambda(f)}{\Lambda_0} - 1, \quad (3.20)$$

where  $\Lambda(f)$  denotes the causal component of the spectral factorization of the inverse of the error spectrum  $|E(f)|^2$  and  $\Lambda_0$  is the average value.

$$\Lambda(f)\Lambda^*(f) = 1/|E(f)|^2. \quad (3.21)$$

In this case the achievable MSE is expressed as

$$\sigma_{MSE}^2(DFE) = 1/|\Lambda_0|^2. \quad (3.22)$$

### 3.2.3.1.2. Conventional decision feedback equalizer

The structure of a conventional DFE is illustrated in Figure 3.6. When the length of the forward filter and that of the feedback filter are not constrained, the structure of a conventional DFE and that of a predictive DFE are proved to be equivalent. In this case the forward filter in Figure 3.6 can be expressed as [79]

$$W(f) = H^*(f)C(f)\{1 + F_{FB}(f)\}. \quad (3.23)$$

It is noted that in a predictive DFE, forward filter errors are fed into the feedback filter, whereas in the conventional DFE detected data are fed. However, the final MSE is the same for the two DFE structures.

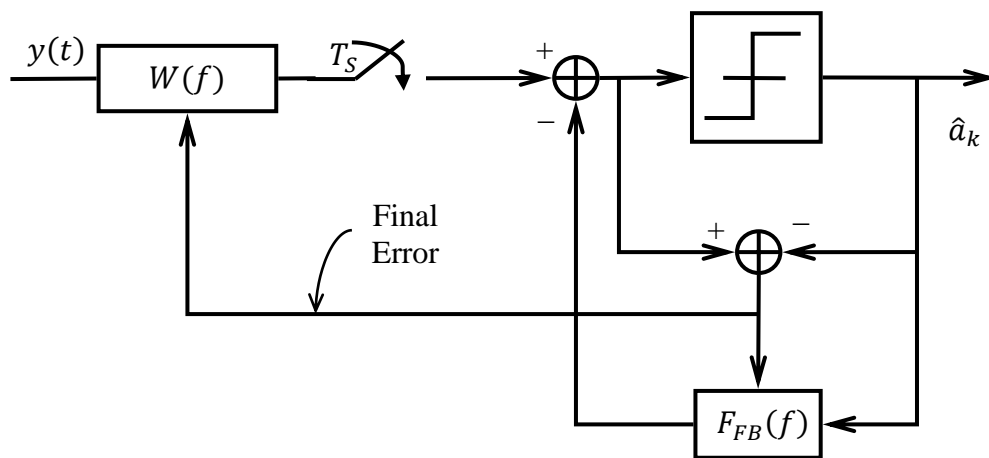


Figure 3.6 – Conventional decision feedback equalizer structure.

### 3.2.3.2. Maximum likelihood sequence estimation

Also since the distortion after an MMSE as shown in Eq. (3.19) is not white in a frequency selective channel, memoryless detection is not optimal. Conventional MLSE techniques use the rule of maximum *a posteriori* probability in order to maximize either the probability of correctly detecting each transmitted symbol or the probability of correctly detecting the entire transmitted sequence. Classical MLSE receivers consist of  $m^{l_m}$  matched filters, where  $m$  denotes the data symbol alphabet size and  $l_m$  is the transmitted sequence length. Each filter corresponds to one sequence among  $m^{l_m}$  possible transmitted sequences. Supposing that the time synchronization is perfect, the outputs of these filters form a set of sufficient statistics for the optimal sequence detection. However, the complexity of such a receiver is prohibitive since it exponentially grows with the message length.

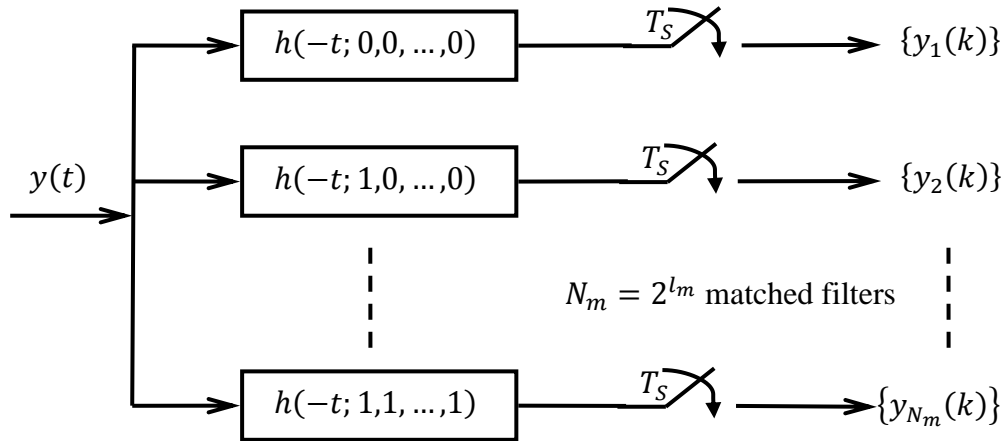


Figure 3.7 – Sufficient statistic illustration for an OOK transmission.

D. Forney showed in [69] that if the receiver filter is a Whitened Match Filter (WMF), its symbol-rate output at perfect timing points also forms a set of sufficient statistic. The transmission system between the data source and the MLSE detector can be considered as a causal discrete channel. Hence, sequence estimation can be carried out with the Viterbi algorithm in order to reduce the receiver complexity. The optimal receiver structure hence consists of a matched filter, a symbol-rate sampling, a symbol-rate noise-whitening filter and a Viterbi-based sequence estimator. In this case the complexity is in the order of  $m^{K-1}$  where  $K$  denotes the number of terms of the equivalent discrete channel impulse response. In practice one cannot design beforehand a receiver filter that matches various channel responses. In addition, in either radio or fiber-based optical transmissions, the channel is in general time-varying. Hence, an adaptive algorithm is necessary to adapt the receiver filter to the channel response. However, it is difficult to implement such a white matched filter due to the constraint of causal ISI after filtering [79].

In the literature, the problem of adaptive filtering in an MLSE-based receiver can be approached by using an FSTF, which can be able to play at the same time the role of a matched filter and the role of a symbol-rate transversal filter. Under the MMSE criterion, the filter taps of such a receiver can be easily adapted by using the LMS method. This is discussed in more details in the next section. Supposing that  $g(t)$  is the desired equivalent channel impulse response with respect to which the MSE is minimized, the FSTF frequency response can be written as

$$W(f) = \frac{H^*(f)G(f)}{N_0 + S_q(f)}. \quad (3.24)$$

From Eq. (3.23) and Eq. (3.24) it is noted that if the desired channel frequency response  $G(f)$  is chosen such that  $G(f) = 1 + F_{FB}(f)$ , then the FSTF can be recognized as the receiver filter in an infinite-length DFE. The structure of such an MLSE receiver is illustrated in Figure 3.8.

It is interesting to note that at high SNRs ( $N_0 \ll S_q(f)$ ), from Eqs. (3.19), (3.20), (3.21) and (3.24) the noise spectrum at the output of the FSTF can be expressed as

$$N_0 S_q(f) \frac{|G(f)|^2}{[N_0 + S_q(f)]^2} \approx \frac{N_0}{|\Lambda_0|^2} \cdot \quad (3.25)$$

Obviously, the noise becomes white after the filtering by the FSTF. Hence, at high SNR this MLSE receiver structure approaches the optimal receiver structure proposed by Forney, where the error sequence after the MLSE is white and the mean square value is equal to the matched filter bound.

In practice, the forward and the feedback filter length cannot be infinite. Hence, a suboptimal receiver can be deduced by fixing the filter length. Moreover, the filter taps can be adapted by the LMS method so that the MSE at the input of the decision block is minimized.

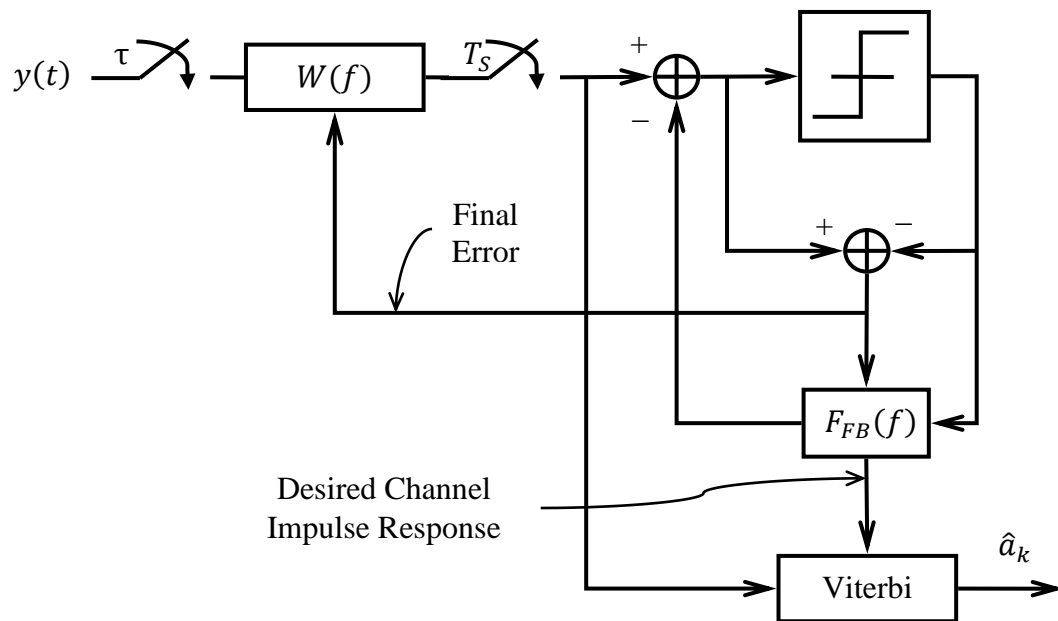


Figure 3.8 – MLSE receiver developed via DFE.

### 3.2.4. Automatic synthesis

So far the structures of conventional equalizers have been investigated. The receiver filter plays a major role in these structures because it matches the channel response, resulting in a maximized SNR. In the case of an FSTF, the receiver filter plays also the role of a symbol-rate transversal equalizer. As mentioned along the chapter, adaptive algorithm (or automatic synthesis) is necessary because the channel response is different *w.r.t* different users and is time-varying. Except the ZF equalizer, the other equalizers always try to minimize the MSE. Because the MSE is a quadratic function of the filter coefficients, one of the most common tap adjustment methods is the LMS method, which consists in updating the filter taps after each symbol interval.

The coefficient adjustment is composed of two stages: a training stage and a decision-piloting stage. During the training stage, a training sequence, which is known by the receiver, is transmitted. According to the value of the square error, the filter coefficients can be adjusted. In general, in the decision-piloting stage the MSE is relatively small. Hence, the transmission BER is also small. So even if the receiver doesn't know the

transmitted data sequence, it can use the detected symbols to adjust the filter taps. This also gives the name “decision-piloting” stage. Figure 3.9 shows a general automatic synthesis scheme. The filter taps  $c_k$  are adjusted by using the square error calculated by the training sequence during training stage and by the detected data sequence during the decision-piloting stage. In the next paragraphs tap adjustment methods are discussed.

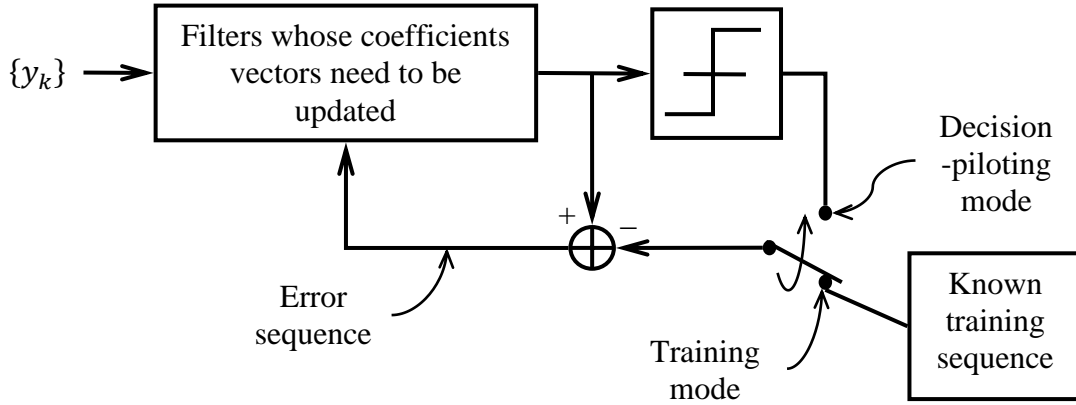


Figure 3.9 – Automatic synthesis scheme.

#### 3.2.4.1. Deterministic gradient algorithm

The filter coefficient vector  $c_k$  are updated every symbol time with the expression below

$$c_{k+1} = (I - \mu R_{yy} r_{ay}) c_k + \mu r_{ay}, \quad (3.26)$$

where  $I$  denotes an identity matrix.  $R_{yy}$  and  $r_{ay}$  denote the covariance matrix and the cross-correlation vector described in section 3.2, respectively.  $\mu$  denotes the adjusting step size, which directly influences the convergence speed and the excess MSE of the adjusting algorithm [79]. The method is called deterministic because the gradient of the MSE is calculated as a function of the covariance matrix and the cross-correlation vector without any approximation. However, this technique is not practical since the channel characteristic is not always available on the receiver side.

#### 3.2.4.2. Stochastic gradient algorithm

When compared to the previously described method, the stochastic gradient algorithm is more practical because in this case the MSE gradient is estimated by  $\mathbf{y}_k^* (\mathbf{y}_k^T c_k - a_k) = \mathbf{y}_k^* e_k$ . And the filter coefficients can be adjusted by the following expression

$$c_{k+1} = c_k - \mu \mathbf{y}_k^* e_k, \quad (3.27)$$

where  $\mathbf{y}_k$  denotes the equalizer input signal vector.  $a_k$  denotes the transmitted data symbol, which can be either the training data or the detected data symbol, and  $e_k$  is the error at the equalizer output.

### 3.3. Optical IMDD receiver design

According to conventional linear and nonlinear equalizers used in radio transmissions to combat a frequency selective channel, in this section some practical equalizers which can be used for optical IMDD OOK NRZ transmissions are discussed. The section starts with the simplest transversal structure.

#### 3.3.1. Finite-length fractionally spaced transversal filter

The  $T_S$ -spaced transversal filter is not considered for two reasons. Firstly, it cannot be used as a matched filter. Hence, the SNR on the receiver side cannot be maximized. Secondly, its performance strongly depends on the receiver sampling phase. On the other hand, by using the least square method, the FSTF coefficients converge so that the filter can be at the same time a matched filter and a  $T_S$ -spaced transversal equalizer. In the context of an OOK NRZ transmission where the signal spectrum is two times as large as the transmission bit rate, the received signal can be oversampled by a factor of two for a complexity-performance compromise. The figure below illustrates the equalizer half-symbol delayed line structure.

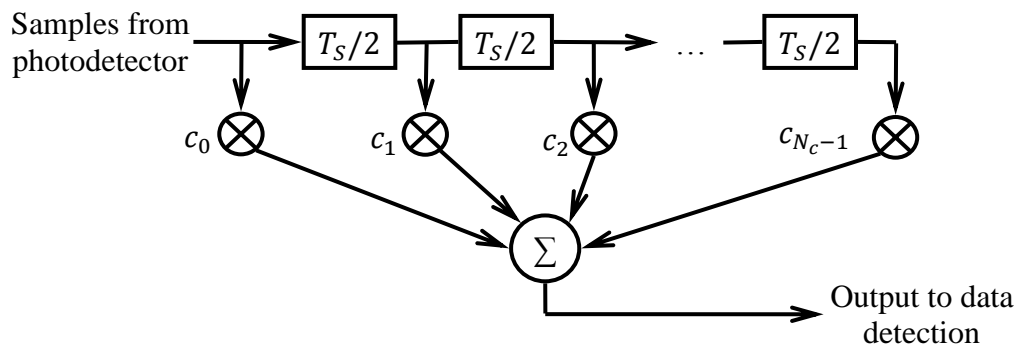


Figure 3.10 – Finite-length fractionally spaced transversal equalizer structure.

It might be noted that although the tap-delayed line is half symbol time, the filter coefficients are still updated at symbol-time rhythm. Due to the symmetric nature of chromatic dispersion, the initial filter coefficient vector is also symmetric. This can be carried out by setting the central tap to unity and the others to zero.

It is noted that in an optical IMDD transmission, the ISI is not linear due to laser chirps, chromatic dispersion and the power-law detection of a photodiode. Hence, the equalizer performance is very limited, especially when the value of laser linewidth enhancement factor is large and/or in relatively long transmissions. Some authors proposed to compensate not only the linear interference but also the pair-wise interference. However, the performance improvement is still limited.

#### 3.3.2. Non-linear receivers

With respect to the criterion of minimum SER, the MMSE linear receiver is optimum only when the channel does not present any amplitude distortion [79]. In practice, this is usually not the case because of frequency-dependent attenuation due to chromatic

dispersion. It is also shown in the literature that the performance of a linear receiver can be improved by nonlinear structures which are described in the following paragraphs.

**3.3.2.1. Finite-length FSTF followed by finite-length DFE**

The performance of an FSTF can be further improved by a decision feedback filter illustrated in Figure 3.11. In this equalizer structure the FSTF compensates for precursor interference (comes from the bits in the future) and the feedback filter compensates for postcursor interference (comes from the bits in the past). The LMS method is applied for adjusting the coefficients of the two filters in order to minimize the overall MSE. In this case the initial coefficients vector of the FSTF is not symmetric. Actually, the last tap ( $c_{N_c-1}$ ) is set to unity and the others are set to zero. As for the feedback filter, the initial vector can be set to zero.

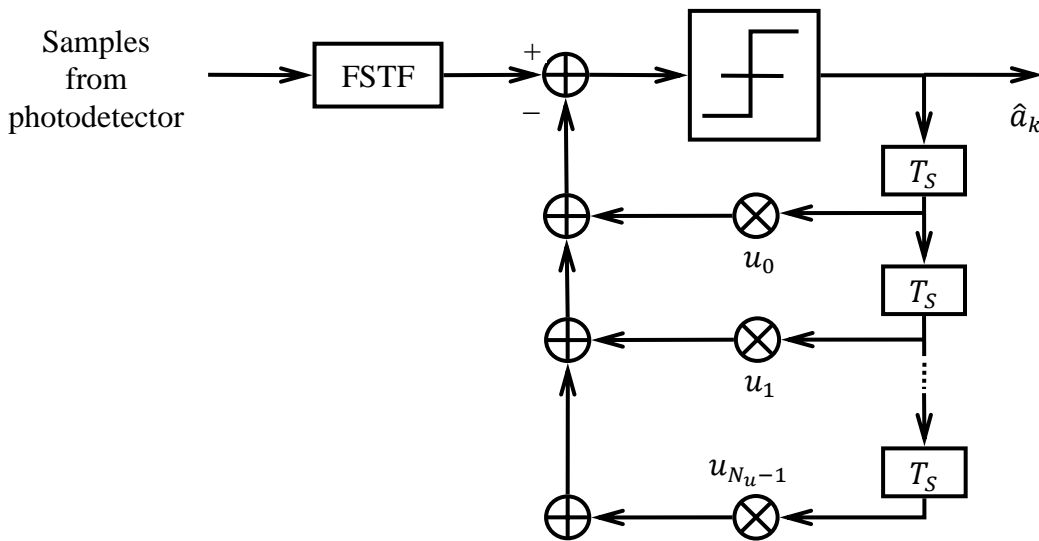


Figure 3.11 – Finite-length fractionally spaced transversal filter with decision feedback equalizer.

**3.3.2.2. Finite-length FSTF followed by Viterbi-based MLSE**

A suboptimal MLSE structure can be deduced from the optimal one proposed by Forney by using truncated FSTF and DFE as illustrated in Figure 3.12. The LMS adjustment method is used to minimize the MSE at the input of the decision block. When the filter taps converge, the FSTF produces a signal sequence with quasi-causal ISI at the input of the Viterbi block. The branch metrics of the Viterbi algorithm can be built by using either the desired impulse response from the feedback filter taps or by histogram method or estimation method [75].

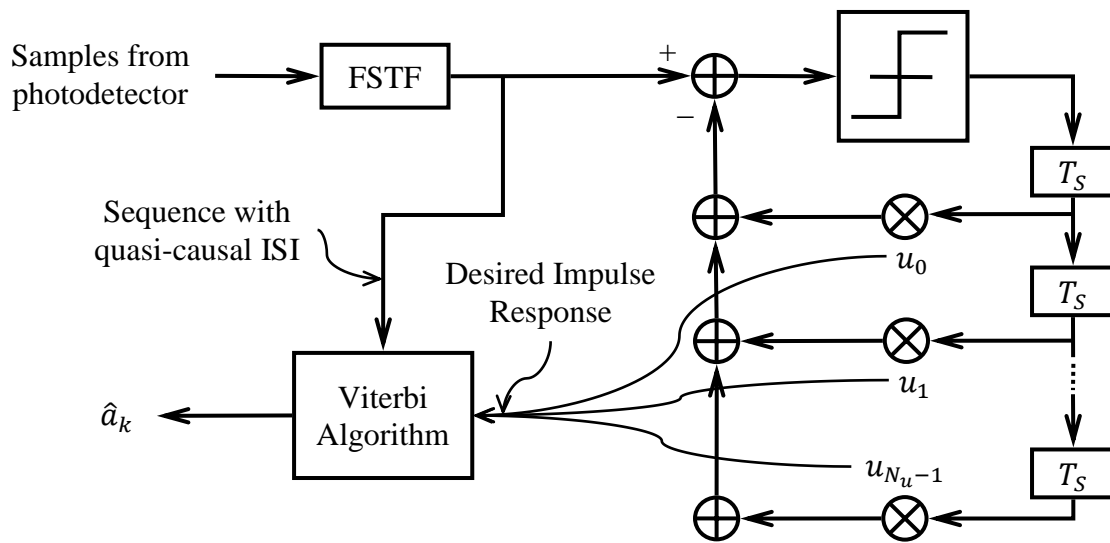


Figure 3.12 – Finite-length FSTF with Viterbi-based MLSE.

### 3.3.2.2.1. Branch metric construction by using desired impulse response

Ideally speaking, in this structure of MLSE receiver, the forward filter should eliminate all the precursor interference. Because the MSE at the input of the Viterbi block is minimized with respect to the output of the feedback filter, the interference in the input of the Viterbi algorithm is causal and its value can be estimated by the feedback filter taps. In this case the feedback filter plays the role of a discrete equivalent channel impulse response.

It is important to note that this technique only gives a good performance for linear channel. In an optical IMDD transmission where the channel is not linear, a linear model might not correctly estimate the branch metric value. In addition, the ringing effect during a bit transition due to laser chirp cannot be considered as a linear effect.

### 3.3.2.2.2. Branch metric construction by using histogram method

In this technique the histogram method [75] is used to estimate the PDF of the branch metrics used in Viterbi algorithm. Due to the data-dependent characteristic of the photodiode shot noise and the PM-to-AM noise [25]–[27], an estimate of the Probability Distribution Function (PDF) of each state transition is more suitable than the Desired Impulse Response (DIR) method. However, to obtain accurate estimates of the PDF of a branch in the trellis diagram, a large number of training samples is needed. This is particularly problematic in the tail regions of the PDF. In the context of access network where no inline optical amplifier is used, the photodetector thermal noise is usually found to be dominant. Hence, we propose to model each state transition in the trellis diagram by a random Gaussian variable whose mean and variance values can be estimated via training samples. In order to adapt the estimated PDFs to a time-varying channel, the mean and variance values of the histogram can be continually updated with detected symbols. According to simulation results, we found that the MLSE method give the best BER performance when compared to the FSFE and the DFE at the expense of increased receiver complexity.

### 3.4. Performance comparison in optical IMDD transmissions

#### 3.4.1. Simulation parameters and set-up

In this chapter 10-Gb/s transmissions over single mode fiber are analyzed. For the laser modeling, the large-signal model described in Chapter 2 is used. The laser is biased with a 60-mA DC current. The corresponding laser adiabatic frequency is equal to 2.1 GHz. This biased point is chosen as the middle point of the linear zone of the P-I transfer curve. The coupled optical power is chosen to be equal to 10 dBm so that acceptable BER performance ( $BER < 10^{-3}$ ) is still guaranteed in relatively long distance ( $L > 80$  km). For characterizing the photodetector, the receiver sensitivity is chosen to be equal to -20 dBm (corresponding to an OOK NRZ transmission operating at  $10^{-9}$  BER), which is a typical value of a PIN-based photodetector. For both NRZ and Nyquist waveforms, the laser power is limited at values corresponding to the bias current values of 30 mA and 90 mA (saturation threshold). The corresponding laser extinction ratio is hence equal to 8 dB. In NRZ transmissions the spectral efficiency is 1 bit/s/Hz. In OOK Nyquist transmissions, the roll-off factor is chosen to be equal to 0.25, resulting in spectral efficiency of 1.6 bit/s/Hz. In NRZ transmissions after the photodetector a low-pass filter having 10-GHz cutoff frequency is used to filter the out-of-band noise. When the Nyquist pulse-shape is used, the receiver filter is replaced by a square-root raised cosine filter.

#### 3.4.2. Optimum number of FSTF and feedback filter taps

Figure 3.13 shows required received optical power to obtain a  $10^{-3}$  BER as a function of the number of FSTF taps in OOK NRZ transmissions. After 50 km, increasing the number of taps from 3 to 11 improves the receiver sensitivity by 3 dB. However, with a one-tap feedback filter the optimal number of FSTF taps is reduced to 7. In short transmissions the feedback filter does not further improve the performance of an FSTF because ISI is still not severe and the DFE suffers from error propagation. It is shown in Figure 3.14 that the receiver sensitivity is improved by 1 dB by increasing the number of feedback filter taps from 1 to 2. Further increase does not improve the performance. Hence, for a DFE, 2 taps are a good compromise between the performance and the complexity.

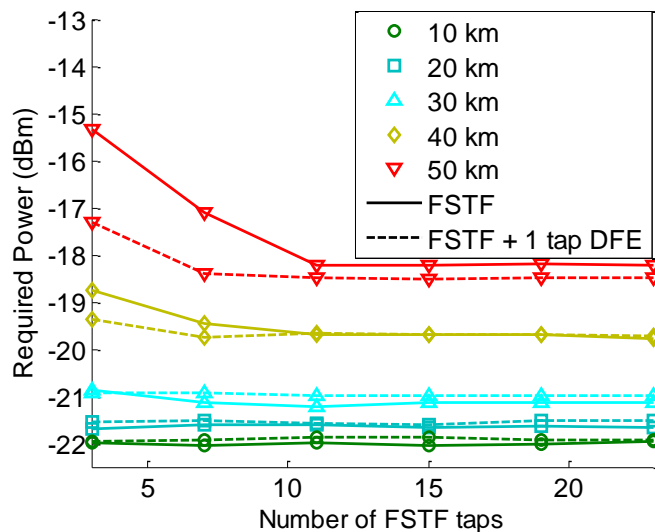


Figure 3.13 – Required optical power as a function of FSTF taps. Laser linewidth enhancement factor is 1.

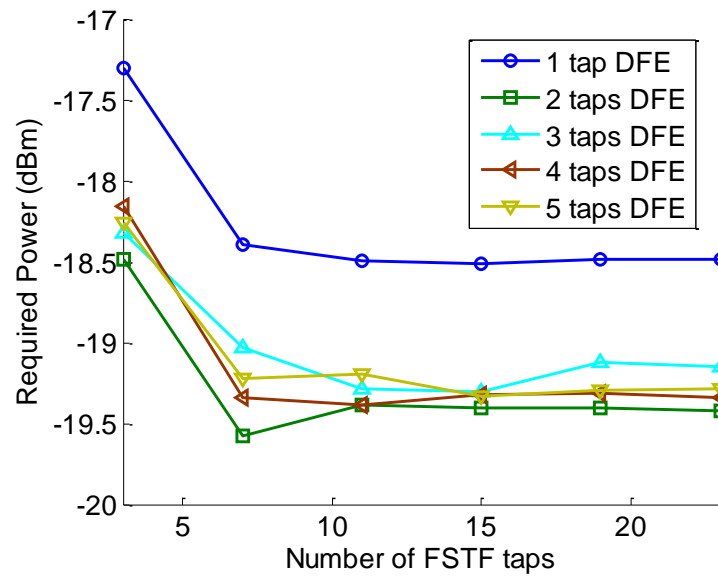


Figure 3.14 – Required optical power as a function of feedback filter taps. Fiber length is 50 km. Laser linewidth enhancement factor is 1.

### 3.4.3. Required optical received power versus transmission distance

Required received optical power at  $10^{-3}$  BER as a function of transmission distance of different equalization schemes is illustrated in Figure 3.15. It is noted that when fiber length increases, the ISI becomes more severe. The DFE improves the transmission reach by 25 km when compared to a single FSTF scheme. Moreover, the MLSE scheme further extends the reach by 25 km. However, all the classical equalization schemes for NRZ transmissions have a limit in terms of transmission reach because of an error floor. When the Nyquist waveform is used, the signal spectrum is reduced by a factor of  $2/(1 + \alpha_{rof})$ , resulting also in a reduced noise power on the receiver side. In addition, the impact of chromatic dispersion on a transmitted signal waveform is reduced thanks to a reduced signal bandwidth. As a consequence, in general the Nyquist pulse shaping increases the transmission reach by tens of kilometers and decreases the power penalty by 2 dB when compared to the classical rectangular pulse shaping technique.

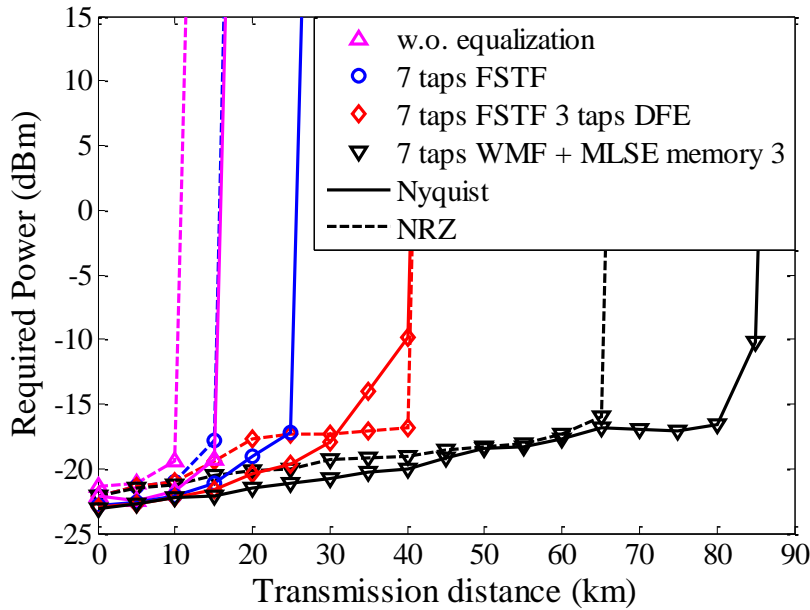


Figure 3.15 – Required power versus reach comparison. Laser linewidth enhancement factor is 2.68.

In both OOK NRZ and Nyquist transmissions, the power penalty strongly increases with fiber length. For example, in the best configuration which is the Nyquist waveform in combination with an MLSE equalizer, the power penalty is still up to 5 dB when fiber length increases from 0 km to 80 km.

#### 3.4.4. Required optical received power versus alpha factor

In an optical IMDD transmission, the BER performance depends not only on transmission distance but also on laser chirps. Indeed the channel frequency response depends on the interplay between these factors. By fixing the fiber length at 30 km, Figure 3.16 presents the required optical power at  $10^{-3}$  BER as a function of linewidth enhancement factor (or alpha factor). As the alpha factor increases, ISI becomes more severe, resulting in increased required optical power for the same BER. It is found that the performance of any conventional equalization scheme is strongly degraded by the laser chirps. Even with a very complex MLSE scheme, the power penalty of an NRZ transmission increases by 3 dB when the alpha factor increases from 0 to 2.5. We have also found that the Nyquist pulse shaping improves transmission robustness against laser chirps. Up to 2 dB power penalty reduction is also observed when compared to the conventional NRZ pulse shaping.

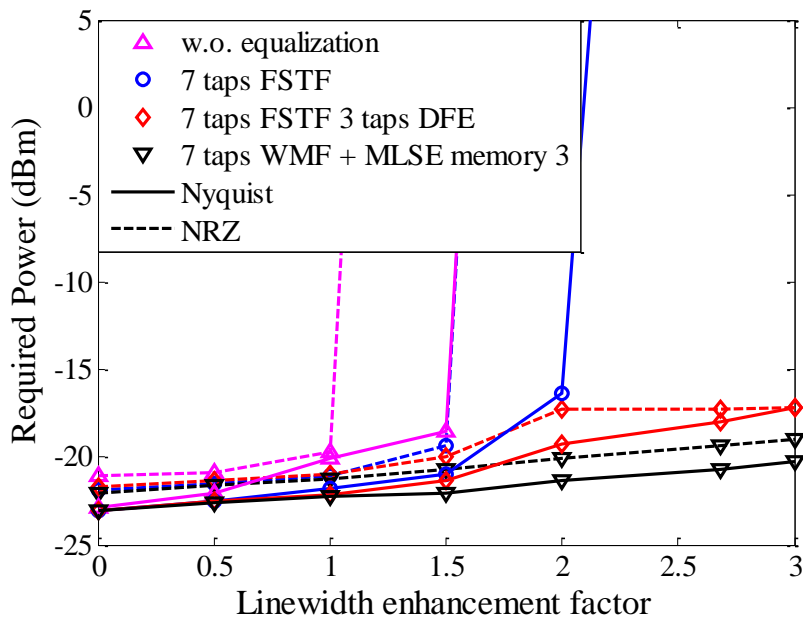


Figure 3.16 – Required power versus laser linewidth enhancement factor. Fiber length is 30 km.

### 3.5. Conclusion

In high-bit-rate and/or long transmissions, the BER performance of a classical NRZ pulse-shaping is strongly degraded due to accumulated chromatic dispersion and laser chirps. Channel equalization is required to improve the performance and to extend the transmission reach. Throughout this chapter we have investigated the structure and the performance of conventional linear and nonlinear equalization techniques. In the context of access networks, 7-tap FSTF and 2-tap feedback filter are found to be a good compromise between receiver complexity and BER performance. The BER performance is significantly improved with an MLSE at the expense of an increased receiver complexity. For this technique, the channel memory of 3 bits is found to be sufficient to model the equivalent discrete channel. For the construction of metric branches for the Viterbi algorithm, the histogram method is proved to be more relevant than the method based on DIR because of channel nonlinearities. When compared to the NRZ pulse-shaping technique, the Nyquist pulse-shaping technique improves the chromatic dispersion-induced power penalty up to 2 dB at  $10^{-3}$  BER and the transmission reach can be extended by tens of kilometers, which corresponds to an increase of about 20%.

However, even with a complex MLSE receiver, the interplay between chromatic dispersion and laser chirps still strongly penalizes the transmission performance. In the context of access network, with a conventional DFB laser whose linewidth enhancement factor is in the order of 3, the power penalty is up to 5 dB when transmission distance increases from 0 km to 80 km. We could hope for a better solution to combat a frequency selective channel. Indeed, in the next chapter, we propose and analyze an alternative scheme based on a multi-carrier modulation as Orthogonal Frequency Division Multiplexing.



### 4.1. Introduction

In the previous chapter, the impact of an IMDD channel on the performance of conventional OOK NRZ transmissions has been analyzed. Conventional equalization techniques have also been reported. In the time domain, the interplay between chromatic dispersion and laser chirps closes the “eye” of a transmitted signal, resulting in an increased BER. Due to the impact of nonlinearities in an IMDD channel, conventional equalization schemes have limited performance. Even with a complex MLSE receiver, power penalty remains important when the value of fiber length and/or that of laser linewidth enhancement factor increase.

Before discussing an alternative technique dealing with ISI problem, let’s have a closer look on what happens in the frequency domain when a signal propagates through a DML-based IMDD channel.

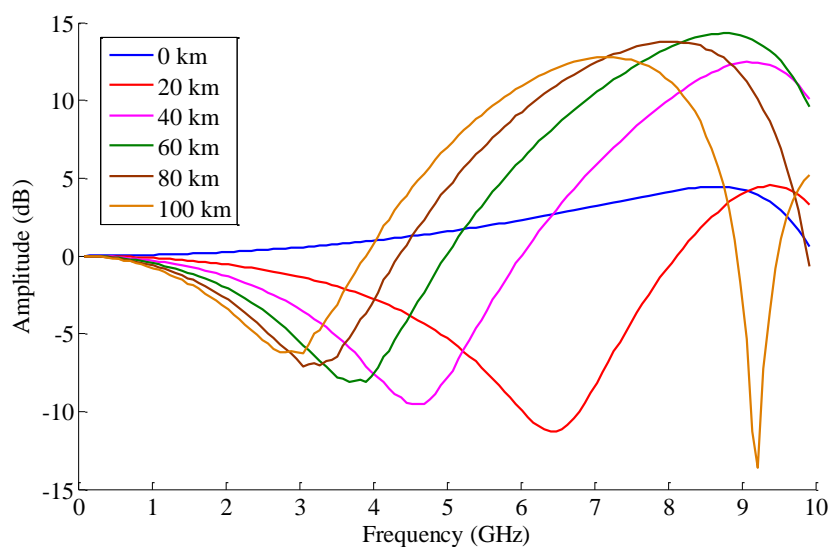


Figure 4.1 – Small-signal IMDD channel response as a function of transmission distance. Laser linewidth enhancement factor is 2.68. Laser adiabatic chirp frequency is 2.1 GHz. Injected optical power is 0 dBm.

Figure 4.1 illustrates the small-signal channel frequency response as a function of fiber length. In a DML-based IMDD system, a transmitted signal is double-side-band because the laser driving signal is real-valued. On the receiver side, dispersion-induced phase change of a positive frequency component is different from that of the corresponding negative frequency component. Under direct detection performed by a photodiode, signal-carrier beats can be constructive or destructive depending on these phase changes [34]–[36]. This results in the frequency-dependent attenuation of the channel frequency response.

In practice, the “small-signal” condition might not be satisfied because transmitted electrical signal power should be large in order to compensate for fiber attenuation. When the laser is driven by a large-band signal and large modulation index is used, nonlinear high-order harmonics can be generated. In addition, PM-to-AM conversion noise power is also proved to be frequency-dependent [25]. When a multicarrier modulation is used, the FWM-induced noise power also varies as a function of frequency [80]. However, the frequency selectivity characteristic of an IMDD channel is still present in a large-signal modulation [81]. Moreover, because of strong resistance against channel frequency selectivity, OFDM modulation has earned its success in various transmission systems including radio and wire-line communications. OFDM modulation is a key technique in various standards such as the LTE, Digital Video Broadcasting – Terrestrial (DVB-T), WIFI and Digital Subscriber Line (DSL).

Despite this success, OFDM modulation has only gained the attention in the optical communication community recently. According to recently reported research, the performance of an OFDM modulation in the context of optical IMDD transmissions is very encouraging. In [11] an Adaptive Modulation Optical (AMO) OFDM modulation is shown to be an excellent cost-effective solution for short-reach and metropolitan optical transmissions since the OFDM modulation has high spectral efficiency and the chromatic dispersion of the fiber link can be easily compensated with simple frequency-domain equalization and adaptive modulation. Moreover, the OFDM modulation makes a transmission system very flexible and robust against chromatic dispersion thanks to the parallel transmission of narrowband subcarriers. The discrete Levin-Campello (LC) bit/power loading technique [82], which is shown to bring a quasi-optimal solution of water-filling technique and is widely implemented in DSL systems, has also been shown to give excellent performance in optical IMDD transmissions [42], [83]. In [42] a 12.5-Gb/s AMOOFDM transmission is proved to be possible over more than 20-km SMF links with low-cost DFB and VCSEL laser intensity modulators and a 2.5-GHz-bandwidth PIN-based photodetector. These results show the great potential of such a modulation scheme for future generations of PONs.

In the first part of this chapter, the fundamental of an OFDM modulation is summarized. Although extensive studies of various AMOOFDM schemes in the context of IMDD transmissions are available thanks to the works reported in [81], the second part of this chapter still gives a closer look at the discrete Levin-Campello bit/power loading technique, which has been shown to be the optimum discrete bit/power loading technique. In the second part of this chapter, a novel rate adaptive OFDM modulation scheme based on symbol precoding is proposed and analyzed. The proposed system is shown to strongly reduce the power consumption of a conventional AMOOFDM system, while preserving all the advantages of such a system. A comparison in terms of power penalty versus reach and laser chirp between conventional OOK and the proposed precoded OFDM systems is also given at the end of the chapter. Thanks to this comparison, the potential of the OFDM modulation in optical access networks is more clearly revealed.

## 4.2. OFDM modulation

Let's come back to the response of a frequency selective channel illustrated in Figure 4.1. One of the reasons explaining the success of an OFDM modulation in various transmission systems might come from a well-known idiom “don't put all your eggs in one basket”. In telecommunication language, this idiom can be translated as “don't put all your data on a single carrier”. Otherwise, when the channel condition *w.r.t* the carrier is severe, you risk losing all the data. More concretely, when a large-band signal is carried by a single carrier, ISI problem arises because of a frequency selective channel according to the Nyquist theorem. The impact of this ISI has already been discussed in the previous chapter. The idea of the OFDM modulation is that, instead of transmitting a single-carrier large-band signal, an OFDM modulator uses a large number of orthogonal subcarriers. Each subcarrier carries a relatively narrow-band signal. By this way the channel response *w.r.t* each subcarrier can be consider flat. Hence, the problem of ISI can be eliminated.

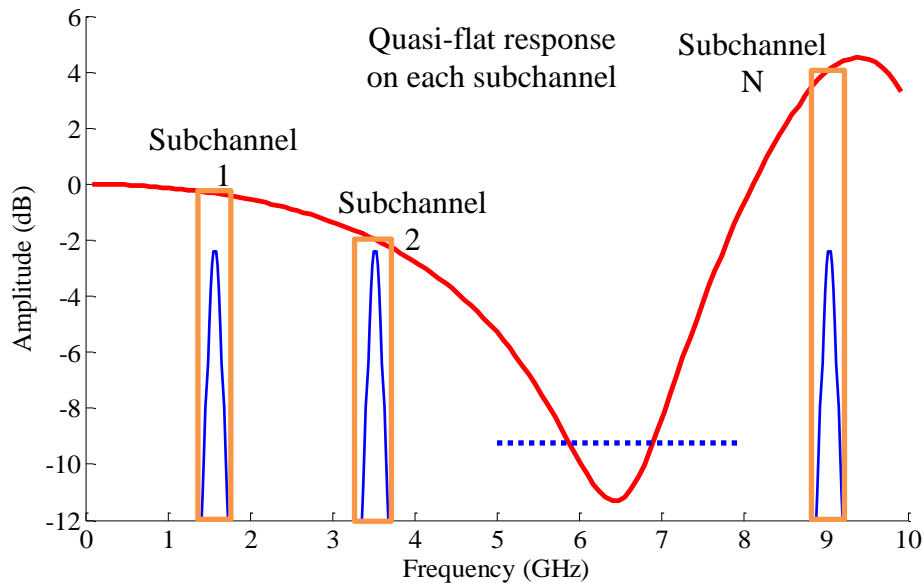


Figure 4.2 – Illustration of parallel sub-channel transmission. For each sub-channel, ISI is negligible because the channel response is quasi-flat.

### 4.2.1. OFDM modulation/demodulation principle

Theoretically, an OFDM signal can be expressed as

$$x(t) = \sum_{n=0}^{N-1} \sum_{k \in \mathbb{Z}} X_n^k g(t - kNT_s) \exp(j2\pi f_n t), \quad (4.1)$$

where  $g(t)$  denotes the pulse-shaping filter impulse response.  $X_n^k$  is a data symbol corresponding to the  $k^{th}$  OFDM symbol and  $n^{th}$  subcarrier.  $N$  is the number of subcarriers.  $T_s$  denotes the sampling time and  $f_n$  is the subcarrier frequency. The orthonormal basis functions of the signal space can be expressed as

$$\Phi_{n,k}(t) = g(t - kNT_S) \exp(j2\pi f_n t). \quad (4.2)$$

The subcarriers are orthogonal when the expression below is satisfied

$$\int \Phi_{n,k}(t) \Phi_{n',k'}(t)^* = \delta_{n,n'} \delta_{k,k'}. \quad (4.3)$$

Supposing that the pulse shaping filter impulse response is a rectangular function, when the spectral efficiency is maximized, the subcarrier frequency can be written as [84]

$$f_n = \frac{n}{NT_S}. \quad (4.4)$$

In this case, it is interesting to note that in the frequency domain, an OFDM signal occupies the frequency range  $[-\frac{f_S}{2}, \frac{f_S}{2}]$  where  $f_S = 1/T_S$ . Hence, an analog OFDM signal can be represented by its  $T_S$ -rate discrete signal without aliasing impacts. The corresponding numerical OFDM signal can be written as

$$x_k(m) = \sum_{n=0}^{N-1} X_n^k \exp(j2\pi \frac{nm}{N}). \quad (4.5)$$

According to Eq. (4.5), it is shown that the  $k^{th}$  OFDM symbol is the output of an Inverse Discrete Fourier Transform (IDFT) of the input data symbols. The modulation scheme of an OFDM modulator can be illustrated in the following figure.

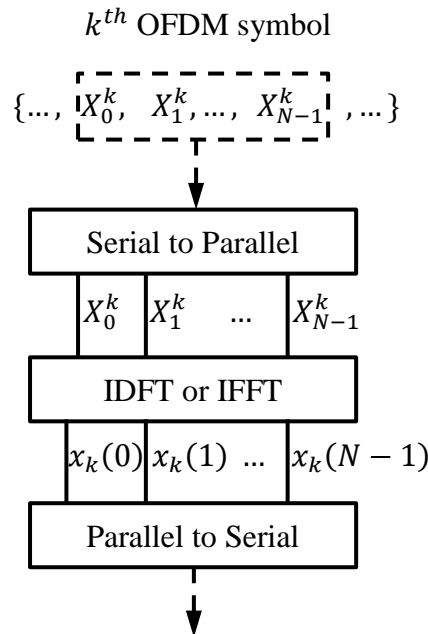


Figure 4.3 – Discrete OFDM signal generation scheme.

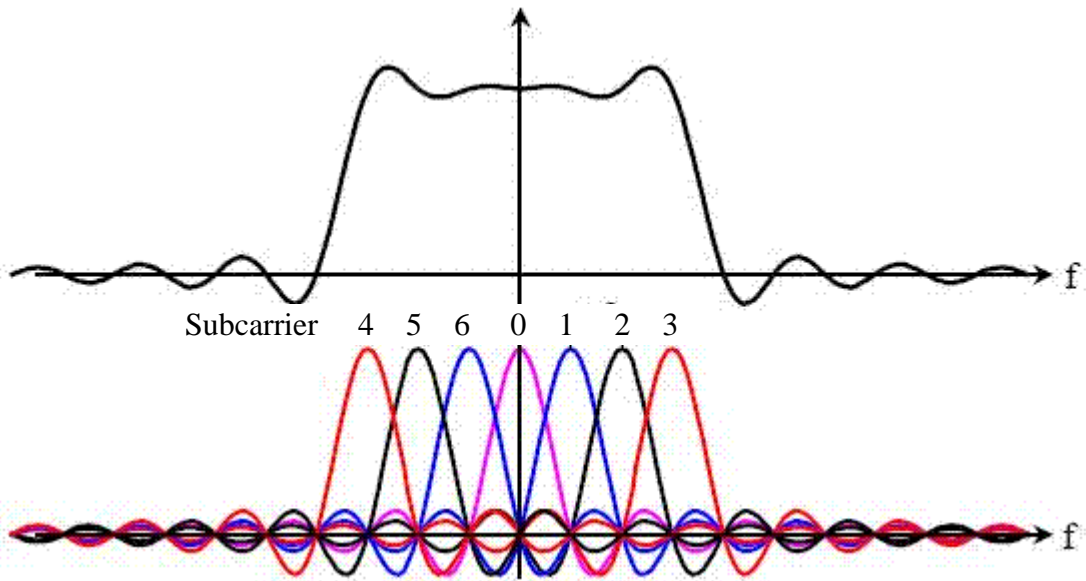


Figure 4.4 – OFDM signal spectrum illustration.

Figure 4.4 illustrates the spectrum of an OFDM signal and the relative frequency position of the subcarriers. Due to the frequency-domain “aliasing” of the subcarriers, the OFDM modulation is interesting for high spectral efficiency. In addition, when the number of subcarriers  $N$  is chosen as a power of two, the IDFT operation can be carried out by means of an Inverse Fast Fourier Transform (IFFT), which strongly reduces multi-carrier modulator complexity. Hence, the complexity challenge of a multi-carrier modulator is solved with an OFDM modulation. On the receiver side, the demodulation can be simply carried out by a  $T_S$ -rate sampling followed by a DFT as shown in Figure 4.5.

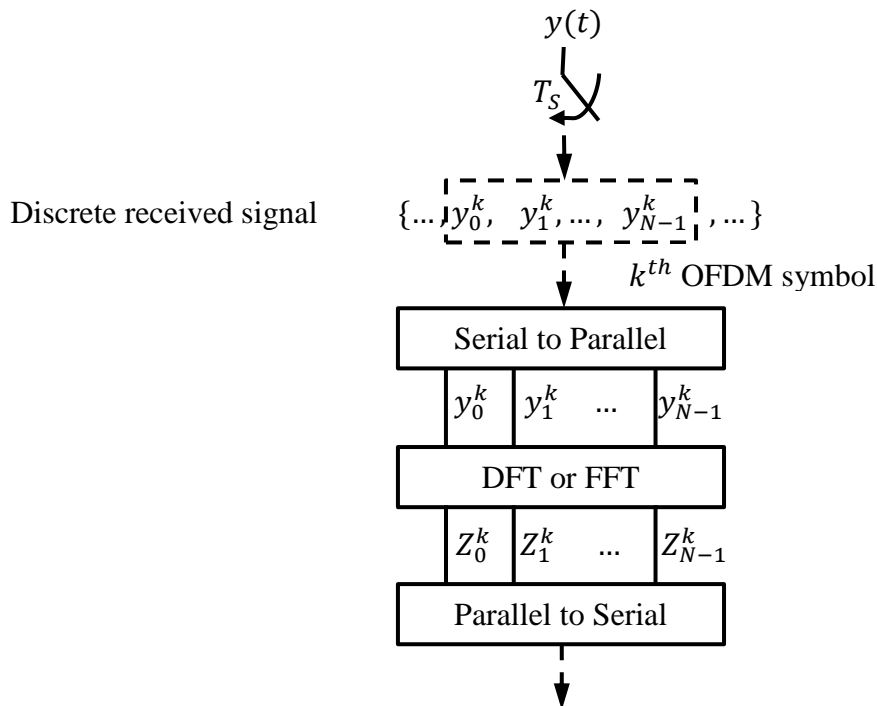


Figure 4.5 – Principal functions of an OFDM receiver.

## 4.2.2. Cyclic prefix – how does it work in an optical IMDD system

### 4.2.2.1. Orthogonality preservation by cyclic prefix in radio transmissions

Until this paragraph the orthonormal bases have been supposed to be unchanged on the receiver side. Hence, by means of an FFT, transmitted data symbols can be demodulated without ICI. In practice, the orthonormal bases change under the impacts of a transmission channel. In general, on the receiver side these functions are no longer orthogonal, resulting in ICI. In addition, when the channel is dispersive, ISI<sup>4</sup> can also be generated.

In radio communications, ICI caused by a multi-path channel can be eliminated by using a cyclic prefix in the time-domain. After the IDFT on the transmitter side, a cyclic prefix of size  $N_g$ , which is the copy of  $N_g$  samples at the end of an OFDM symbol, is inserted into the symbol beginning. Hence, *w.r.t* an OFDM symbol, the convolution between a multi-path channel and a transmitted OFDM symbol becomes a circular convolution. As a consequence, ICI is proved to be eliminated. On the receiver side, after the DFT an OFDM symbol can be expressed as a function of the transmitted symbol multiplied by a channel frequency response term

$$Z_n^k = Q_n X_n^k, \quad n = 0, 1, \dots, N - 1, \quad (4.6)$$

where  $Q_n$  is the Discrete Fourier Transform (DFT) of the equivalent discrete channel impulse response. Hence, a simple ZF technique can be used for channel equalization. Cyclic prefix insertion is illustrated in the figure below.

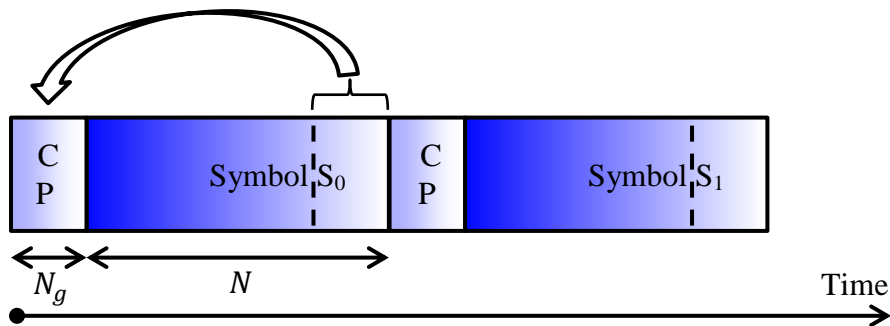


Figure 4.6 – Cyclic prefix insertion principle.

### 4.2.2.2. Cyclic prefix for optical IMDD OFDM transmissions

It is shown in the previous paragraphs that a cyclic prefix can preserve the orthogonality between subcarriers in a multi-path radio channel. Unlike radio multi-path channel where dispersion is in the time domain, it is in the frequency domain in a fiber-based optical channel. Strictly speaking, ICI caused by FWM products [80], [85] and intermodulation terms [86] cannot be eliminated by a prefix cyclic. For the sake of simplicity, only ICI caused by second order chromatic dispersion is concerned. An IMDD channel is simplified

<sup>4</sup> The term “symbol” denotes an OFDM symbol which has  $N$  samples where  $N$  is the FFT size.

and linearized so that a received OFDM signal is composed of subcarriers having various delays as shown in Figure 4.7. Here a color corresponds to a subcarrier.

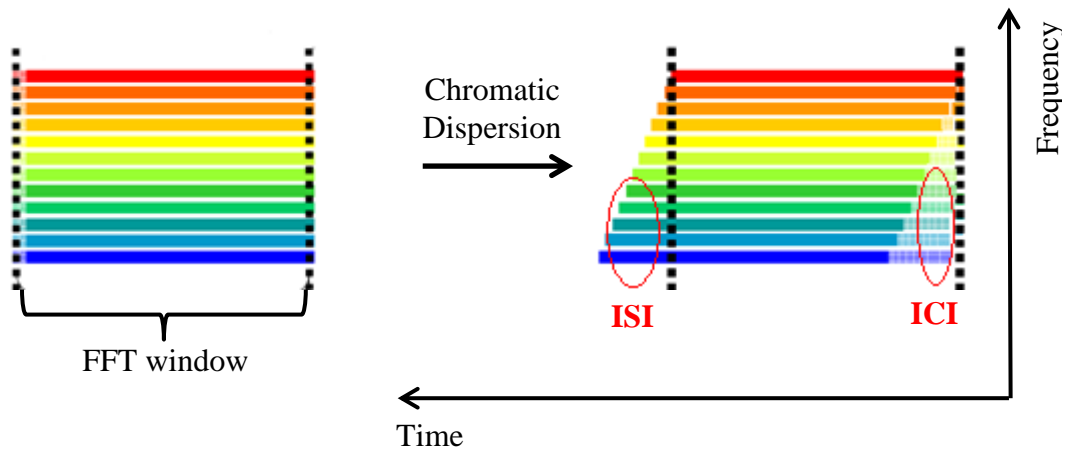


Figure 4.7 – Chromatic dispersion in simplified linearized IMDD transmission without cyclic prefix.

As shown in Figure 4.7, in the case of a transmission without cyclic prefix, delays caused by chromatic dispersion generate ISI and ICI. As a part of delayed subcarriers shift outside the FFT window, ICI comes from the fact that the projection of one orthonormal basis function to one another is not any more a Kronecker function. This is mathematically illustrated as

$$\int \Phi_{n,k}^q(t) \Phi_{n',k'}^q(t)^* \neq \delta_{n,n'} \delta_{k,k'} , \quad (4.7)$$

where  $\Phi_{n,k}^q(t)$  is an orthonormal basis function of the received signal. It can be expressed as the convolution between the corresponding transmitted signal orthonormal basis function  $\Phi_{n,k}(t)$  and the end-to-end channel impulse response  $q(t)$

$$\Phi_{n,k}^q(t) = \Phi_{n,k}(t) \circledast q(t), \quad (4.8)$$

where  $\circledast$  denotes a convolution operation. On the other hand, when a cyclic prefix is large enough to cover the largest delay, the problem of ISI and ICI can be eliminated. As shown in Figure 4.8, ISI is directly absorbed by the cyclic prefix. In an FFT window, delays caused by chromatic dispersion only result in a phase rotation of the subcarriers. Therefore, the orthogonality of the subcarriers is preserved.

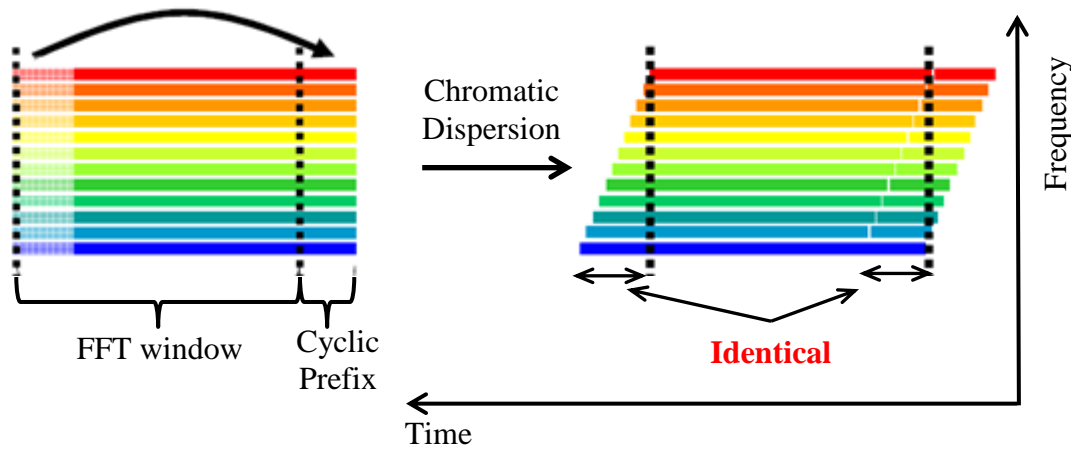


Figure 4.8 – Chromatic dispersion in simplified linearized IMDD transmission with cyclic prefix.

#### 4.2.2.3. Optimal cyclic prefix length

It is concluded from the previous section that a cyclic prefix must cover at least the maximum delay in order to preserve subcarrier orthogonality. Supposing that the OFDM signal has a bandwidth of  $\Delta f$  Hz, the maximum delay can be expressed as

$$\begin{aligned}\Delta\tau &= DL\Delta\lambda \\ &\approx DL\frac{c\Delta f}{\nu^2},\end{aligned}\quad (4.9)$$

where  $\nu$  denotes the optical carrier frequency. As a rule of thumb when designing a cyclic prefix for an OFDM transmission, a cyclic prefix must be larger than this maximum delay

$$\Delta g \geq DL\frac{c\Delta f}{\nu^2}. \quad (4.10)$$

### 4.3. The water-filling optimization

Because of the frequency selectivity of an optical IMDD channel, the performance of conventional OFDM transmissions is governed by subcarriers having the worst SNRs. In practice, interleaving techniques can be used to distribute errors over subcarriers. Then, a Forward Error Correction (FEC) can be implemented to obtain an error-free transmission. This technique is shown to increase system complexity. Another approach is to adapt the constellation size and the power of each subcarrier to channel condition in order to optimize transmission performance. In the literature, such an optimization can be divided into two dual approaches as follows.

- **Rate adaptive approach**

In the Rate Adaptive (RA) approach, transmission bit rate is maximized, while an energy constraint is imposed as in the following equations.

$$\text{Maximizing } R_{BR} = \sum_{n=0}^{N-1} b_n = \sum_{n=0}^{N-1} \log_2 \left( 1 + \frac{\mathcal{E}_n |Q_n|^2}{\sigma_n^2 \mathcal{E}} \right). \quad (4.11)$$

$$\text{Constant energy constraint } \sum_{n=0}^{N-1} \mathcal{E}_n = N\bar{\mathcal{E}}, \quad (4.12)$$

where  $R_{BR}$  denotes the transmission bit rate,  $Q_n$  is the channel gain on the  $n^{\text{th}}$  subcarrier,  $\mathcal{E}_n$  denotes subcarrier energy and  $\bar{\mathcal{E}}$  is the average power.  $\sigma_n^2$  denotes the variance of equivalent noise<sup>5</sup>.  $\mathcal{E}$  is the SNR gap which depends on constellation type and desired Symbol Error Rate (SER) [87].

- **Margin adaptive approach**

In this case, the symbol energy is minimized, while a data rate constraint is imposed. This approach is usually used in transmission systems where variable bit rate is not acceptable.

$$\text{Minimizing } \sum_{n=0}^{N-1} \mathcal{E}_n. \quad (4.13)$$

$$\text{Desired bit rate constraint } \sum_{n=0}^{N-1} b_n = R_{BR}. \quad (4.14)$$

In these approaches, the solutions of such optimization problems are unique because of convexness. Regardless of which approach is concerned, the optimum water-filling transmit energies always satisfy the following equation.

$$\mathcal{E}_n + \mathcal{E} \frac{\sigma_n^2}{|Q_n|^2} = \text{constant}, \quad (4.15)$$

In Eq. (4.15), the term  $\mathcal{E} \frac{\sigma_n^2}{|Q_n|^2}$  can be considered as the inverse function of channel gain.

Hence, the term “water-filling” arises from the analog of  $\mathcal{E} \frac{\sigma_n^2}{|Q_n|^2}$  being a bowl into which water (energy) is filled. In an RA approach, all available water/energy, which is determined by the energy constraint, is poured into the bowl. In a Margin Adaptive (MA) approach, water/energy is poured into the bowl until the bit rate objective is achieved. Remaining water/energy represents the margin. This also raises the term “margin”. Water-filling technique is illustrated in the figure below.

---

<sup>5</sup> The equivalent noise includes receiver noise and nonlinearity-induced noise. When the number of subcarriers is large, the equivalent noise is supposed to be centered and Gaussian.

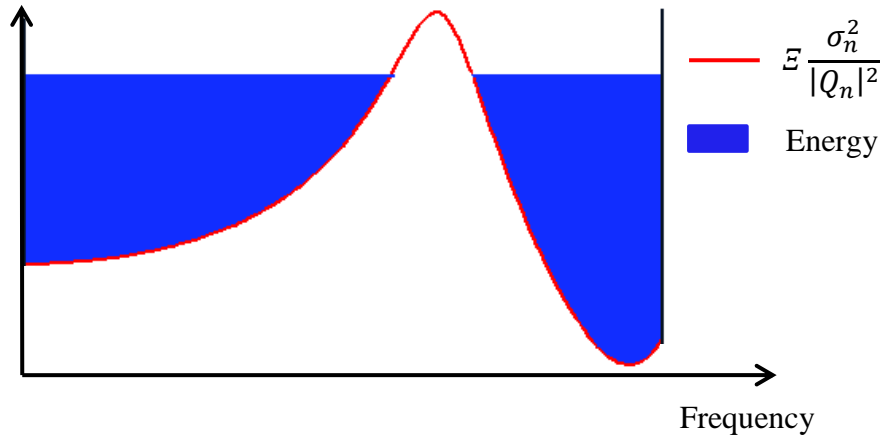


Figure 4.9 – Illustration of the water-filling technique.

#### 4.4. Levin-Campello discrete bit/power loading

Water-filling optimizations may give real-valued bit distributions where  $b_n$  can be any real number. In practice, realization of such a non-integer bit distribution can be difficult. Alternative loading algorithms allow the computation of more practical bit distributions which have a finite granularity. The granularity of a transmission system is the smallest incremental information unit that can be transmitted. Typically, granularity  $\zeta$  takes values such as 0.25, 0.5, 0.75, 1, or 2 bits, where a non-integer granularity can be found in coded systems. In this case, the number of bits carried by a subchannel can be written as

$$b_n = B_n \zeta, \quad (4.16)$$

where  $B_n$  is a positive integer. An  $m$ -Quadrature Amplitude Modulation ( $m$ -QAM where  $m = 1, 2, \dots$ ) transmission system is a typical example of integer granularity  $\zeta = 1$ .

There are two approaches to finite granularity. The first approach is to round approximate water-fill results. This approach was developed by Peter Chow and is reported in [88], [89]. Chow proposed to round a non-integer bit distribution to the nearest integer value. The author managed to verify that: as long as Chow's bit distributions use the same or nearly the same transmission band as optimal water-filling distributions, they exhibit negligible loss when compared to the optimal water-filling method.

The second approach which is based on "greedy" methods in mathematics was developed by Levin and Campello [82]. The basic principle of this bit/power loading technique is that each unity of incremental information will be placed in the sub-carrier that requires the least incremental energy. The algorithm has the name "greedy" because when the channel gain of a subcarrier is high, more bit and energy are put into that subcarrier. Such a loading algorithm is optimum when the information granularity is the same for all subchannels [89], which is usually the case in practical transmission systems.

Historically, the LC bit/power loading technique was developed for DSL systems [90], in which the transmission channel is relatively static and introduces frequency-dependent attenuation. According to available SNR on each subcarrier, the loading algorithm computes optimum bit and power distributions. In the context of optical IMDD transmissions, the channel response is also frequency selective due to chromatic dispersion and laser chirps. Thanks to a direct detection by photodiode, IMDD channel is relatively

static when compared to coherent optical systems. Due to this analogy between a DSL channel and an optical IMDD channel, several authors have shown excellent performance of such a bit/power loading scheme for optical IMDD transmissions [11], [42], [46], [81]. For the sake of a reference for the proposed technique that is later discussed in this chapter, in the next paragraphs the LC bit/power loading algorithm is summarized. For the performance of Chow's method in an optical IMDD channel, the reader is invited to read the details in [81]. In addition, although the performance of the LC algorithm has been reported, none of the authors in [11], [42], [46], [81] compared the performance of such a multicarrier transmission scheme with conventional PAM transmission schemes. For this reason, we also give a comparative study of the OFDM modulation and the conventional OOK NRZ modulation in order to more clearly reveal the potential of such a multicarrier modulation scheme. Before describing the LC loading techniques, it is worth noting several important definitions.

#### 4.4.1. Definitions and notations

##### 4.4.1.1. Definition 1 – Bit distribution vector

A bit distribution vector for  $N$  sub-channels is written as

$$\mathbf{b} = [b_0 \ b_1 \ \dots \ b_{N-1}], \quad (4.17)$$

where  $b_i$  is the number of bit per symbol carried by the  $i^{th}$  sub-carrier.

##### 4.4.1.2. Definition 2 – Symbol incremental energy

The energy  $E_n$  of a symbol carrying  $b_n$  information unit on the  $n^{th}$  subchannel can be generalized by a function of  $b_n$

$$E_n = E_n(b_n). \quad (4.18)$$

Actually, this symbol energy function depends on the subchannel gain, the number of bits carried by the subchannel, the modulation constellation type and the minimal distance between two points in a constellation, which can be deduced from a desired SER.

The incremental energy to transmit  $b_n$  information units on a subchannel is the energy required to transmit one more information unity ( $b_n - \zeta \rightarrow b_n$  bits), which means

$$e_n(b_n) = E_n(b_n) - E_n(b_n - \zeta), \quad (4.19)$$

where  $\zeta$  is the constellation granularity.

##### 4.4.1.3. Definition 3 – Bit distribution efficiency

A bit distribution vector  $b_n$  is considered to be efficient if

$$\max_n \{e_n(b_n)\} \leq \min_m \{e_m(b_{m+\zeta})\}; \quad n, m = 0, \dots, N - 1. \quad (4.20)$$

The left-hand side of Eq. (4.20) represents the maximum energy obtained if one removes one information unity from the  $n^{th}$  subchannel, whereas the right side represents the minimum energy required to put one more information unit on the  $m^{th}$  subchannel.

Therefore, a bit distribution vector  $b_n$  is said to be efficient if no transmitted information movement from one sub-channel to another reduces the entire symbol energy. In other words, when a bit distribution is efficient, available energy is used the most efficiently.

#### 4.4.2. Levin-Campello efficientizing algorithm

Levin and Campello developed an iterative algorithm in order to obtain an efficient bit distribution.

---



---

#### Algorithm 4.1 – LC efficientizing

---

**input** : An arbitrary bit distribution

**output** : Efficient bit distribution

---

$m = \arg \left\{ \min_{0 \leq i \leq N-1} [e_i(b_i + \zeta)] \right\};$  /\* Subcarrier having smallest incremental energy \*/

$n = \arg \left\{ \max_{0 \leq j \leq N-1} [e_j(b_j)] \right\};$  /\* Subcarrier having largest incremental energy \*/

**while** ( $e_m(b_m + \zeta) < e_n(b_n)$ ) **do** /\* When incremental energy on the  $m^{th}$  subcarrier is smaller than that of the  $n^{th}$  subcarrier \*/

$b_m = b_m + \zeta;$  // Put one information unity on the  $m^{th}$  subcarrier

$b_n = b_n - \zeta;$  // Withdraw one information unity from the  $n^{th}$  subcarrier

$m = \arg \left\{ \min_{0 \leq i \leq N-1} [e_i(b_i + \zeta)] \right\};$

$n = \arg \left\{ \max_{0 \leq j \leq N-1} [e_j(b_j)] \right\};$

**end while**

---



---

#### 4.4.3. Levin-Campello rate adaptive algorithm

The RA algorithm optimizes useful data rate while respecting the constraint of the total symbol power. A bit distribution vector is considered to be a solution of the RA algorithm if it respects the E-tight constraint

$$0 \leq N\bar{E} - \sum_{n=0}^{N-1} E_n(b_n) \leq \min_{0 \leq i \leq N-1} [e_i(b_i + \zeta)]. \quad (4.21)$$

Eq. (4.21) implies that no additional information unit can be transmitted without violating the symbol energy constraint. An RA solution is a bit distribution vector where useful data rate is maximal given an available symbol energy budget. The algorithm is fed with an efficient bit distribution obtained by the LC efficientizing algorithm.

**Algorithm 4.2 – LC E-tightness****input** : An efficient bit distribution**output** : Optimum RA bit distribution

$$S = \sum_{n=0}^{N-1} E_n(b_n);$$

**while**  $(N\bar{E} - S < 0) \parallel (N\bar{E} - S \geq \min_{0 \leq i \leq N-1} [e_i(b_i + \zeta)])$  **do**

<b>if</b> $(N\bar{E} - S < 0)$ <b>do</b> /* Symbol energy exceeds the limit. The number of	bits is reduced */
--	--------------------

$n = \arg \left\{ \max_{0 \leq i \leq N-1} [e_i(b_i)] \right\};$
--

$S = S - e_n(b_n);$
---------------------

$b_n = b_n - \zeta;$
----------------------

<b>else</b> // Otherwise, add additional bits
---

$m = \arg \left\{ \min_{0 \leq i \leq N-1} [e_i(b_i + \zeta)] \right\};$
--

$S = S + e_m(b_m + \zeta);$
-----------------------------

$b_m = b_m + \zeta;$
----------------------

<b>end if</b>
---------------

**end while**

Basically, the LC E-tightness algorithm reduces the number of bits when the symbol energy exceeds the power constraint limit. When energy is sufficiently<sup>6</sup> below the limit, the LC E-tightness algorithm puts additional bits into subcarriers where incremental energy is the lowest.

Indeed, an RA solution can be obtained if one always transmits an additional information unit on the sub-channel that requires the lowest incremental energy under the constraint of total symbol energy. Hence, an equivalent RA algorithm can be written as follows.

---

<sup>6</sup> which means that the available energy is still enough for the lowest additional incremental energy.

**Algorithm 4.3 – Equivalent LC RA loading****input** : Initial bit distribution  $\mathbf{b} = [0 \ 0 \ \dots \ 0]$ **output** : Optimum RA bit distributionUsed energy so far  $S = 0$ ;**while** ( $S \leq N\bar{\epsilon}$ ) **do** // When the symbol energy is still below the limit
$$m = \arg \left\{ \min_{0 \leq i \leq N-1} [e_i(b_i + \zeta)] \right\};$$
 // Subcarrier having the lowest incremental energy

$$b_m = b_m + \zeta;$$
 // Put one additional information unity

// Update the symbol energy

$$S = \sum_{n=0}^{N-1} E_n(b_n);$$

**end while****4.4.4. Levin-Campello margin adaptive algorithm**

In practice, some transmission systems require fixed useful data rate. In this case the LC MA algorithm can be used. Under a data rate constraint, the MA algorithm minimizes the total symbol energy. Starting from an efficient bit distribution, each additional information unit is placed on the sub-channel requiring the least incremental energy until the target bit rate is achieved. If the input bit distribution gives a total bit rate that exceeds the target, the number of bits is reduced. The LC MA algorithm is described by the following B-tight algorithm.

**Algorithm 4.4 – LC B-tight****input** : An efficient bit distribution**output** : Optimum MA bit distribution

$$\tilde{b} = \sum_{n=0}^{N-1} b_n;$$

**while** ( $\tilde{b} \neq b$ ) **do**

<b>if</b> ( $\tilde{b} > b$ ) <b>do</b>	*/ Total bit rate exceeds the target one	*/
---	--	----

$n = \mathit{arg} \left\{ \max_{0 \leq i \leq N-1} [e_i(b_i)] \right\};$
--

$\tilde{b} = \tilde{b} - \zeta;$
----------------------------------

$b_n = b_n - \zeta;$
----------------------

<b>else</b>	*/ Total bit rate is below the target one	*/
-------------	---	----

$m = \mathit{arg} \left\{ \min_{0 \leq i \leq N-1} [e_i(b_i + \zeta)] \right\};$
--

$\tilde{b} = \tilde{b} + \zeta;$
----------------------------------

$b_m = b_m + \zeta;$
----------------------

<b>end if</b>
---------------

**end while****4.4.5. Levin-Campello bit/power loading for optical IMDD systems**

In LC bit/power loading techniques, in order to compute optimum bit/power distributions, a transmitter must know beforehand the SNR on each subcarrier. In practice, this parameter can be estimated on the receiver side by training sequences. Then, by means of a feedback link, the transmitter can be informed by the receiver about the channel information. In DSL systems, channel gain and receiver noise might be independent in signal bit/power distribution vectors. Hence, as long as power amplifiers are not saturated, one can assume that the SNR on each subcarrier is proportional to transmitted subcarrier power. When the power of a subcarrier increases/decreases, the corresponding SNR is also supposed to increase/decrease. Hence, the application of LC RA or MA algorithms is straightforward in DSL channels.

However, this is not always the case in an optical IMDD channel. Due to nonlinear effects including laser nonlinearities, FWM products and intermodulation noise [26], [86], channel gain and noise power may depend on the electrical power of a transmitted signal. Moreover, the power of FWM products and inter-modulation noise on each subcarrier also depends on the bit distribution vector. At the initialization stage, channel gain and noise variance are estimated by training sequences. The estimated values depend on the bit and power distributions of the training sequences. However, these parameters may change

when a data signal, which has a different bit/power distribution from that of the training sequences, is transmitted. It is interesting to consider the two following cases.

- **Dominant photodetector thermal noise**

The thermal noise of a photodetector usually becomes dominant when received optical power is low. In the context of optical access networks, this is usually the case because no in-line optical amplifier is implemented. In this case, the SNR of a sub-channel can be considered to be proportional to the transmitted subcarrier power. Hence, the LC RA and MA algorithms can be straightforwardly applied for an optical IMDD channel.

- **Non-dominant photodetector noise**

Assuming that transmitted symbol power is fixed, the power of FWM products and inter-modulation noise may vary as a function of bit distribution vector. Because the bit/power distribution of training symbols can be different from that of data symbols, the power of noise in a data transmission may differ from the noise power estimated by training sequences. Hence, bit/power distribution vectors, which are computed according to channel information obtained from training sequences, may not be the optimum ones. As a consequence, the SER of a transmission may differ from the desired SER defined by an SNR gap  $\mathcal{E}$ . To the best of the author's knowledge, no study about optimum bit/power distribution for an optical IMDD channel is reported. However, suboptimal bit/power distributions can be easily obtained by increasing the SNR gap until the desired SER is achieved. In this case the transmission bit rate might be lower than the optimum one.

When the LC MA algorithm is used, it is important to verify if the desired bit rate can be achievable or not. In the case where nonlinear noise is dominant when compared to the receiver thermal noise, the increase of the power of transmitted signal does not always increase the SNR on the receiver side. In some cases, it results in the decrease of the SNR. The verification of achievable data rate can be carried out by applying beforehand an RA algorithm.

## 4.5. The proposed rate adaptive precoded OFDM system

Although OFDM modulation has been shown to give excellent performance in terms of resistance to chromatic dispersion as reported in [11], [42], [46], this type of modulation has its own drawbacks. The principal disadvantages of OFDM modulation and techniques to compensate for them will be detailed in the next chapter. In this section, we are interested in a major disadvantage which is an important Peak-to-Average Power Ratio (PAPR). By definition, the PAPR of an OFDM signal is defined as the ratio between the maximum peak power and the average power over a symbol interval

$$PAPR = \max_{0 \leq i \leq N-1} \frac{|x_k(i)|^2}{E\{|x_k(i)|^2\}}. \quad (4.22)$$

Indeed, an OFDM signal has large maximum power peaks when compared to its average power. Due to an important PAPR, the efficiency of power amplifiers (PAs) in OFDM transmissions might be low [91]. Moreover, large power peaks of an OFDM signal may also saturate the laser, resulting in in-band noise which degrades the SNR on the receiver side and out-of-band radiations which cause inter-channel interference. Recently, a multiband DFT-Spread OFDM system has been proposed for long-haul coherent optical

(CO) transmissions [92]. The idea is to divide the whole OFDM band into several subbands then precode the data carried by subcarriers on each subband with a DFT matrix. The technique is shown to bring good performance in terms of PAPR reduction and fiber nonlinearity mitigation. Sung *et al.* proposed in [93] a new precoding technique which consists in separately coding the real and imaginary parts of transmitted data symbols by a DFT matrix. Precoded complex symbols are then input to a conventional OFDM modulator. The new precoding technique was shown to bring better performance in terms of PAPR maintenance along the fiber and nonlinearity mitigation at the expense of increased system complexity. DFT-spread OFDM technique has also been used in wireless radio communications, and is already adopted by the 4G mobile standard for the uplink [94]. It is important to note that the precoding techniques proposed in [92] and [93] are only suitable for CO-OFDM transmissions because in this context chromatic dispersion only results in a phase rotation of OFDM subcarriers. This means that on the receiver side, simple channel phase compensation can be used to equalize the received signal. Equalized OFDM symbols can then be demodulated to detect the transmitted data. On the contrary, in the context of an optical IMDD transmission, the interplay between laser chirps and chromatic dispersion results in attenuation dips in the frequency channel response [33]. Noise power on deeply attenuated subcarriers might be increased after a channel equalizer. In DFT-spread systems, power-increased noise is also spread over different data subcarriers. This results in the degradation of overall BER performance. Hence, in the context of transmissions in PONs, the performance of conventional DFT-spread techniques is governed by subcarriers having deep attenuation.

In order to solve this problem, we propose a rate adaptive DFT-precoded system, which optimizes the transmission data rate under the constraint of transmitted electrical power and SER performance in the context of optical IMDD transmissions. To the best of author's knowledge, the performance of DFT-spread techniques has not yet been adequately analyzed in this context. Moreover, this is the first time an RA algorithm is proposed for optical IMDD DFT-spread OFDM transmissions, although the Levin-Campello rate adaptive technique is well-known in conventional OFDM transmissions. From now on the term POFDM, which stands for Precoded OFDM, denotes the proposed system. According to numerical simulations, it is shown that the proposed POFDM system has the same performance in terms of data bit rate when compared to that of the conventional LC AMOOFDM system. However, the proposed transmission scheme gives a large power saving due to PAPR reduction.

#### **4.5.1. Transmission schemes**

##### **4.5.1.1. Conventional LC AMOOFDM modem**

A DML-based SMF-channel IMDD transmission diagram is illustrated in Figure 4.10. The precoding block on the transmitter side and the decoding block on the receiver side are only used in the proposed POFDM system. By referring to Figure 4.10, general functions of an LC AMOOFDM modem can be described as follows. On the transmitter side, a transmitted binary sequence is mapped onto a complex QAM sequence. A serial-to-parallel converter distributes the complex data over a large number of subcarriers to form frequency-domain OFDM symbols. According to the SNR on each subcarrier, the order of QAM constellation and the power of subcarriers can differ from one subcarrier to another. An IFFT is then applied to each frequency-domain OFDM symbol to generate real-valued time domain OFDM symbols. It is noted that real-valued symbols are obtained by using a

Hermitian symmetry. This means that data carried by negative frequency subcarriers are the complex conjugates of data carried by the corresponding positive frequency subcarriers, and the DC subcarrier carries no data. Here a CP is inserted into each OFDM symbol to reduce ICI caused by the chromatic dispersion of the fiber link. A parallel-to-serial converter serializes IFFT-output symbols to form a digital LC AMOOFDM transmitted sequence. According to a pre-determined clipping rate, a DAC performs a clipping of the digital signal to limit the power dynamic range. The digital clipped signal is then quantized on a given number of bits. A zero-order hold followed by a Low Pass Filter (LPF) is then performed in order to generate an analog signal waveform, which is then biased with a DC component before driving a DFB laser. The peak-to-peak value of the analog laser-driving signal can be adjusted by means of a Power Amplifier (PA). It is later shown that the optimal peak-to-peak value of the driving current, which brings the best performance in terms of throughput, varies as a function of transmission distance. The power of an optical signal is limited by an optical attenuator before being coupled into the fiber link. On the receiver side, after a photodiode, received signal is demodulated with a processing dual to the transmitter's one.

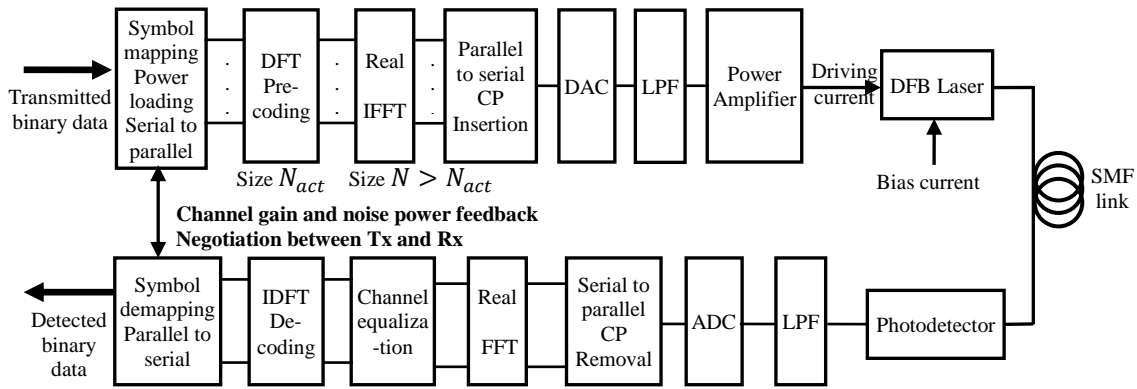


Figure 4.10 – Transmission diagram of the LC AMOOFDM and POFDM modems.

According to the principle of the LC AMOOFDM technique, in order to compute optimal bit/power distributions, one of the input parameters of the LC algorithm is the SNR on each subcarrier [42]. At the initial stage of a transmission, this parameter can be obtained via noise estimation and feedbacks between the transmitter and the receiver. A certain number of OFDM training symbols, which are known by the receiver, can be sent so that the SNR on each subcarrier can be estimated on the receiver side.

#### 4.5.1.2. The proposed POFDM modem

The transmission scheme of the proposed POFDM modem is similar to that of a LC AMOOFDM modem described above except two significant differences as follows.

- 1) The same QAM constellation is used for all active subcarriers and the power distribution of subcarriers is uniform. If a subcarrier is inactive, it carries null data. In addition, whether a subcarrier carries null data or not is defined by a null-subcarrier pattern.
- 2) On the transmitter side, before the IFFT, the frequency-domain data of active subcarriers are coded by a DFT matrix. The precoding makes the frequency-domain data of an OFDM symbol correlated. Hence, the PAPR of a transmitted signal is

reduced. In addition, by appropriately choosing the DFT matrix size, the precoding can be carried out by a complexity-reduced FFT operation.

According to the SNR on each subcarrier, there are some subcarriers that carry null data because of deep attenuation. The precoding of a frequency-domain OFDM symbol is twofold. Firstly, it results in a correlation between IFFT-input data. This decreases the appearance probability of large peaks of a transmitted signal. Hence, the PAPR of a laser-driving current is reduced. The interests of PAPR reduction are discussed in detail in section 4.6.3. Secondly, the precoding is also a good way to benefit from the frequency selectivity of an optical IMDD channel. The overall BER of a transmission is no longer governed by subcarriers having the worst SNRs. It is later shown that by appropriately selecting null-subcarrier patterns and the corresponding signal constellations, the performance in terms of data rate of the proposed POFDM technique can be equivalent to that of the conventional LC AMOOFDM technique, which is known as an approximate solution of the optimal water-filling technique.

In order to find optimal QAM constellations and null-subcarrier patterns in a POFDM system, a rate adaptive algorithm is proposed. The proposed RA algorithm is based on the power of system equivalent noise. In the next paragraphs the analytical expression of the equivalent noise and methods for estimating its value are discussed.

## 4.5.2. Theoretical basis

### 4.5.2.1. Equivalent channel model

Under the assumption of perfect time and frequency synchronizations, according to the analyses reported in [86] the equivalent channel model of the precoded OFDM system can be described as in the following figure

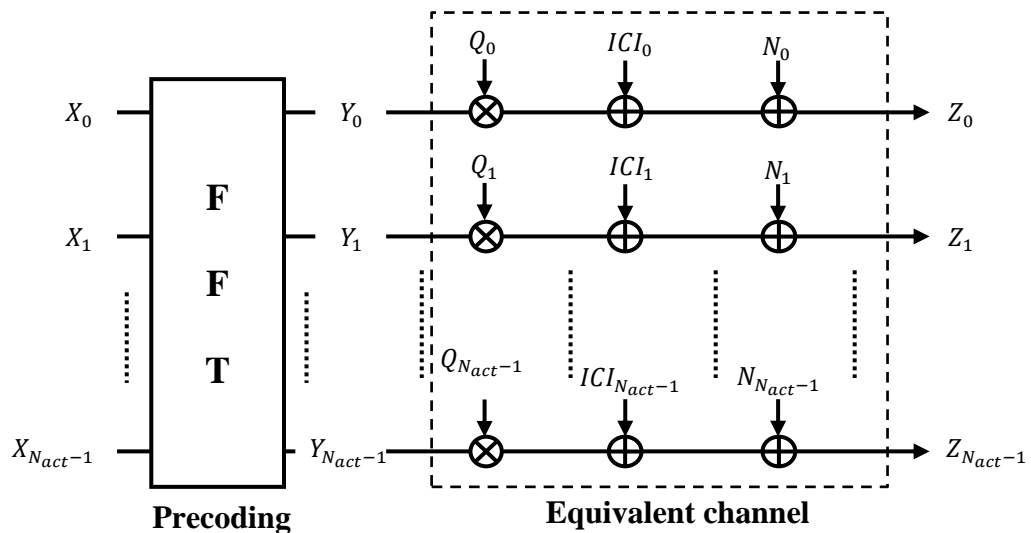


Figure 4.11 – Equivalent channel model for a POFDM transmission.

A transmitted data symbol is referred to as

$$\mathbf{X} = [X_0 \ X_1 \ \dots \ X_{N_{act}-1}]^T, \quad (4.23)$$

where  $\{X_n, n = 0, 1, \dots, N_{act} - 1\}$  is a transmitted symbol whose value is taken from QAM constellations.  $N_{act}$  denotes the number of active subcarriers. In the proposed precoded OFDM system, OFDM data symbols are coded by a DFT matrix. The resulting frequency-domain symbol  $\mathbf{Y}$  is expressed as

$$\mathbf{Y} = [Y_0 \ Y_1 \ \dots \ Y_{N_{act}-1}]^T = DFT\{\mathbf{X}\}. \quad (4.24)$$

In general, the number of active subcarriers  $N_{act}$  is smaller than the total number of data subcarriers. A received sample  $Z_n$  corresponding to the  $n^{th}$  active subcarrier after the FFT on the receiver side is expressed as

$$Z_n = Y_n Q_n + ICI_n + N_n, \quad (4.25)$$

where  $Q_n$  denotes channel gain on the  $n^{th}$  subcarrier.  $ICI_n$  denotes nonlinear ICI including intermodulation terms [86], FWM products [80] that fall into the  $n^{th}$  sub-channel, the clipping noise and the quantization noise of the Analog-to-Digital Converter (ADC) and  $N_n$  denotes the photodetector noise. Assuming that the channel response is known on the receiver side and the ZF channel equalization technique is used, a received data symbol before the IDFT decoding can be written as

$$\hat{\mathbf{Y}} = [\hat{Y}_0 \ \hat{Y}_1 \ \dots \ \hat{Y}_{N_{act}-1}]^T = \begin{bmatrix} Z_0 & Z_1 & \dots & Z_{N_{act}-1} \\ Q_0 & Q_1 & \dots & Q_{N_{act}-1} \end{bmatrix}^T. \quad (4.26)$$

Then, transmitted OFDM data can be detected by decoding equalized symbols

$$\hat{\mathbf{X}} = [\hat{X}_0 \ \hat{X}_1 \ \dots \ \hat{X}_{N_{act}-1}]^T = IDFT\{\hat{\mathbf{Y}}\}, \quad (4.27)$$

where

$$\begin{aligned} \hat{Y}_n &= Y_n + \frac{ICI_n}{Q_n} + \frac{N_n}{Q_n} \\ &= Y_n + ICI'_n + N'_n, \end{aligned} \quad (4.28)$$

and

$$\begin{aligned} \hat{X}_m &= \frac{1}{\sqrt{N_{act}}} \sum_{n=0}^{N_{act}-1} \left( Y_n + \frac{ICI_n}{Q_n} + \frac{N_n}{Q_n} \right) e^{\frac{j2\pi mn}{N_{act}}} \\ &= X_m + \frac{1}{\sqrt{N_{act}}} \sum_{n=0}^{N_{act}-1} ICI'_n e^{j2\pi mn/N_{act}} + \frac{1}{\sqrt{N_{act}}} \sum_{n=0}^{N_{act}-1} N'_n e^{j2\pi mn/N_{act}}, \end{aligned} \quad (4.29)$$

with  $ICI'_n = ICI_n/Q_n$  and  $N'_n = N_n/Q_n$ ,  $m = 0, \dots, N_{act} - 1$ .

In an optical IMDD transmission, the optical channel is relatively static. The channel gain  $Q_n$  is a deterministic unknown parameter which can be estimated by channel estimation techniques. Therefore, the random variables  $ICI'_n$  and  $N'_n$  are still central

Gaussian. The expression of demodulated samples in precoded OFDM system can be expressed with a more succinct form

$$\hat{X}_m = X_m + N_{equiv, m}, \quad (4.30)$$

where

$$N_{equiv, m} = \frac{1}{\sqrt{N_{act}}} \sum_{n=0}^{N_{act}-1} ICI'_n e^{j2\pi mn/N_{act}} + \frac{1}{\sqrt{N_{act}}} \sum_{n=0}^{N_{act}-1} N'_n e^{j2\pi mn/N_{act}} \quad (4.31)$$

is defined as the equivalent noise of nonlinear ICI noise and receiver noise.  $N_{equiv, m}$  is also a central Gaussian noise because of the central limit theorem. Because the transmitted data and the photodetector noise are independent, the nonlinear ICI noise and the photodetector noise are hence independent. The power of equivalent noise can be written as

$$\begin{aligned} \sigma_{equiv, m}^2 &= E\{N_{equiv, m}(N_{equiv, m})^*\} \\ &= \frac{1}{N_{act}} E\left\{\sum_{n=0}^{N_{act}-1} |ICI'_n|^2\right\} + \frac{1}{N_{act}} E\left\{\sum_{n=0}^{N_{act}-1} |N'_n|^2\right\} \\ &\quad + \frac{1}{N_{act}} E\left\{\sum_{i=0}^{N_{act}-1} \sum_{\substack{j=0 \\ j \neq i}}^{N_{act}-1} ICI'_i ICI'_j{}^* e^{\frac{j2\pi m(i-j)}{N_{act}}}\right\} \\ &= \frac{1}{N_{act}} \sum_{n=0}^{N_{act}-1} (\sigma_{ICI', n}^2 + \sigma_{N', n}^2) + \frac{1}{N_{act}} E\left\{\sum_{i=0}^{N_{act}-1} \sum_{\substack{j=0 \\ j \neq i}}^{N_{act}-1} ICI'_i ICI'_j{}^* e^{\frac{j2\pi m(i-j)}{N_{act}}}\right\}, \end{aligned} \quad (4.32)$$

where  $\sigma_{ICI', n}^2$  and  $\sigma_{N', n}^2$  are the power of nonlinear ICI noise and receiver noise after channel compensation, respectively. The second sum in Eq. (4.32) corresponds to correlation between nonlinear ICI terms on different subchannels.

#### 4.5.2.2. Equivalent noise power estimation

For the estimation of equivalent noise power, two methods are proposed. The first one consists in estimating the noise power on the receiver side after the IDFT decoding. The estimated noise power can be expressed as

$$\hat{\sigma}_{equiv, m}^2 = \frac{1}{l_N} \sum_{k=1}^{l_N} |\hat{X}_m^k - X_m^k|^2, \quad m = 0, \dots, N_{act} - 1, \quad (4.33)$$

where  $l_N$  denotes the number of training symbols. This estimation technique gives a good estimate of the equivalent noise power since it takes into account all possible noise sources in the system. However, by estimating the noise power after the decoding, the noise power

on each individual sub-channel is not available. Hence, in order to find the optimal null-subcarrier pattern, it is necessary to send at least one training sequence for each pattern. The initialization of such a modem may take a long time to finish.

To reduce the modem initialization time, the second method of noise power estimation involves approximating the equivalent noise power. By neglecting the second term in Eq. (4.32), from Eq. (4.28) approximate noise power can be estimated on the receiver side before the IDFT decoding

$$\begin{aligned}\hat{\sigma}_{equiv, approx, m}^2 &= \frac{1}{N_{act}} \sum_{n=0}^{N_{act}-1} \left( \hat{\sigma}_{ICI',n}^2 + \hat{\sigma}_{N',n}^2 \right) \\ &= \frac{1}{N_{act}} \sum_{n=0}^{N_{act}-1} \hat{\sigma}_n^2 = \frac{1}{N_{act}} \sum_{n=0}^{N_{act}-1} \frac{1}{l_N} \sum_{k=1}^{l_N} |\hat{Y}_n^k - Y_n^k|^2.\end{aligned}\quad (4.34)$$

By neglecting the second term in Eq. (4.32), the equivalent noise power is the same for all detected data symbols  $\hat{X}_m, m = 0, \dots, N_{act} - 1$ . And by estimating noise power before decoding, the noise power of each individual sub-channel is available. Actually, with just one training sequence the noise power of the  $n^{th}$  sub-channel can be estimated by

$$\hat{\sigma}_n^2 = \hat{\sigma}_{ICI',n}^2 + \hat{\sigma}_{N',n}^2 = \frac{1}{l_N} \sum_{k=1}^{l_N} |\hat{Y}_n^k - Y_n^k|^2, n = 0, \dots, N - 1, \quad (4.35)$$

Once the noise power on each sub-channel is available, equivalent noise power in transmissions using an arbitrary null-subcarrier pattern can be estimated by using Eq. (4.34). In practice, this method allows the initialization to finish faster as only one training sequence is required.

#### 4.5.2.3. Approximation error analysis

In the second method of noise power estimation, the approximation is valid only when the power of the second term in Eq. (4.32) is negligible when compared to that of the first term. In an OFDM transmission where the frequency subcarrier spacing is in the order of hundreds of MHz, the strength of FWM products may become important [80], [85]. Particularly, in the context of access networks where power budget is relatively low, transmitted optical power may need to be high to obtain a high bit-rate transmission. The effects of nonlinearity noise could become important. Hence, the power of the neglected term in Eq. (4.32) is expected to be important. Figure 4.12 illustrates the power of approximation error as a function of transmitted optical power and transmission distance. The simulation parameters are given in Table 2.3 and the transmission configuration is detailed in section 4.6.1. Photodetector noise is not considered in this simulation in order to isolate the nonlinear ICI noise from the receiver noise. As expected, when transmitted optical power and/or fiber length increase, the power of correlation of FWM products falling into different sub-channels increases because the strength of each FWM product increases. In addition, noise power is also increased because of frequency response dips caused by chromatic dispersion and laser chirps. In Figure 4.12 the quantization noise is shown to have negligible impact on the approximation error. Indeed, as reported in [95] quantization noise is found to be a quasi white noise. On the receiver side, after the FFT it

can also be considered white. Therefore, the power of the neglected term in Eq. (4.32), which is the correlation between noise samples on different subchannels, is expected to be negligible. The same conclusion is found for the clipping noise caused by laser saturation. According to [96] the clipping noise is an uncorrelated noise. After the FFT on the receiver side, according to the central limit theorem it is found to be an uncorrelated Gaussian noise. Because noise is uncorrelated, the correlation between noise samples on different subchannels is also expected to be negligible.

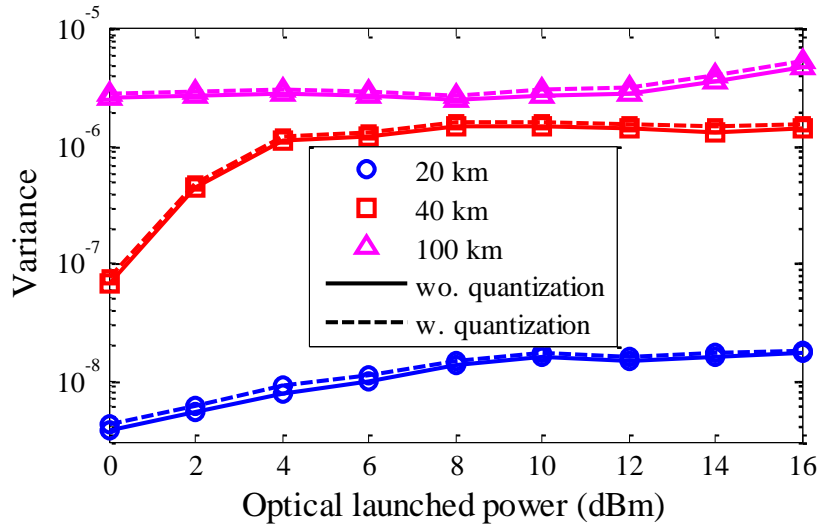


Figure 4.12 – Approximation error power as a function of transmitted optical power and fiber length. 16-QAM constellation, 8-bit quantization. Modulation index  $m = 0.9$ . Received signals are equalized and the power is normalized to unity.

In order to analyze the importance of the approximation error when compared to the overall noise power we consider the Coefficient of Variation of the Root Mean Square Deviation (RMSD)

$$CV_{RMSD} = \frac{\sqrt{E\{(\hat{\sigma}_{equiv, appro, n}^2 - \hat{\sigma}_{equiv, n}^2)^2\}}}{E(\hat{\sigma}_{equiv, appro, n}^2)}, \quad (4.36)$$

which is the ratio between the RMSD and the mean value of the estimate of the second method of noise power estimation. In dB the coefficient of variation is expressed as  $CV_{RMSD, dB} = 10 \log_{10}(CV_{RMSD})$ . As shown in Figure 4.13, even in a relatively long transmission (100 km) and with strong transmitted power, the coefficient of variation is always in the order of -15 dB. It is important to note that when transmitted power and/or fiber length increase, the power of the first term in Eq. (4.32) also increases. Hence, even though the approximation error power increases due to fiber nonlinearity, the coefficient of variation is still small. Obviously, the approximation error can be considered negligible in the context of access networks, which is the scope of this thesis.

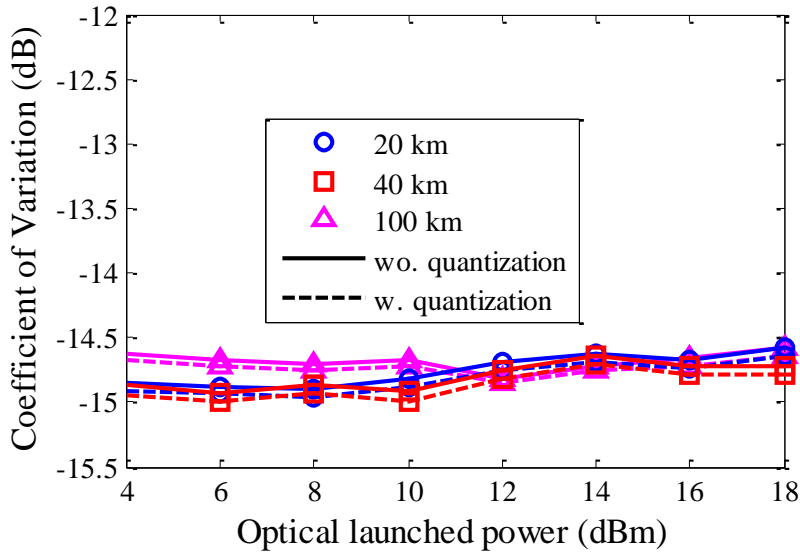


Figure 4.13 – Coefficient of variation as a function of transmitted optical power and fiber length. The approximation error is found to be negligible. Quantization noise has no significant impacts on the approximation.

### 4.5.3. Algorithm description

Inspired by the RA algorithm proposed by Levin and Campello [82], [87] which is used in LC AMOOFDM system, the proposed RA algorithm for POFDM transmissions also involves optimizing the capacity of a transmission under a constraint of electrical transmitted signal power and the desired SER of the transmission. The objective of the proposed algorithm is to obtain an optimal active subcarrier pattern (or null-subcarrier pattern) and the corresponding QAM constellation based on the estimated equivalent noise power. In an OFDM transmission where the number of subcarriers is significant, the total number of possible null-subcarrier patterns might be huge. Hence, an exhaustive searching for the optimal pattern may result in a long initialization time of a POFDM modem. From Eq. (4.34), the power of equivalent noise in a POFDM system is found to be the average of noise power on each active subchannel. Hence, in order to optimize the equivalent SNR of a POFDM system, if a subcarrier must carry null data, it must be the subcarrier having the worst SNR. In a POFDM system, the transmission capacity depends on two factors: the number of active subcarriers and the corresponding constellation size, which is determined by the equivalent noise power in the system. When the number of active subcarriers is fixed, the optimal null-subcarrier pattern is the one in which subcarriers having the worst SNRs carry null data. By using this remark the number of possible null-subcarrier patterns is reduced to  $N$ , which is the total number of subcarriers. The algorithm needs to check only  $N$  patterns in which the number of active subcarriers varies from 1 to  $N$ .

**Algorithm 4.5: Rate Adaptive POFDM**

**input** : Vector  $\hat{\sigma}'^2$  of length  $N$  with positive elements containing noise power on each sub-channel after channel equalization

**output** : Optimal active-subcarrier pattern  $ptn_{act}$   
Optimal number of bits per QAM symbol  $m_{opt}$

$R_{BR} \leftarrow 0$ ; /\* Initialize the maximum bit rate \*/

**for**  $i \leftarrow N$  **to** 1 **do** /\* loop to check  $N$  possible patterns \*/

$N_{act} \leftarrow i$ ;

$N_{null} \leftarrow (N - N_{act})$ ; /\*  $N_{null}$ : the number of null subcarriers \*/

/\* Initialization of noise power on active subcarriers \*/

$\hat{\sigma}'_{act}{}^2 \leftarrow \hat{\sigma}'^2$ ;

/\* Discard the null subcarriers which have the worst SNRs. The corresponding noise power values are set to 0 so that they are not considered in the equivalent SNR. \*/

set  $N_{null}$  largest values in  $\hat{\sigma}'_{act}{}^2$  to zero ;

/\* Calculate the equivalent SNR from Eq. (4.34) \*/

$$SNR_{equiv} \leftarrow \left( \frac{N_{act}}{\text{sum}(\hat{\sigma}'_{act}{}^2)} \frac{N}{N_{act}} \right); \quad (4.37)$$

/\*  $N/N_{act}$  is the energy normalizing factor. The number of active subcarriers can change but the electrical power budget is fixed. \*/

/\* Calculate the number of bits carried by the corresponding QAM symbol according to the SNR gap  $\mathcal{E}$  [87], [97] \*/

$$m \leftarrow \text{floor} \left( \log_2 \left( 1 + \frac{SNR_{equiv}}{\mathcal{E}} \right) \right); \quad (4.38)$$

/\* Calculate the transmission bit rate \*/

$$\text{bit\_rate} \leftarrow (m * N_{act}); \quad (4.39)$$

**if**  $\text{bit\_rate} \geq R_{BR}$  **then** /\* Update the optimal values \*/

$R_{BR} \leftarrow \text{bit\_rate}$ ; /\* Update the maximum bit rate \*/

$m_{opt} \leftarrow m$ ; /\* Optimal number of bits per QAM symbol \*/

/\* As the values corresponding to null subcarriers in  $\hat{\sigma}'_{act}{}^2$  are set to 0, we deduce the active subcarrier pattern by finding the positions of positive values. \*/

$ptn_{act} \leftarrow (\hat{\sigma}'_{act}{}^2 > 0)$ ;

**end if**

**end for**

#### 4.5.4. Model mismatch

It must be noted that nonlinear ICI noise depends itself on the null-subcarrier pattern. Hence, nonlinear ICI noise power in a transmission with the optimal null-subcarrier patterns may differ from that of the transmission of training sequences. Similar to the impact of nonlinear ICI noise on an LC AMOOFDM system described in section 4.4.5, the dependence in null-subcarrier pattern of nonlinear ICI noise may result in an SER variation. This means that, when ICI nonlinear noise is dominant when compared to thermal noise, the value of SER may differ from the desired one. In a system using RA algorithm, it is important to always achieve the targeted SER. Hence, similarly to the suboptimal solution for an LC AMOOFDM system, in a POFDM system a suboptimal solution is to increase the SNR gap until the desired SER is achieved.

#### 4.6. Performance analysis

According to the dispersion-induced channel gain attenuation of an optical IMDD channel, conventional OFDM techniques use an adaptive modulation in order to maximize the transmission data rate. Among adaptive modulation schemes in the literature, the one of Levin and Campello is shown to give a quasi-optimal solution of the water-filling technique. In terms of transmission bit rate, this solution is shown to give excellent performance in an optical IMDD channel [42]. However, the inherent important PAPR of an OFDM signal makes the efficiency of the PA low.

We propose a DFT-precoded OFDM system, which consists in precoding a frequency OFDM symbol by a DFT matrix before the IFFT on the transmitter side. The precoding makes the frequency data of an OFDM symbol correlated, resulting in the PAPR reduction of the transmitted OFDM signal. The proposed rate adaptive algorithm also optimizes the position of active subcarriers according to the attenuation profile. This also maximizes the transmission data rate of the proposed system. In this section, by means of numerical simulation, we are going to compare the performance in terms of PAPR and data rate of the conventional LC AMOOFDM and the proposed systems.

##### 4.6.1. Simulation setup

The parameters used in the simulation of different components in the transmission link are given in Table 2.3. For the OFDM modulation, the FFT size is 256. However, only 107 subcarriers can carry useful data. The DC subcarrier carries null data and 20 subcarriers at the edge of the spectrum are set to zero to reduce aliasing impact. The 128 negative-frequency subcarriers are the complex conjugates of the 128 corresponding positive-frequency subcarriers. After the IFFT, 16 last samples of a time-domain OFDM symbol are copied to the beginning of the symbol to form a Cyclic Prefix (CP). In the context of access networks this CP length is sufficient to cover largest delays caused by chromatic dispersion. The DAC functions at 12 GS/s and has 8 quantization bits and the clipping rate, which is the ratio between the maximal quantized power and the average power, is 13 dB. These values are adopted according to [11], which are shown to generate negligible quantization noise and clipping noise. The optical power coupled into the fiber link is 0 dBm. Transmission distance can vary from 0 km to 100 km in the simulations. On the receiver side the received optical power can vary according to insertion loss in the transmission link. For channel estimation, because the IMDD optical channel is relatively static, the simple least square method is used to estimate the channel response. In order to

reduce the impact of noise on channel estimation performance, estimated channel response is then averaged over 30 training symbols. Further increase of the number of training symbols does not improve the estimation performance. For noise estimation, during the initialization stage 1000 OFDM training symbols are transmitted.

#### 4.6.2. Optimum operating parameters of the laser

Figure 4.14 illustrates transmission data rate as a function of laser bias current and transmission distance. It is noted that in both LC AMOOFDM and POFDM systems, the SNR gap  $\mathcal{E}$  is chosen so that the SER of each subcarrier converges to  $10^{-3}$ . The corresponding BER is hence always lower than  $10^{-3}$ , which allows error-free transmission with an appropriate FEC. Transmission data rate is then calculated as the sum of bits carried by each subcarrier per second. In short-reach transmissions ( $< 30$  km), data line rate drops when the value of bias current decreases. This is due to the fact that when laser bias current decreases, the value of adiabatic chirp also decreases [36]. The first attenuation zone of channel transfer function might be very deep due to the small value of adiabatic chirp [98], which results in data rate loss. On the contrary, in transmissions longer than 30 km, nonlinear ICI noise becomes significant when transmission distance increases [86]. It is also shown in Figure 4.15 that the peak-to-peak value of a driving current might become large in order to compensate for the fiber loss. Hence, the increase of adiabatic chirp (equivalent to an increase of bias current) might enhance the FM modulation of the laser, resulting in increased nonlinear ICI noise power, which decreases the system performance.

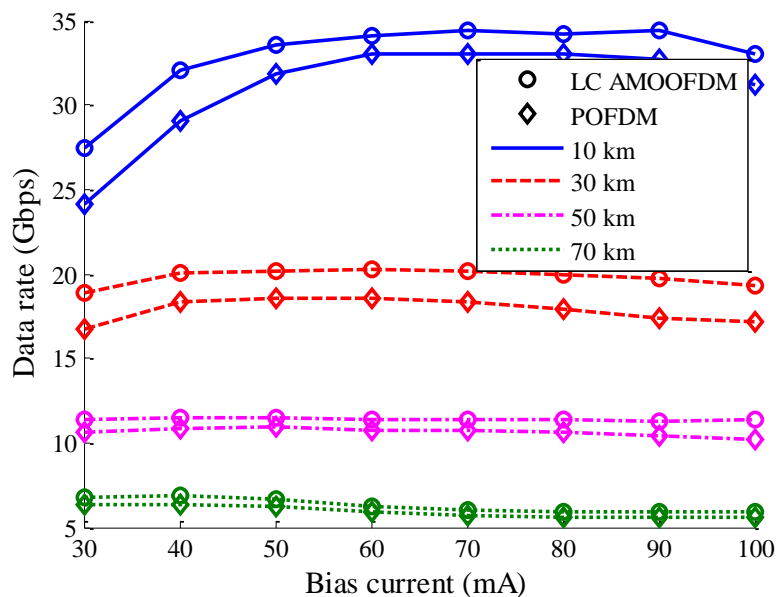


Figure 4.14 – Transmission data rate as a function of laser bias current and fiber length at optimal modulation indices. Insertion loss is 4 dB.

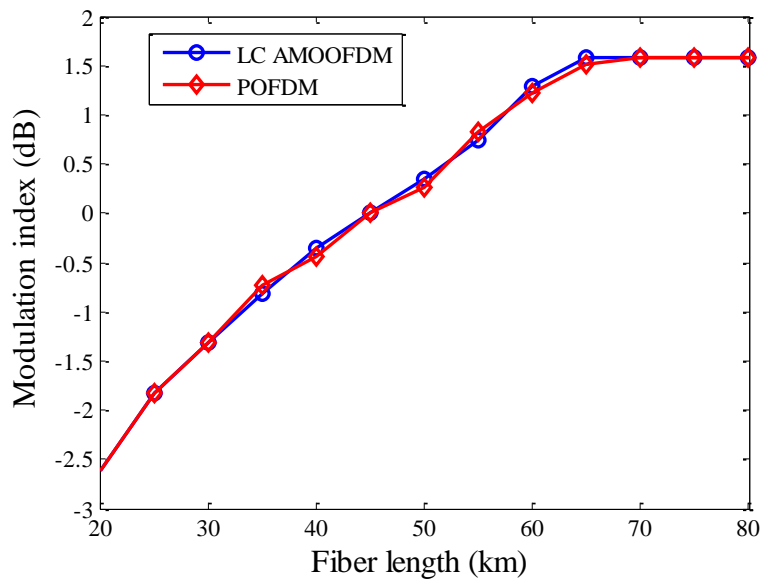


Figure 4.15 – Modulation index as a function of fiber length. The modulation index increases with the fiber length to compensate for the fiber loss. Laser bias current is 60 mA. Insertion loss is 4 dB.

Transmission data rate becomes relatively stable for bias current values larger than 60 mA. When the value of bias current continues to increase, the data rate begins to drop which is due to significant adiabatic chirp and the saturation of laser. In practice, larger bias current also results in a more power-consuming transmitter. For a compromise between channel throughput and power consumption, bias current is chosen to be 60 mA from now to the end of the chapter. The corresponding adiabatic frequency is 2 GHz. It is noted that for each fiber length value, the modulation index, which is the ratio between the clipped amplitude of the driving current and the bias current, can vary from -10 to 1.6 dB in order to find the optimal value which is a compromise between different noise sources. In the case of Figure 4.15 in particular, modulation index values are chosen close to the optimal ones in order that the two systems almost have the same average power as shown in Figure 4.18. However, in general the optimal modulation index values of the two systems are very close to each other. In most cases the performance of the POFDM system is equivalent to that of the LC AMOOFDM system. In short-reach transmissions (< 30 km), thanks to the adaptive modulation, the LC AMOOFDM system brings a little gain in terms of data rate. However, in all cases, no important gain is observed.

### 4.6.3. Power consumption analysis

#### 4.6.3.1. PAPR reduction by precoding

Indeed, the fact that the data carried by different subcarriers are independent makes the appearance probability of large peaks high. In practice, an OFDM signal is amplified by a Power Amplifier (PA) before modulating the laser. Hence, the largest peaks of an OFDM signal are always clipped due to the saturation of the amplifier. Given a fixed input average power and a fixed saturation power of an amplifier, when PAPR increases the clipping probability also increases. We recall that signal clipping results in in-band noise which degrades the SNR and out-of-band radiations which cause inter-channel interference. For this reason, the average power of an OFDM signal must be adjusted so that it is rarely

clipped due to amplifier saturation. This means that, one has to apply to the OFDM signal an Input Backoff (IBO) before the amplifier, which is the ratio between the minimum input power that saturates the amplifier and the average power of the input signal. In order to examine PAPR characteristics of an OFDM signal it is common in the literature for authors to use the Complementary Cumulative Distribution Function (CCDF) of the PAPR, which gives the clipping probability of an OFDM signal.

Figure 4.16 shows the CCDF of OFDM and POOFDM signals before and after the DAC. It is noted that in this simulation all the data subcarriers carry 16-QAM symbols. Due to the precoding by a DFT matrix, the PAPR of a POOFDM signal is strongly reduced when compared to that of OFDM signals. This is because of the correlation between different frequency-domain subcarrier data after the precoding. For example, at the same clipping probability of  $10^{-3}$ , the PAPR is reduced by 2 dB. It is shown in the next paragraphs that this PAPR reduction has a straightforward relationship with the reduction of power consumption of a power amplifier.

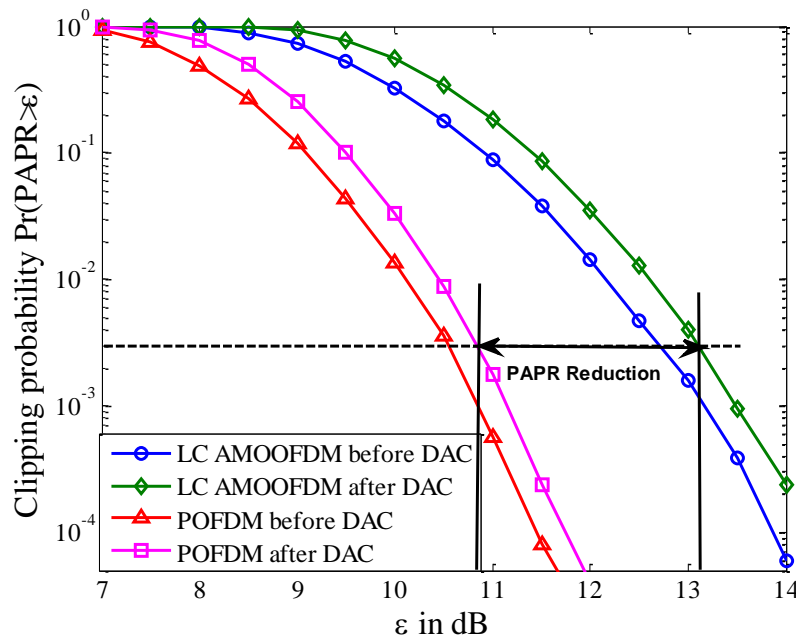


Figure 4.16 – OFDM and POOFDM signals CCDF comparison.

#### 4.6.3.2. Power saving analysis

Power amplifier efficiency is defined as

$$\rho = \frac{\bar{P}_{out}}{P_{DC}}, \quad (4.40)$$

where  $\bar{P}_{out}$  is output average power and  $P_{DC}$  is delivered DC power which is also the power consumed by a PA. Under assumption of an ideal linear amplifier, according to [91] power amplifier efficiency can be written as

$$\rho = \frac{0.5}{\varepsilon}, \quad (4.41)$$

where  $\varepsilon$  is the inverse function of CCDF at a given clipping probability  $p$ . In other words,  $\varepsilon$  is the corresponding abscissa value of a CCDF in Figure 4.16 given the ordinate value  $p$  which is the clipping probability. It is noted that  $\varepsilon$  is also the IBO one must apply to an OFDM signal given the clipping probability  $p$ . Hence, it is straightforward that, for the same clipping probability  $p$ , when PAPR is reduced ( $\varepsilon$  is reduced) amplifier efficiency is also improved, resulting in power consumption reduction. Power saving due to PAPR reduction can be expressed as

$$P_{\text{saving}} = P_{DC,1} - P_{DC,2} = 2(\bar{P}_{out,1}\varepsilon_1 - \bar{P}_{out,2}\varepsilon_2), \quad (4.42)$$

where the subscript 1 denotes the LC AMOOFDM system and the subscript 2 denotes the POFDM system.

For a fixed clipping probability of  $3 \cdot 10^{-3}$ , the PAPR of POFDM and LC AMOOFDM signals in an unamplified transmission is illustrated in Figure 4.17. The PAPR of LC AMOOFDM signals decreases for longer transmission distances because the number of active subcarriers also decreases with distance due to fiber loss. The PAPR of POFDM signals depends on three factors: the number of active subcarriers, their position in the signal spectrum and the data constellation [94]. Because of adaptive modulation, all these three factors can be adapted to the channel condition. As a consequence, in Figure 4.17 the PAPR of a POFDM signal varies as a function of fiber length. Unlike the PAPR of conventional OFDM signals, the PAPR of a POFDM signal is more sensitive to data constellation [94]. The PAPR fluctuations when the fiber length increases from 20 km to 25 km, 25 km to 30 km, 30 km to 35 km and 45 km to 50 km correspond to the constellation changes from 64-QAM to 32-QAM, 32-QAM to 64-QAM, 64-QAM to 32-QAM and 32-QAM to 16-QAM, respectively. The PAPR increase or decrease when the constellation changes is also validated according to [94]. When fiber length increases from 25 km to 30 km, although the corresponding constellation size increases from 32-QAM to 64-QAM, the number of active subcarriers is strongly reduced from 92 to 68. Hence, the resulting bit rate decreases. When the data constellation is fixed, a small PAPR fluctuation is observed due to the variation of the number of active subcarriers and their position in the signal spectrum.

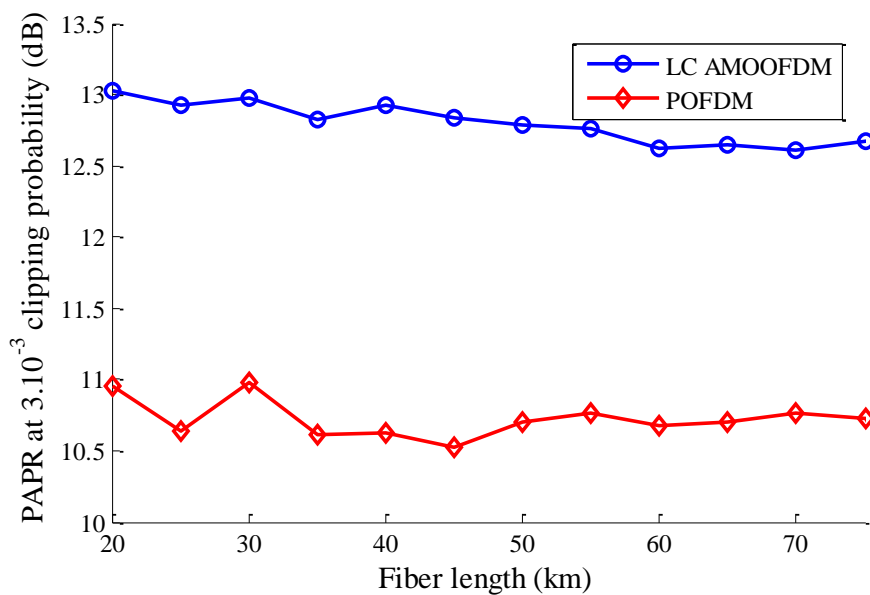


Figure 4.17 – PAPR performance as a function of transmission distance.

Supposing a 50-Ohm equivalent load resistance in the system, the power of laser-driving signals can be calculated. Due to the IBO applied to the driving signal, the DC power which supplies the PA is much more significant than the average power of the driving signal as shown in Figure 4.18. The gross power saving of a POFDM system is deduced by using Eq. (4.42). In order to calculate the net power saving of a POFDM system when compared to a LC AMOOFDM system, power cost due to precoding on the transmitter side and decoding on the receiver side must be taken into account. Supposing that the precoding can be done by using an FFT and the Digital Signal Processing (DSP) works for the same amount of time as the power amplifier, it is shown in [91] that power cost is in the order of  $\mu\text{W}$ , whereas gross power saving is in the order of  $\text{W}$ . Obviously, the POFDM technique provides large net power saving when compared to the LC AMOOFDM technique. It is interesting to note that the amount of power saving is comparable to the power consumed by the laser, which is one of the most power-consuming components of a transmitter.

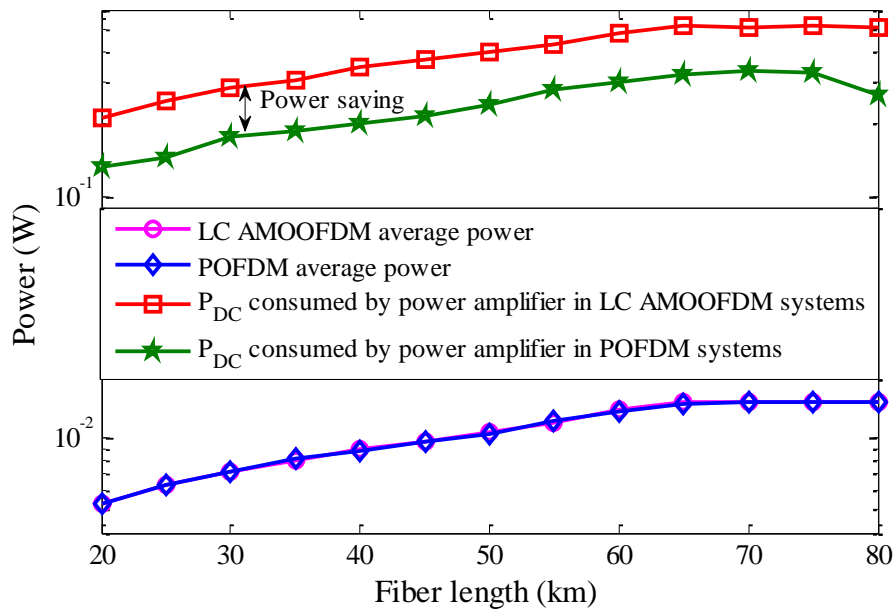


Figure 4.18 – Average power of driving signals and the corresponding DC power supply for the PA as a function of transmission distance. Insertion loss is 4 dB.

#### 4.6.4. Reach-versus-data rate performance comparison

In the previous section the proposed POFDM system is shown to outperform the conventional LC AMOOFDM system in terms of PAPR and power consumption. It is also shown in [11], [42] that unamplified AMOOFDM system employing IMDD technique can be a good solution for a cost-effective optical communication system in the context of access networks. Therefore, it is interesting to compare the performance in terms of data rate of the proposed POFDM and the LC AMOOFDM systems with the same unamplified configurations. Figure 4.19 illustrates data line rate as a function of fiber length with different values of insertion loss. In most cases, the POFDM system has the same performance as the LC AMOOFDM system. When the insertion loss is small, in short transmissions ( $< 30$  km) the LC AMOOFDM system outperforms the POFDM system. However, when the insertion loss becomes significant, the adaptive modulation becomes unnecessary. In this case the performance of the POFDM system is almost the same as that

of the LC AMOOFDM system. This is because when channel gain and SNR are low due to chromatic dispersion and fiber loss, the number of active subcarriers in LC AMOOFDM system becomes small. Hence, adaptive modulation does not bring much gain when compared to the proposed precoding technique where all the active subcarriers have the same modulation constellation.

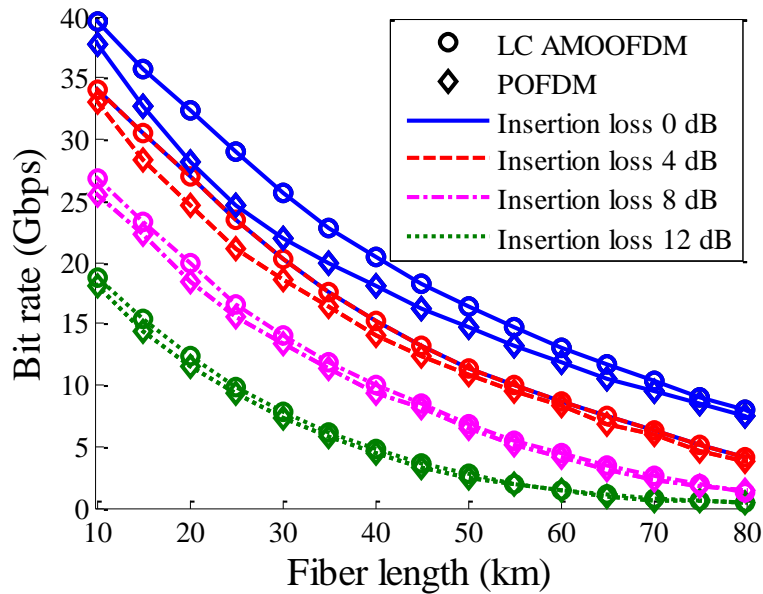


Figure 4.19 – Capacity-versus-reach performance as a function of insertion loss.

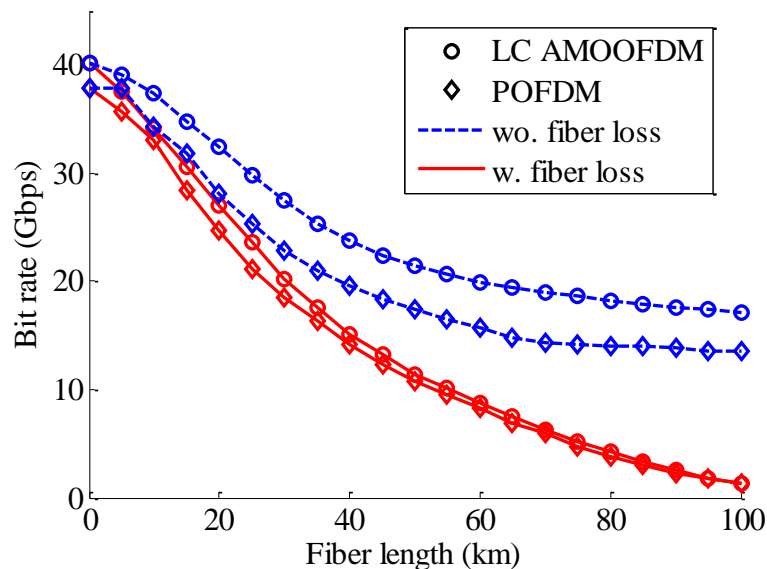


Figure 4.20 – Capacity-versus-reach performance with and without fiber loss. Insertion loss is 4 dB.

#### 4.6.4.1. Impact of fiber loss

From Figure 4.19 it is shown that in both systems, data line rate drops sharply as transmission distance increases. In order to analyze the impact of fiber loss on the transmission data rate, the performance of the two modulation techniques in unamplified

configuration with and without fiber loss is illustrated in Figure 4.20. It is observed that in both cases with or without fiber loss, for any transmission distance shorter than 30 km the data rate sharply drops when distance increases. This is because of the interplay between laser chirps and chromatic dispersion. Indeed, when transmission distance increases, the first deep null of channel frequency response shifts into the low-frequency zone and begins to exist in the signal frequency band. In the case of no link loss, longer transmission distance does not decrease transmission capacity because within the transmission range and within the signal band of concern, the second deep null of frequency response still does not exist. However, when fiber loss is taken into account, transmission throughput continues to drop at longer transmission distance due to poor SNRs at the receiver input.

#### 4.6.4.2. Impact of laser frequency chirps

Considering a “small signal” optical channel frequency response, the laser linewidth enhancement factor amplifies the channel gain of all the subcarriers by a factor of  $\sqrt{1 + \alpha^2}$  [33], and when the adiabatic chirp is taken into account, the first dip of channel frequency response is improved [35]. These results may lead to the conclusion that laser frequency chirps may be an advantage of a DML modulator when compared to a perfect, no-chirp intensity modulator. However, as mentioned before, in a dispersive channel laser frequency chirps cause intermodulation noise. Indeed, because of laser chirps, an intensity modulation provokes itself a phase modulation. After a dispersive channel, on the receiver side this phase modulation results in intensity distortion. In an OFDM system, intermodulation distortion causes ICI that cannot be suppressed even with a sufficiently large cyclic prefix. It is also reported in [11] that laser-induced frequency chirp is one of the key limiting factors of an optical OFDM IMDD transmission. In order to show the impact of laser frequency chirps on a transmission capacity, the performance of LC AMOOFDM and POFDM systems with a DML modulator and that with a perfect intensity modulator (no-chirp) are illustrated in Figure 4.21. For transmission distances shorter than 60 km, laser frequency chirps degrade the transmission capacity due to intermodulation noise. In practice, under a large-signal modulation regime, laser chirps are considered as a detriment factor rather than a good factor even though the gain they introduce in a small-signal frequency response. For transmission distances longer than 60 km, the performance of a perfect modulator is almost the same as that of a DML modulator. This is because in long-distance transmissions, fiber loss becomes the main capacity-limiting factor. The performance of a DML modulator with and without laser phase noise is also shown in Figure 4.21. It is observed that in the context of access networks, laser phase noise-induced PM-to-AM noise conversion [25] has little impact on the transmission throughput.

#### 4.6.5. Conclusion

It can be concluded that for transmission distances shorter than 60 km, the main capacity-limiting factors are chromatic dispersion and laser frequency chirps. However, for transmission distances longer than 60 km, fiber loss becomes the main capacity-limiting factor. In unamplified configuration, the proposed system significantly reduces the PAPR of a transmitted signal, resulting in significant power consumption reduction of the PA. Moreover, the performance in terms of useful data rate of the proposed system is almost the same as that of the conventional LC AMOOFDM system. In particular, when the noise margin is important (or important insertion loss), the adaptive modulation brings negligible

gain when compared to the proposed modulation scheme. The proposed system can be hence an alternative transmission system for future PONs.

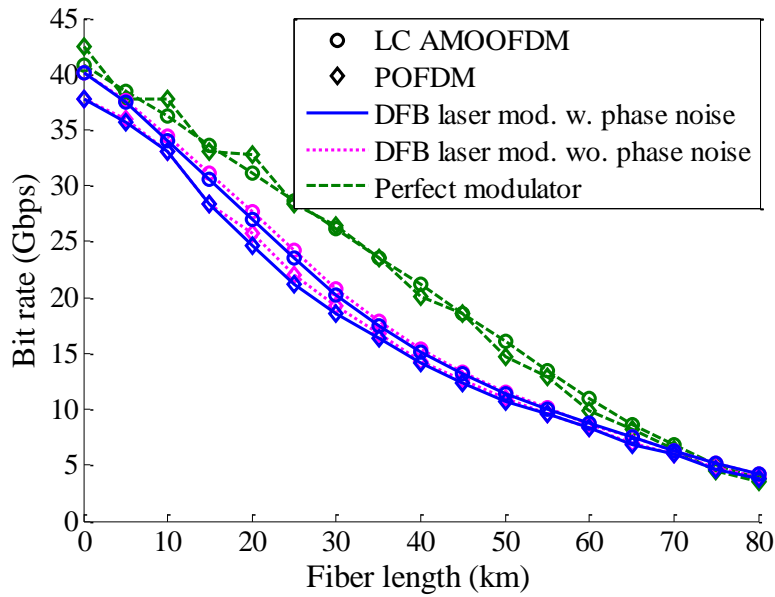


Figure 4.21 – Capacity-versus-reach performance of different modulators: perfect modulator; DML modulator with and without laser phase noise. Insertion loss is 4 dB.

## 4.7. Proposed system versus conventional NRZ system

In Chapter 3, the conventional OOK NRZ system has been shown to have poor performance when data rate and/or fiber length increase. We have adopted several equalization schemes, which have been used in radio communications, in order to increase system robustness. We have also proposed to use a Nyquist pulse-shaping instead of the conventional rectangular pulse-shaping in order to increase the spectral efficiency. However, despite all these solutions, the power penalty of an OOK NRZ/Nyquist transmission is still significant.

For the sake of revealing the potential of OFDM modulation in optical access networks, it is interesting to compare the performance of OFDM modulation to that of conventional OOK NRZ modulation. In this section, the performance in terms of tolerance to fiber length and laser chirps of the conventional OOK, LC AMOOFDM and the proposed POFDM modulation schemes is illustrated. Simulation parameters and transmission configurations are the same as those described in Chapter 3.

### 4.7.1. Tolerance to chromatic dispersion

Figure 4.22 shows required received optical power to achieve BER of  $10^{-3}$  as a function of fiber length. Unlike the performance of OOK NRZ/Nyquist modulation which is sensitive to chromatic dispersion (or fiber length), the performance of the LC AMOOFDM and the proposed POFDM systems does not strongly depend on fiber length. Indeed, the variation of transmission distance shifts the position of frequency-domain attenuation dips as illustrated in Figure 4.1. This variation also changes the gain in the high frequency zone of the channel response. Thanks to an adaptive modulation, the power and constellation size of each subcarrier in an LC AMOOFDM transmission are adapted to the channel gain,

resulting in strong robustness against chromatic dispersion of the LC AMOOFDM technique. Similarly to the LC AMOOFDM technique, the proposed POFDM technique also optimizes the position of the active subcarriers according to the attenuation profile. As shown in Figure 4.22, the proposed POFDM system is also found to have strong robustness against chromatic dispersion.

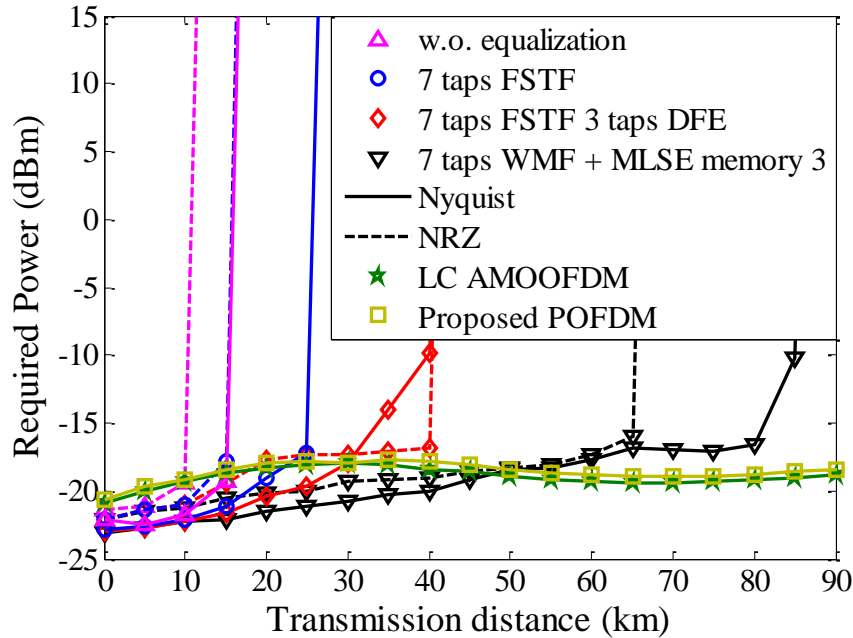


Figure 4.22 – Required power versus reach performance comparison. Bit rate is 10 Gb/s. Laser linewidth enhancement factor is 2.68.

When ISI<sup>7</sup> is very small (*e.g.* in a very short transmission distance), the conventional OOK NRZ/Nyquist modulation outperforms the LC AMOOFDM modulation. This is because in short-distance transmissions, the frequency selectivity of an optical IMDD channel is still not severe. In addition, because of fixed laser dynamic, which is the range from the emission threshold and the saturation level, OFDM and POFDM systems are strongly penalized by the important PAPR. More concretely, given a fixed laser dynamic, the variance of an OFDM/POFDM signal having larger PAPR should be lower than that of an OOK NRZ/Nyquist signal having lower PAPRs. This results in the worse performance of the LC AMOOFDM and the proposed systems when compared to that of the conventional OOK NRZ/Nyquist systems. However, conventional OOK NRZ/Nyquist systems are strongly penalized when transmission distance increase which is due to the impact of accumulated chromatic dispersion. On the other hand, thanks to an adaptive modulation, conventional LC AMOOFDM and the proposed systems are shown to have strong robustness against this impact. This gives better performance for long transmission distance when compared to the conventional OOK NRZ/Nyquist systems.

<sup>7</sup> ISI here denotes interference between consecutive OOK samples. It is hence different from the interference between OFDM symbols.

#### 4.7.2. Tolerance to laser linewidth enhancement factor

Figure 4.23 shows required received optical power to achieve the BER of  $10^{-3}$  as a function of laser linewidth enhancement factor. Interestingly, when the LC AMOOFDM or the proposed systems are used, transmission performance does not strongly depend on laser linewidth enhancement factor. It can be observed from Figure 4.24 that, the variation of laser linewidth enhancement factor changes the channel frequency response. The frequency position of attenuation dips varies as a function of laser linewidth enhancement factor. This behavior is analogy to when the value of accumulated chromatic dispersion changes. Thanks to adaptive modulation, this position variation does not strongly affect the overall data rate. The LC AMOOFDM and the proposed systems are hence more robust to laser linewidth enhancement factor than the conventional OOK NRZ/Nyquist modulation. This is very interesting since the proposed system can be directly implemented on the existing transmission infrastructure where a laser may have a large linewidth enhancement factor.

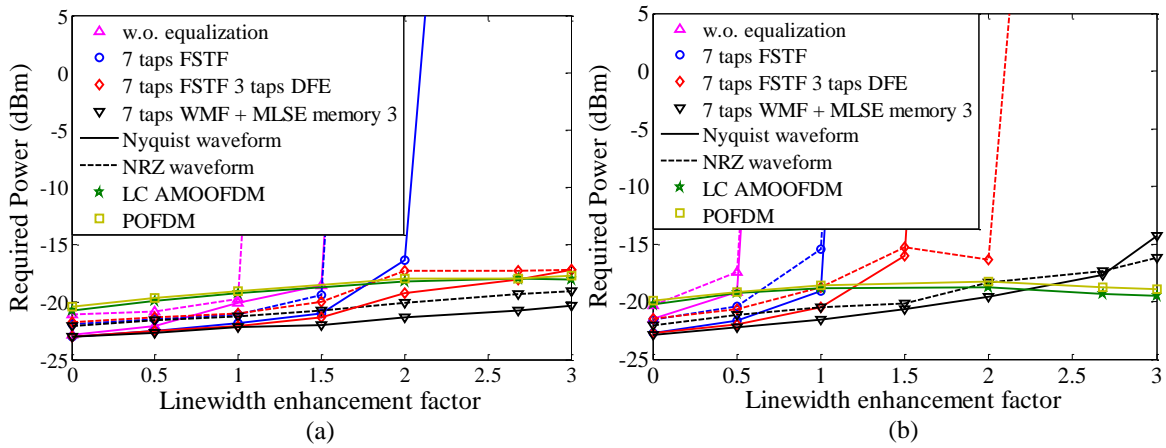


Figure 4.23 – Required power versus linewidth enhancement factor performance comparison. Bit rate is 10 Gb/s. (a) Fiber length is 30 km. (b) Fiber length is 60 km.

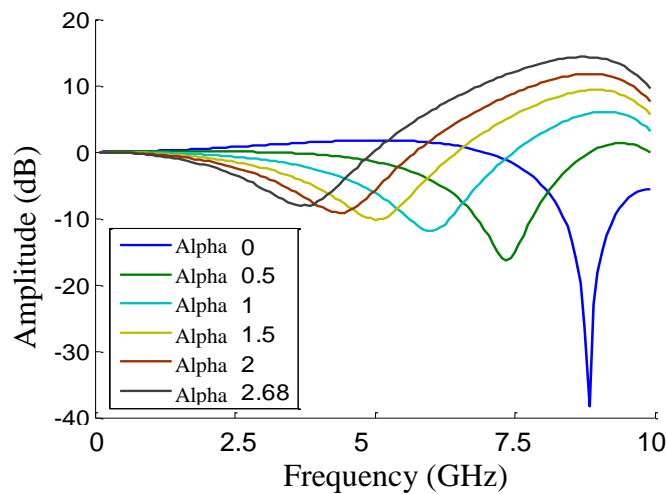


Figure 4.24 – Channel frequency response as a function of laser linewidth enhancement factor. Fiber length is 60 km. Laser adiabatic frequency  $f_c = 2.1$  GHz.

## 4.8. Conclusion

OFDM modulation has earned its success in various wireline and radio communication standard thanks to high spectral efficiency, strong resistance to frequency selectivity and low-complexity frequency domain equalization. However, in the context of optical access networks, where an IMDD technique is employed, the potential of such a modulation scheme has only been revealed very recently thanks to the works of authors in [42], [81]. Throughout this chapter, we have made clear that OFDM modulation is more robust to chromatic dispersion and laser chirps than conventional mono-carrier modulation schemes. When data rate is below 10 Gb/s and fiber length is below 20 km, an OFDM transmission has no interest when compared to OOK NRZ/Nyquist ones because of important PAPR. Therefore, in actual PONs, OFDM transmission schemes might not be interesting and fall out of the focus of access network designers. However, in the future when transmission bit rate and reach are about to further increase, OFDM modulation might become a strong candidate thanks to its robustness to chromatic dispersion and laser chirps. Moreover, another strong argument of using an OFDM modulation is that a frequency-domain equalization scheme is far less complex than a time-domain equalization scheme.

We have also proposed in this chapter an alternative modulation scheme based on a DFT precoding. The proposed system, which is reported in [1], is shown to strongly reduce the PAPR of a transmitted signal when compared to conventional AMOOFDM systems without degrading the performance in terms of useful data rate. This PAPR reduction directly leads to the significant power consumption reduction of the power amplifier. Hence, the proposed DFT-precoded OFDM modulation can be an alternative transmission scheme for future generations of PON. In the next chapter, we will take a closer look on the characteristics of an OFDM modulation. We are going to deal in depth with the disadvantages of the OFDM modulation and techniques to compensate for them.



# CHAPTER **Proposed OFDM techniques** **5** **for future PONs**

## **5.1. Introduction**

In the previous chapter we have clearly revealed the potential of an OFDM modulation for optical access networks. Conventional AMOOFDM techniques adapt the constellation size and the power of each subcarrier to the channel gain, resulting in optimized transmission throughput. Thanks to adaptive modulation, AMOOFDM transmissions are robust against the interplay of chromatic dispersion and laser chirps in an IMDD channel. The modulation is also shown to have high tolerance to transmission distance. In addition, the proposed DFT-precoded OFDM technique also shows that RA modulation is possible in a DFT-precoded system. The proposed technique strongly reduces the PAPR of a conventional AMOOFDM signal, while maintaining all the advantages of an OFDM modulation in the context of PONs. These results confirm the high potential of the OFDM modulation for next generations of optical access networks.

However, the OFDM modulation has its own drawbacks. As mentioned in the previous chapter, the PAPR of an OFDM signal is high, resulting in low efficiency of a power amplifier on the transmitter side. In addition, because of laser saturation, the variance of a laser driving current should be reduced by an important PAPR. A second important disadvantage of the OFDM modulation is its sensitivity to timing and frequency synchronizations. An offset in the time domain of an FFT window may result in ICI and ISI, and Carrier Frequency Offset (CFO) or Sampling Frequency Offset (SFO) always result in a phase rotation of subcarriers and ICI [99]. In this chapter we are going to analyze the impacts of such disadvantages of an OFDM modem. Although techniques to compensate for these drawbacks have been extensively studied in the context of radio communications, they have not yet been adequately analyzed in an optical IMDD transmission. This is the reason why in this chapter the performance of conventional techniques used for radio communication is evaluated in the context of an optical IMDD channel. According to the particular characteristics of an IMDD channel, novel techniques are also proposed and analyzed. This chapter is organized as follows. In section 5.2, we give an analysis of the PAPR of a real-valued OFDM signal. Conventional PAPR reduction techniques are also summarized in this section. According to the frequency-dependent attenuation of an IMDD channel frequency response, we also propose a PAPR reduction scheme for optical IMDD OFDM transmissions [5]. Section 5.3 is dedicated to the synchronization issue, which includes time synchronization and frequency

synchronization, of an OFDM transmission. Conventional preamble-based synchronization techniques, which have been proposed for radio communications, are analyzed in the context of an optical IMDD transmission. We also introduce in this section two proposed time synchronization schemes [2], [3], which outperform conventional techniques in terms of variance of timing offset with significantly reduced receiver complexity.

## 5.2. Peak-to-average power ratio

The penalty of the important PAPR of an OFDM signal has been already discussed in Chapter 4, section 4.7. In this section we give a closer look at the statistical characteristics of the PAPR. Various PAPR reduction schemes are also analyzed in details.

### 5.2.1. PAPR of real-valued OFDM signals

The PAPR of an OFDM signal is already discussed in Chapter 4. To recall, the PAPR of the  $k^{th}$  OFDM symbol  $x_k(t)$  is defined as the ratio between the maximal instantaneous power and the average power of the transmitted signal

$$PAPR = \frac{\max_{i \in \{0, \dots, N-1\}} |x_k(i)|^2}{E\{|x_k(i)|^2\}}, \quad (5.1)$$

where  $N$  denotes the number of subcarriers. When a large number of subcarriers are used, an OFDM signal can be considered as a random Gaussian variable according to the central limit theorem. It is noted that in an optical IMDD transmission, an OFDM signal which modulates the laser is real-valued. Hence, the PAPR, which is represented by the square of a real-valued Gaussian variable as shown in Eq. (5.1), follows the  $\chi^2$  distribution with one degree of freedom. In the context of radio communications, the reader should easily find a PAPR analysis of conventional OFDM signals, which are usually complex-valued. In the literature, the PAPR of an OFDM signal is found to follow the  $\chi^2$  distribution with two degrees of freedom [100]. The reader should not confuse this result, which is related to complex-valued, baseband OFDM signals, with the result obtained in this section, which is related to real-valued, baseband OFDM signals. Supposing that the signal power is normalized to unity, in the case of a non-oversampled OFDM signal, one can easily deduce the CCDF of the PAPR as in the following equation.

$$\begin{aligned} Pr(PAPR \geq \varepsilon) &= 1 - Pr(PAPR \leq \varepsilon) \\ &= 1 - Pr\left(\prod_{i=0}^{N-1} (|x_k(i)|^2 \leq \varepsilon)\right). \end{aligned} \quad (5.2)$$

Suppose that transmitted samples are independent, which is true for non-oversampled OFDM signal, one can rewrite Eq. (5.2) as

$$Pr(PAPR \geq \varepsilon) = 1 - \prod_{i=0}^{N-1} Pr(|x_k(i)|^2 \leq \varepsilon)$$

$$= 1 - \left( \gamma \left( \frac{\varepsilon}{2}, \frac{1}{2} \right) \right)^N, \quad (5.3)$$

where  $\gamma(d, a)$  is the incomplete gamma function which is defined as

$$\gamma(d, a) = \frac{1}{\Gamma(a)} \int_0^d t^{a-1} e^{-t} dt, \quad (5.4)$$

where  $\Gamma(\cdot)$  denotes the gamma function.

In the case of real-valued, oversampled OFDM signals, the independence assumption applied in Eq. (5.3) no longer holds. However, one can use an approximation used in [101] to calculate the CCDF of a real-valued, oversampled OFDM signal:

$$Pr(PAPR \geq \varepsilon) \cong 1 - \left( \gamma \left( \frac{\varepsilon}{2}, \frac{1}{2} \right) \right)^{2.8N}. \quad (5.5)$$

The figure below illustrates the CCDF of a real OFDM signal. In this simulation the Quadrature Phase Shift Keying (QPSK) constellation is used. We remark that simulation results perfectly fit analytical results.

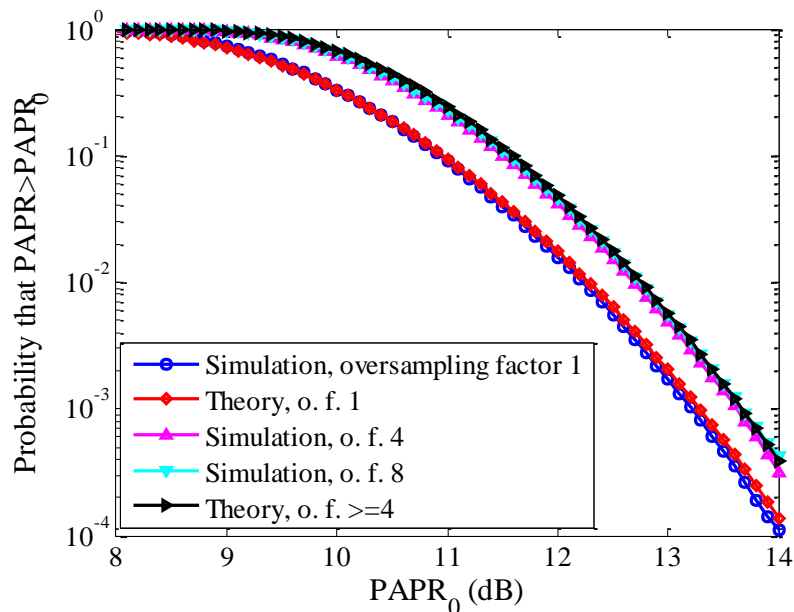


Figure 5.1 – CCDF of a real-valued OFDM signal. FFT size is 256. The QPSK constellation is used.

### 5.2.2. Consequences of high PAPR

The large PAPR of an OFDM signal leads to two important consequences. Firstly, the efficiency of PAs is low. Secondly, the large power peaks of an OFDM signal might be clipped because of laser saturation. In addition, an important PAPR can also increase the power of quantization noise of an ADC/DAC. In practice, quantization noise power can be significantly reduced by increasing the number of quantization bits [102] at the expense of

an increase of component cost. In the next paragraphs we are going to study the impact of PAPR on the amplifier efficiency and nonlinear noise caused by laser saturation.

### 5.2.2.1. PAPR-induced low-efficiency power amplifier

The impact of PAPR on the efficiency of PAs is already discussed in Chapter 4, section 4.6.3. Basically, PAs must be supplied by a DC current, which is usually also the maximum input value at which the PA is saturated. In general, signal clipping caused by PA saturation generates in-band nonlinear noise and out-of-band radiations which cause inter-channel interference. In order to avoid such signal clipping, the supply DC power must be larger than the signal average input power, resulting in the low-efficiency of a PA [91]. Figure below illustrates the typical characteristic of a PA.

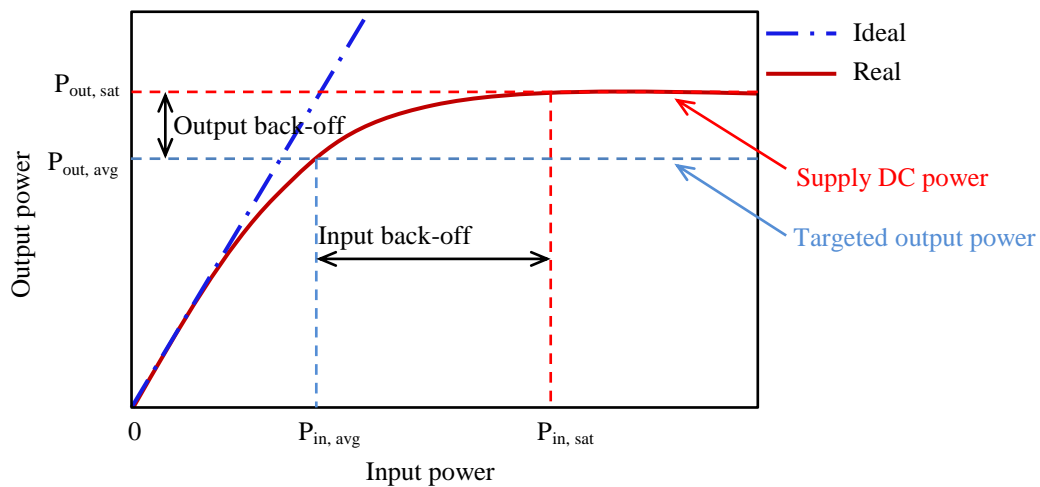


Figure 5.2 – Power transfer function of a typical power amplifier. High IBO leads to low PA efficiency.

### 5.2.2.2. Clipping due to laser saturation

Besides clipping caused by PA saturation, large power peaks of an OFDM signal might also be clipped due to laser saturation. According to the well-known Busgang theorem [103], the signal clipping results in the power reduction of useful signal and the generation of nonlinear noise. As a consequence, effective SNRs on the receiver side are reduced [102]. When clipping noise is dominant when compared to receiver noise, power penalty due to clipping noise is found to be in the order of 1 dB at optimal clipping rate. In practice, particularly in the context of access networks where no in-line optical amplifier is used, power penalty due to laser-saturation-induced signal clipping might be lower because of the presence of receiver thermal noise and nonlinear ICI noise (*c.f.* section 4.5.2.1).

### 5.2.3. PAPR reduction techniques

PAPR reduction techniques have been extensively studied for radio communications. A panorama of OFDM PAPR reduction can be found in [100]. In this section we summarize some conventional techniques. We then point out some relevant techniques for optical IMDD transmissions.

### 5.2.3.1. Coding

The idea of this method is to reduce the PAPR of an OFDM signal by using coding. For example, given a specific modulation constellation and a fixed FFT length, we have a set of all possible transmitted sequences. The idea of this technique is to avoid sequences having the largest PAPRs. This can be carried out by block coding the input data such that  $n_d$  data bits are mapped onto  $n_c$  codeword bits ( $n_d < n_c$ ). Since the number of data bits is smaller than that of codeword bits, one can avoid codewords with which generated sequences have the worst PAPRs.

A disadvantage of this method is that one needs to perform an exhaustive search to find good codes and to store large lookup tables for encoding and decoding. Hence, the method is limited to the case with a small number of subcarriers. Moreover, a large amount of bit rate needs to be sacrificed to obtain good PAPR performance since the number of data bits must be smaller than the number of codeword bits.

### 5.2.3.2. Amplitude clipping and filtering

This is one of the simplest PAPR reduction techniques. Before being transmitted, an OFDM signal is clipped at a specific level in order to reduce the PAPR. This clipping operation results in in-band noise and out-of-band radiations. In order to reduce the impact of inter-channel interference, the clipping-induced out-of-band radiations should be filtered before the signal is transmitted. Filtering out-of-band radiations after clipping may also cause peak re-growth so that the signal after filtering can exceed the clipping level at some points. Hence, the clipping-filtering operation can be repeated for several iterations until a desired peak level is obtained.

In practice, this technique is usually exploited in conjunction with other PAPR reduction techniques in order to achieve good PAPR performance. In radio communications, a spectral mask [104], which is intended to reduce inter-channel interference by limiting excessive radiation at frequencies beyond the necessary bandwidth, is usually required. In the context of optical IMDD transmissions, due to large frequency bandgap between adjacent channels, the constraint of spectral mask can be relaxed. The filtering stage can be hence omitted. However, in the case of ultra-dense WDM transmissions, the filtering should be implemented.

### 5.2.3.3. Selected mapping

Selected Mapping (SLM) technique [105], [106] was created from the fact that the PAPR of an OFDM signal is very sensitive to the phase change of frequency domain OFDM symbols. The principle of the SLM technique is illustrated in Figure 5.3. The idea of the SLM technique is to introduce some branches having different phase sequences. An original OFDM symbol is passed through these branches. At the output of each branch the phases of OFDM subcarriers change according to the corresponding phase sequence. An IFFT is then applied to all phase-changed OFDM symbols to generate the corresponding time-domain OFDM sequences. The sequence having the smallest PAPR is then transmitted.

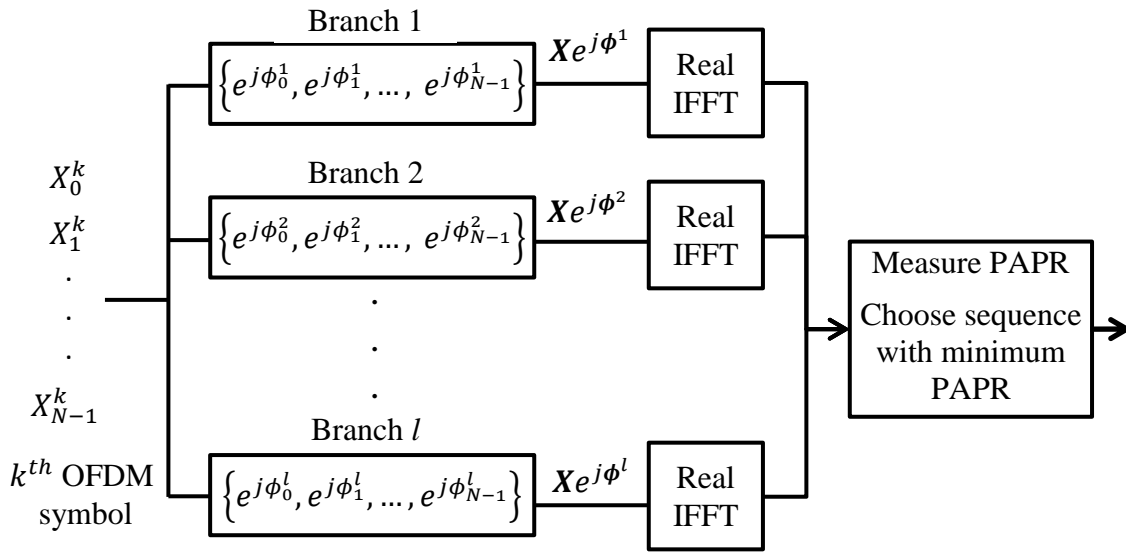


Figure 5.3 – The block diagram of the SLM technique.

Figure 5.4 shows the performance in terms of PAPR reduction of the SLM technique. With only four phase branches, up to 2.5 dB of PAPR reduction is achieved at  $10^{-3}$  clipping rate. The performance of the SLM technique is improved with the number of phase branches at the expense of increased complexity.

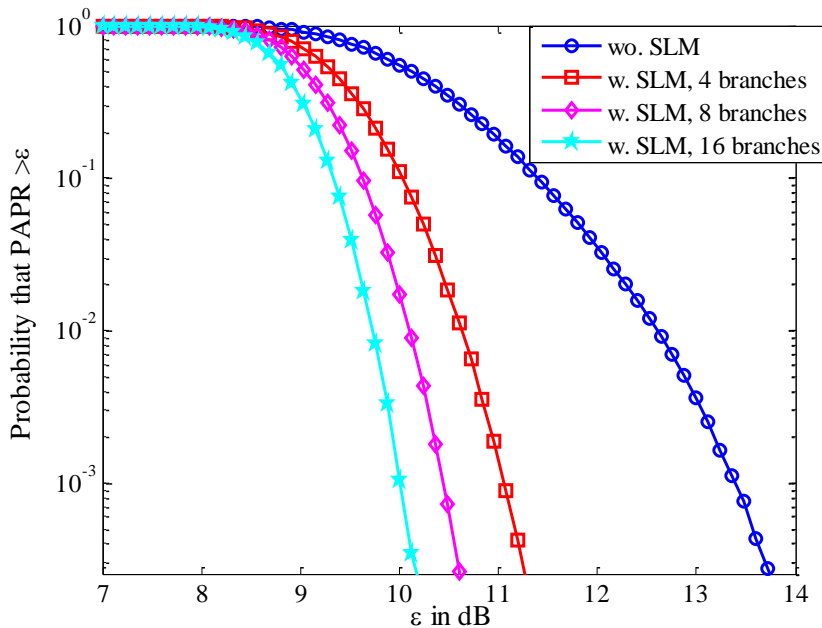


Figure 5.4 – CCDF performance of the SLM technique. FFT size is 256. 16-QAM constellation is used. Phase factors are taken from the set  $\{0, \frac{\pi}{2}, -\frac{\pi}{2}, \pi\}$ .

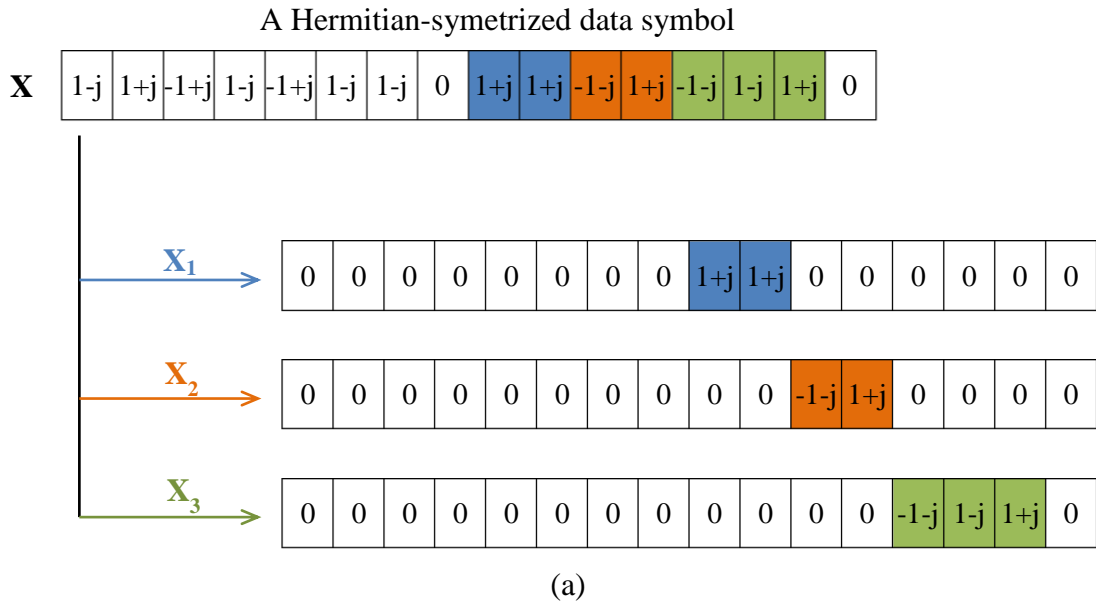
In order to recover a transmitted OFDM symbol, on the receiver side the corresponding phase sequence must be known. Side information indicating phase sequences must be transmitted along with useful data. In practice, side information can be carried by sub-carriers having high SNRs in order to avoid error amplification occurring

when a phase sequence is wrongly detected. However, side information transmission results in the loss of useful data rate.

In radio transmissions it is fairly difficult to guarantee a robust transmission of side information because of a fast time-varying channel. Moreover, without a quick feed-back, the transmitter has no information about the channel. On the other hand, in optical IMDD transmissions, the channel is relatively static. With a feed-back from the receiver at the modem initialization stage, channel information can be available on the transmitter side. This specific characteristic makes an SLM method more interesting in optical IMDD transmissions than in radio transmissions. However, the complexity of this method is really a critical problem since the number of IFFTs is proportional to the number of phase sequences (or branches). In order to obtain a good PAPR performance, a large number of branches must be used, resulting in increased complexity.

**5.2.3.4. Partial transmitted sequence**

In the Partial Transmitted Sequence (PTS) method [105]–[107], a frequency-domain transmitted OFDM symbol is partitioned into  $n_p$  adjacent disjoint subblocks. An IFFT is applied for each subblock to generate a PTS. A transmitted signal is a sum of PTSs weighted by a phase factor. The phase factors are selected such that the PAPR of the transmitted signal is minimized. Figure 5.5 illustrates a block diagram of the PTS technique. Unlike radio communications where an OFDM signal is in general complex-valued, in an optical IMDD transmission there is a constraint of a real-valued signal. A simple way to adapt the PTS technique to an optical IMDD OFDM transmission is to partition positive frequency components and the corresponding negative frequency components are set to zero. After weighted by a phase factor, the imaginary part of a PTS is discarded in order to generate a real-valued transmitted signal.



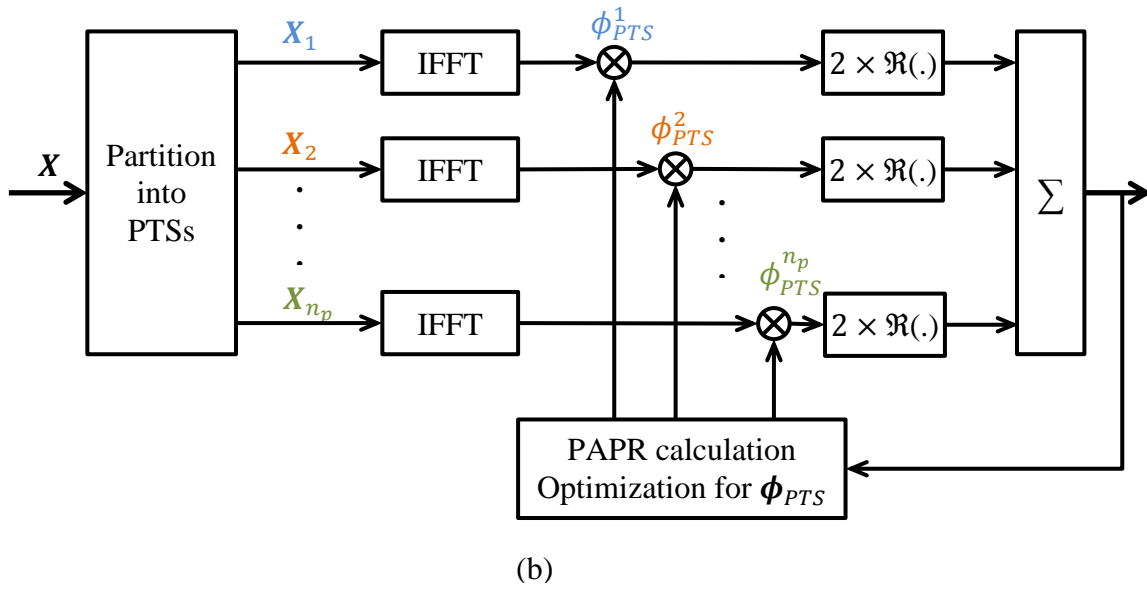


Figure 5.5 – PTS technique. (a) An example of adjacent partitioning. (b) A block diagram of the PTS technique for optical IMDD transmissions.

In general, a phase factor for each subblock belongs to a finite set of phase elements. For each transmitted OFDM symbol, an exhaustive searching for the best combination of phase factors is carried out. Figure 5.6 illustrates the performance of the PTS technique. With only two partitions, it brings 2 dB of PAPR reduction at  $10^{-3}$  clipping rate.

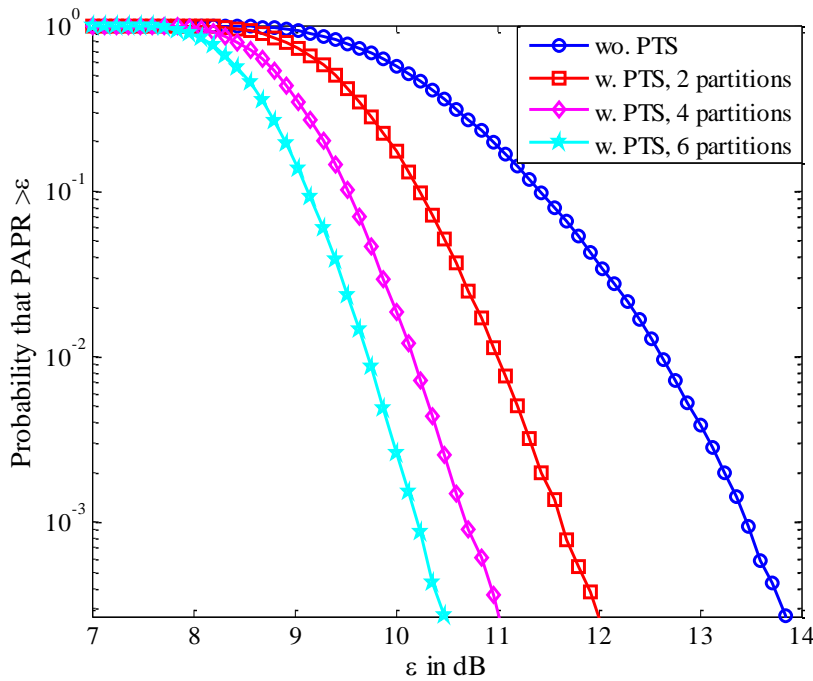


Figure 5.6 – CCDF performance of the PTS technique. FFT size is 256. 16-QAM constellation is used. Phase factors are taken from the set  $\{0, \frac{\pi}{2}, -\frac{\pi}{2}, \pi\}$ .

In this method, the amount of PAPR reduction depends on the number of subblocks and the number of phase elements. PAPR reduction performance also depends on the method of partitioning. In principle, there are three ways of building disjoint subblocks: adjacent, interleaved and pseudo-random partitioning. In Figure 5.5 the adjacent partitioning is illustrated as an example. It is reported in [108] that pseudo-random partitioning bring the best PAPR reduction performance.

Similar to the SLM technique, in the PTS technique, side information indicating subblock partitioning and the corresponding set of phase factors must be known on the receiver side in order to recover transmitted symbols. Hence, useful data rate must be sacrificed for side information transmission and the transmitter complexity is important since a large number of IFFTs are used to generate PTSs. In addition, the complexity of phase factor optimization is proportional to the number of allowed phase elements.

### 5.2.3.5. Tone injection

The idea of Tone Injection (TI) technique [109] is to increase the constellation size so that an original symbol can be mapped to another point in the new expanded constellation. This operation is equivalent to injecting a tone of an appropriate frequency in the multi-carrier signal. The PAPR performance of this technique depends on the number of modified constellation points and the design of the expanded constellation.

In the TI technique, the injection of new tones to the signal band results in the power increase of a transmitted signal. As a consequence, the PAPR reduction achieved by this technique is reduced by this power increase. In addition, *w.r.t* a data subcarrier, an injected tone is considered as a noise. Hence, this technique also results in the degradation of SNR on the receiver side. In the next paragraph we study another type of the TI technique which does not present additional noise to data subcarriers. In addition, we also show that this technique is well suited for optical IMDD transmissions.

### 5.2.3.6. Tone reservation

Similar to the TI technique, in the Tone Reservation (TR) technique [101], [109], [110] we inject some tones at appropriate frequencies into a transmitted signal except that injected tones do not occupy the same frequency band as data subcarriers. In this technique, we dedicate a set of subcarriers to the PAPR reduction of a transmitted signal.

The TR technique has earned its success in the DVB-T2 standard, where it is used as a PAPR reduction method. In the context of radio transmission, one has to sacrifice a portion of bandwidth for PAPR Reduction Tones (PRTs), resulting in the decrease of transmission data rate. On the other hand, in an optical IMDD transmission, because of the frequency-dependent attenuation that we have discussed all along this report, there is a set of subcarriers in which SNR is too low to guarantee good BER performance. We also observe in Chapter 4 that subcarriers having the worst SNRs are not used in an AMOOFDM transmission. From this remark, we proposed to take advantage of these null subcarriers to introduce PRTs without decreasing the overall bit rate of a transmission [5].

In the TR technique, a PAPR correction signal  $c_{PRT}(t)$ , which is responsible for correcting large power peaks, is built only from the PRTs. Hence, no interference is introduced to data signal band. There are two techniques to construct such a correction signal.

### 5.2.3.6.1. Clipping-based technique

In this technique, an OFDM signal is clipped at a desired amplitude level. An error signal, which is the difference between the original signal and the clipped signal, is transformed to the frequency domain by an FFT. Here, frequency positions not corresponding to PRTs are set to zero. Then, an IFFT is used in order to construct a time-domain correction signal. The clipping-based TR technique principle is shown in Figure 5.7.  $1_{PRT}$  is a frequency-domain kernel vector whose elements are equal to ones at positions corresponding to PRTs and zeros at the others.

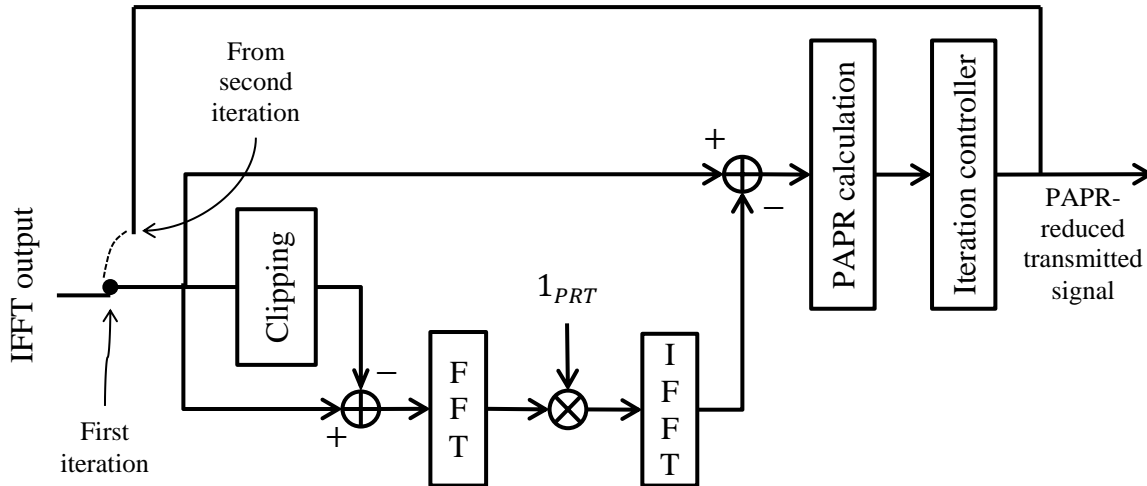


Figure 5.7 – Clipping-based TR technique principle.

In principle, the idea of this technique is to guarantee that the amplitude of a transmitted signal is below a desired value. To achieve this, a correction signal is built to correct all large peaks. However, because a correction signal is built by only PRTs, some large peaks might not be corrected and new large peaks may also be generated. Hence, in practice, this process can be iterated several times in order to obtain the desired PAPR reduction performance.

### 5.2.3.6.2. Gradient-based technique

During each iteration, unlike the clipping-based technique which tries to correct all large peaks, in the gradient-based technique, only one or several largest peaks of an OFDM symbol are corrected. The correction is carried out by means of a kernel signal (or reference signal) built with PRTs. The PRTs are designed such that a kernel signal has an impulse-like shape. According to [110], the best kernel signal<sup>8</sup> is obtained when all the PRTs have the same value. Then, an optimal correction signal can be computed by a gradient-based iterative algorithm as described in the following paragraphs.

When  $x(t)$  is an original OFDM signal, a PAPR-reduced signal can be written as

$$x_{TR}^k(t) = x(t) + c_{PRT}^k(t), \quad (5.6)$$

<sup>8</sup> The best kernel signal is the one having the largest difference between the highest amplitude value and the second highest value.

where  $k$  is the iteration index and  $c_{PRT}(t)$  denotes a PAPR correction signal which can be calculated by an iterative algorithm as in the equation below.

$$c_{PRT}^k(t) = c_{PRT}^{k-1}(t) + \alpha_{i_k}^k K_{i_k} \quad . \quad (5.7)$$

$i_k$  corresponds to the index of the largest peak of a transmitted OFDM symbol at  $(k - 1)^{th}$  iteration.

$$i_k = \underset{0 \leq i \leq Nf_{os}-1}{\operatorname{argmax}} \{x_{TR}^{k-1}(i)\} \quad . \quad (5.8)$$

$f_{os}$  denotes the oversampling factor.  $K_0$  denotes an impulse-like kernel signal which is illustrated in the subset of Figure 5.8.

$$K_0 = \frac{Nf_{os}}{\sqrt{N_{PRT}}} \operatorname{IFFT}(1_{PRT}) \quad , \quad (5.9)$$

where  $N_{PRT}$  is the number of PRTs.  $K_{i_k}$  in Eq. (5.7) is a circular-shift version of the reference signal  $K_0$  such that  $K_{i_k}(i_k)$  corresponds to the maximum value of the kernel signal. The scaling factor  $\alpha_{i_k}^k$  is expressed as

$$\alpha_{i_k}^k = \zeta \cdot \operatorname{sign}(x_{TR}^{k-1}(i_k)) - x_{TR}^{k-1}(i_k), \quad (5.10)$$

where  $\zeta$  denotes the desired amplitude level by which we define the TR threshold

$$T_{TR} = \frac{\zeta^2}{E\{|x(t)|^2\}} \quad . \quad (5.11)$$

Intuitively speaking, at the  $k^{th}$  iteration, the TR gradient-based algorithm searches for the largest term of  $x_{TR}^{k-1}$  and subtracts a circular-shift, scaled kernel signal in order to cancel that peak. Indeed, circular shift, scaling and subtraction operations correct the largest peak of an OFDM symbol to the desired amplitude level  $\zeta$ . This results in the PAPR reduction of a transmitted signal. It is also possible that several peaks are canceled in the same iteration. It is noted that a time-domain circular shift only results in a phase shift in the frequency domain. This circular shift has hence no influence on the position of the PRTs. Therefore, no ICI is generated. The gradient-based TR technique is illustrated in Figure 5.8.

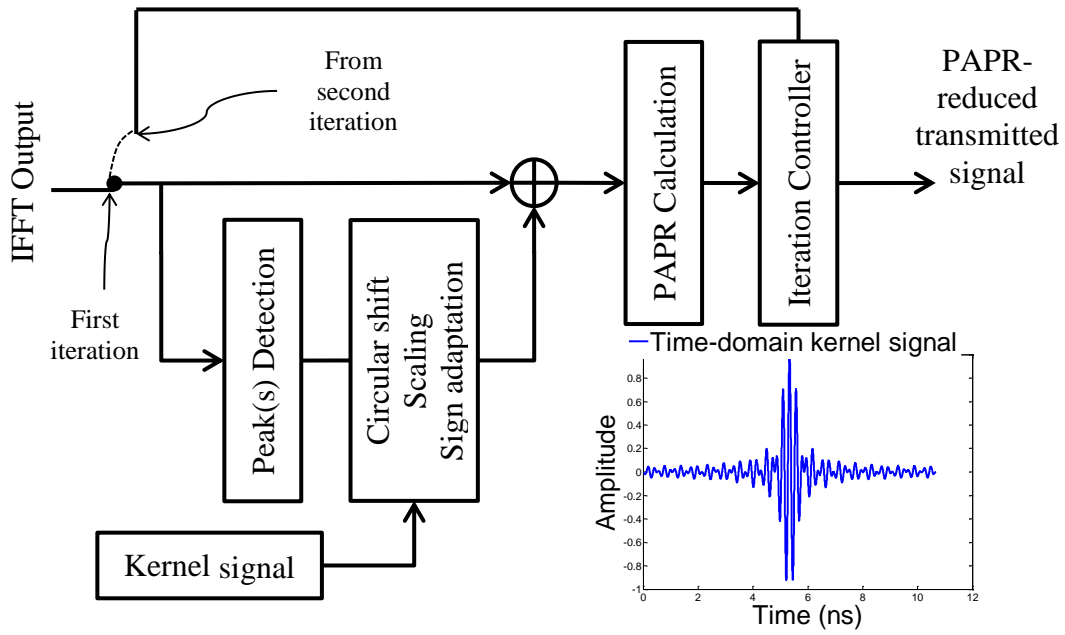


Figure 5.8 – Gradient-based TR technique principle.

**5.2.3.6.3. Tone reservation technique for optical IMDD OFDM transmissions**

We have proposed in [5] a contiguous-tone TR scheme for AMOOFDM transmissions. Because of the frequency-dependent attenuation of the channel response, certain subcarriers should not carry user data. Instead of doing nothing with these null subcarriers, we proposed to use them as PRTs for the sake of the PAPR reduction of a transmitted signal.

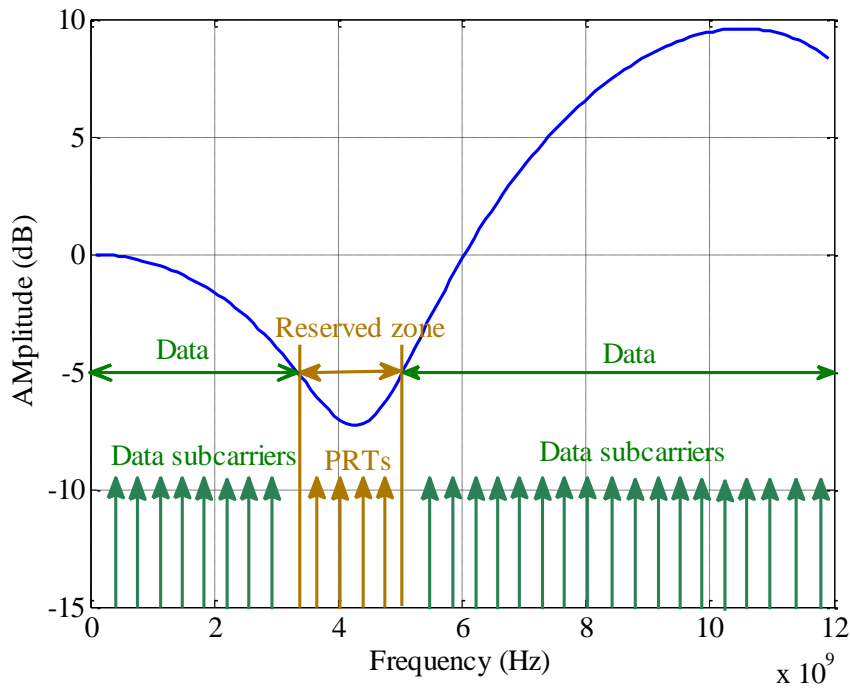


Figure 5.9 – PAPR reduction tones pattern in a 40-km AMOOFDM transmission.

Figure 5.9 illustrates the distribution of PRTs in the frequency domain of a 40-km AMOOFDM transmission. In this transmission, PRTs are located at subcarriers having the worst channel gain. More concretely, in this PRT pattern, PRTs occupy the 34<sup>th</sup> to 53<sup>rd</sup> subcarriers, which correspond to the first frequency attenuation dip of the channel frequency response. Figure 5.10 shows the PAPR reduction performance of the proposed scheme. When the gradient-based technique is used, 5 iterations bring 1 dB of PAPR reduction at  $10^{-3}$  clipping rate and 10 iterations bring 0.7 dB additional gain. Further increase of the number of iterations does not improve the performance. The clipping-based technique outperforms the gradient-based technique at very low clipping rate. However, for each iteration, the clipping-based technique requires an FFT/IFFT pair to generate the PAPR correction signal. High complexity when compared to the gradient-based technique makes it less preferable in practical systems.

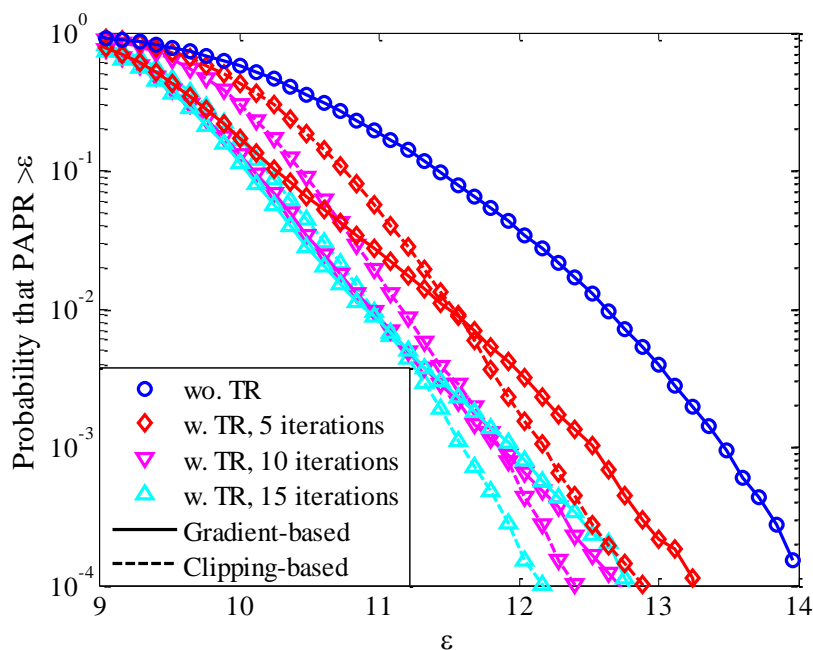


Figure 5.10 – PAPR reduction performance of the proposed contiguous-tone TR technique in a 40-km AMOOFDM transmission. TR threshold  $T_{TR} = 9$  dB.

When compared to other PAPR reduction techniques described in the previous paragraphs, this PAPR reduction scheme brings lower gain. This comes from the fact that among possible PRT patterns, a contiguous-tone pattern is not the optimal one [111]. In addition, the performance of the TR technique also depends on the number of PRTs. However, the proposed TR scheme is suitable for an optical IMDD channel in terms of optimized data rate. It is interesting to note that the proposed contiguous-tone TR scheme can also be used in the proposed DTF-precoded system (*c.f.* Chapter 4, section 4.5) in order to further reduce the PAPR of a transmitted signal. In this TR-aided DFT-precoded OFDM system, the PAPR reduction is up to 3.5 dB as illustrated in the figure below [5]. Because the PAPR of a POFDM signal is already lower than that of a conventional AMOOFDM signal, the TR threshold described in Eq. (5.11) is chosen to be equal to 8 dB.

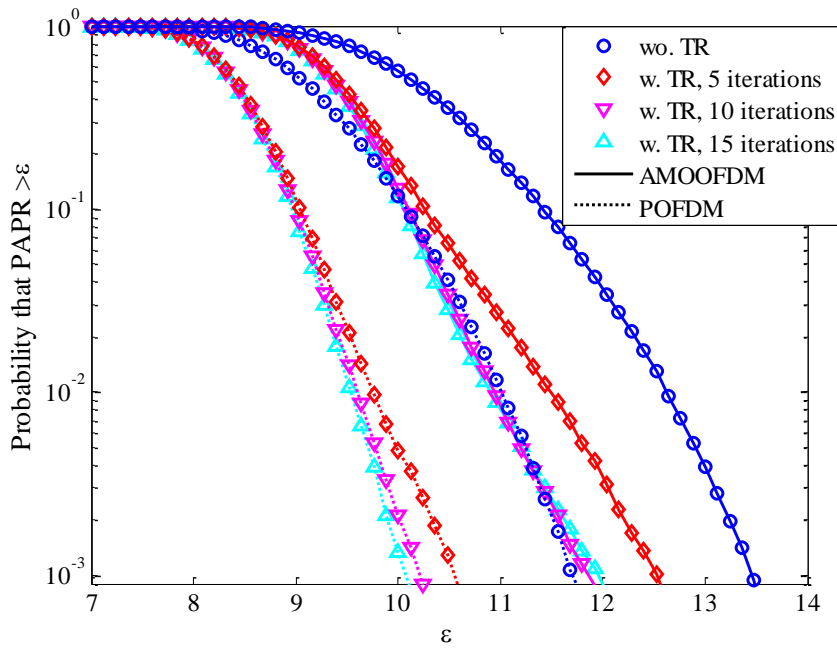


Figure 5.11 – PAPR reduction performance of the proposed contiguous-tone TR technique in a 40-km POFDM transmission. TR threshold  $T_{TR} = 8$  dB.

### 5.2.3.7. PAPR reduction through precoding

The independence in the frequency domain of OFDM subcarriers causes important PAPR of transmitted OFDM signals. Hence, one idea of PAPR reduction is to make OFDM subcarriers more correlated. This can be carried out by using a mapping matrix to mix OFDM subcarriers before transmitting. It may be noted that in the case of large number of subcarriers, the complexity of such mappings and the de-mappings can be prohibitive and a practical implementation may be difficult. However, if a DFT matrix is used as the mapping matrix, by choosing an appropriate matrix size, one can take advantage of the FFT/IFFT blocks for the mapping/de-mapping stages. We have made use of this technique to significantly improve the power consumption of a conventional AMOOFDM transmission. Figure 5.11 illustrates the performance of this technique in a 40-km transmission. For further details of the proposed precoding technique, the reader is invited to read Chapter 4, section 4.5.

### 5.2.3.8. Other techniques

#### 5.2.3.8.1. Interleaving

By rearranging the frequency position of OFDM subcarriers, one can also reduce the PAPR of an OFDM signal. Similar to the SLM technique, an original OFDM symbol passes through several branches corresponding to different interleavers. An interleaver is responsible for permuting the frequency position of each OFDM subcarrier. Then, the frequency-position-permuted OFDM symbol having the lowest PAPR is transmitted. On the receiver side, corresponding de-interleavers are used to recover the original transmitted symbol.

Similar to the SLM and the PTS techniques, in the interleaving technique one needs to transmit side information indicating which interleaver is used on the transmitter side.

### 5.2.3.8.2. Active constellation extension

The Active Constellation Extension (ACE) technique [112]–[114] is similar to the TI technique except that in this technique we only change constellation points located at the outer boundaries of an original constellation. The fact that one only extends the points at the boundaries reduces the PAPR of a transmitted signal without degrading the BER performance [100].

Similar to the TI technique, the ACE technique results in the increase of average transmitted symbol power. Hence, for the same electrical power budget, this power increase due to the extension of boundary constellation points results in the power decrease of other constellation points. The SNR of data subcarriers is hence reduced. Moreover, the PAPR reduction performance of this technique is very limited in the case of high-order constellation size.

### 5.2.4. Conclusion

In this section, the PAPR of a real-valued OFDM signal is analyzed. Conventional PAPR reduction techniques have also been studied. In general, the PAPR reduction is achieved always with some costs. In practice, there are many factors that should be considered before choosing a PAPR reduction technique for the OFDM transmission. In the next paragraphs we briefly discuss some main factors including PAPR reduction capability, complexity, BER increase, data rate loss and transmitted signal power increase.

- **PAPR reduction capability:**

This is one of the most important criteria since good PAPR reduction directly results in improved power amplification efficiency. However, it is not the only criterion because some PAPR reduction techniques also result in other negative effects such as increased complexity, data rate loss, *etc.* that will be discussed next.

- **Computational complexity:**

Some techniques such as TR and PTS require many iterations which increase computation complexity. In SLM technique, the PAPR reduction capability is proportional to the number of phase branches, which is directly related to complexity. In future PONs, the complexity of the transmitter and that of the receiver is a critical criterion since the transmission data rate is in the order of Gb/s.

- **Transmitted signal power increase:**

Some techniques result in power increase of a transmitted signal. Techniques such as TR and TI require more signal power because some of its power is used for PAPR correction signals. When the power of a signal after PAPR reduction is normalized to be equal to that of the signal before PAPR correction, the BER should be degraded.

- **BER increase:**

This can be resulted from transmitted signal power increase discussed above. In addition, BER increase can also be resulted from in-band distortion generated by some techniques such as clipping-filtering, TI and ACE techniques. In interleaving, SLM and PTS techniques, BER performance can also be degraded due to incorrect side information detection.

- **Data rate loss:**

The transmission of side information in SLM, PTS or interleaving techniques reduces the useful data rate. In the context of IMDD transmissions, this data rate loss can be avoided by using the proposed contiguous-tone TR technique in which PRTs are placed at subcarriers having the worst SNRs.

The characteristics of the PAPR reduction techniques considered are summarized in the following table.

Techniques	Inband distortion	Power increase	Data rate loss	Tx and Rx processing
<b>Clipping and filtering</b>	Yes	No	No	Tx: Clipping, filtering Rx: None
<b>Coding</b>	No	No	Yes	Tx: Coding or lookup table Rx: Decoding or lookup table
<b>SLM</b>	No	No	Yes	Tx: 1 IDFTs Rx: Side information reception, inverse SLM
<b>PTS</b>	No	No	Yes	Tx: $n_p$ IDFTs, phase factors optimization Rx: Side information reception, inverse PTS
<b>TI</b>	Yes	Yes	No	Tx: IDFTs, tone modification Rx: Additional operation for symbol detection
<b>TR</b>	No	Yes	Yes	Tx: IDFTs, correction signal generation Rx: Ignore PRTs
<b>Symbol precoding</b>	No	No	No	Tx: Precoding (DFT) Rx: Decoding (IDFT)
<b>Interleaving</b>	No	No	Yes	Tx: IDFTs, interleaving Rx: Side information reception, inverse interleaving
<b>ACE</b>	No	Yes	No	Tx: IDFTs, constellation modification Rx: None

Table 5.1 – PAPR reduction technique comparison.

In future PONs where the data rate is more than 10 Gb/s, Interleaving, SLM, PTS and clipping-based TR techniques might not be good candidates due to high complexity. TI technique is less preferable than TR technique since a PAPR correction signal occupies the same frequency band as a useful signal, resulting in increased BER on the receiver side. However, gradient-based TR technique using a contiguous PRT pattern is shown to be a good candidate since it gives a compromise between complexity and PAPR reduction capability. In practice, this technique can be followed by a clipping-filtering stage in order to obtain better PAPR reduction performance.

### 5.3. OFDM timing synchronization

Besides an important PAPR of OFDM signals, the OFDM modulation is well-known for its sensitivity to timing and frequency synchronization. On the receiver side, synchronization in an OFDM transmission involves three important processes as follows.

- 1) Timing synchronization: This process consists in detecting the beginning of a transmitted OFDM symbol. An FFT is then applied in order to demodulate the detected symbol. In the literature, this process is sometimes called the detection of FFT windows.
- 2) Carrier frequency synchronization: In OFDM transmissions where local oscillators are used, it is possible that local oscillator frequencies are different. In this case, CFO is a value to be estimated and compensated on the receiver side since it can generate ICI.
- 3) Sampling frequency synchronization: In practice, the sampling frequency of a DAC on the transmitter side might be different from that of an ADC on the receiver side. SFO is found to cause ICI in an OFDM transmission. In addition, it also causes slowly FFT window drift, which may generate additional ICI and ISI.

In the scope of this thesis, a real-valued OFDM signal is generated by means of a Hermitian symmetry (*c.f.* section 4.5.1.1). On both the transmitter and the receiver sides, there are no local oscillators. Hence, a transmission is not susceptible to CFO. In broadcast transmissions, the SFO may generate slow time drift, which in turns generates a timing offset. In the context of PONs where communication is usually in burst mode, this phenomenon is less significant. In addition, carrier phase rotation caused by the SFO can be compensated by means of channel estimation techniques.

On the other hand, timing synchronization plays an important role in an OFDM transmission since it detects the frame beginning for a demodulation by FFT on the receiver side. In addition, in the context of optical transmissions where data rate is in the order of multiple Gb/s, the complexity of a time acquisition technique must be carefully studied. For these reasons, in this thesis we focus on timing synchronization techniques. In the following sections this problem will be thoroughly discussed in the context of optical IMDD channel. New synchronization techniques are also proposed and compared with conventional techniques.

An offset from correct timing points can cause, in most cases, ICI and sometimes ISI, resulting in the degradation of transmission performance. In radio communications, timing synchronization for OFDM transmissions has been extensively studied and reported in [115]–[123]. However, in the context of optical IMDD OFDM transmissions, this issue has not yet been thoroughly examined. In the literature, one of the first timing synchronization techniques for OFDM transmissions was proposed by Jan-Jaap van de Beek [121], who used the cyclic prefix to find the symbol timing. Recently, a cyclic-prefix-based synchronization technique was proposed for IMDD OFDM transmissions [124]. However, this technique requires a large cyclic prefix, resulting in reduced transmission spectral efficiency. In the context of access networks, where the transmission distance is relatively short, the required cyclic prefix length might not be large. Hence, the technique proposed in [124] may not be an interesting solution for this application. Actually, in modern OFDM transmission systems, timing synchronization is carried out mostly by means of a preamble. On the transmitter side the header of an OFDM frame includes a preamble having a specific structure. Then, based on the structure of the transmitted preamble, a

synchronization metric is calculated on the receiver side. In general, this metric will introduce a peak based on which the receiver detects the beginning of the data frame. Preamble-based synchronization techniques are interesting for timing synchronization for two reasons. Firstly, they are robust against the Gaussian channel noise. According to the SNR on the receiver side, the preamble length and/or the number of preambles can be adjusted to increase robustness. Secondly, the preamble can be built by the same procedure as that of OFDM data symbols. Hence, on the receiver side the preamble can be demodulated and the preamble data can be used for signalization such as general information about the modulation and system identification, *etc.*

In this section novel preamble-based synchronization techniques for burst-mode optical IMDD OFDM transmission are proposed. By means of numerical simulations, a comparative study of the proposed methods and conventional synchronization methods is given. According to simulation results, the proposed techniques are shown to provide a more precise timing position, resulting in better performance in terms of BER and transmission throughput with reduced receiver complexity.

### 5.3.1. Simulation setup

In order to simulate burst-mode transmissions, a transmitted signal frame is made up of one preamble and one OFDM data symbol. The frame is preceded and followed by null samples. In the context of optical Gb/s transmissions, the complexity of an IFFT may become a challenge. For this reason small-size-FFT systems are considered in this section. The FFT size is equal to 256. The DC subcarrier (subcarrier index is 0) and Nyquist subcarrier (subcarrier index is 128) are filled with zeroes. 40 subcarriers at the edge of the spectrum (subcarrier indices from -127 to -108 and from 108 to 127) are set to zero to reduce the aliasing impact. 107 positive-frequency subcarriers (subcarrier indices from 1 to 107) carry useful data. To generate a real-valued OFDM signal, negative-frequency subcarriers (subcarrier indices from -1 to -107) are the complex conjugates of the 107 corresponding positive-frequency subcarriers. The frequency-domain data of OFDM symbols and those of the preamble are randomly chosen from a QPSK constellation. The DAC is quantized over 8 bits and the clipping rate, which is the ratio between the maximal quantized power and the average power, is 13 dB. The optical launch power is 0 dBm and fiber length varies from 0 to 100 km. At the receiver end, the received optical power varies according to insertion loss in the transmission link. For the channel equalization, zero-forcing technique using several training symbols is found to give good performance. For simplicity this technique is used for simulations.

In the context of future PONs, a single channel might support data transmission of tens of Gb/s, for which the impact of chromatic dispersion on transmission performance might be significant. As discussed in [1], [11], [42], OFDM modulation is a strong candidate for future PONs thanks to high tolerance to chromatic dispersion. For these reasons, it is worth studying synchronization techniques in the context of large-band OFDM signals. In this section, the sampling frequency of the DAC is supposed to be equal to 12 GS/s. Because of null subcarriers at the edge of the spectrum, for each transmitted burst described in this section, the effective bandwidth of OFDM signals is 10 GHz.

On the receiver side, the sampling frequency of the ADC is 12 GS/s, which is the same as that of the DAC. In order to simulate an analog transmission, OFDM signals are oversampled by a factor of 12. Oversampling is necessary for well simulating high-order harmonics generated due to nonlinearities. The oversampling factor of 12 is chosen as a

compromise between simulation time and precision. Received discrete samples  $y_d$  after the ADC can be expressed as

$$y_d = y(dT_s + t_0), \quad (5.12)$$

$$t_0 = kT_s/12, \quad (5.13)$$

where  $y(t)$  is the analog signal at the photodetector output.  $d$  is the sample index and  $T_s$  is the sampling time of the ADC. Because the receiver has no information about the arrival time of OFDM symbols, the ADC may sample between two consecutive transmitted samples, resulting in an inherent timing offset  $t_0$  given in Eq. (5.13). In OFDM systems, with the cyclic prefix, this inherent timing offset results in phase rotation of OFDM subcarriers. This phenomenon is referred to as the Random Sampling Phase (RSP) of the ADC. In order to simulate the RSP, for each received burst the value of  $k$  in Eq. (5.13) is randomly chosen from one of 12 integer values from 0 to 11. Statistically,  $k$  has a uniform distribution.

### 5.3.2. State-of-the-art preamble-based OFDM synchronization techniques

#### 5.3.2.1. Schmidl-Cox's technique

One of the first preamble-based synchronization techniques for OFDM transmissions was proposed by Schmidl and Cox (SC). The SC's time domain preamble consists of two identical sequences [115]

$$Preamble_{SC} = [A_{N/2} \ A_{N/2}]. \quad (5.14)$$

Each sequence is made up of  $N/2$  samples, where  $N$  refers to the IFFT size. The training sequence  $A$  can be generated by taking a real IFFT of size  $N/2$  of a random QPSK sequence. It is noted that in the context of optical IMDD transmission, the training sequence must be real-valued. On the receiver side, the synchronization metric takes the form

$$M_{SC}(d) = \left| \frac{P_{SC}(d)}{R_{SC}(d)} \right|^2, \quad (5.15)$$

where

$$P_{SC}(d) = \sum_{i=0}^{\frac{N}{2}-1} y_{d+i} y_{d+i+\frac{N}{2}}. \quad (5.16)$$

$$R_{SC}(d) = \sum_{i=0}^{\frac{N}{2}-1} \left| y_{d+i+\frac{N}{2}} \right|^2. \quad (5.17)$$

In the context of optical IMDD transmissions, the receiver performs only real-valued operations because the received signal after a photodiode is real-valued. The conjugate operator in synchronization metrics for radio communications can be dropped. In the

equations above,  $R_{SC}(d)$  is a power normalizing factor, whereas  $P_{SC}(d)$  is the correlation of two identical sequences of a preamble. Because of the cyclic prefix, the SC's synchronization metric presents a plateau, which leads to uncertainties of the frame beginning detection. To reduce this effect, Schmidl and Cox proposed an averaging method which decides the timing point as the middle point between the two 90%-of-the-maximum-metric points. However, the variance of the timing estimator is still large. In addition, the metric is not sharp but spreads over the whole OFDM symbol as illustrated in Figure 5.12. It will be shown later that because of this, the receiver requires a large memory to identify the maximum metric point and the two 90%-maximum points.

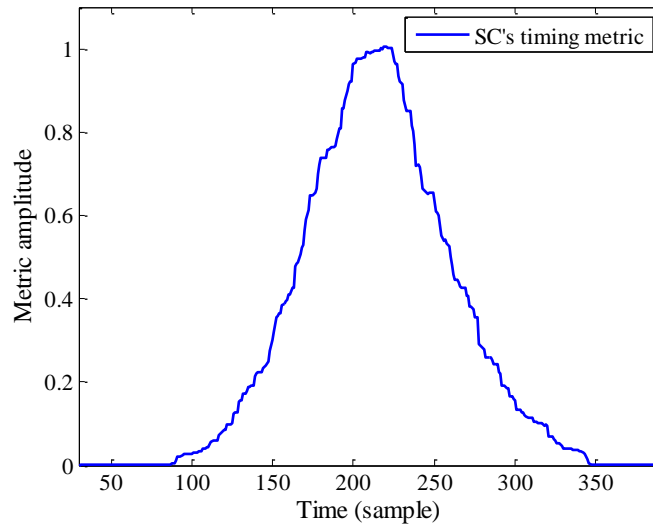


Figure 5.12 – Timing metric of Schmidl-Cox's technique in a 10-km IMDD channel.

It is interesting to note that the SC's timing metric can be recursively calculated, resulting reduced complexity. Without recursive calculation, the receiver must compute  $N/2 - 1$  additions (and  $N/2$  multiplications) for each timing metric value. When recursive computation is used, the number of additions and multiplications is reduced to only 4 and 4, respectively. Hence, recursive calculation reduces the receiver complexity by a factor of about  $N/8$ . For this reason this technique has been adopted in many modern communication standards as a coarse timing synchronization technique. The analysis of synchronization complexity is later discussed in more details in section 5.3.4.8.

### 5.3.2.2. Minn's technique

Minn *et al.* proposed in [117] a new preamble structure  $[B_{N/4} B_{N/4} -B_{N/4} -B_{N/4}]$  in order to obtain a sharper timing metric when compared to that of the SC's method. The preamble structure of Minn's method is expressed as

$$Preamble_{Minn} = [B_{N/4} \quad B_{N/4} \quad -B_{N/4} \quad -B_{N/4}]. \quad (5.18)$$

The timing metric on the receiver side is defined as

$$M_{Minn}(d) = \left| \frac{P_{Minn}(d)}{R_{Minn}(d)} \right|^2, \quad (5.19)$$

where

$$P_{Minn}(d) = \sum_{k=0}^1 \sum_{i=0}^{\frac{N}{4}-1} y_{d+\frac{N}{2}k+i} y_{d+\frac{N}{2}k+i+\frac{N}{4}}^* \quad (5.20)$$

$$R_{Minn}(d) = 0.5 \sum_{i=0}^{N-1} |y_{d+i}|^2 \quad (5.21)$$

Here,  $R_{Minn}(d)$  is a power normalizing factor, whereas  $P_{Minn}(d)$  is a sum of two correlation terms which are: the correlation of the first and the second sequence; the correlation of the third and the fourth sequence in a preamble. The timing metric of Minn's method is sharper than that of SC's method and it does not introduce a plateau, which reduces the variance of the timing estimator. Moreover, similar to an SC's metric, Minn's metric can also be recursively computed in order to reduce hardware complexity. However, Minn's timing metric introduces some minor peaks around the main peak as illustrated in Figure 5.13. In a noisy channel the magnitude of minor peaks may be larger than that of the main peak. Hence, it is possible that the receiver detects a secondary peak rather than the main peak, resulting in severe ICI and ISI.

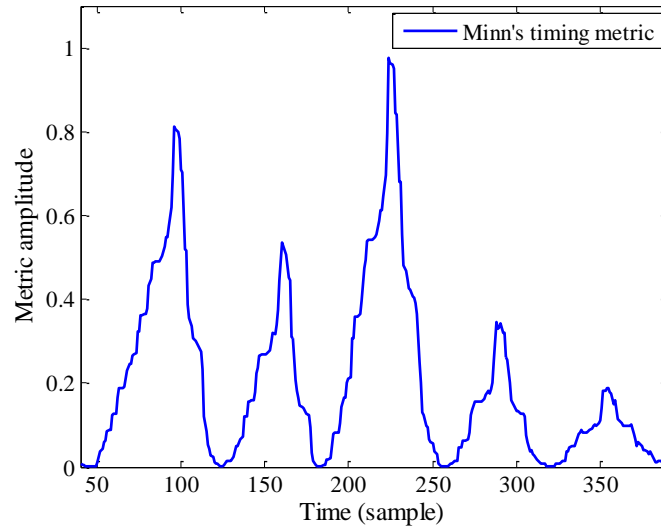


Figure 5.13 – Timing metric of Minn's technique in a 10-km IMDD channel.

### 5.3.2.3. Shi-Serpedin's technique

Based on the preamble structure family proposed by Minn, Shi and Serpedin published in [115] a maximum likelihood timing estimator. The time-domain preamble structure of Shi-Serpedin's technique is expressed as

$$Preamble_{shi} = [D_{N/4} \ D_{N/4} \ -D_{N/4} \ D_{N/4}]. \quad (5.22)$$

The maximum likelihood timing metric is defined as

$$M_{Shi}(d) = \frac{P_{Shi}(d)}{R_{Shi}(d)} = \frac{|P_1(d)| + |P_2(d)| + |P_3(d)|}{\frac{3}{2} \sum_{i=1}^4 |R_i|^2}, \quad (5.23)$$

where  $R_i$  denotes a vector of received signal samples

$$R_i = \left[ y_{d+\frac{(i-1)N}{4}}, \dots, y_{d+\frac{iN}{4}-1} \right]^T, \quad i = 1, \dots, 4 \quad (5.24)$$

and

$$P_1(d) = R_1^T R_2 - R_2^T R_3 - R_3^T R_4. \quad (5.25)$$

$$P_2(d) = R_2^T R_4 - R_1^T R_3. \quad (5.26)$$

$$P_3(d) = R_1^T R_4. \quad (5.27)$$

Shi's timing metric introduces no minor peak. However, since the metric is built based on repetitive sequences, two consecutive metric values have strong correlation as illustrated in Figure 5.14. Hence, the variance of timing offset is still large even with high received optical power. In addition, the method of Shi and Serpedin is more complex than the ones of SC and Minn since it requires more operations to be computed.

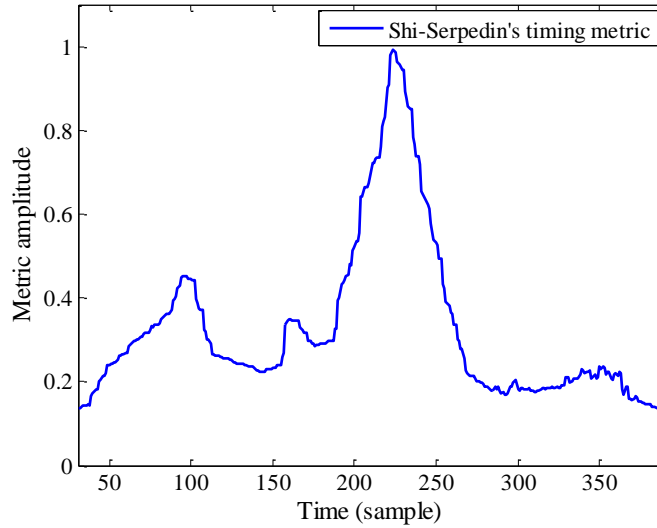


Figure 5.14 – Timing metric of Shi-Serpedin's technique in a 10-km IMDD channel.

#### 5.3.2.4. Park's technique

In order to minimize the correlation between two consecutive metric values, Park later proposed his new synchronization scheme in [119]. The new preamble structure is written as

$$Preamble_{Park} = [C_{N/4} \text{fliplr}(C_{N/4}) \quad C_{N/4} \text{fliplr}(C_{N/4})], \quad (5.28)$$

where  $\text{fliplr}(\cdot)$  denotes the left-right-flipped operation. The timing metric is defined as

$$M_{Park}(d) = \left| \frac{P_{Park}(d)}{R_{Park}(d)} \right|^2, \quad (5.29)$$

where

$$P_{Park}(d) = \sum_{i=0}^{\frac{N}{2}-1} y_{d-i} y_{d+i}. \quad (5.30)$$

$$R_{Park}(d) = \sum_{i=0}^{\frac{N}{2}-1} |y_{d+i}|^2. \quad (5.31)$$

By maximizing the number of different terms between two consecutive timing metric points, Park's method gives an impulse-like timing metric. However, Park's timing metric still introduces two minor peaks around the main peak. Moreover, in an optical IMDD channel, the combined impact of chromatic dispersion and laser chirps destroys the symmetric characteristic of the preamble. Therefore, the level of the main peak is strongly degraded. In a noisy channel, the receiver may detect one of the minor peaks or a peak generated by noise rather than the principal peak, resulting in increased timing offset variance and BER degradation [120].

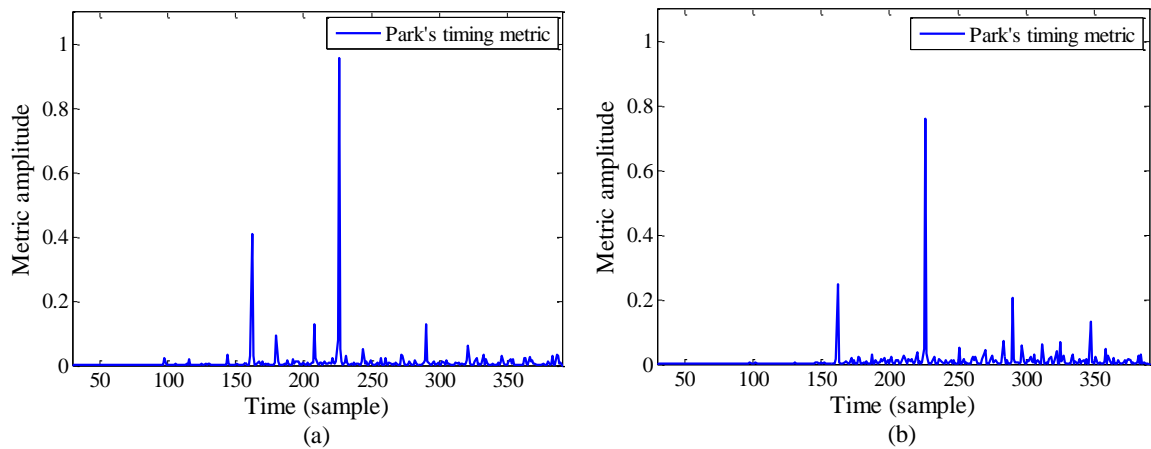


Figure 5.15 – Timing metric of Park's technique. (a) Fiber length is 0 km. (b) Fiber length is 40 km.

Inspired by Park's idea of an impulse-like timing metric, several other techniques are reported in [120], [123]. In [120] a modified version of Park's method is proposed in order to suppress the minor peaks. However, similar to Park's method, recursive computation is not possible with the new preamble structure, resulting in a complex receiver. In the context of multi Gb/s optical communications, this might not be practical. In [123] the authors proposed to multiply the SC's preamble with a random sequence in order to obtain an impulse-like timing metric. The minor peaks are also suppressed. However, both techniques proposed in [120], [123] do not have a strong principal peak due to the combined impact of chromatic dispersion and laser chirps. Moreover, metric computation is far more complex than that of other techniques because recursive computation is not possible.

### 5.3.3. Proposed timing synchronization methods

Before presenting the proposed techniques, two important remarks should be made.

- 1) Firstly, the performance of the synchronization techniques strongly depends on the value of chromatic dispersion. A slowly varying time domain signal is less sensitive to chromatic dispersion than a fast varying preamble because the delay caused by chromatic dispersion is proportional to the signal bandwidth. (i)
- 2) Secondly, the repetitive structure of a preamble makes the recursive calculation of synchronization metric possible, resulting in a less complex receiver. Receiver complexity is a critical criterion for designing a synchronization technique since the transmission bit rate is of tens of gigabits per second. (ii)

By using the first remark (i), we have reported in [2] an improvement of Park's method. By using only low-frequency sub-carriers to build the preamble, one can improve the quality of the main peak. The proposed method in [2] gives a better performance in terms of timing offset variance at moderate and high SNRs. However, at low SNRs the proposed method does not guarantee reliable time synchronization.

We later reported in [3] a new preamble structure in order to consider both remarks (i) and (ii). Based on the proposed preamble, a two-stage synchronization algorithm is proposed. The coarse packet detection and the fine timing synchronization are effectuated by using one unique preamble symbol. Thanks to the particular structure of the preamble, a first coarse synchronization metric does not present minor peaks. In addition, without the knowledge of the preamble waveform the receiver can perform both coarse and fine synchronization steps. By means of numerical simulations, when compared to conventional methods, the proposed method is shown to provide better performance in terms of timing offset variance with reduced receiver complexity. In unamplified optical IMDD transmissions, the proposed technique guarantees a quasi-optimal transmission capacity even with a short cyclic prefix. For the sake of convention, "proposed I" and "proposed II" denote the first and the second propositions, respectively.

#### 5.3.3.1. First proposition – an improved version of Park's technique

Inspired by the technique proposed by Park, we propose a modified preamble structure written as

$$Preamble_I = [C_{N/4} \quad C_{N/4} \quad \text{fliplr}(C_{N/4}) \quad \text{fliplr}(C_{N/4})]. \quad (5.32)$$

The timing metric is defined as

$$M_{proposed I}(d) = \frac{|P_{proposed I}(d)|^2}{|R_{proposed I}(d)|}, \quad (5.33)$$

where

$$P_{proposed I}(d) = \sum_{i=0}^{\frac{N}{2}-1} y_{d-i} y_{d+i}. \quad (5.34)$$

$$R_{Proposed I}(d) = 0.5 \sum_{i=0}^{N-1} |y_{d+i}|^2. \quad (5.35)$$

Similar to Park's method,  $R_{Proposed I}(d)$  is simply a power normalizing factor, whereas  $P_{Proposed I}(d)$  is designed such that the symmetric structure of the preamble is exploited to produce an impulse-like timing metric. It is important to note that the length of the sequence  $C$  must be an odd value in order to attenuate minor peak amplitude. In addition, in order to improve the level of the principle peak under a dispersive channel, we propose to use only certain low-frequency subcarriers to generate the training sequence  $C$ . Figure 5.16 is an illustration of the proposed timing metric.

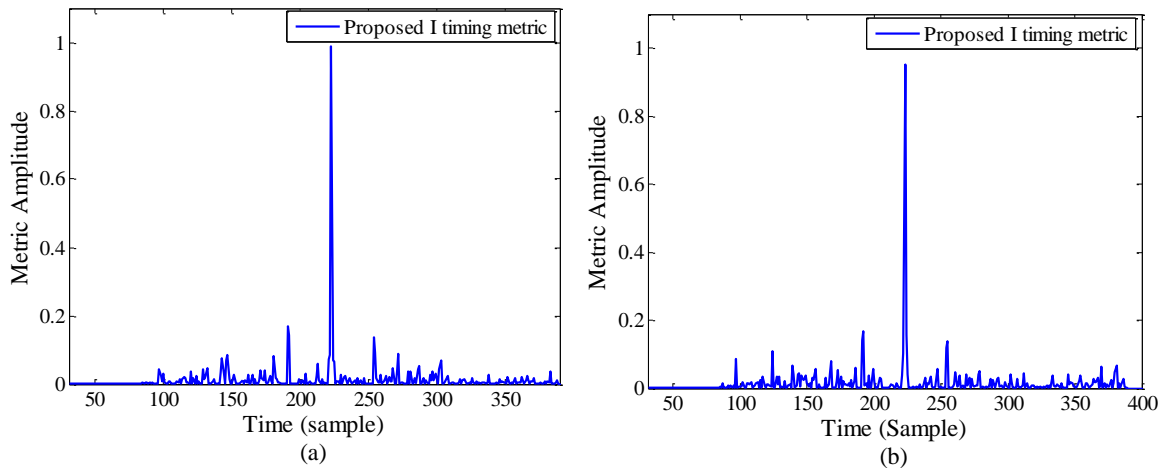


Figure 5.16 – Timing metric of the Proposed I technique. Only 15% low-frequency subcarriers is used to build the preamble. (a) Fiber length is 0 km. (b) Fiber length is 40 km.

As shown in the figure above, the fact that the preamble is built only with low-frequency components strongly improves the magnitude of the principle peak when fiber length increases. However, similar to Park's technique, our first proposition still does not solve the complexity problem cited in the second remark (ii). In the next section we propose the second technique to deal with this problem.

### 5.3.3.2. Second proposition – a hybrid two-stage synchronization technique

In the proposed II method, the time-domain preamble can be written as

$$Preamble_{II} = [T_{l_1} \quad T_{l_1} \quad U_{l_2} \quad U_{l_2}], \quad (5.36)$$

where  $U = \text{fliplr}(T)_{l_2}$  and  $l_1 + l_2 = \frac{N}{2}$ .  $\text{fliplr}(T)_{l_2}$  can be described as follows. The row vector  $T$  is left-right-flipped. Then, the vector  $U$  corresponds to the first  $l_2$  elements of the resulting vector. Figure 5.17 illustrates the proposed preamble structure.

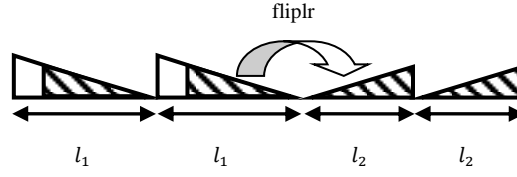


Figure 5.17 – The Proposed II preamble structure.

The time-domain sequence  $T_{l_1}$  in the proposed preamble is created by using an  $l_1$ -point IFFT of random QPSK data. The first timing metric, which measures the correlation between identical sequences of the preamble, serves coarse synchronization. The metric is defined as

$$M_{Coarse}(d) = \left| \frac{P_{Coarse}(d)}{R_{Coarse}(d)} \right|^2, \quad (5.37)$$

where

$$P_{Coarse}(d) = \sum_{i=0}^{l_1-1} y_{d+i} y_{d+i+l_1} + \sum_{i=0}^{l_2-1} y_{d+i+2l_1} y_{d+i+2l_1+l_2}, \quad (5.38)$$

$$R_{Coarse}(d) = 0.5 \sum_{i=0}^{N-1} |y_{d+i}|^2. \quad (5.39)$$

$R_{Coarse}(d)$  in Eq. (5.39) is simply a power normalizing factor of the coarse metric. In Eq. (5.38), the first sum corresponds to the correlation between the first two sequences  $T_{l_1}$  of the preamble. Similarly, the second sum is the correlation between the last two sequences  $U_{l_2}$  of the preamble. As shown in Figure 5.18(b), the coarse metric is built according to Eq. (5.37) so that it introduces a peak when the signal preamble is present on the receiver side. Moreover, minor peaks are not present.

By making use of the symmetric structure of the preamble, a second metric is computed for fine synchronization.

$$M_{Fine}(d) = \left| \frac{P_{Fine}(d)}{R_{Fine}(d)} \right|^2, \quad (5.40)$$

where

$$P_{Fine}(d) = \sum_{i=0}^{l_2-1} [y_{d+i+l_1-l_2} y_{d-i+2l_1+l_2-1} + y_{d+i+2l_1-l_2} y_{d-i+2l_1+2l_2-1}]. \quad (5.41)$$

$$R_{Fine}(d) = 0.5 \left\{ \sum_{i=0}^{l_2-1} [ |y_{d+i+l_1-l_2}|^2 + |y_{d+i+2l_1-l_2}|^2 ] + \sum_{i=0}^{2l_2-1} |y_{d+i+2l_1}|^2 \right\}. \quad (5.42)$$

Here  $R_{Fine}(d)$  is a power normalizing factor. As shown in Figure 5.17, a symmetric structure exists between the first sequence  $T_{l_1}$  and the third sequence  $U_{l_2}$ . Similarly, a symmetric structure also exists between the second sequence  $T_{l_1}$  and the fourth sequence  $U_{l_2}$  of a preamble. In Eq. (5.41), the first sum corresponds to the correlation between the third sequence  $U_{l_2}$  and its symmetric version in the first sequence  $T_{l_1}$ . Similarly, the second sum is the correlation between the fourth sequence  $U_{l_2}$  and its symmetric version in the second sequence  $T_{l_1}$ . As shown in Figure 5.18(b), the fine metric is built according to Eq. (5.40) so that it results in an impulse-like timing metric, which improves synchronization precision. According to Eq. (5.41), the performance of fine synchronization explicitly depends on  $l_2$ . Therefore, synchronization performance is improved when  $l_2$  approaches  $l_1$ . We recall that  $l_2$  and  $l_1$  must not be equal in order to avoid secondary peaks of the coarse synchronization step. In the context of IMDD transmissions the receiver performs only real-valued operations because the received signal after a photodiode is real-valued. The conjugate operator in synchronization metrics for radio communications can be dropped.

Based on the two timing metrics described above, a two-stage timing acquisition similar to that in [118] is proposed. This involves a coarse detection followed by a fine detection as illustrated in Figure 5.18.

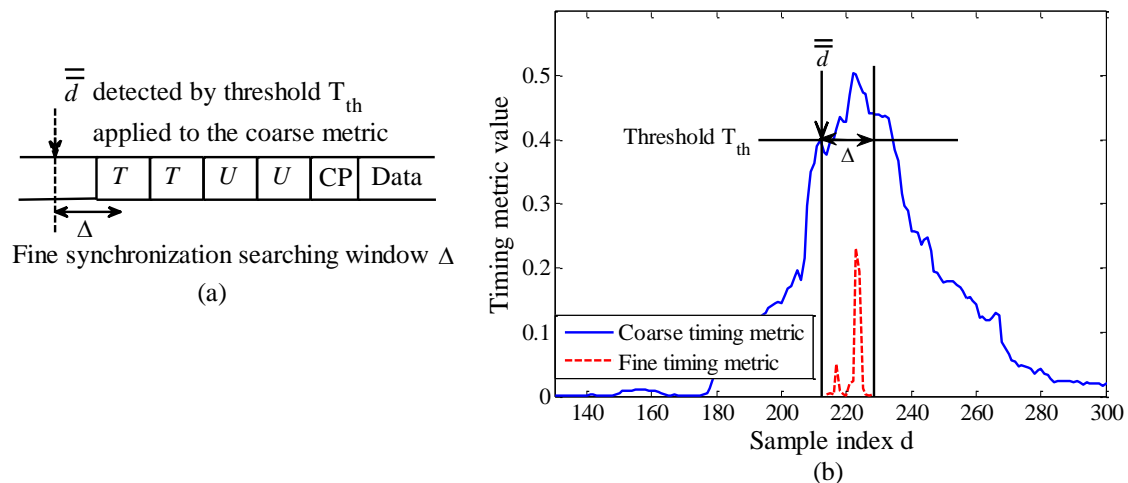


Figure 5.18 – (a) Two-stage synchronization illustration. (b) An example of the proposed coarse and fine metrics. Fiber length is 20 km. Received optical power is -20 dBm.

It is noted that the coarse metric can be recursively computed. The coarse metric value at sample index  $d$  can be computed according to that at sample index  $d - 1$ , resulting in reduced complexity (see Appendix A). Thanks to an impulse-like shape, in general, the fine metric gives more precise timing positions than the coarse metric. However, it is more complex because recursive computation is not possible. Actually, one can use only the fine metric for the synchronization. However, complexity in this case might be prohibitive. For this reason, in this chapter a two-stage timing acquisition is proposed. A transmitted signal burst is firstly detected by means of the coarse metric for reduced complexity. Then, the fine metric is used only in a reduced searching window in order to detect the frame beginning with better precision at a reduced computation cost. The proposed timing acquisition is described as follows.

**Step 1 – Coarse synchronization:** the timing metric  $M_{Coarse}(d)$  is compared to a pre-chosen threshold  $T_{th}$ . The threshold can be chosen according to a desired packet miss

probability. This is discussed in more detail in section 5.3.4.6. Once  $M_{Coarse}(d) > T_{th}$ , the detected position  $\bar{d}$  is stored. The receiver defines the searching range  $\Delta$  and the synchronization algorithm proceeds to the next step.

**Step 2 – Fine synchronization:** the timing metric  $M_{Fine}(d)$  is calculated for each time index  $d$  in the searching window  $= [\bar{d}, \dots, \bar{d} + \Delta]$ . The final timing point  $d_{timing\ point}$ , which corresponds to the maximum value of  $M_{Fine}(d)$  in the window  $W$ , is given by

$$d_{timing\ point} = \underset{d}{argmax}\{M_{Fine}(d)\}, \quad d \in [\bar{d} - \Delta, \dots, \bar{d} + \Delta]. \quad (5.43)$$

In Eq. (5.43),  $M_{hybrid}(d) = M_{Coarse}(d)M_{Fine}(d)$  can be used to replace  $M_{Fine}(d)$  to improve the timing estimator precision at the expense of increased receiver complexity.

In an IMDD channel, the interplay between chromatic dispersion and laser chirp can present strong high-frequency channel gain [11], [86]. Although we have shown in [2] that a narrow-band preamble is robust against chromatic dispersion, it does not benefit from this high-frequency channel gain. Hence, the choice of preamble bandwidth is a compromise between various system parameters including laser chirps, chromatic dispersion, signal level and noise power, *etc.* With the system parameters described in this chapter, the timing offset variance of the proposed technique as a function of preamble bandwidth is shown in Figure 5.19. In this case, received optical power is -14 dBm. The bias current is 60 mA and modulation index, which is defined as the ratio between the peak amplitude of the transmitted signal current and the bias current, is equal to 0.6. In this configuration, a preamble is optimized when its bandwidth is equal to 50 percent of the OFDM signal bandwidth. It is later shown that, with this percentage level, the proposed technique still outperforms conventional techniques in various channel conditions. From now on this percentage level is used for the proposed technique.

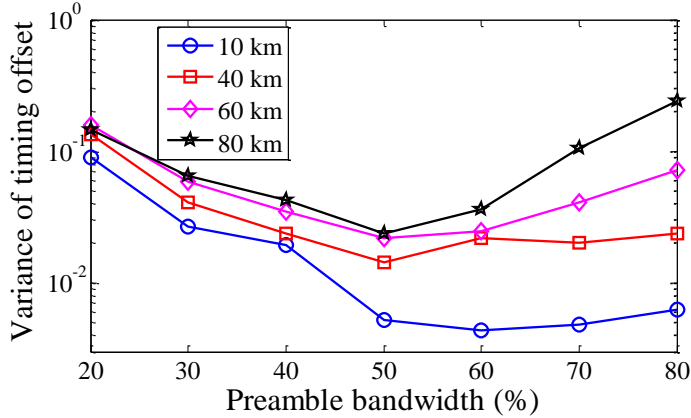


Figure 5.19 – Timing offset variance of the proposed technique versus preamble bandwidth. Received optical power is -14 dBm. Bias current is 60 mA. Modulation index is 0.6.

### 5.3.4. Performance analysis

In this performance evaluation section the time synchronization techniques are evaluated with several criteria:

- The robustness of the techniques under different channel conditions. This robustness is measured by the variance of the timing offset, which is the mean square of the deviation from the correct timing point of the detected timing points;
- False detection and missing probabilities as a function of timing threshold;
- Performance in terms of transmission capacity – the ultimate performance.

In the simulations, the lengths  $l_1$  and  $l_2$  of the sub-sequences of the proposed preamble are 68 and 60, respectively.

#### 5.3.4.1. Tolerance to laser bias current

In practice, laser bias current may change to adjust the optical power coupled to the fiber link. Hence, the tolerance of a synchronization technique to various laser launching conditions is a crucial criterion. Figure 5.20 illustrates the timing offset variance of different synchronization techniques as a function of laser bias current. It is observed that the performance of all the reported techniques does not depend on launching condition. Indeed, a change in bias current changes the AM and FM response of laser. Furthermore, the adiabatic chirp frequency also changes. As a consequence, intermodulation noise power varies as a function of bias current due to FM-to-AM conversion [86]. However, performance remains stable as long as the fiber length and the received optical power remain unchanged. In the next paragraphs it will be shown that the performance of a synchronization technique depends more strongly on the received optical power. For the sake of comparison between different techniques, from now on the laser bias current is kept at 60 mA for all the simulations.

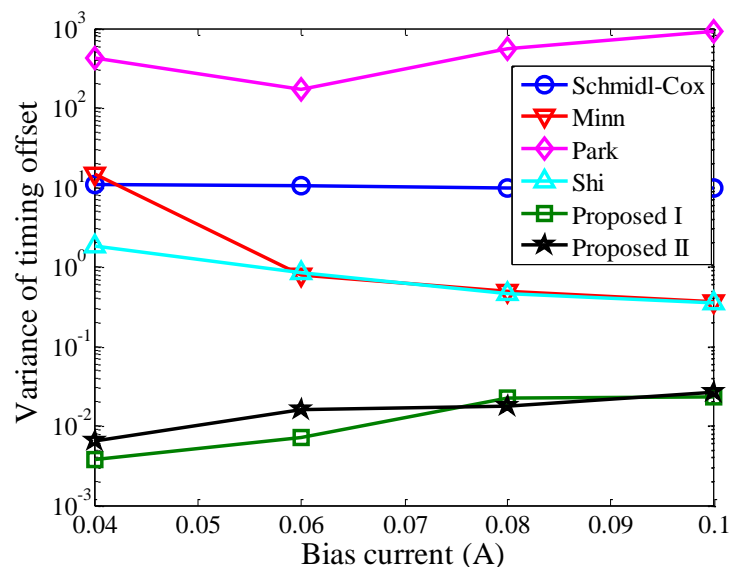


Figure 5.20 – Timing offset variance as a function of laser bias current. Fiber length is 40 km. Received optical power is -14 dBm.

#### 5.3.4.2. Impact of modulation index

When transmission distance increases, the modulation index of transmitted signals can also increase to improve the signal to photodetector noise ratio (SPNR) on the receiver side. However, an increase of modulation index may also result in an increase of nonlinear noise

power [86]. We have also shown in [1] that for each value of fiber length, an optimal modulation index, which is a compromise between photodetector noise and nonlinear noise, must be found in order to optimize transmission capacity. Hence, it is important to study the impact of modulation index on the performance of synchronization techniques. In order to study the impact of nonlinear noise, we consider two transmission configurations: short-reach transmission (10 km) and relatively long-reach transmission (80 km). In the considered system examples, the clipping rate, which is the ratio between the clipped power of the DAC and the signal average power, is 13 dB.

**5.3.4.2.1. 10-km transmission**

The timing offset variance versus modulation index is shown in Figure 5.21. When the SPNR is high, as shown in Figure 5.21(a), the performance of synchronization techniques does not strongly depend on modulation index because the power of nonlinear noise is still low. In Figure 5.21(b), when the received optical power is low, an increase of modulation index improves the SPNR, resulting in the performance improvement of synchronization techniques. When modulation index is larger than 1.2, further increase of modulation index does not improve the synchronization performance because of laser saturation.

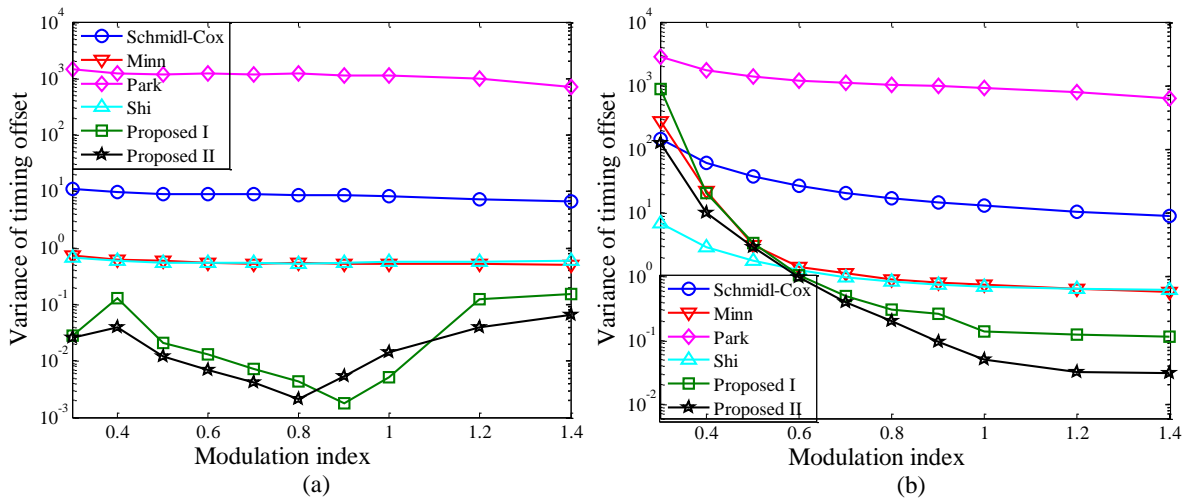


Figure 5.21 – Variance of timing offset as a function of modulation index. Fiber length is 10 km. (a) Received optical power is -14 dBm. (b) Received optical power is -20 dBm.

**5.3.4.2.2. 80-km transmission**

In this case the nonlinear noise power might become more significant than in the previous case [86]. At high SPNRs, when modulation index increases, nonlinear noise power also increases. This results in performance degradation of synchronization techniques as shown in Figure 5.22(a). In the case where both photodetector noise and nonlinear noise are significant as shown in Figure 5.22(b), when modulation index increases from 0.3 to 0.6, the performance of synchronization techniques is improved thanks to an improved SPNR. However, further increase of modulation index degrades the synchronization performance due to significant nonlinear noise.

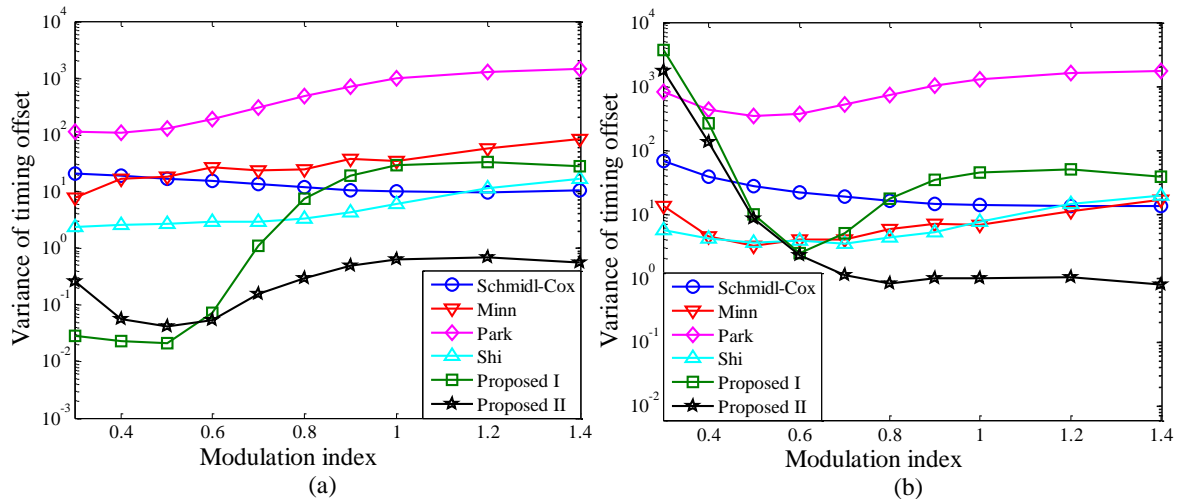


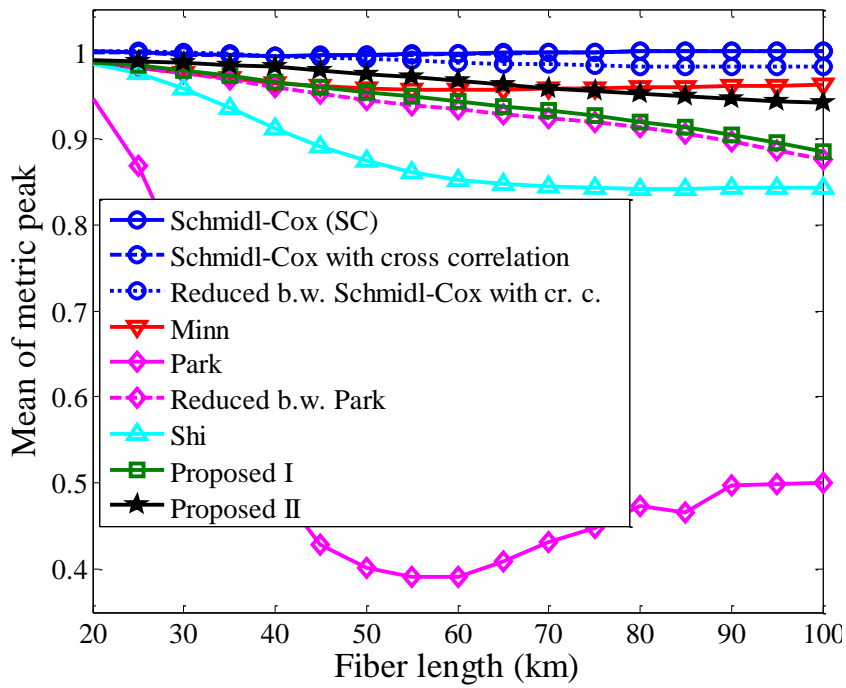
Figure 5.22 – Variance of timing offset as a function of modulation index. Fiber length is 80 km.  
 (a) Received optical power is -14 dBm. (b) Received optical power is -20 dBm.

From Figure 5.22, Park technique and the proposed I technique, which are only based on the symmetric structures of the preamble, are found to have low tolerance to nonlinear noise. Because of high minor peaks, the performance of Minn's technique is found to be sensitive to nonlinear noise. The maximum likelihood timing estimator of Shi's technique, which was built based on the assumption of white Gaussian noise, is also found to have low robustness against nonlinear noise. On the contrary, the use of repetitive structures in SC and the proposed II techniques results in better performance when nonlinear noise is present.

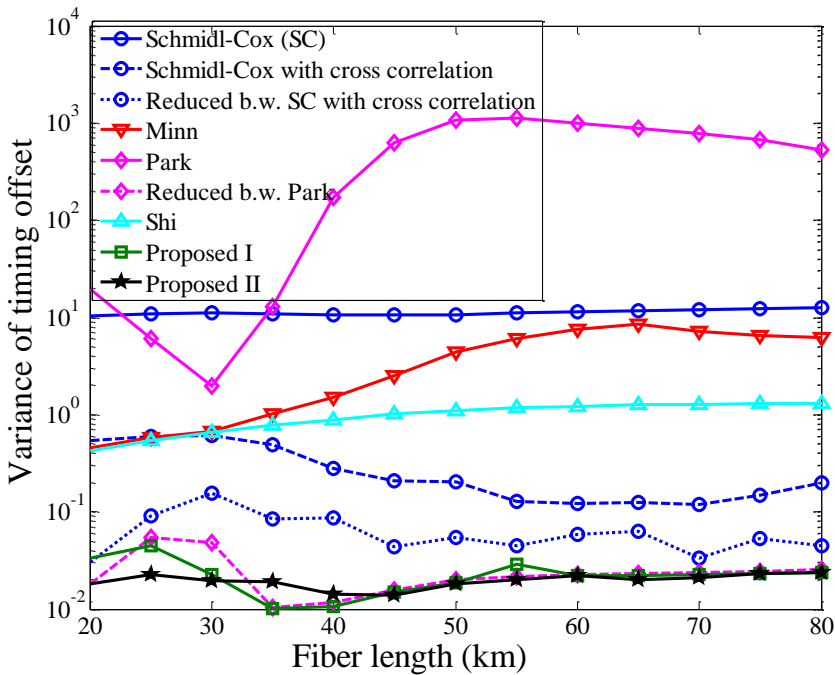
For the sake of simplicity, from now on the modulation index is kept at 0.6. As shown in Figure 5.22(b), although this value is not the optimum for SC and the proposed II techniques, it is the optimum for other techniques when both nonlinear and photodetector noise are significant.

### 5.3.4.3. Tolerance to transmission distance

In general, Optical Network Units (ONUs) locate at various distances from the Optical Line Terminal (OLT). In order to guarantee the reliability of transmissions for all users, it is necessary for a synchronization technique to be robust against transmission distance. As illustrated in Figure 5.23(b), as long as the received optical power is fixed, the performance of all the techniques except the Park's one does not depend on transmission distance. In the methods having repetitive preamble structure, several identical sequences are transmitted. On the receiver side, even if the channel frequency response changes according to the transmission distance, the received sequences still have strong correlation because they propagate through the same channel. Hence, these techniques are robust against the channel. On the other hand, a dispersive channel significantly destroys the symmetric property of the preamble used in Park's method. As a consequence, the main peak of the synchronization metric is strongly degraded when transmission distance increases as shown in Figure 5.23(a), resulting in large timing offset variance as shown in Figure 5.23(b).



(a)



(b)

Figure 5.23 – Tolerance to fiber length performance comparison. (a) Mean of peaks of the timing metric versus transmission distance. Received optical power is -8 dBm. In order to isolate the impact of a random sampling phase, for each value of the fiber length the sampling instant is chosen to give the best performance. (b) Variance of timing offset as a function of transmission distance. Received optical power is -14 dBm.

As shown in Figure 5.23, the proposed I method outperforms Park’s method although both methods make use of preambles having a symmetric structure. This comes from the fact that the preamble used in the proposed I method is built with only low-frequency

components. Hence, the channel impact on the preamble is reduced. However, when the preamble in Park's method is also built with low-frequency components, the performance of Park's method in terms of timing offset variance approaches that of the proposed I method. In the proposed II method, the coarse metric makes use of the repetitive structure of the preamble. This results in a stronger coarse metric peak when compared to that of proposed I method as shown in Figure 5.23(a). However, in the fine synchronization step, both methods are based on impulse-like metrics. Hence, they have the same performance in terms of timing offset variance.

It is also shown in Figure 5.23(b) that the proposed II method outperforms the SC's method aided by a cross-correlation [122]. Actually, when cross-correlation between the stored preamble and the received signal is used for the fine synchronization step, the fine metric does not have an impulse-like shape as shown in Figure 5.24(a). In general, this is because the autocorrelation function of a specific preamble is not perfectly impulse-like. On the contrary, the proposed method introduces an impulse-like fine metric, resulting in a more precise timing detection. It is also noted that when SC preamble's bandwidth is reduced, its performance is also improved.

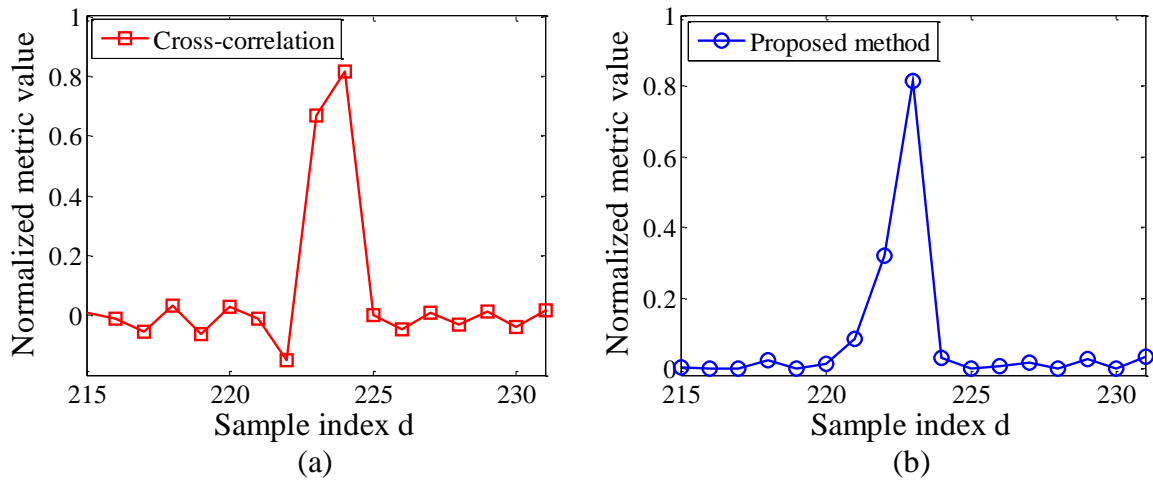


Figure 5.24 – Fine timing metrics. (a) Cross-correlation method used in [122]. (b) The proposed II method. Fiber length is 20 km. Received optical power is -10 dBm.

#### 5.3.4.4. Tolerance to ADC random sampling phase

In the time domain, RSP may have an impact on the structure of a transmitted preamble. Therefore, the magnitude level of synchronization metric peak might be degraded depending on the value of the inherent timing offset. In order to evaluate the tolerance to RSP of a technique, we calculate the variance of metric peak magnitude, which measures the variation of metric peak magnitude level as the inherent timing offset  $t_0$  described in Eqs. (5.12) and (5.13) randomly changes. The variance of metric peak magnitude is hence different from the timing offset variance, which measures the deviation of detected timing points from the correct timing point. When other system parameters such as fiber length, received optical power, *etc.* are fixed, synchronization techniques having larger values of variance of metric peak magnitude are found to be more sensitive to RSP. It is shown in Figure 5.25 that the techniques using a preamble with a repetitive structure are not sensitive to RSP. When the transmission distance increases the variance of metric peak also increases because chromatic dispersion destroys the perfect repetitive structure of the preamble. However, the variance of the detected peaks is still in the order of  $10^{-3}$  even in

relatively long transmissions ( $> 80$  km). On the contrary, the proposed I technique and that of Park, which rely only on the symmetric structure of the preamble, are shown to be the most sensitive to RSP. It is observed that even in back-to-back configuration, on the receiver side the symmetric property of a preamble is no longer preserved. When the bandwidth of a preamble tends to zero, the autocorrelation function of the time-domain preamble tends to a constant. Hence, in proposed I method, the correlation between a discrete transmitted preamble and a discrete received preamble with random sampling phase is stronger than the one in the case of Park's method. This explains better performance of the proposed I method. The performance of Park's method also approaches that of the proposed I method when only low-frequency subcarriers are used to build Park's preamble. The notch of Park's performance curve in Figure 5.23(b) can be explained by the filter effect of the optical channel. For fiber lengths longer than 30 km, chromatic dispersion-induced frequency attenuation dip begins to exist in the signal band. The channel response is equivalent to a low-pass filter thanks to which received preambles become slowly time-varying signals. As a consequence, Park's method is less sensitive to RSP. Hence, the proposal to use only low-frequency components to build a preamble is twofold: firstly, chromatic dispersion has less impact on the preamble and secondly, a slowly varying time-domain preamble is robust against the random sampling phase of an ADC.

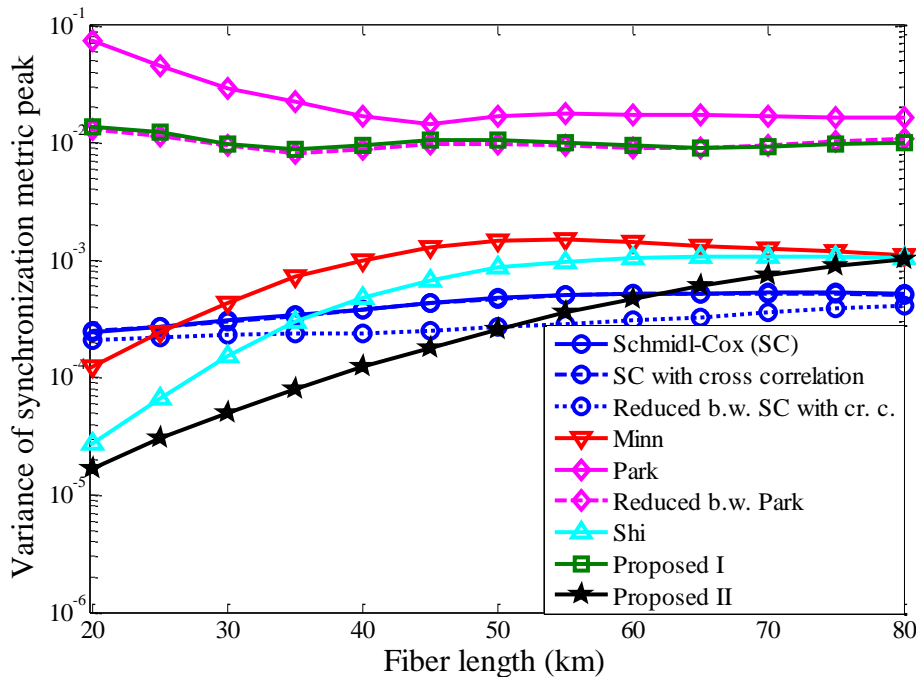


Figure 5.25 – Variance of metric's peak as a function of transmission distance. Received optical power is -8 dBm.

#### 5.3.4.5. Tolerance to noise

Due to fiber attenuation, users located far from an OLT may have weak received optical power. Hence it is important for a synchronization technique to be able to locate the frame beginning even at low received optical power. Figure 5.26 illustrates the variance of timing offset as a function of received optical power. Because the fine synchronization step is aided by the coarse step, proposed II method outperforms the proposed I method at low SNRs. At high SNRs, the proposed methods perform better than the other methods thanks

to impulse-like timing metrics and high tolerance to RSP. Furthermore, the performance of Park's method with a reduced-bandwidth preamble approaches that of proposed methods. The proposed techniques can guarantee the timing offset deviation of only 1 sample as long as the received optical power is kept above -19 dBm, which corresponds to an unamplified 100-km fiber link.

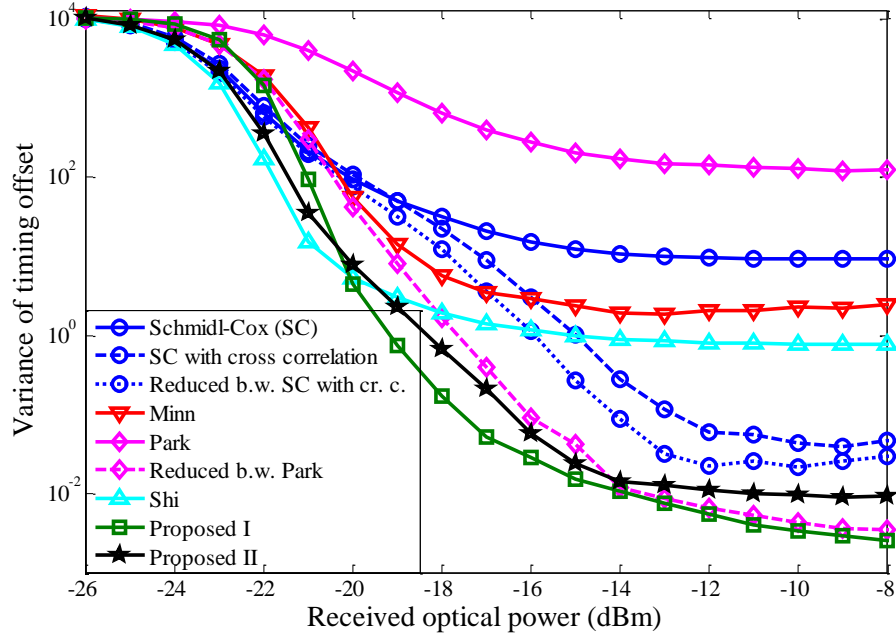


Figure 5.26 – Variance of timing offset as a function of received optical power. Fiber length is 40 km.

#### 5.3.4.6. False detection and packet miss probabilities performance

In the coarse synchronization step, the coarse metric value is compared to threshold  $T_{th}$  to detect the presence of a transmitted frame. In the context of burst transmission, the value of  $T_{th}$  must be chosen to minimize false-alarm and packet miss probabilities. False-alarm probability is shown to be negligible when the timing threshold is higher than 0.5 [2]. Packet miss probability as a function of timing threshold is illustrated in Figure 5.27(a). Because of the dispersive channel and random sampling phase, the metric peak magnitude of Park's method is strongly degraded, resulting in high packet miss probability when the threshold increases. By reducing the preamble bandwidth, the performance of Park's method is improved and approaches that of the proposed I method. Thanks to strong robustness against the channel and random sampling phase, the techniques using preambles having repetitive structures perform the best. By using a slowly varying time-domain preamble, the proposed II method is less sensitive to RSP (Figure 5.25), resulting in a better performance in terms of packet miss probability when compared to other methods.

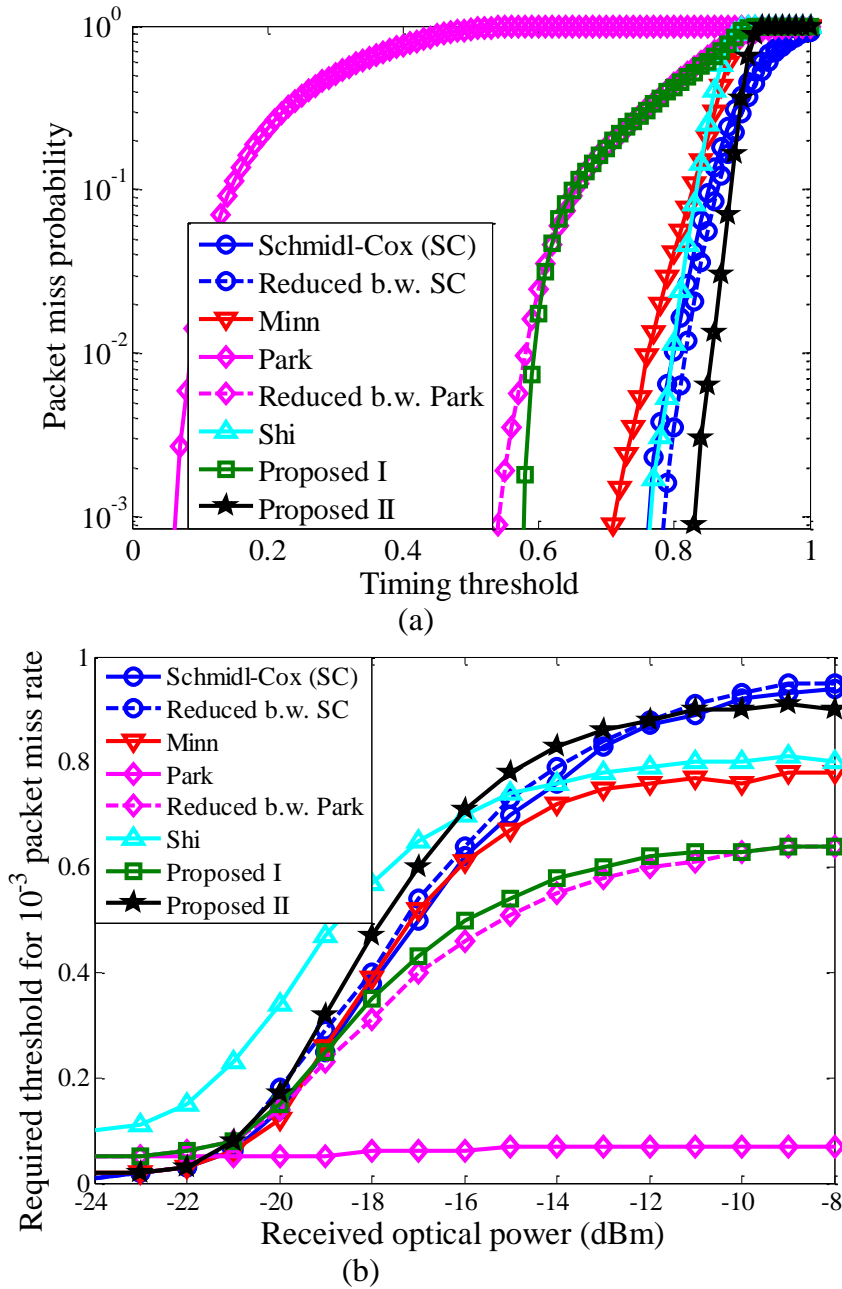


Figure 5.27 – Packet miss probability performance comparison. (a) Packet miss probability as a function of timing threshold. Fiber length 40 km. Received optical power -14 dBm. (b) Required threshold for  $10^{-3}$  packet miss rate as a function of received optical power.

In addition to false-alarm and packet miss probabilities, the searching range  $\Delta$  in the fine synchronization step also depends on  $T_{th}$ . In general, a coarse timing position  $\bar{d}$  approach the correct timing point when  $T_{th}$  increases. This results in a reduced searching range  $\Delta$  which in turns reduces the receiver complexity. However, an increase of  $T_{th}$  also increases the packet miss probability. Therefore, there are several rules of thumb for designing the timing threshold  $T_{th}$  and the searching range  $\Delta$  for a synchronization technique:

- Firstly,  $T_{th}$  is chosen as the largest value that still respects the packet miss probability constraint. The threshold value  $T_{th}$  as a function of received optical

power and fiber length can be calculated beforehand by numerical simulation (e.g. Figure 5.27(b)). During the initialization stage, transmission training sequences can be sent to estimate channel information such as distance and received optical power according to which an optimal threshold can be deduced;

- Secondly, the value of  $\Delta$  should be chosen as a compromise between the receiver complexity and the probability that correct timing points fall into the research window as illustrated in Figure 5.29.

### 5.3.4.7. Transmission throughput performance

Transmission capacity is always one of the first interests for a communication system designer. It is well known that in an OFDM transmission, an offset from the correct timing point may cause inter-carrier interference which decreases the SNR on the receiver side and limits the transmission throughput. In order to evaluate the impact of a time synchronization technique on the transmission capacity, the Levin-Campello adaptive modulation scheme [42], [81], [83], which is shown to be a cost-effective solution for access optical networks, is used in unamplified transmissions. The targeted symbol error rate is  $10^{-3}$ . The corresponding BER is hence always lower than  $10^{-3}$ , which allows error-free transmission with an appropriate Forward Error Correction. It is shown in Figure 5.28(a) that when the cyclic prefix is large all the reported techniques allow a quasi-optimal transmission in terms of useful data rate. This is because as long as the channel impulse response still remains within the cyclic prefix, no ICI occurs [89]. However, large cyclic prefix decreases the transmission spectral efficiency.

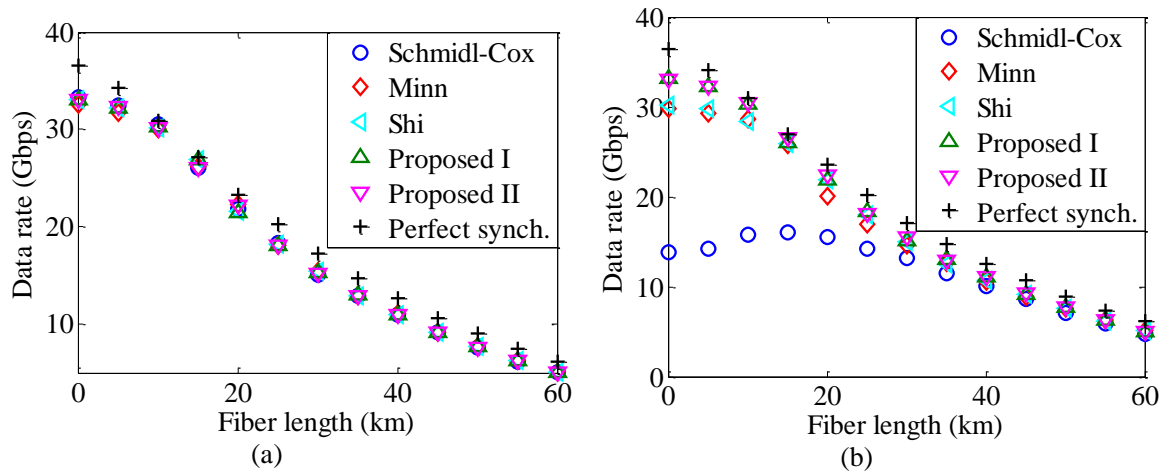


Figure 5.28 – Capacity of transmissions employing different synchronization techniques. (a) 8-sample cyclic prefix. (b) 4-sample cyclic prefix.

In the case where the cyclic prefix is made up of only four samples, the channel impulse response can fall out of the cyclic prefix even with small timing offset, resulting in inter-carrier interference. This scenario is well illustrated in Figure 5.28(b) where the SC's method significantly reduces the throughput due to a large timing offset. On the contrary, thanks to a precise timing detection, the proposed methods always guarantee a quasi-optimal transmission bit rate.

### 5.3.4.8. Complexity analysis

In optical communication systems where data are transmitted at Gigabits per second, the complexity of the synchronization technique used in the receiver is critical. Table 5.2 illustrates the complexity in terms of number of operations (additions, multiplications and divisions) required to compute coarse timing metrics of different synchronization techniques. It is noted that with a preamble having a repetitive structure the metric can be recursively calculated, resulting in a significantly reduced receiver complexity.

	Addition	Multiplication	Division
Schmidl	4	4	1
Minn	6	7	1
Park	$N/2 + 1$	$N/2 + 3$	1
Shi	16	14	1
Proposed I	$N/2 + 1$	$N/2 + 3$	1
Proposed II	6	7	1

Table 5.2 – Number of operations per received sample for coarse metric computation.

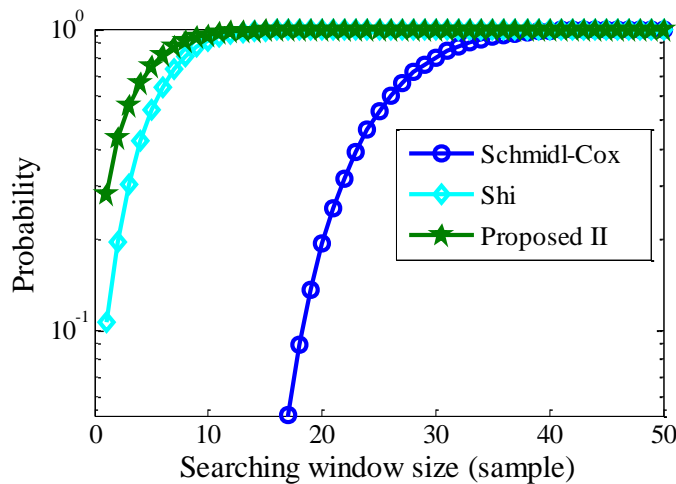


Figure 5.29 – Probability that the searching window covers the correct timing point as a function of the window size. The larger the research window, the more probably the correct timing point falls into this window. The timing thresholds are chosen so that the packet miss probability is maintained at  $10^{-3}$ . Fiber length is 40 km. Received optical power is -14 dBm.

In the fine synchronization step, the research window length depends on the coarse synchronization precision. When the timing position detected by the coarse metric is close to the correct timing point, a small window is required. On the contrary, a large searching window is necessary if the coarse detected timing point is far away from the correct timing point. Despite the simplicity of the SC's method, coarse detected timing positions are located far from the correct timing points. This results in a large searching window during the fine synchronization stage. Thanks to a less spread coarse metric, the proposed II method reduces the searching window length as illustrated in Figure 5.29.

In order to compare the complexity of different synchronization techniques, let us refer to the XG-PON standard where an upstream signal is composed of different packets

coming from different users. The minimum guard-time between consecutive packets is 64 bits (or samples) [6]. At the end of each packet the OLT must calculate the coarse metric in order to delimit the next signal frame. Hence, for each received frame the receiver must calculate at least 64 coarse metric points and  $\Delta$  fine metric points, where  $\Delta$  denotes the searching window length. Since the number of divisions is the same for all techniques, we consider only the number of additions and multiplications. In the next equations  $C_A$  and  $C_M$  denote the complexity of different techniques in terms of the number of additions and multiplications, respectively. We have several possible scenarios as follows.

- **Classical cross-correlation method:**

As indicated in the XG-PON standard, the synchronization consists in calculating the correlation between the preamble and the received signal. Ideally, the receiver identifies the correct timing point after the first 64 guard-time samples. Complexity can be expressed as

$$\begin{aligned} C_A &= 64 \times (N - 1) = 16320, \\ C_M &= 64 \times N = 16384. \end{aligned} \quad (5.44)$$

- **Improved Schmidl-Cox method with cross-correlation :**

According to Table 5.2 an interesting synchronization scheme can be described as follows. During the coarse step the SC method is used to reduce complexity. Then, during the fine step the cross-correlation technique is used in order to improve the precision [122]. Complexity in this case is thus given by

$$\begin{aligned} C_A &= 64 \times 4 + (N - 1) \times \Delta, \\ C_M &= 64 \times 4 + N \times \Delta. \end{aligned} \quad (5.45)$$

From Figure 5.29 the value of  $\Delta$  must be at least 40 so that in 99% of the cases the searching window covers the correct timing point. The complexity can be deduced as  $C_A = 10456$  and  $C_M = 10496$ .

- **The proposed II method:**

During the fine synchronization step, the proposed method required  $2l_2 - 2$  additions for calculating  $P_{Fine}(d)$  and 4 additions for recursively computing  $R_{Fine}(d)$ . The corresponding numbers of multiplications are  $2l_2$  and 4. It is noted that there is one additional multiplication for computing the metric  $M_{Fine}(d)$ . The 99%-covering-probability searching window length is 12 samples. Hence, complexity can be expressed as

$$\begin{aligned} C_A &= 64 \times 6 + (2l_2 + 2) \times \Delta = 1848, \\ C_M &= 64 \times 7 + (2l_2 + 5) \times \Delta = 1948, \end{aligned} \quad (5.46)$$

which is significantly reduced when compared to conventional schemes. This complexity reduction comes from the fact that the proposed coarse metric is less spread than the one of Schmidl and Cox, resulting in a smaller searching window in the fine synchronization step. It is noted that the proposed two-stage synchronization method can also be used with the Park, Minn and Shi's preambles. However, the fact that the four sequences in Park and Minn's preambles have the same length generates minor peaks located before the principal peak. If the coarse synchronization detects a minor peak rather than the principal one, the

searching window must be large so that the principal peak will not be missed. This results in increased receiver complexity. In the case where the level of minor peaks is higher than that of the principal one, a technique may detect a minor peak instead of the principal one, resulting in severe ICI and ISI. Shi's method does not present minor peaks. However, in this technique the number of operations required for each received sample in the coarse synchronization step is three times larger than that of the proposed technique.

### 5.3.5. Conclusion

In this section conventional preamble-based timing synchronization techniques are studied. Two novel timing synchronization techniques for optical IMDD OFDM transmissions are also proposed. Based on Park's technique, the first proposition reduces the level of secondary peaks and brings good performance in high SNR values. In our second proposition, which is published in *Optic Express* [3], a novel preamble structure is introduced. A threshold-based two-stage synchronization technique is also developed. By means of numerical simulations a comparative study of the proposed techniques and conventional timing synchronization techniques is given. The proposed method is shown to give better performance in terms of timing offset variance with a reduced complexity for two reasons.

- Firstly, the coarse synchronization step makes use of a preamble with repetitive structures, which are robust against the transmission channel. In addition, the proposed coarse metric introduces no secondary peak. The precision of the timing estimator is improved by an impulse-like metric in the fine synchronization step. The complexity of the coarse step is reduced by recursive calculation.
- Secondly, the fact that the preamble is built only with low-frequency sub-carriers reduces the impact of chromatic dispersion and laser chirps. In addition, a slowly varying time-domain preamble is shown to have strong tolerance to the random sampling phase of an ADC.

It is interesting to note that our proposed techniques can be exploited not only in optical IMDD transmissions but also in optical coherent systems. The repetitive structure of the preamble is preserved in order to face a possible frequency synchronization problem.

## 5.4. Conclusion

Throughout the chapter, we have addressed two major issues of the OFDM modulation as follows: the PAPR of an OFDM signal and the time synchronization.

The statistic property of the PAPR and conventional PAPR reduction techniques are studied in section 5.2. According to the dispersion-induced attenuation of an optical IMDD channel, we propose a tone reservation-based PAPR reduction scheme for both conventional OFDM and the proposed POFDM system [5]. The proposed scheme is shown to bring up to 2 dB PAPR reduction for the conventional OFDM modulation. When the DFT-precoded technique is used, up to 4 dB PAPR reduction is observed with the proposed PAPR reduction scheme. The proposed scheme does not present noise in the useful signal band. In addition, it does not introduce any data rate loss.

In section 5.3, the time synchronization for an OFDM transmission is addressed. The performance of conventional preamble-based synchronization techniques are evaluated by means of numerical simulation. In order to improve the precision of time synchronization techniques, two propositions have also been reported [2], [3]. The technique proposed in [2] is a modified version of Park's technique [119]. In this proposed technique, the new preamble structure degrades the magnitude level of minor peaks appearing in Park's technique. In addition, the proposition to use only low-frequency components to build a preamble reduces the impact of chromatic dispersion, resulting in better performance in terms of timing offset variance. However, the complexity of the proposed technique is still high. In [3] we propose a new preamble structure along with a two-stage timing acquisition algorithm. In this technique, the first coarse timing metric presents no minor peak. The timing synchronization precision is improved thanks to the second fine timing metric. The proposed technique is shown to give better performance in terms of timing offset variance with reduced receiver complexity when compared to conventional techniques.

In an OFDM transmission system, on the receiver side it is also important to estimate and compensate for the channel gain on each subcarrier. In the literature, channel estimation techniques have been extensively studied and reported. For further details the reader is invited to read the Appendix B.



# Conclusion

In the context of optical access networks, fiber-based optical IMDD transmission infrastructures have been rapidly expanding all over the world since conventional copper-wire systems seem to be saturated by actual bandwidth demand. Throughout this thesis, it has been clear that when data rate and/or transmission distance increases, ISI is one of the major problems which degrade the performance of an IMDD transmission. In order to deal with such a problem, this thesis described one promising approach which is the use of signal processing techniques in the electrical domain.

Chapter 1 introduced the optical IMDD channel and detriments it may cause to a transmitted signal. Particularly, fiber attenuation is one of the key capacity-limiting factors since it directly limits the received optical power, resulting in poor SNRs on the receiver side. In addition, due to the double-side-band nature of a transmitted optical signal, the interplay between chromatic dispersion and laser chirps introduces attenuation dips in the frequency domain. Unless chromatic dispersion is compensated by in-line DCFs or low-chromatic-dispersion fibers are used, this phenomenon generates severe ISI, which should require complex equalization schemes on the receiver side. Given that the implementation of DCFs is usually bulky and expensive, and a telecom operator often prefers to exploit its already implemented fiber infrastructures, the use of equalization schemes seems to be inevitable in future PONs.

Chapter 2 described the numerical modeling of key components in an optical IMDD communication link. In the literature, the propagation of an optical signal over a fiber is described by the well-known nonlinear Schrödinger equation, of which a numerical solution can be found using the split-step Fourier method. For the photodetector modeling, in the context of access networks, the value of receiver sensitivity given by the manufacturer can be used for noise modeling. Laser modeling, however, is more complicated than the modeling of the two other components since it requires a value extraction of the parameters presented in the laser intrinsic rate equation model. Thanks to the help of the ASHA team, in particular Mrs. Neveena Genay, the adopted channel model was validated in both small-signal and large-signal modulation regime.

In Chapter 3, we discussed conventional linear and nonlinear channel equalization structures for a 10-Gb/s OOK NRZ transmission. In the literature, transversal filters are considered as one of the simplest equalization structures. Because a fractionally spaced transversal filter can play at once the role of a matched filter and an equalizer, it usually brings better performance when compared to a symbol-rate delay line equalizer. In the context of optical access networks, an 11-tap FSTF was found to be a good performance-complexity compromise. In order to further improve the BER performance of an FSTF, nonlinear structures including decision feedback filter and MLSE can be used. When an

FSTF followed by a DFE is used, a 7-tap FSTF and a 2-tap feedback filter were found to be a good performance-complexity compromise. When compared to transversal filter and decision feedback structures, an MLSE performs the best. In this technique, the channel memory of 3 bits was found to be sufficient to model the equivalent discrete channel. For the construction of metric branches for the Viterbi algorithm, the histogram method was shown to be more relevant than the method based on the DIR because of the channel nonlinearities. In this chapter we also introduced the Nyquist pulse shaping technique for future PONs. When compared to the NRZ pulse shaping, the more complex Nyquist pulse shaping improves the chromatic dispersion-induced power penalty up to 2 dB at  $10^{-3}$  BER and the reach can be extended by tens of kilometers, which corresponds to a reach increase of about 20%. In addition, the rectangular spectral form of a Nyquist pulse should also reduce inter-channel interference in a WDM transmission.

Although nonlinear equalizer structures significantly improve the performance of a conventional OOK NRZ/Nyquist modulation, chromatic dispersion-induced power penalty is still large when fiber length increases. For this reason, Chapter 4 was dedicated to the analysis of multicarrier modulation schemes. In the literature, beside the equalizer structures described in Chapter 3, these multicarrier modulation schemes are alternatives to compensate for a frequency-selective channel. Particularly, the OFDM modulation was considered in our study because the modulation/demodulation can be simply carried out by means of IFFT/FFT operations. Although the optical IMDD channel is frequency-selective, it is relatively static. Hence, the channel information can be known on the transmitter side via channel estimation and a feedback link. In this case, an adaptive modulation scheme can be used in order to optimize the transmission capacity. These are the reasons why the conventional Levin-Campello bit/power loading technique has earned its success in optical IMDD transmission systems. In this chapter, this technique was detailed and its performance was evaluated by means of numerical simulations. Besides, in this chapter the author also proposed a DFT-precoded OFDM system, which is based on the precoding of OFDM symbols by a DFT matrix. A simple rate adaptive algorithm was also proposed to maximize the transmission throughput. Thanks to the precoding, the PAPR of a transmitted signal was reduced, resulting in significant power consumption reduction of the power amplifier. Moreover, in terms of transmission capacity performance, the proposed system was shown to perform as well as the conventional LC system. The proposition also resulted in a publication in the *Journal of Lightwave Technology* [1]. In order to reveal the potential of multicarrier modulation schemes for future PONs, the proposed system performance was also compared to that of conventional OOK NRZ/Nyquist systems. It was shown that the proposed system is more robust to chromatic dispersion and laser linewidth enhancement factor. Moreover, a simple frequency-domain zero-forcing equalization technique used in the proposed system is much less complex than conventional time-domain equalization techniques. Given that future PONs should support multi-Gb/s transmissions, a complexity-reduced equalizer should be an important advantage of the proposed system over conventional OOK NRZ/Nyquist systems.

Finally, in Chapter 5 we studied significant disadvantages of the OFDM modulation including large PAPR and sensitivity to timing synchronization. Conventional and proposed techniques to compensate for these disadvantages were also addressed. Based on the conventional tone reservation technique, the author proposed in [5] a contiguous-tone tone reservation technique to reduce the PAPR of an OFDM signal in the context of optical IMDD transmissions. In a proposed DFT-precoded transmission, the proposed tone reservation technique brings a PAPR reduction gain of up to 4 dB at  $10^{-3}$  clipping rate. In

addition, the proposed PAPR reduction scheme does not decrease the transmission throughput. For the timing synchronization, conventional preamble-based synchronization techniques were analyzed. The author also proposed two new techniques which significantly improve the performance in terms of timing offset variance and receiver complexity. In the context of high-bit-rate transmissions, the impact of chromatic dispersion on a transmitted signal might be significant. Since the delay in arrival time of different frequency components of a signal also depends on the signal bandwidth, a slowly varying time-domain preamble was found to be more robust than a fast varying one. Thanks to the particular structure of the proposed preamble and a two-stage time acquisition algorithm, the second proposed technique is at once less complex and more precise than conventional techniques. The first proposed synchronization technique also resulted in a conference paper [2]. The second proposed technique resulted in a publication in the journal *Optics Express* [3] and a patent was also submitted [4].

Finally, for future works, we have several perspectives as follows.

- Given the same transmission data rate, the rectangular spectrum of a Nyquist pulse might be an advantage over an NRZ pulse in the context of WDM transmission. Future works can concentrate on inter-channel interference of a WDM transmission using Nyquist shaping technique. The same study for the OFDM modulation should also be interesting.
- In practice, the optical carrier wavelengths used at different ONUs might not be perfectly identical. This might cause severe crosstalk on the uplink when the Orthogonal Frequency Division Multiple Access (OFDMA) is used. In this case, methods for eliminating crosstalk should be an interesting subject for future works.
- In the proposed DFT-precoded OFDM technique, all the active subcarriers were supposed to be precoded by a DFT matrix. In an OFDMA scheme, the active subcarriers can be divided into sub-blocks corresponding to different users. Each sub-block can then be precoded by a DFT matrix. In this case, the performance in terms of throughput and PAPR reduction of the technique should require further study.



# Contributions

## Journal papers

1. T.-A. Truong, M. Arzel, H. Lin, B. Jahan, and M. Jezequel, “DFT Precoded OFDM - An Alternative Candidate for Next Generation PONs,” *J. Light. Technol.*, vol. 32, pp. 1228 – 1238, Mar. 2014.
2. T. A. Truong, M. Arzel, H. Lin, B. Jahan, and M. Jezequel, “A new low-complexity and robust time synchronization technique for optical IMDD OFDM transmissions,” *Opt. Express*, vol. 22, no. 12, pp. 14322–14340, Jun. 2014.

## Conference papers

1. T.-A. Truong, H. Lin, B. Jahan, L. Anet Neto, M. Arzel, and M. Jezequel, “On the performance of timing synchronization techniques for optical OFDM IMDD transmission,” in *2012 IEEE Photonics Conference (IPC)*, 2012, pp. 179–180.
2. T.-A. Truong, M. Arzel, H. Lin, B. Jahan, B. Charbonnier, and M. Jezequel, “PAPR Reduction Using Contiguous-tone Tone Reservation Technique in Optical OFDM IMDD Transmissions,” in *Optical Fiber Communication Conference/National Fiber Optic Engineers Conference 2013*, 2013, p. JTh2A.67.

## Patents

1. T. A. Truong, B. Jahan, and H. Lin, “Synchronisation de cadre dans un récepteur en utilisant un préambule ayant une structure spécifique,” Patent number WO2014044989. Mar. 2014.
2. T. A. Truong, B. Jahan, and H. Lin, “Système de transmission à fibre optique monomode pour réseau d’accès,” demand for publication on Nov. 2014.



# Appendix A Recursive computation of the proposed synchronization technique

The coarse synchronization metric can be recursively computed. The metric value at time instant  $d + 1$  can be computed according to that at time instant  $d$

## Correlation computation

$$\begin{aligned}
 P_{Coarse}(d + 1) &= \sum_{i=0}^{l_1-1} y_{d+1+i} y_{d+1+i+l_1} + \sum_{i=0}^{l_2-1} y_{d+1+i+2l_1} y_{d+1+i+2l_1+l_2} \\
 &= \sum_{i=0}^{l_1-1} y_{d+i} y_{d+i+l_1} + y_{d+l_1} y_{d+2l_1} - y_d y_{d+l_1} + \sum_{i=0}^{l_2-1} y_{d+i+2l_1} y_{d+i+2l_1+l_2} \\
 &\quad + y_{d+l_2+2l_1} y_{d+2l_1+2l_2} - y_{d+2l_1} y_{d+2l_1+l_2} \\
 &= P_{Coarse}(d) + y_{d+l_1} y_{d+2l_1} - y_d y_{d+l_1} + y_{d+l_2+2l_1} y_{d+2l_1+2l_2} - y_{d+2l_1} y_{d+2l_1+l_2} \quad (\text{A.1})
 \end{aligned}$$

## Power normalizing factor computation

$$R_{Coarse}(d + 1) = R_{Coarse}(d) + 0.5|y_{d+N}|^2 - 0.5|y_d|^2 \quad (\text{A.2})$$

## Additional operations for the metric value

$$M_{Coarse}(d + 1) = \left( \frac{P_{Coarse}(d + 1)}{R_{Coarse}(d + 1)} \right)^2 \quad (\text{A.3})$$

The number of operations given in Table 5.2 can be deduced from Eqs. (A.1), (A.2) and (A.3) as follows: 6 additions, 7 multiplications and 1 division.



# Appendix B      Channel      estimation techniques

Under the assumption of perfect time and frequency synchronization, a demodulated data symbol after the FFT can be expressed as a function of the transmitted data symbol (*c.f.* Eq. (4.25))

$$Z_k = X_k Q_k + n_k. \quad (\text{B.1})$$

Or under matrix form

$$\mathbf{Z} = \begin{bmatrix} Z_0 \\ \vdots \\ Z_{N-1} \end{bmatrix} = \text{diag}(\mathbf{X})\mathbf{Q} + \mathbf{n} = \begin{bmatrix} X_0 & \ddots & 0 \\ \vdots & \ddots & \vdots \\ 0 & \ddots & X_{N-1} \end{bmatrix} \begin{bmatrix} Q_0 \\ \vdots \\ Q_{N-1} \end{bmatrix} + \begin{bmatrix} n_0 \\ \vdots \\ n_{N-1} \end{bmatrix}. \quad (\text{B.2})$$

where  $\text{diag}(\mathbf{X})$  is an  $N \times N$  matrix whose diagonal contains transmitted data and  $n_k$  denotes an equivalent noise including nonlinear noise and receiver noise (*c.f.* Chapter 4, section 4.5.2). In an OFDM transmission, channel equalization is responsible for compensating the channel gain  $Q_k$ , which change the amplitude and the phase of a transmitted data subcarrier. Channel equalization is important since the variation of the amplitude or the phase of signal constellation might result in the severe degradation of BER performance. In general, channel equalization is carried out on condition that the channel information is known by means of channel estimation techniques. In some transmission systems, channel equalization can also be carried out without the knowledge of channel information [125]. However, blind equalization techniques are out of the scope of this thesis.

Basically, channel estimation techniques derive from two basic principles: Maximum Likelihood (ML) estimation and MMSE estimation. Depending on specific applications, a large variety of channel estimation techniques have been developed based on these two fundamental principles, which are discussed in the following paragraphs.

## B.1. Maximum likelihood channel estimation

An ML channel estimator gives an estimate  $\hat{Q}_k$ ,  $k = 0, \dots, N - 1$  which maximize the following conditional probability

$$P(Z_0, Z_1, \dots, Z_{N-1} | Q_0, Q_1, \dots, Q_{N-1}) \sim \exp \left\{ - \sum_{k=0}^{N-1} \frac{(Z_k - X_k Q_k)^* (Z_k - X_k Q_k)}{2\sigma_k^2} \right\}, \quad (\text{B.3})$$

where  $\sigma_k$  is the standard deviation of the noise for the  $k^{th}$  subcarrier. It is noted that Eq. (B.3) is valid when the channel gain of different subcarriers are independent and the noise on each subcarrier has a Gaussian distribution. Equivalently, the ML channel estimation search for  $Q_k$  that minimizes the likelihood function

$$A_l(Z_0, Z_1, \dots, Z_{N-1}) = \sum_{k=0}^{N-1} \frac{(Z_k - X_k Q_k)^* (Z_k - X_k Q_k)}{2\sigma_k^2}. \quad (\text{B.4})$$

By setting to zero the differential of the likelihood function against the variable  $Q_k$ , we arrive at the ML estimate

$$\hat{Q}_k^{ML} = \frac{Z_k}{X_k} = Q_k + \frac{n_k}{X_k}. \quad (\text{B.5})$$

The ML estimation is equivalent to what is also referred to as the zero-forcing estimator or the least square estimator [126]. In practice, the implementation of an ML channel estimator is simple. However, the performance of such an estimator strongly depends on the power of noise. In order to evaluate the effective SNR of each subcarrier in an OFDM transmission using the ML channel estimation, we suppose that zero-forcing channel compensation is used. The estimated information symbol is given by

$$\hat{X}_k = \frac{Z_k}{\hat{Q}_k^{ML}} = \frac{X_k Q_k + n_k}{\hat{Q}_k^{ML}} = \frac{X_k Q_k + n_k}{Q_k + \frac{n_k^0}{X_k^0}} = X_k + \frac{n_k - X_k \frac{n_k^0}{X_k^0}}{Q_k + \frac{n_k^0}{X_k^0}} = X_k + \tilde{n}_k, \quad (\text{B.6})$$

$$\tilde{n}_k = \frac{n_k - X_k \frac{n_k^0}{X_k^0}}{Q_k + \frac{n_k^0}{X_k^0}}. \quad (\text{B.7})$$

The subscript 0 refers to the training stage. The performance of the ML channel estimation can be improved by two approaches: averaging in the time domain and averaging in the frequency domain.

- **Averaging in the time domain**

Supposing  $l_c$  training symbols are transmitted and  $l_c$  corresponding ML estimates are given by Eq. (B.5), average channel response can be written as

$$\bar{Q}_k^{ML} = \frac{1}{l_c} \sum_{l=1}^{l_c} \hat{Q}_{k,l}^{ML} = Q_k + \bar{n}_k, \quad (\text{B.8})$$

$$\bar{n}_k = \frac{1}{l_c} \sum_{l=1}^{l_c} \frac{n_k^l}{X_k^l}, \quad (\text{B.9})$$

where  $l$  denotes the index of training symbols. Suppose that training data symbols are designed such that their amplitude is constant (e.g. QPSK constellation), the power of noise in Eq. (B.8) can be expressed as

$$E\{\bar{n}_k^2\} = \frac{1}{l_c} E\{n_k^2\}. \quad (\text{B.10})$$

Hence, by transmitting  $l_c$  training symbols, the power of noise in an ML estimate is reduced by a factor of  $l_c$ . However, the increase of the number of training symbols results in reduced transmission spectral efficiency since overhead increases.

- **Averaging in the frequency domain**

Since an averaging in the time domain consumes spectral efficiency, the authors in [127] proposed an intra-symbol channel estimate averaging in order to reduce the noise power. Within one training symbol, the ML estimate of the channel response on a subcarrier is improved by averaging the estimates of several adjacent subcarriers. Mathematically, an improved channel response estimate on the  $k^{\text{th}}$  subcarrier is written as

$$\begin{aligned} \bar{Q}_k^{ML} &= \frac{1}{2l_a + 1} \sum_{l=k-l_a}^{k+l_a} \hat{Q}_l^{ML} = \frac{1}{2l_a + 1} \sum_{l=k-l_a}^{k+l_a} \left[ Q_l + \frac{n_l}{X_l} \right] \\ &= \frac{1}{2l_a + 1} \sum_{l=k-l_a}^{k+l_a} \left[ Q_k + \Delta_{l,k} + \frac{n_l}{X_l} \right] \\ &= Q_k + \frac{1}{2l_a + 1} \sum_{l=k-l_a}^{k+l_a} \Delta_{l,k} + \frac{1}{2l_a + 1} \sum_{l=k-l_a}^{k+l_a} \frac{n_l}{X_l} \end{aligned} \quad (\text{B.11})$$

$$\Delta_{l,k} = Q_l - Q_k, \quad (\text{B.12})$$

where  $l$  is the index of subcarriers.  $2l_a$  is the number of adjacent subcarriers for the averaging. The third term and the second term on the right hand side of Eq. (B.11) stand for power-reduced noise and excess noise, respectively. This technique generates an excess noise due to the fact that channel response is different from one subcarrier to another. In this technique, the performance improvement depends on two factors: the number of adjacent subcarriers taken for the averaging and the channel response. The choice of  $l_a$  is a compromise between noise power reduction and the power of excess noise. In practice, both time domain and frequency domain averaging techniques can be used.

## B.2. Minimum mean square error channel estimation

### B.2.1. Conventional minimum mean square error technique

An MMSE estimator searches for an  $N \times N$  matrix  $\mathbf{W}_{MMSE}$  so that the estimate  $\hat{\mathbf{Q}}_{MMSE} = \mathbf{W}_{MMSE} \mathbf{Z}$  minimizes the MSE written as

$$MSE = E \left\{ (\hat{\mathbf{Q}}_{MMSE} - \mathbf{Q})^H (\hat{\mathbf{Q}}_{MMSE} - \mathbf{Q}) \right\}, \quad (\text{B.13})$$

where  $(\cdot)^H$  denotes an Hermitian conjugate operation which performs a transpose and complex conjugate. Minimizing the MSE gives the solution expressed as [126]

$$\mathbf{W}_{MMSE} = \mathbf{R}_{qz} (\mathbf{R}_{zz})^{-1}, \quad (\text{B.14})$$

where

$$\mathbf{R}_{qz} = E \{ \mathbf{Q} \mathbf{Z}^H \}, \quad (\text{B.15})$$

$$\mathbf{R}_{zz} = E \{ \mathbf{Z} \mathbf{Z}^H \}. \quad (\text{B.16})$$

The MMSE channel estimation technique requires the knowledge of the two matrices  $\mathbf{R}_{qz}$  and  $\mathbf{R}_{zz}$  on the receiver side. In addition, the implementation of this technique is a real challenge because of high complexity.

### B.2.2. Linear minimum mean square error technique

Suppose that with the ML technique, we have an estimated channel response vector  $\hat{\mathbf{Q}}^{ML} = [\hat{Q}_0^{ML}, \hat{Q}_1^{ML}, \dots, \hat{Q}_{N-1}^{ML}]^T$ . A Linear Minimum Mean Square Error (LMMSE) estimator searches for an  $N \times N$  matrix  $\mathbf{W}_{LMMSE}$  so that the estimate  $\hat{\mathbf{Q}}_{LMMSE} = \mathbf{W}_{LMMSE} \hat{\mathbf{Q}}^{ML}$  minimizes the MSE. Minimizing the MSE gives the solution expressed as [128]

$$\mathbf{W}_{LMMSE} = \mathbf{R}_{qq_{ml}} (\mathbf{R}_{q_{ml}q_{ml}})^{-1}, \quad (\text{B.17})$$

where

$$\mathbf{R}_{qq_{ml}} = E \left\{ \mathbf{Q} (\hat{\mathbf{Q}}^{ML})^H \right\} = E \left\{ \mathbf{Q} \left( \mathbf{Q} + (\text{diag}(\mathbf{X}))^{-1} \mathbf{n} \right)^H \right\} = E \{ \mathbf{Q} \mathbf{Q}^H \} = \mathbf{R}_{qq}, \quad (\text{B.18})$$

$$\begin{aligned} \mathbf{R}_{q_{ml}q_{ml}} &= E \left\{ \hat{\mathbf{Q}}^{ML} (\hat{\mathbf{Q}}^{ML})^H \right\} \\ &= E \left\{ \left( \mathbf{Q} + (\text{diag}(\mathbf{X}))^{-1} \mathbf{n} \right) \left( \mathbf{Q} + (\text{diag}(\mathbf{X}))^{-1} \mathbf{n} \right)^H \right\} \\ &= \mathbf{R}_{qq} + \mathbf{R}_{nn} (\mathbf{X} \mathbf{X}^H)^{-1}, \end{aligned} \quad (\text{B.19})$$

$$\mathbf{R}_{nn} = \begin{bmatrix} \sigma_0^2 & \ddots & 0 \\ \vdots & \ddots & \vdots \\ 0 & \ddots & \sigma_{N-1}^2 \end{bmatrix}. \quad (\text{B.20})$$

The LMMSE estimator is of considerable complexity since a matrix inversion is needed every time the training data  $\mathbf{X}$  change. In order to reduce the complexity, the term  $\mathbf{X} \mathbf{X}^H$  can be replaced by its expectation  $E \{ \mathbf{X} \mathbf{X}^H \}$ . Further complexity reduction can also be achieved by using the singular value decomposition technique [128].

# References

- [1] T. A. Truong, M. Arzel, H. Lin, B. Jahan, and M. Jezequel, "DFT Precoded OFDM - An Alternative Candidate for Next Generation PONs," *J. Light. Technol.*, vol. 32, pp. 1228 – 1238, Mar. 2014.
- [2] T. A. Truong, H. Lin, B. Jahan, L. Anet Neto, M. Arzel, and M. Jezequel, "On the performance of timing synchronization techniques for optical OFDM IMDD transmission," in *2012 IEEE Photonics Conference (IPC)*, 2012, pp. 179–180.
- [3] T. A. Truong, M. Arzel, H. Lin, B. Jahan, and M. Jezequel, "A new low-complexity and robust time synchronization technique for optical IMDD OFDM transmissions," *Opt. Express*, vol. 22, no. 12, pp. 14322–14340, Jun. 2014.
- [4] T. A. TRUONG, B. Jahan, and H. Lin, "Synchronisation de cadre dans un récepteur en utilisant un preambule ayant une structure spécifique," Patent number WO2014044989. Mar. 2014.
- [5] T. A. Truong, M. Arzel, H. Lin, B. Jahan, B. Charbonnier, and M. Jezequel, "PAPR Reduction Using Contiguous-tone Tone Reservation Technique in Optical OFDM IMDD Transmissions," in *Optical Fiber Communication Conference/National Fiber Optic Engineers Conference 2013*, 2013, p. JTh2A.67.
- [6] Recommendation ITU-T G.987.3, "10-Gigabit-capable passive optical networks (XG-PON): Transmission convergence (TC) layer specification." Oct-2010.
- [7] P. J. Winzer and R. Essiambre, "Advanced Optical Modulation Formats," *Proc. IEEE*, vol. 94, no. 5, pp. 952–985, May 2006.
- [8] Govind P. Agrawal, *Nonlinear Fiber Optics*, 4th ed. San Diego: Academic Press, 2007.
- [9] J. Fatome, "Propagation d'impulsions ultra-courtes à 160-Gb/s dans des lignes de fibres optiques gérées en dispersion," Université de Bourgogne, Dec. 2004.
- [10] K. J. Blow and D. Wood, "Theoretical description of transient stimulated Raman scattering in optical fibers," *IEEE J. Quantum Electron.*, vol. 25, no. 12, pp. 2665–2673, Dec. 1989.
- [11] J. M. Tang and K. A. Shore, "30-Gb/s signal transmission over 40-km directly modulated DFB-laser-based single-mode-fiber links without optical amplification and dispersion compensation," *J. Light. Technol.*, vol. 24, no. 6, pp. 2318–2327, 2006.
- [12] J. M. Tang, P. M. Lane, and K. A. Shore, "High-speed transmission of adaptively modulated optical OFDM signals over multimode fibers using directly Modulated DFBs," *J. Light. Technol.*, vol. 24, no. 1, pp. 429 – 441, Jan. 2006.
- [13] M. M. E. Said, J. Sitch, and M. I. Elmasry, "An electrically pre-equalized 10-Gb/s duobinary transmission system," *J. Light. Technol.*, vol. 23, no. 1, pp. 388 – 400, Jan. 2005.

- 
- [14] Govind P. Agrawal, *Fiber-Optic Communication Systems*, 3rd ed. New York: John Wiley & Sons, 2002.
- [15] A. R. J. Marshall, J. P. R. David, and C. H. Tan, "Impact Ionization in InAs Electron Avalanche Photodiodes," *IEEE Trans. Electron Devices*, vol. 57, no. 10, pp. 2631–2638, Oct. 2010.
- [16] K. Petermann, *Laser Diode Modulation and Noise*. Kluwer Academic, 1988.
- [17] William Shieh and Ivan Djordjevic, *Orthogonal Frequency Division Multiplexing for Optical Communications*. San Diego: ELSEVIER Inc., 2010.
- [18] J. Treichler, M. Larimore, and J. C. Harp, "Practical blind demodulators for high-order QAM signals," *Proc. IEEE*, vol. 86, no. 10, pp. 1907–1926, 1998.
- [19] L. M. Pessoa, H. M. Salgado, and I. Darwazeh, "Performance Evaluation of Phase Estimation Algorithms in Equalized Coherent Optical Systems," *IEEE Photonics Technol. Lett.*, vol. 21, no. 17, pp. 1181–1183, 2009.
- [20] X. Yi, W. Shieh, and Y. Tang, "Phase Estimation for Coherent Optical OFDM," *IEEE Photonics Technol. Lett.*, vol. 19, no. 12, pp. 919–921, 2007.
- [21] Y. Tang and W. Shieh, "Coherent Optical OFDM Transmission Up to 1 Tb/s per Channel," *J. Light. Technol.*, vol. 27, no. 16, pp. 3511–3517, Aug. 2009.
- [22] S. L. Jansen, I. Morita, T. C. W. Schenk, N. Takeda, and H. Tanaka, "Coherent Optical 25.8-Gb/s OFDM Transmission Over 4160-km SSMF," *J. Light. Technol.*, vol. 26, no. 1, pp. 6–15, 2008.
- [23] S. L. Jansen, I. Morita, T. C. W. Schenk, and H. Tanaka, "121.9-Gb/s PDM-OFDM Transmission With 2-b/s/Hz Spectral Efficiency Over 1000 km of SSMF," *J. Light. Technol.*, vol. 27, no. 3, pp. 177–188, 2009.
- [24] I. M. Sander L. Jansen, "16x52.5-Gb/s, 50-GHz spaced, POLMUX-CO-OFDM transmission over 4,160 km of SSMF enabled by MIMO processing," *Opt. Commun. - Post-Deadline Pap. Publ. 2008 2007 33rd Eur. Conf. Exhib. Of*, pp. 1 – 2, 2007.
- [25] S. Yamamoto, N. Edagawa, H. Taga, Y. Yoshida, and H. Wakabayashi, "Analysis of laser phase noise to intensity noise conversion by chromatic dispersion in intensity modulation and direct detection optical-fiber transmission," *J. Light. Technol.*, vol. 8, no. 11, pp. 1716–1722, Nov. 1990.
- [26] K. Petermann and J. Wang, "Large signal analysis of FM-AM conversion in dispersive optical fibres and its application to PCM systems," *Electron. Lett.*, vol. 27, no. 25, pp. 2347–2348, Dec. 1991.
- [27] A. R. Charaplyvy, R. W. Tkach, L. L. Buhl, and R. C. Alferness, "Phase modulation to amplitude modulation conversion of CW laser light in optical fibres," *Electron. Lett.*, vol. 22, no. 8, pp. 409–411, 1986.
- [28] H. T. Friis, "Noise Figures of Radio Receivers," *Proc. IRE*, vol. 32, no. 7, pp. 419–422, Jul. 1944.
- [29] "Fiber Optic Attenuators Information," *GlobalSpec*. [Online]. Available: [http://www.globalspec.com/learnmore/optics\\_optical\\_components/fiber\\_optics/fiber\\_optic\\_attenuators](http://www.globalspec.com/learnmore/optics_optical_components/fiber_optics/fiber_optic_attenuators).

- [30] G. Colavolpe, T. Foggi, E. Forestieri, and G. Prati, "Robust Multilevel Coherent Optical Systems With Linear Processing at the Receiver," *J. Light. Technol.*, vol. 27, no. 13, pp. 2357–2369, 2009.
- [31] M. Kuschnerov, F. N. Hauske, K. Piyawanno, B. Spinnler, M. S. Alfiad, A. Napoli, and B. Lankl, "DSP for Coherent Single-Carrier Receivers," *J. Light. Technol.*, vol. 27, no. 16, pp. 3614–3622, 2009.
- [32] R. Kudo, T. Kobayashi, K. Ishihara, Y. Takatori, A. Sano, and Y. Miyamoto, "Coherent Optical Single Carrier Transmission Using Overlap Frequency Domain Equalization for Long-Haul Optical Systems," *J. Light. Technol.*, vol. 27, no. 16, pp. 3721–3728, 2009.
- [33] F. Devaux, Y. Sorel, and J. F. Kerdiles, "Simple measurement of fiber dispersion and of chirp parameter of intensity modulated light emitter," *J. Light. Technol.*, vol. 11, no. 12, pp. 1937–1940, Dec. 1993.
- [34] Hugues LE BRAS, "Étude des réseaux radio sur fibre dans le contexte des réseaux d'accès et privés." Signal and Image processing. Université Pierre et Marie Curie - Paris VI, 2008. French. <NNT : 2007PA066325>. <tel-00812485>.
- [35] J. Wang and K. Petermann, "Small signal analysis for dispersive optical fiber communication systems," *J. Light. Technol.*, vol. 10, no. 1, pp. 96–100, 1992.
- [36] L. Bjerkan, A. Royset, L. Hafskjaer, and D. Myhre, "Measurement of laser parameters for simulation of high-speed fiberoptic systems," *J. Light. Technol.*, vol. 14, no. 5, pp. 839–850, May 1996.
- [37] J. McNicol, M. O'Sullivan, K. Roberts, A. Comeau, D. McGhan, and L. Strawczynski, "Electrical domain compensation of optical dispersion [optical fibre communication applications]," in *Optical Fiber Communication Conference, 2005. Technical Digest. OFC/NFOEC, 2005*, vol. 4, p. 3 pp. Vol. 4–.
- [38] P. M. Watts, V. Mikhailov, S. Savory, P. Bayvel, M. Glick, M. Lobel, B. Christensen, P. Kirkpatrick, S. Shang, and R. I. Killey, "Performance of single-mode fiber links using electronic feed-forward and decision feedback equalizers," *IEEE Photonics Technol. Lett.*, vol. 17, no. 10, pp. 2206–2208, 2005.
- [39] F. Buchali, H. Bulow, W. Baumert, R. Ballentin, and T. Wehreu, "Reduction of the chromatic dispersion penalty at 10 Gbit/s by integrated electronic equalisers," in *Optical Fiber Communication Conference, 2000*, vol. 3, pp. 268–270 vol.3.
- [40] M. Schuster, S. Randel, C. A. Bunge, S. C. J. Lee, F. Breyer, B. Spinnler, and K. Petermann, "Spectrally Efficient Compatible Single-Sideband Modulation for OFDM Transmission With Direct Detection," *IEEE Photonics Technol. Lett.*, vol. 20, no. 9, pp. 670–672, May 2008.
- [41] D. J. F. Barros and J. M. Kahn, "Comparison of Orthogonal Frequency-Division Multiplexing and On-Off Keying in Amplified Direct-Detection Single-Mode Fiber Systems," *J. Light. Technol.*, vol. 28, no. 12, pp. 1811–1820, 2010.
- [42] T.-N. Duong, N. Genay, M. Ouzzif, J. Le Masson, B. Charbonnier, P. Chanclou, and J.-C. Simon, "Adaptive Loading Algorithm Implemented in AMOOFDM for NG-PON System Integrating Cost-Effective and Low-Bandwidth Optical Devices," *IEEE Photonics Technol. Lett.*, vol. 21, no. 12, pp. 790–792, 2009.

- [43] E. Giacomidis, J. L. Wei, X. L. Yang, A. Tsokanos, and J. M. Tang, "Adaptive-Modulation-Enabled WDM Impairment Reduction in Multichannel Optical OFDM Transmission Systems for Next-Generation PONs," *IEEE Photonics J.*, vol. 2, no. 2, pp. 130–140, Apr. 2010.
- [44] H. Paul, A. Ali, J. Leibrich, K. Kammeyer, and W. Rosenkranz, "Bit and power loading for optical IM/DD transmission," in *Multi-Carrier Systems Solutions (MCSS), 2011 8th International Workshop on*, 2011, pp. 1–5.
- [45] X. Q. Jin, J. L. Wei, R. P. Giddings, T. Quinlan, S. Walker, and J. M. Tang, "Experimental Demonstrations and Extensive Comparisons of End-to-End Real-Time Optical OFDM Transceivers With Adaptive Bit and/or Power Loading," *IEEE Photonics J.*, vol. 3, no. 3, pp. 500–511, Jun. 2011.
- [46] L. A. Neto, P. Chanclou, B. Charbonnier, N. Genay, F. Saliou, R. Xia, M. Ouzzif, C. Aupetit-Berthelemot, J. Le Masson, E. Grard, and V. Rodrigues, "Up to 40Gb/s optically amplified AMOOFDM for next generation PON networks," in *Optical Fiber Communication Conference and Exposition (OFC/NFOEC), 2011 and the National Fiber Optic Engineers Conference*, 2011, pp. 1–3.
- [47] C. D. Poole and R. E. Wagner, "Phenomenological approach to polarisation dispersion in long single-mode fibres," *Electron. Lett.*, vol. 22, no. 19, p. 1029, 1986.
- [48] Recommendation ITU-T G.652, "Transmission media and optical systems characteristics – Optical fibre cables." Nov-2009.
- [49] ITU-T Recommendation G.691, "Optical interfaces for single channel STM-64 and other SDH systems with optical amplifiers." Mar-2006.
- [50] K. Uchiyama, S. Kawanishi, and M. Saruwatari, "Multiple-channel output all-optical OTDM demultiplexer using XPM-induced chirp compensation (MOXIC)," *Electron. Lett.*, vol. 34, no. 6, pp. 575–576, Mar. 1998.
- [51] T. Morioka, K. Mori, and M. Saruwatari, "Ultrafast polarisation-independent optical demultiplexer using optical carrier frequency shift through crossphase modulation," *Electron. Lett.*, vol. 28, no. 11, pp. 1070–1072, May 1992.
- [52] X. Wu, A. Bogoni, O. F. Yilmaz, S. R. Nuccio, J. Wang, and A. E. Willner, "8-fold 40-to-320-Gbit/s phase-coherent WDM-to-TDM multiplexing and 320-to-40-Gbit/s demultiplexing using highly nonlinear fibers," in *Optical Fiber Communication (OFC), collocated National Fiber Optic Engineers Conference, 2010 Conference on (OFC/NFOEC)*, 2010, pp. 1–3.
- [53] R. Tucker, "High-speed modulation of semiconductor lasers," *J. Light. Technol.*, vol. 3, no. 6, pp. 1180–1192, décembre 1985.
- [54] T. Ioannis, R. Ioannis, H. Robert, A. Neophytos, B. Aleksandra, and V. Richard, "Extraction of laser rate equations parameters for representative simulations of metropolitan-area transmission systems and networks," *Opt. Commun.*, vol. 194, pp. 109–129, 2001.
- [55] J. C. Cartledge and R. C. Srinivasan, "Extraction of DFB laser rate equation parameters for system simulation purposes," *J. Light. Technol.*, vol. 15, no. 5, pp. 852–860, May 1997.

- [56] J. J. Moré, "The Levenberg-Marquardt algorithm: Implementation and theory," in *Numerical Analysis*, vol. 630, G. A. Watson, Ed. Springer Berlin Heidelberg, pp. 105–116.
- [57] P. A. Morton, T. Tanbun-Ek, R. A. Logan, A. M. Sergent, P. F. Sciortino, and D. L. Coblentz, "Frequency response subtraction for simple measurement of intrinsic laser dynamic properties," *IEEE Photonics Technol. Lett.*, vol. 4, no. 2, pp. 133 – 136, Feb. 1992.
- [58] M. Ferrario, L. Marazzi, P. Boffi, A. Righetti, and M. Martinelli, "Impact of Rayleigh Backscattering on Stimulated Brillouin Scattering threshold evaluation for 10Gb/s NRZ-OOK signals," in *Conference on Lasers and Electro-Optics, 2008 and 2008 Conference on Quantum Electronics and Laser Science. CLEO/QELS 2008*, 2008, pp. 1–2.
- [59] O. V. Sinkin, R. Holzlohner, J. Zweck, and C. R. Menyuk, "Optimization of the split-step Fourier method in modeling optical-fiber communications systems," *J. Light. Technol.*, vol. 21, no. 1, pp. 61 – 68, Jan. 2003.
- [60] Q. Zhang and M. I. Hayee, "Symmetrized Split-Step Fourier Scheme to Control Global Simulation Accuracy in Fiber-Optic Communication Systems," *J. Light. Technol.*, vol. 26, no. 2, pp. 302 –316, Jan. 2008.
- [61] C. Schramm, "43 Gbit/s High-Gain PHOTORECEIVER." u2t photonics, 10 January 2003.
- [62] M. Morelli and M. Moretti, "Fine carrier and sampling frequency synchronization in OFDM systems," *IEEE Trans. Wirel. Commun.*, vol. 9, no. 4, pp. 1514–1524, Apr. 2010.
- [63] J. M. Cioffi and T. Kailath, "Fast, recursive-least-squares transversal filters for adaptive filtering," *IEEE Trans. Acoust. Speech Signal Process.*, vol. 32, no. 2, pp. 304–337, 1984.
- [64] J. M. Cioffi and T. Kailath, "An Efficient Exact-Least-Squares Fractionally Spaced Equalizer Using Intersymbol Interpolation," *IEEE J. Sel. Areas Commun.*, vol. 2, no. 5, pp. 743–756, 1984.
- [65] R. D. Gitlin and S. B. Weinstein, "Fractionally-Spaced Equalization: An Improved Digital Transversal Equalizer," *Bell Syst. Tech. J.*, vol. 60, no. 2, pp. 275–296, 1981.
- [66] Martin E. Austin, "Decision-feedback equalization for digital communication over dispersive channels," *MIT Lincoln Lab., Tech. Rep. 437*, Aug. 1967.
- [67] C. A. Belfiore and J. Park, J.H., "Decision feedback equalization," *Proc. IEEE*, vol. 67, no. 8, pp. 1143–1156, 1979.
- [68] D. George, R. Bowen, and J. Storey, "An Adaptive Decision Feedback Equalizer," *IEEE Trans. Commun. Technol.*, vol. 19, no. 3, pp. 281–293, 1971.
- [69] G. D. Forney, "Maximum-likelihood sequence estimation of digital sequences in the presence of intersymbol interference," *IEEE Trans. Inf. Theory*, vol. 18, no. 3, pp. 363–378, 1972.
- [70] G. Ungerboeck, "Adaptive Maximum-Likelihood Receiver for Carrier-Modulated Data-Transmission Systems," *IEEE Trans. Commun.*, no. 5, pp. 624 – 636, 1974.

- [71] D. G. Messerschmitt, "Design of a finite impulse response for the Viterbi algorithm and decision-feedback equalizer," in *International Conference on Communications, 10th, Minneapolis, Minn, 1974*, p. 37.
- [72] D. D. Falconer and F. R. Magee, "Adaptive channel memory truncation for maximum likelihood sequence estimation," *Bell Syst. Tech. J.*, vol. 52, pp. 1541–1562, Nov. 1973.
- [73] V. Curri, R. Gaudino, A. Napoli, and A. Nespola, "Advantages of using the electronic equalization together with innovative modulation formats in dispersion-limited systems," in *The 17th Annual Meeting of the IEEE Lasers and Electro-Optics Society, 2004. LEOS 2004, 2004*, vol. 2, pp. 749–750 Vol.2.
- [74] O. E. Agazzi and V. Gopinathan, "The impact of nonlinearity on electronic dispersion compensation of optical channels," in *Optical Fiber Communication Conference, 2004. OFC 2004, 2004*, vol. 1, p. 434–.
- [75] O. E. Agazzi, M. R. Hueda, H. S. Carrer, and D. E. Crivelli, "Maximum-likelihood sequence estimation in dispersive optical channels," *J. Light. Technol.*, vol. 23, no. 2, pp. 749–763, 2005.
- [76] H.-M. Bae, J. B. Ashbrook, J. Park, N. R. Shanbhag, A. C. Singer, and S. Chopra, "An MLSE Receiver for Electronic Dispersion Compensation of OC-192 Fiber Links," *IEEE J. Solid-State Circuits*, vol. 41, no. 11, pp. 2541–2554, 2006.
- [77] R. I. Killey, M. Sezer Erkilinc, R. Maher, M. Paskov, S. Kilmurray, R. Bouziane, B. C. Thomsen, S. J. Savory, and P. Bayvel, "Nyquist-WDM-based system performance evaluation," in *2013 15th International Conference on Transparent Optical Networks (ICTON), 2013*, pp. 1–4.
- [78] J. A. Lazaro, S. Knorr, B. Schrenk, I. Cano, V. Polo, J. Prat, A. Carena, and G. Bosco, "Digital Nyquist WDM for access networks using limited bandwidth reflective semiconductor optical amplifiers," in *Optical Fiber Communication Conference and Exposition (OFC/NFOEC), 2012 and the National Fiber Optic Engineers Conference, 2012*, pp. 1–3.
- [79] S. U. H. Qureshi, "Adaptive equalization," *Proc. IEEE*, vol. 73, no. 9, pp. 1349–1387, 1985.
- [80] A. J. Lowery, S. Wang, and M. Premaratne, "Calculation of power limit due to fiber nonlinearity in optical OFDM systems," *Opt. Express*, vol. 15, no. 20, p. 13282, 2007.
- [81] L. Anet Neto, "Etude des potentialités des techniques de modulation multiporteuse pour les futurs réseaux d'accès optique WDM et TDM PON," Thèse de doctorat: électronique des hautes fréquences et optoélectronique. Limoges : Université de Limoges, 2012.
- [82] J. Campello, "Optimal discrete bit loading for multicarrier modulation systems," in *1998 IEEE International Symposium on Information Theory, 1998. Proceedings, 1998*, p. 193.
- [83] B. Charbonnier, P. Urvoas, M. Ouzzif, and J. Le Masson, "Capacity optimisation for optical links using DMT modulation, an application to POF," in *34th European Conference on Optical Communication, 2008. ECOC 2008, 2008*, pp. 1–2.

- [84] R. van Nee and R. Prasad, *OFDM for Wireless Multimedia Communications*, 1st ed. Norwood, MA, USA: Artech House, Inc., 2000.
- [85] R. W. Tkach, A. R. Chraplyvy, F. Forghieri, A. H. Gnauck, and R. M. Derosier, "Four-photon mixing and high-speed WDM systems," *J. Light. Technol.*, vol. 13, no. 5, pp. 841–849, 1995.
- [86] E. Peral and A. Yariv, "Large-signal theory of the effect of dispersive propagation on the intensity modulation response of semiconductor lasers," *J. Light. Technol.*, vol. 18, no. 1, pp. 84–89, Jan. 2000.
- [87] J. M. Cioffi, "A multicarrier primer," *ANSI T1E1.4 Committee Contribution*, Nov. 1991.
- [88] P. S. Chow, J. M. Cioffi, and J. A. C. Bingham, "A practical discrete multitone transceiver loading algorithm for data transmission over spectrally shaped channels," *IEEE Trans. Commun.*, vol. 43, no. 234, pp. 773–775, Feb. 1995.
- [89] J. M. Cioffi, Class Textbook, EE379C "Advanced Digital Communications", <http://www.stanford.edu/class/ee379c/>.
- [90] Thomas Starr, John M. Cioffi, and Peter J. Silverman, *Understanding Digital Subscriber Line Technology*. New Jersey: Prentice Hall, 1999.
- [91] R. J. Baxley and G. T. Zhou, "Power savings analysis of peak-to-average power ratio in OFDM," *IEEE Trans. Consum. Electron.*, vol. 50, no. 3, pp. 792–798, 2004.
- [92] Y. Tang, W. Shieh, and B. S. Krongold, "DFT-Spread OFDM for Fiber Nonlinearity Mitigation," *IEEE Photonics Technol. Lett.*, vol. 22, no. 16, pp. 1250–1252, 2010.
- [93] M. Sung, S. Kang, J. Shim, J. Lee, and J. Jeong, "DFT-Precoded Coherent Optical OFDM With Hermitian Symmetry for Fiber Nonlinearity Mitigation," *J. Light. Technol.*, vol. 30, no. 17, pp. 2757–2763, 2012.
- [94] H. G. Myung, J. Lim, and D. Goodman, "Peak-To-Average Power Ratio of Single Carrier FDMA Signals with Pulse Shaping," in *2006 IEEE 17th International Symposium on Personal, Indoor and Mobile Radio Communications*, 2006, pp. 1–5.
- [95] D. Dardari, "Joint clip and quantization effects characterization in OFDM receivers," *IEEE Trans. Circuits Syst. Regul. Pap.*, vol. 53, no. 8, pp. 1741–1748, 2006.
- [96] S. Dimitrov, S. Sinanovic, and H. Haas, "Clipping Noise in OFDM-Based Optical Wireless Communication Systems," *IEEE Trans. Commun.*, vol. 60, no. 4, pp. 1072–1081, 2012.
- [97] A. Garcia-Armada, "SNR Gap Approximation for M-PSK-Based Bit Loading," *IEEE Trans. Wirel. Commun.*, vol. 5, no. 1, Jan. 2006.
- [98] B. Wedding, "Analysis of fibre transfer function and determination of receiver frequency response for dispersion supported transmission," *Electron. Lett.*, vol. 30, no. 1, pp. 58–59, 1994.
- [99] M. Speth, S. A. Fechtel, G. Fock, and H. Meyr, "Optimum receiver design for wireless broad-band systems using OFDM. I," *IEEE Trans. Commun.*, vol. 47, no. 11, pp. 1668–1677, Nov. 1999.

- [100] S. H. Han and J. H. Lee, "An overview of peak-to-average power ratio reduction techniques for multicarrier transmission," *IEEE Wirel. Commun.*, vol. 12, no. 2, pp. 56 – 65, Apr. 2005.
- [101] R. van Nee and A. de Wild, "Reducing the peak-to-average power ratio of OFDM," in *48th IEEE Vehicular Technology Conference, 1998. VTC 98, 1998*, vol. 3, pp. 2072 –2076 vol.3.
- [102] E. Vanin, "Performance evaluation of intensity modulated optical OFDM system with digital baseband distortion," *Opt. Express*, vol. 19, no. 5, pp. 4280–4293, Feb. 2011.
- [103] Julian J. Bussgang, "Crosscorrelation Functions of Amplitude-Distorted Gaussian Signals," PhD thesis, Massachusetts Institute of technology, 1952.
- [104] T. Frank, A. Klein, and T. Haustein, "A Survey on the Envelope Fluctuations of DFT Precoded OFDMA Signals," in *IEEE International Conference on Communications, 2008. ICC '08, 2008*, pp. 3495–3500.
- [105] R. W. Bauml, R. F. H. Fischer, and J. B. Huber, "Reducing the peak-to-average power ratio of multicarrier modulation by selected mapping," *Electron. Lett.*, vol. 32, no. 22, pp. 2056 –2057, Oct. 1996.
- [106] S. H. Muller and J. B. Huber, "A comparison of peak power reduction schemes for OFDM," in , *IEEE Global Telecommunications Conference, 1997. GLOBECOM '97, 1997*, vol. 1, pp. 1 –5 vol.1.
- [107] S. H. Müller, R. W. Bäuml, R. F. H. Fischer, J. B. Huber, and L. F. Nachrichtentechnik, *OFDM with Reduced Peak-to-Average Power Ratio by Multiple Signal Representation*. 1997.
- [108] S. H. Muller and J. B. Huber, "A novel peak power reduction scheme for OFDM," in , *The 8th IEEE International Symposium on Personal, Indoor and Mobile Radio Communications, 1997. Waves of the Year 2000. PIMRC '97, 1997*, vol. 3, pp. 1090–1094 vol.3.
- [109] T. Wattanasuwakull and W. Benjapolakul, "PAPR Reduction for OFDM Transmission by using a method of Tone Reservation and Tone Injection," in *2005 Fifth International Conference on Information, Communications and Signal Processing, 2005*, pp. 273 –277.
- [110] Mohamad Mroué, Amor Nafkha, Jacques Palicot, Benjamin Gavalda, and Nelly Dagherne, "Performance and Implementation Evaluation of TR PAPR Reduction Methods for DVB-T2," *International Journal of Digital Multimedia Broadcasting*, p. 10, 2010.
- [111] T. José and John M. Cioffi, "Peak Power Reduction for Multicarrier Transmission," *Proc. IEEE GLOBECOM*, 1998.
- [112] H. Liang, K.-C. Chung, H. Chen, and Y.-F. Huang, "A modified constellation extension scheme with low complexity for PAPR reduction in OFDM systems," in *Wireless and Optical Communications Conference (WOCC), 2010 19th Annual*, 2010, pp. 1 –4.
- [113] R. S. Prabhu and E. Grayver, "Active constellation modification techniques for OFDM PAR reduction," in *2009 IEEE Aerospace conference, 2009*, pp. 1 –8.

- [114] B. S. Krongold and D. L. Jones, "PAR reduction in OFDM via active constellation extension," *IEEE Trans. Broadcast.*, vol. 49, no. 3, pp. 258 – 268, Sep. 2003.
- [115] T. M. Schmidl and D. C. Cox, "Robust frequency and timing synchronization for OFDM," *IEEE Trans. Commun.*, vol. 45, no. 12, pp. 1613 –1621, Dec. 1997.
- [116] H. Minn, V. K. Bhargava, and K. B. Letaief, "A robust timing and frequency synchronization for OFDM systems," *IEEE Trans. Wirel. Commun.*, vol. 2, no. 4, pp. 822 – 839, Jul. 2003.
- [117] H. Minn, M. Zeng, and V. K. Bhargava, "On timing offset estimation for OFDM systems," *IEEE Commun. Lett.*, vol. 4, no. 7, pp. 242 –244, Jul. 2000.
- [118] K. Shi and E. Serpedin, "Coarse frame and carrier synchronization of OFDM systems: a new metric and comparison," *IEEE Trans. Wirel. Commun.*, vol. 3, no. 4, pp. 1271 – 1284, Jul. 2004.
- [119] B. Park, H. Cheon, C. Kang, and D. Hong, "A novel timing estimation method for OFDM systems," *IEEE Commun. Lett.*, vol. 7, no. 5, pp. 239 –241, May 2003.
- [120] G. Yi, L. Gang, and G. Jianhua, "A novel time and frequency synchronization scheme for OFDM systems," *IEEE Trans. Consum. Electron.*, vol. 54, no. 2, pp. 321 –325, May 2008.
- [121] J. J. van de Beek, M. Sandell, and P. O. Borjesson, "ML estimation of time and frequency offset in OFDM systems," *IEEE Trans. Signal Process.*, vol. 45, no. 7, pp. 1800 –1805, Jul. 1997.
- [122] A. Awoseyila, C. Kasparis, and B. Evans, "Improved preamble-aided timing estimation for OFDM systems," *IEEE Commun. Lett.*, vol. 12, no. 11, pp. 825 –827, Nov. 2008.
- [123] G. Ren, Y. Chang, H. Zhang, and H. Zhang, "Synchronization method based on a new constant envelop preamble for OFDM systems," *IEEE Trans. Broadcast.*, vol. 51, no. 1, pp. 139 – 143, Mar. 2005.
- [124] X. Q. Jin and J. M. Tang, "Optical OFDM Synchronization With Symbol Timing Offset and Sampling Clock Offset Compensation in Real-Time IMDD Systems," *IEEE Photonics J.*, vol. 3, no. 2, pp. 187 –196, Apr. 2011.
- [125] D. Godard, "Self-Recovering Equalization and Carrier Tracking in Two-Dimensional Data Communication Systems," *IEEE Trans. Commun.*, vol. 28, no. 11, pp. 1867–1875, 1980.
- [126] J.-J. van de Beek, O. Edfors, M. Sandell, S. K. Wilson, and P. Ola Borjesson, "On channel estimation in OFDM systems," in *Vehicular Technology Conference, 1995 IEEE 45th*, 1995, vol. 2, pp. 815–819 vol.2.
- [127] X. Liu and F. Buchali, "Intra-symbol frequency-domain averaging based channel estimation for coherent optical OFDM," *Opt. Express*, vol. 16, no. 26, pp. 21944–21957, Dec. 2008.
- [128] O. Edfors, M. Sandell, J.-J. van de Beek, S. K. Wilson, and P. O. Borjesson, "OFDM channel estimation by singular value decomposition," in *Vehicular Technology Conference, 1996. Mobile Technology for the Human Race., IEEE 46th*, 1996, vol. 2, pp. 923–927 vol.2.

## Résumé

Cette thèse vise à améliorer l'efficacité spectrale des transmissions sur fibres optiques dans le cadre de réseaux d'accès où une technique de modulation d'intensité et détection directe (IMDD) est utilisée. Dans un tel contexte, une augmentation de la longueur de fibre ou du débit pourrait conduire à une importante interférence entre symboles. Dans cette thèse, l'utilisation des techniques de traitement du signal pour compenser des défauts du canal de transmission est analysée. En outre, le potentiel de la technique de multiplexage par répartition orthogonale de la fréquence (OFDM) est également étudié. Puisque les études décrites dans cette thèse sont largement basées sur les résultats de simulations numériques, la première partie de ce mémoire est dédiée à la modélisation avancée d'une liaison de transmission sur fibres optiques. À la fois l'extraction des paramètres et la validation du modèle sont réalisées avec des mesures expérimentales.

La première étude concerne les techniques d'égalisation de canal pour une transmission classique de type non retour à zéro (NRZ). Il se trouve que les techniques d'égalisation linéaires peuvent augmenter la portée de transmission par une douzaine de kilomètres. Lorsque des égaliseurs non linéaires sont utilisés, la portée est davantage augmentée par plusieurs dizaines de kilomètres et la pénalité de puissance à cause de la dispersion chromatique est améliorée jusqu'à 2 dB. En outre, lorsque le filtre de mise en forme de Nyquist est utilisé, la pénalité de puissance est encore améliorée par 2 dB.

La deuxième étude concerne l'évaluation des performances de la modulation OFDM. En particulier, les systèmes conventionnels de modulation adaptée proposés par Levin-Campello sont étudiés. En précodant des symboles OFDM par une matrice de la transformation de Fourier discrète (DFT), un système OFDM précodé est également proposé. Ayant les mêmes performances en termes de débit par rapport au système Levin-Campello, le système proposé permet de réduire de manière significative le facteur de crête (PAPR) d'un signal transmis, ce qui réduit la consommation de puissance d'un amplificateur de puissance à l'émetteur. De plus, par rapport à la modulation tout ou rien (OOK), la modulation OFDM se révèle être plus robuste contre la dispersion chromatique et les chirps du laser.

Enfin, les techniques conventionnelles et proposées pour compenser des défauts d'une modulation OFDM, y compris l'important PAPR et la sensibilité à la synchronisation temporelle sont étudiées. Les techniques proposées pour la synchronisation temporelle ont des meilleures performances en termes de précision et complexité par rapport aux techniques classiques. Pour réduire le PAPR d'un signal OFDM, une technique basée sur des pilotes réservées est proposée. Dans un système OFDM précodé, cette technique apporte une réduction de PAPR pouvant atteindre 4 dB.

**Mots-clés :** Traitement du signal – Techniques numériques, Télécommunications optiques, Fibres optiques, Modulation d'intensité, Détection directe, Multiplexage par répartition orthogonale de la fréquence, Réseaux d'accès optiques, Synchronisation

## Abstract

This thesis aims at improving the spectral efficiency of fiber-based optical transmissions in the context of access networks where an Intensity Modulated/Direct Detected (IMDD) technique is used. In such a context, an increase of fiber length or data rate might lead to significant inter symbol interference problem. For the reason of cost, instead of investing in expensive technologies, a telecom operator might prefer compensating transmission detriments by means of signal processing techniques. In this thesis, the compensation of transmission detriments using signal processing techniques is addressed. In addition, the potential of advanced modulation techniques such as the Orthogonal Frequency Division Multiplexing (OFDM) is also studied. The studies described in this thesis are extensively based on numerical simulation results. Therefore, the first part of this thesis is dedicated to the modeling of an optical transmission link. Both model parameter extraction and model validation are carried out by means of experimental measures.

Based on the channel model, the first study concerns channel equalization techniques for a conventional on-off-keying non return-to-zero transmission. It is found that linear equalization techniques may extend transmission reach by tens of kilometers. When nonlinear equalizers are used, reach is further extended by tens of kilometers and chromatic dispersion-induced power penalty is improved by up to 2 dB. Moreover, when the Nyquist pulse-shaping technique is used, the power penalty is further improved by 2 dB.

The second study in this thesis is dedicated to the performance evaluation of OFDM modulation. Particularly, conventional Levin-Campello bit/power loading OFDM systems are subjected to the study. Based on the Discrete Fourier Transform (DFT) precoding technique, a precoded OFDM system is also proposed. Having the same data-rate performance when compared to the Levin-Campello system, the proposed system significantly reduces the Peak-to-Average Power Ratio (PAPR) of a transmitted signal, resulting in reduced power consumption of the power amplifier on the transmitter side. Moreover, when compared to the actual on-off-keying modulation, the OFDM modulation is shown to be more robust against chromatic dispersion and laser chirps.

Finally, conventional and proposed techniques to compensate for OFDM disadvantages including the important PAPR and the sensitivity to timing synchronization are investigated. The proposed synchronization techniques are shown to outperform conventional techniques in terms of timing offset variance and complexity. To reduce the PAPR of a transmitted OFDM signal, a contiguous-tone tone reservation technique is proposed. When this technique is used in a precoded OFDM system, the PAPR is shown to be reduced by up to 4 dB.

**Keywords :** Signal processing – Digital techniques, Optical communications, Optical fibers, Intensity-modulated, Direct-detected, Orthogonal frequency division multiplexing, Passive optical networks, Synchronization